

# Time-Resolved Two-Photon Photoemission of NiO Ultra-Thin Films on Ag(001)

## Dissertation

zur Erlangung des akademischen Grades  
Doctor rerum naturalium (Dr. rer. nat.)

vorgelegt von

Dipl. Phys. Mario Kiel

geboren am 05. August 1980 in Halle



Institut für Physik  
der Naturwissenschaftlichen Fakultät II  
der Martin-Luther-Universität Halle-Wittenberg

Gutachter:

1. Prof. Dr. W. Widdra  
Martin-Luther-Universität Halle-Wittenberg
2. PD Dr. G. Seifert  
Martin-Luther-Universität Halle-Wittenberg
3. Prof. Dr. M. Bauer  
Christian-Albrechts-Universität Kiel

Halle (Saale), verteidigt am 21.03.2012



*A second can be calculated by*

$$T_{exp} \cdot f_{laser} \cdot t_{pulse} ,$$

*where  $T_{exp}$  is the total working time at the experimental setup,  
 $f_{laser}$  the repetition rate of the laser,  
and  $t_{pulse}$  the duration of a single pulse.*

—  
*Thus, the present work documents one second of photoemission.*



# Contents

<b>Abbreviations</b>	<b>3</b>
<b>1 Introduction</b>	<b>5</b>
<b>2 Fundamentals</b>	<b>9</b>
2.1 Angle-resolved photoemission . . . . .	9
2.2 Two-photon photoemission . . . . .	10
2.3 Time-resolved two-photon photoemission . . . . .	12
<b>3 Experimental</b>	<b>13</b>
3.1 The UHV-apparatus . . . . .	13
3.1.1 Basic setup . . . . .	13
3.1.2 Sample preparation and NiO film growth . . . . .	15
3.1.3 Electron energy analyzer . . . . .	16
3.2 The fs-laser system . . . . .	19
3.3 Software development . . . . .	20
<b>4 Results and discussion</b>	<b>23</b>
4.1 Growth of NiO on Ag(001) . . . . .	23
4.1.1 Introduction . . . . .	23
4.1.2 Thickness-dependent electronic and morphological structure . . . . .	24
4.2 Image-potential states of NiO/Ag(001) . . . . .	28
4.2.1 Introduction . . . . .	28
4.2.2 IPS of Sub-ML NiO coverages . . . . .	30
4.2.3 Image states of 2 ML NiO/Ag(001) . . . . .	38
4.2.4 Image states of lacerated NiO films – Heating the monolayer and bilayer . . . . .	44
4.2.5 Image states of higher NiO coverages . . . . .	49
4.3 Unoccupied Ni-3 <i>d</i> states of NiO films . . . . .	58
4.3.1 Introduction . . . . .	58
4.3.2 The first monolayer NiO/Ag(001) . . . . .	60
4.3.3 The bi- and trilayer of NiO/Ag(001) . . . . .	66
4.3.4 Heating the monolayer and bilayer of NiO . . . . .	68
4.3.5 Four and eight monolayers NiO/Ag(001) . . . . .	72
4.3.6 Unoccupied states – comparison of experimental methods . . . . .	77
4.4 NiO assisted observation of Ag bulk bands . . . . .	83
4.4.1 Introduction . . . . .	83
4.4.2 Ag- <i>sp</i> band resonance – surface-assisted umklapp process at the NiO monolayer . . . . .	86
4.4.3 Umklapp process mediated by antiferromagnetic NiO(001) . . . . .	93

<b>5 Summary</b>	<b>103</b>
<b>6 Appendix</b>	<b>105</b>
6.A Intensity correction of 2PPE data due to laser fluctuations . . . . .	105
6.B Methods for background subtraction . . . . .	108
6.C Lifetime analysis using integrated intensities . . . . .	110
6.D Method-intrinsic energy shift in STS . . . . .	112
<b>7 Bibliography</b>	<b>115</b>

---

# Abbreviations

<b>2PPE</b>	two-photon photoemission
<b>BZ</b>	Brillouin zone
<b>EELS</b>	electron energy loss spectroscopy
<b>FER</b>	field emission resonance
<b>IPE</b>	inverse photoemission spectroscopy
<b>IPS</b>	image-potential state
<b>LEED</b>	low energy electron diffraction
<b>ML</b>	monolayer
<b>NOPA</b>	non-collinear optical parametric amplifier
<b>PES</b>	photoelectron spectroscopy
<b>SBZ</b>	surface Brillouin zone
<b>SHG</b>	second harmonic generation
<b>STM</b>	scanning tunneling microscopy
<b>STS</b>	scanning tunneling spectroscopy
<b>THG</b>	third harmonic generation
<b>UPS</b>	ultra-violet photoelectron spectroscopy
<b>XPS</b>	X-ray photoelectron spectroscopy





# 1 Introduction

From a scientific point of view, transition metal oxides are very interesting materials with a large variety of physical and chemical properties. This variety is barely found in any other class of materials. These oxides can show insulating as well superconducting properties, they have ferromagnetic or antiferromagnetic ordering, and they can have catalytic as well as gas and pressure sensitive properties, to mention only a few important issues. Most of the functional properties are determined by the electronic structure of the oxide. Depending on the particular application, the bulk or surface properties lead to the functionality. For the case of a catalyst in heterogeneous catalysis the surface electronic structure is responsible for the preferred adsorption site of molecules and determines the sticking, the diffusion, the decomposing, and the reaction with other adsorbed atoms. An adsorption-induced change of the electronic structure and thereby a change of e.g., the electric resistance is applicable in gas sensors. On the other side bulk properties enable functionality as well. The splitting of metal  $d$  states in the crystal field of the surrounding oxygen in transition metal oxides determines the optical absorption. The crystal field leads to a partial lifting of the parity selection rule which enables  $d-d$  transitions [1,2]. This determines the color of the compound. This effect is explicitly used in solid state lasers. The crystal field splitting of a chromium substitutional impurity ( $\rightarrow\text{Cr}^{3+}$ ) in sapphire ( $\text{Al}_2\text{O}_3$ ) enables the characteristic radiation of the ruby laser ( $\lambda=694.3\text{ nm}$ ). Using titanium instead ( $\rightarrow\text{Ti}^{3+}$ ) leads to the Ti:sapphire laser ( $\lambda=670\text{--}1100\text{ nm}$ ).

In most cases, it is not only the pure scientific interest, which drives the investigation of physical and chemical processes at surfaces and interfaces. Two famous examples with oxides involved have to be mentioned, namely the heterogeneous catalysis and the giant magneto resistance (GMR). Both effects are of great industrial interest. The optimization of chemical processes is mainly a question of efficiency and costs. Therefore, most industrial important materials are produced by catalytic processes. The heterogeneous catalysis is a special case with often gaseous reagenting materials and solid catalysts. The Haber-Bosch process is one of the important processes for the production of ammonia<sup>1</sup>. The main chemical reaction to produce ammonia<sup>2</sup> is



Although it is an exothermic reaction, the energy barrier between reagents and product is large. This prevents a spontaneous reaction. The energy barrier could be reduced in the presence of a suitable catalyst. However, still a high temperature of

---

<sup>1</sup>Ammonia is one of the mostly produced chemical and the basis for all other nitrogen based compounds e.g., fertilizers.

<sup>2</sup>The starting reagents are nitrogen (from air), methane, and water vapor. To produce the reactants of equation 1.1 some other, partially catalytic supported reactions and purifications are necessary.

approx. 700 K and a pressure of around  $3 \times 10^5$  hPa is necessary to enable an efficient reaction. The starting material of the catalyst is magnetite (iron(II,III) oxide  $\text{Fe}_3\text{O}_4$  or  $\text{FeO} \cdot \text{Fe}_2\text{O}_3$ ). This is reduced to iron in the presence of hydrogen. The nitrogen and hydrogen molecules adsorb at the iron surface and decompose. The adsorption of  $\text{N}_2$  and the subsequent decomposition to individual nitrogen atoms has been identified as the rate limiting process [3]. Once the reagents are adsorbed they react with each other to ammonia in three additional steps  $\text{NH} \rightarrow \text{NH}_2 \rightarrow \text{NH}_3$  [3,4]. The ammonia desorbs from the surface and is separated from the gas phase in another cooling unit. The remaining unreacted nitrogen and hydrogen is returned for further reaction. The importance of the investigation of catalytic processes is emphasized by several Nobel prizes of chemistry for the work in this field to Fritz Haber (1918), Carl Bosch and Friedrich Bergius (1931), as well as Gerhard Ertl (2007). Another famous example of functional thin films becomes evident in everyday life when using the hard disc drive in a computer. Modern read heads consists of specially designed multi-layer systems which use the GMR effect to detect small magnetic features reliably. This enables to increase the bit density on a hard disc significantly. The physical process behind is the resistance between a stack of two magnetic layers separated by an oxide spacer of few atomic layers thickness<sup>3</sup>. The difference of the resistance between the parallel or antiparallel magnetic alignment is used to determines the state of the stored bit. The Nobel prize of physics to Albert Fert and Peter Grünberg (2007) demonstrates the importance of these scientific investigations.

The progressive miniaturization of electronic devices demands for new fabrication methods of well defined functional structures on one side and a detailed understanding of the physical and chemical processes on the other side. The smaller the devices get the larger are contributions of surface and interface effects to the functionality of active components. The development of new devices based on ultra-thin films and multi-layer systems is one of the main field of work with promising new properties of active materials. The expected change of the structural and electronic properties of ultra-thin films compared to bulk ones allows to tune the properties of a device to the requested characteristic. Therefore, it is inevitable to investigate the properties from a fundamental point of view, to understand the basic physical and chemical processes.

The transition metal oxide NiO is neither a pure Mott-Hubbard insulator nor a pure charge transfer insulator [6]. However, it is the prototype to investigate the physical properties of charge transfer insulators. The origin of the insulating character of MnO, CoO or NiO is the strong localization of the  $3d$  electrons within the partially filled  $d$  states. The calculation of the band structure in the single particle picture fails for these system. This is the reason for intense investigations for the last decades to develop new approaches for the description of this fascinating class of materials. The investigation of ultra-thin oxide films on metal substrates enables to study e.g, the thickness-dependent electronic structure, the influence of the substrate as well as the decoupling from the substrate for larger film thicknesses, and the transition to bulk-like properties with the formation of a band gap.

Up to now only little is known about the electronic structure of unoccupied states in transition metal oxides, and almost nothing about the electron dynamics. In

---

<sup>3</sup>Referring to the investigated NiO in the present work, the applicability of NiO as the oxidic part in a read head based on GMR has been reported by Nakamoto *et al.* [5].

the present work the electronic structure of NiO ultra-thin films on a Ag(001) substrate has been investigated by time-resolved two-photon photoemission (2PPE). This method is the *state of the art* for the investigation of unoccupied electronic states. It provides a better energy resolution as compared to inverse photoemission. In addition, the utilization of two fs-laser pulses allows a direct investigation of the electron dynamics in the time domain. As will be shown in section 2.2 the 2PPE is intrinsically limited to the energy range between the Fermi and the vacuum level. In the present work the laser setup delivers two independently tunable fs-laser pulses. This enables to tune the photon energies directly to the needs of the investigated system. It is possible to adjust the photon energy close to the position of the vacuum level for the excitation of all states below. On the other side a targeted adjustment to resonant electron transitions between initial and intermediate or intermediate and final states becomes possible. The center of interest is the identification of electronic states of ultra-thin NiO films, their thickness-dependent properties, the influence of the underlying substrate and the decoupling of the same, and the investigation of the electron dynamics. In the following these particular issues will be discussed in more detail to bring them closer to the context of nickel oxide.

A first approach to the properties of the surface electronic structure is the investigation of image-potential states. These electrons in front of the sample surface form a Rydberg series which converges to the vacuum level [7,8]. They do not belong directly to the band structure of the thin film<sup>4</sup>, however, their properties allow definite conclusion about the same. In section 4.2 the experimental observations of image-potential states on NiO ultra-thin films will be discussed. They are used as sensors to characterize the macroscopic permittivity of the sample. This allows to investigate the behavior of the NiO ultra-thin films and to compare the results with the expected bulk properties. For the NiO bilayer a good agreement with the bulk value of  $\epsilon_r=12$  [9] is already observed. The energetic position of the band gap with respect to the vacuum level influences the binding energy of the image-potential state as well as the coupling of the wave function to the bulk. The latter one has a strong impact on the electron dynamics and the observed lifetimes. Since the lifetime of image-potential states is sensitive to surface defects (e.g., adatoms or steps [10–14]) the observed large value of the lifetime evidences a well-ordered surface. Thereby, the local character of the image-potential states serves as a local probe of the otherwise spatially integrative method two-photon photoemission.

Beside the observation of image-potential states, unoccupied Ni-3*d* states has been investigated as presented in section 4.3. Thereby, the evolution of the electronic states in dependence of the film thickness is one of the major interests. The developing band gap with increasing thickness provokes the question about the involved initial and intermediate states during the 2PPE process. The expected correlation effects of the electron system in the presence of holes or excess electrons has to be considered in the interpretation of photoemission data as well. However, the comparison with scanning tunneling spectroscopy data reveals a good agreement over a large thickness variation [15], although it is a complementary technique with respect to the electronic final state. This allows to characterize the pump-probe mechanism with an electron transfer from the metal substrate to the oxide film, accompanied with only small contributions of correlation effects.

---

<sup>4</sup>They are neither bulk nor surface states in the normally used manner.

The last section 4.4 is devoted to electron transitions in the Ag(001) substrate in the presence of a thin NiO film. A surface-assisted umklapp process, which is mediated by the reconstruction of the NiO overlayer, is able to explain otherwise not assigned features in the 2PPE spectra. This effect is independent of whether the reconstruction is due to a structural relaxation as observed for the NiO monolayer (section 4.4.2) or due to antiferromagnetic ordering of thicker films (section 4.4.3). The latter one could be used to determine the thickness-dependent Néel temperature of NiO thin films with a high sensitivity.

---

## 2 Fundamentals

### 2.1 Angle-resolved photoemission

The photoelectric effect describes the interaction between photons and solids. Experimentally it has been demonstrated the first time by Hertz [16] and Hallwachs [17] in 1887. The theoretical description has been given by Einstein in 1905 [18] and is one of the main contributions for the Nobel prize in 1921. The photoemission spectroscopy is based on the photoelectric effect. Energetically, the process is characterized by

$$E_{kin} = h\nu - E_B - \Phi , \quad (2.1)$$

where  $E_{kin}$  is the kinetic energy of the photoelectron,  $h\nu$  the photon energy of a photon with the frequency  $\nu$ ,  $E_B$  the binding energy of the electron before excitation, and  $\Phi$  the work function. Depending on the photon energy one discriminates between ultra-violet and X-ray photoemission electron spectroscopy (UPS and XPS, in general called photoelectron spectroscopy PES). The PES is applicable to determine the electronic structure of occupied states. Equation 2.1 is used to calculate the binding energies of the occupied states. The energy diagram is depicted in Fig. 2.1 (a) (page 11). The gray shaded areas indicate the projected band structure of the occupied (dark gray) and the unoccupied (light gray) states. However, one has to consider that the final state in photoemission is characterized by the photoelectron itself *and* the remaining hole in the sample<sup>1</sup> as indicated by the open red circle. Thus, the calculated binding energy corresponds not necessarily to the ground state of the electronic system.

The photoemission can be described by the three-step model which is surely not accurate but it helps to illustrate the basic mechanisms. The three steps are:

1. inner photoelectric effect: dipole-allowed electron excitation by a photon within the solid
2. transport of the electron to the surface, whereby also scattering could occur
3. escape of the electron off the surface by overcoming the surface potential.

The first step describe the electron excitation between Bloch states in the solid. According to Fermi's golden rule, the transition probability  $w$  between the initial states  $\Psi_i$  at  $E_i$  and the final state  $\Psi_f$  at  $E_f$  due to a small perturbation  $\Delta$  is calculated by

$$w \propto |\langle \Psi_f | \Delta | \Psi_i \rangle|^2 \delta(E_f - E_i - h\nu) . \quad (2.2)$$

This equation considers elastic electron transitions as indicated by the delta function  $\delta(E_f - E_i - h\nu)$ . The perturbation operator  $\Delta$  in the transition matrix element

---

<sup>1</sup>A remaining hole is only a simple picture. One has to consider that the whole crystal reacts on electron excitations due to band structure and correlation effects.

is given by  $-\frac{e}{m_e c} \vec{A} \cdot \vec{p}$  within the dipole approximation ( $\vec{A}$  vector potential of the incident light,  $\vec{p}$  momentum operator). Note that the transition between the initial and the final state underlies the dipole selection rules [19]. Thus, not only the energy difference between electronic bands but also the type of the involved bands determines the transition matrix element. The second step describes the scattering processes which lead to a structureless background in the photoemission spectra. Thereby, the mean free path of electrons of a few atomic distances bases the surface sensitivity of PES. The third step takes the change of the electron momentum during pass through the surface potential into account. The intensity of the emitted photoelectrons is directly related to the transition probability  $w$  and is plotted as a function of the kinetic energy.

The emission angle of the photoelectron could be attributed to a line within the Brillouin zone. All electron transitions with wave vectors along this lines contribute to the photoelectron signal. The experimental setup allows to separate the wave vector into a parallel momentum ( $k_{\parallel}$ ) and a perpendicular momentum ( $k_{\perp}$ ). The parallel component is conserved upon photoemission which leads to the well known relationship

$$k_{\parallel} = \sin\theta \sqrt{\frac{2m}{\hbar^2} E_{kin}} \quad (2.3)$$

$$k[\text{\AA}^{-1}] = 0.5123 \sin\theta \sqrt{E_{kin}[\text{eV}]} , \quad (2.4)$$

where  $\theta$  is the emission angle and  $E_{kin}$  the kinetic energy of the electron in front of the sample. However, the perpendicular component of the wave vector is not conserved. Thus, it could not be derived from a single photoemission experiment. To analyze the electronic structure for all wave vectors, photoemission with different photon energies and at different surface orientations are necessary. This allows to deduce the complete  $k$  information which is condensed under the generic name *band mapping*. For detailed discussions on this topic the reader is referred e.g., to the review article of Feuerbacher and Willis [20] and the overview article of Reinert and Hüfner [21].

## 2.2 Two-photon photoemission

In contrast to PES, the two-photon photoemission spectroscopy (2PPE) allows to determine the electronic structure of unoccupied states. It is a pump-probe spectroscopy, where a first laser pulse excites electrons from an occupied into an unoccupied state. A second laser pulse excites the electrons of the transiently occupied intermediate state into the continuum above the vacuum level, where the electron is detected with an electron energy analyzer. The calculation of the parallel momentum according to equation 2.4 is similar to PES. Figure 2.1 (b) depicts five different excitations schemes. For simplicity, the final state energy is assumed to be equivalent for all discussed scenarios. Two different photon energies in the UV ( $h\nu_{UV}$ ) and IR range ( $h\nu_{IR}$ ) are indicated by different length and colors of the corresponding arrows. The cases ① and ② show the non-resonant 2PPE excitations of an occupied state into the final state via a virtual intermediate state. The black line below  $E_F$  indicates the initial state. This could originate from an energetically sharp bulk band or

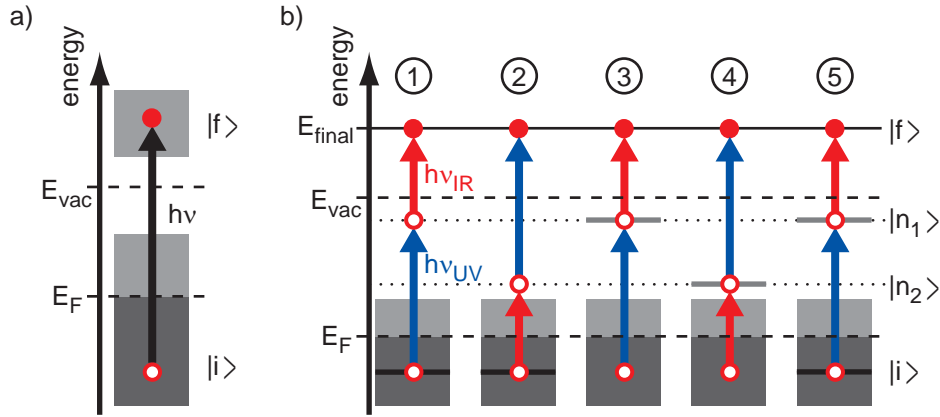


**Figure 2.1:** (a) Energy diagram for PES. The gray shaded areas indicate the projected band structure of the sample. (b) Different excitation schemes in 2PPE which lead to a similar final state energy. ① and ② excitation from an occupied state via a virtual intermediate state. ③ and ④ excitation from transiently occupied intermediate states. ⑤ resonance between initial and intermediate state.

from a surface/interface state. The gray-shaded areas indicates the projected band structure of the bulk. Both excitations ① and ② are indistinguishable in the spectrum due to the virtual character of the intermediate states. The final state energy depend on both photon energies similarly and the feature originates (or involves) an occupied state. Similar to the previous scenarios, the cases ③ and ④ depict the excitation of a real intermediate states. The final state energy in ③ depends on the IR but not on the UV energy, and vice versa for the case ④. Thus, the photon energy dependent shift of a feature in the 2PPE spectrum reveals one of the pump-probe schemes ①–④. This has been investigated by Wallauer and Fauster at the Cu(111) surface [22] where the feature originating from the occupied surface state shows a larger energy shift as the unoccupied image-potential state. A resonant transition from an energetically sharp initial into an intermediate state is shown in scenario ⑤. The final state energy depends again on the IR energy (IR-probed). But tuning the UV energy off the resonance between initial and intermediate state, the feature vanishes. If the two bands exhibit an additional dispersion in  $k_{\perp}$  (not shown here), the resonance might be realized at different momenta. This is accompanied with a change of the observed intermediate state energy in dependence of the pump photon energy. This shift is not necessarily equivalent to the change of the photon energy (energy shift  $\geq$  or  $\leq$  pump photon energy). For completeness, it has to be mentioned that the final state contributes to the 2PPE signal as well. If the energy matches an unoccupied state of the sample a resonance could occur. This leads again to a photon-energy dependent peak position of the feature in the 2PPE spectrum as exemplary reported for combined 1PPE and 2PPE studies of intra-band transition observed at Ag(111) [23,24] and 2PPE on Cu(111) [25], recently. These five scenarios show that a wide-range tunability of the photon energies is of great interest for the investigation of the electronic structure of complicated systems. It enables to discriminate between different excitation schemes and to determine the influence of the initial, intermediate, and final state to the 2PPE signal. The laser adjustment

of two independently tunable fs-laser pulses allows three important measurement modes. At first, it is possible to investigate the influence of the initial state by changing the pump-photon energy (constant-intermediate/final states). Secondly, the influence of the final state is examined by changing the probe-photon energy (constant-initial/intermediate states). And third, the contribution of the intermediate state could be investigated by changing both photon energies simultaneously (constant initial/final states). The detailed analysis allows a targeted adjustment to resonances between involved states which could increase the photoemission yield. This will be applied to laser-excited time-resolved two-photon photoemission electron microscopy (tr-2P PEEM) in future projects. The expected differences of the electronic structure of spatially distributed islands or domains lead to an increase of the contrast in the PEEM image in dependence of the applied photon energies.

## 2.3 Time-resolved two-photon photoemission

In a two-color 2PPE experiment, as depicted in Fig. 2.1 (b), it is possible to change the temporal delay between the two laser pulses as well. The analysis of the time-dependent 2PPE intensity allows to investigate the electron dynamics. The electron excitation in the 2PPE process can be described by a three-level system, namely the initial (also: ground state), the intermediate, and final state. Typical lifetimes of the excited states are in the order of femtoseconds and therefore in the same order of the duration of the laser pulses. Thus, the population of the states changes during the excitation process. The dynamic within the three-level system can be generally described by the Liouville-von Neumann equation. It describes the temporal evolution of the density matrix. Applying the rotating wave approximation one obtains the well-known optical Bloch equations [26–30]. They are used for numerical simulation of the energy and time-resolved 2PPE data. However, the large amount of parameters e.g., the dephasing rates of the involved states or the exact position of the temporal overlap of both laser pulses, lead to some necessary considerations the fit the equations to the experimental data properly.

For the case of a large pure dephasing rate of the intermediate state in addition to a lifetime comparable to the pulse duration, the optical Bloch equations reduce to rate equations [27]. In the present work the lifetime will be derived from the time-resolved 2PPE intensities assuming simple exponential decays of the intermediate state population which reflects the 2PPE intensity. The finite duration of the laser pulses is considered by a Gaussian-shaped experimental function, namely the cross-correlation. The convolution of both is fitted to the experimental data. The lifetime of the excited states is assumed to be equal to the time constant of the exponential decay. The applicability of this method has been proved at the well-known image-potential states on Ag(001). A good agreement with literature data has been obtained [10,31–33]. This might not work for more sophisticated electronic systems as e.g., the strongly-correlated electron system of the NiO observed here. However, the time constant of an assumed exponential decay reveals the upper limit of any involved inverse decay rate. This is assumed to be sufficient for the first-time analysis of this class of materials presented here. For the deeper understanding of the processes involved in the electron dynamics a more accurate description in terms of optical Bloch equations will become necessary in future work.



## 3 Experimental

In this chapter the experimental setup will be described. At first the ultra-high vacuum chamber and its components will be discussed. The characterization of the electron analyzer regarding the energy and angular resolution will be depicted. The second part will deal with the laser system. In the last part the main aspects of the data acquisition will be discussed.

### 3.1 The UHV-apparatus

#### 3.1.1 Basic setup

A schematic top view of the vacuum chamber is shown in Fig. 3.1 (a). It is specially designed for photoemission experiments. The electron analyzer (*Phoibos 150mm*, Specs, Berlin) on the right side will be discussed in more detail in section 3.1.3. On the left side the main parts for sample preparation and characterization are depicted. The chamber has a cylindrical shape. A differentially pumped rotary flange with a diameter of  $\sim 400$  mm is mounted on top (gray striped area, angle  $\Delta$ ). The whole manipulator is excentrically mounted on the large rotary flange. It enables to move the sample in all three dimensions ( $x$  and  $y \pm 10$  mm and  $z \sim 500$  mm). An additional small rotary flange (also differentially pumped) enables to rotate the sample continuously in polar direction  $\delta$ . This special design allows to arrange the vacuum equipment on the periphery of the cylinder (at different angles and different heights). The position of the sample with respect to different sites is mainly

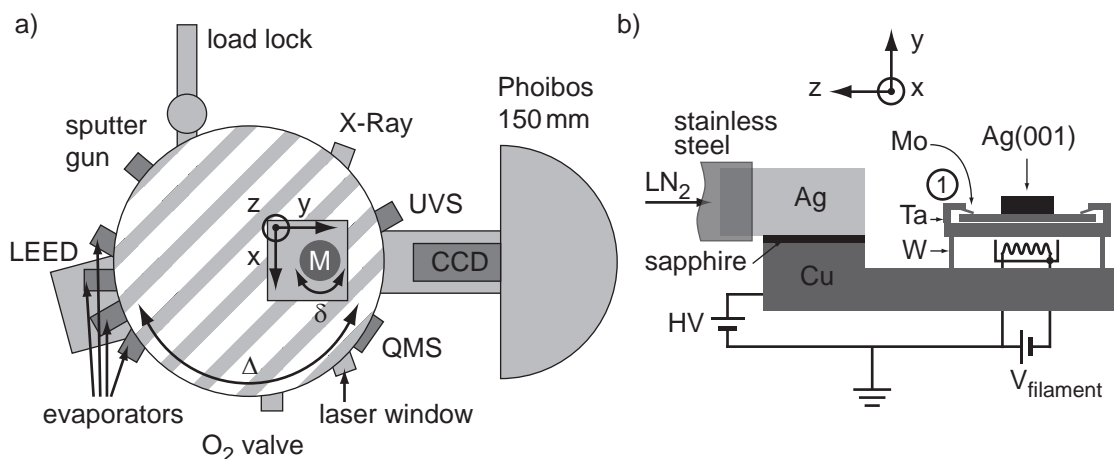


**Figure 3.1:** (a) Schematic top view the UHV chamber. The gray levels of the single components indicate different heights  $z$ . The manipulator (M) is movable in three directions  $x$ ,  $y$ , and  $z$  and rotatable by  $\delta$ . (b) Schematic side view of the manipulator head (details see text).

adjusted via  $\Delta$  and  $z$ . The final adjustment is realized via  $x$ ,  $y$ , and  $z$  directions and the angle  $\delta$ .

The chamber is pumped via two turbomolecular pumps (TMP, 5001/s and 601/s, Pfeiffer vacuum, Asslar) and a scroll pump (SH-110, Varian). The smaller TMP and scroll pump are additionally used for the differentially pumped rotary flanges. The load lock enables to change samples without breaking the vacuum of the main chamber. It is pumped via an TMP (601/s, Pfeiffer, Asslar) and a scroll pump. The two pumps of the load lock are used for differential pumping of the UV source (UVS) as well. The chamber is baked using hot-air circulation in a specially designed cover (double-walled aluminum plates). This ensures a constant baking temperature of all components (temperature differences  $<10$  K within the cover). After baking at 420 K a base pressure of  $1 \times 10^{-10}$  hPa is reached. A sample storage in the main chamber enables to keep up to six samples on hand. To transfer the samples from the load lock a magnetically coupled linear drive is used. The sample could be transferred in the sample storage as well as directly into the manipulator. Additionally, a wobble stick with a pincer grip can be used to transfer the sample between storage and manipulator.

The preparation of the sample is realized via the following tools. For cleaning the sample the sputter gun delivers  $\text{Ar}^+$  ions with kinetic energies between 0.2 and 2 keV. Different evaporators enables the preparation of ultra-thin films e.g., NiO and  $\alpha$ -sexithiophene. For the preparation of oxide films the oxygen background pressure is controlled by a leak valve. Figure 3.1 (b) shows a schematic view of the sample mounting with a Ag(001) crystal. The samples are mounted on a commercial sample holder plate in so called *Omicron design*<sup>1</sup>. The head consists of a Ta sample holder slot which is connected via four W rods to a Cu body. The Cu body is fixed again on a Ag body which is brazed in a stainless steel tube. The Cu and the Ag is thermally connected (electrically isolated) with a sapphire plate. The whole setup enables to cool the sample to low temperatures. Therefore, the Ag body is cooled via a bath of liquid nitrogen or helium in the stainless steel tube as indicate in Fig. 3.1 (b). Alternatively, the Ag body could be cooled via evaporation of the liquid phase of nitrogen using a special transfer tube and a diaphragm pump. To reach higher sample temperatures the sample mounting allows heating via electron bombardment. This is realized via emitted electrons from a W filament behind the sample which are accelerated in the electric field of an applied high voltage (HV). The approximate temperature of the sample is determined by a thermocouple (type K) below the Mo spring plates at the position ①. During heating the temperature at ① is below the real temperature of the sample and depends strongly on the actual temperature of the Cu body. However, in a measurement period it was possible to fix a thermocouple directly at the sample (no change of the sample possible). This enables to determine the sample temperature with a high accuracy ( $\pm 5$  K). In the other case the temperatures will be given by approximated values (indicated by  $\sim \dots$  K).

For the characterization of the sample the following tools are available. The chamber pressure is determined with a hot-filament ionization gauge. A quadrupole mass analyzer (QMA 400, Pfeiffer vacuum, Asslar) allows to determine the composition

---

<sup>1</sup>Most of the plates are fabricated in the mechanical workshop of the university, however, the design is identical to the commercial ones.

of the residual gas or to check the quality of process gases. For the sample characterization low-energy electron diffraction (LEED, ErLEED digital, Specs, Berlin) X-ray and ultra-violet photoelectron spectroscopy (XPS and UPS, XR 50-Z50 and UVS 10/35, Specs, Berlin) is used. The laser beams for 2PPE measurements are directed through a fused-silica window (LewVac, Burgess Hill (UK)) which is transparent in the UV. The angle with respect to the electron analyzer axis is fixed at  $70^\circ$  (a second UV transparent view port with an angle of  $45^\circ$  is available but not used here).

### 3.1.2 Sample preparation and NiO film growth

The Ag(001) sample has been prepared by cycles of  $\text{Ar}^+$  ion sputtering (1 keV,  $\sim 5 \mu\text{A}/\text{cm}^2$ , for 20 minutes) and subsequent annealing at 620 K. The sample cleanliness and ordering has been verified with XPS and LEED. The NiO thin films have been prepared by molecular beam epitaxy in an oxygen atmosphere. The metal has been evaporated from different evaporators. The home-made Knudsen cell by Höfer [34] has been used the first time to evaporate a metal from the newly designed evaporator. The ceramic crucible contains a piece of highly-pure Ni rod. Secondly, a commercial electron beam evaporator (Focus, Hünstetten) has been used to evaporate the Ni from a the directly heated Ni rod. The NiO films has been prepared at an oxygen partial pressure of  $1 \times 10^{-6}$  hPa. The flux of the Ni evaporator is adjusted to obtain a growth rate of 0.4 ML/min. The characterization of the film growth will be shown in section 4.1.2.

The preparation of a wedge-shaped film profile is possible as well. The preparation of the wedge is realized via an additional shadow plate between the sample and the evaporator. It can be fixed to the manipulator during preparation. Figure 3.2 (a) shows a schematic view of the alignment (note lengths and angles not to scale). The plate causes a shadowing of the evaporation cone as indicated by the light gray area. The dimension of the plate is adjusted to reach a completely shadowed sample (diameter 10 mm) at an angle  $\delta = -20^\circ$  as shown in Fig. 3.2 (b). A continuous rotation leads to a nearly linear shift of the shadow with respect to the x direction as indicated

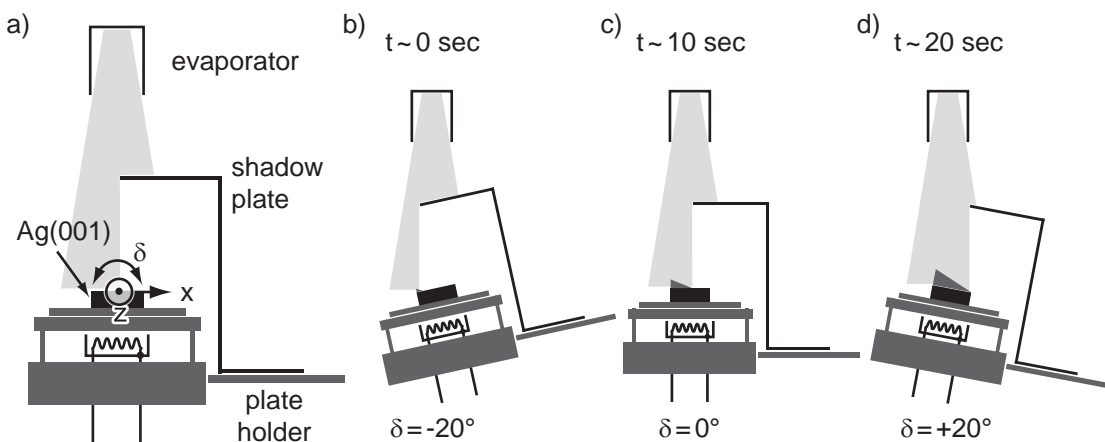


**Figure 3.2:** (a) Schematic view of the wedge-shaped film preparation using an additional shadow plate. (b)-(d) Same as (a) at different times  $t$  during continuous variation of the angle  $\delta$  (lengths and angles not to scale).

in Fig. (c) and (d)<sup>2</sup>. The dark gray triangles illustrate the wedge-shaped profile. The wedge preparation has been used for the calibration of the evaporator in section 4.1.2 and for the measurements of the sub-monolayer coverage in section 4.2.2. This allows to measure a continuous thickness variation within a single preparation. A second application of the wedge for 2PPE measurements is the preparation of a small variation around a certain nominal thickness. This allows to adjust the laser to a sample position with the highest signal of characteristic features<sup>3</sup>. This has been applied for the measurements of 2 and 4 ML film thicknesses.

### 3.1.3 Electron energy analyzer

For the detection of the photoelectrons a hemispherical analyzer with a radius of 150 mm is used (Phoibos 150 mm, Specs, Berlin). The detector unit consists of a multi-channel plate (MCP) and a phosphor screen in the UHV. The screen is imaged with a Peltier-cooled CCD camera (Sensicam qe, PCO, Kelheim). This enables to detect a two-dimensional image (2D-CCD detector). The direction parallel to the line between the entrance and exit of the hemispheres refers to the kinetic energy of the photoelectrons. A lens system in front of the hemispheres is used to focus the photoelectrons to the entrance slit. Depending on the lens mode the second dimension of the detector refers to the spatial coordinate of the sample or the emission angle [35].

For the 2PPE the angle-resolved lens modes are used (*LowAngularDispersion* or *WideAngleMode*). The analyzer is operated in the constant pass energy mode. Since the kinetic energies of the photoelectrons in 2PPE are small, the electron trajectories between the sample and the lens entrance are very sensitive to any residual electric or magnetic field. To minimize the influence of magnetic fields an integrated  $\mu$ -metal shielding is mounted in front of the entrance of the lens system.

For the characterization of the electron analyzer the Shockley-type surface state of the Au(111) surface [36] has been analyzed by angle-resolve photoemission spectroscopy as shown in Fig. 3.3 (a) for a sample temperature of  $\sim 100$  K. The analyzer settings are *LowAngularDispersion* lens mode with a pass energy of 10 eV. This allows to span a energy range of 1.3 eV and detect emission angles of  $\pm 6.5^\circ$  on the MCP simultaneously. Figure 3.3 (b) shows a line profile through (a) in angular direction at a final state energy of 21.20 eV as indicated by the orange bar. The width of the profile is 10 meV. The two spin states are well separated at  $\pm 4.12^\circ$  and  $\pm 4.77^\circ$  with a width of  $0.51^\circ$  and  $0.40^\circ$ , respectively. This agrees well with literature data [37,38] and determines the angular resolution of the electron analyzer. Figure 3.3 (c) shows a line profile through (a) in energy direction as indicated by the green bar. The data points (red circles) have been fitted by the product of the density of states (represented by a  $2^{nd}$  order polynomial, blue curve) and the Fermi-Dirac distribution with  $k_B T = 8.6$  meV (according to a sample temperature of 100 K, green curve). The resolution of the analyzer is determined by an additional Gaussian broadening. The

<sup>2</sup>Due to the small angles between  $\pm 20^\circ$  the thickness increases nearly linear in x direction. Deviation from that linear dependence are mainly influenced by inhomogeneities of the evaporation cone.

<sup>3</sup>Inhomogeneities within the films, i.e., the distribution of islands with different film thicknesses lead to a deviation between nominal thickness (evaporation rate times evaporation time) and maximum 2PPE signal (determined by the relative surface area fraction).

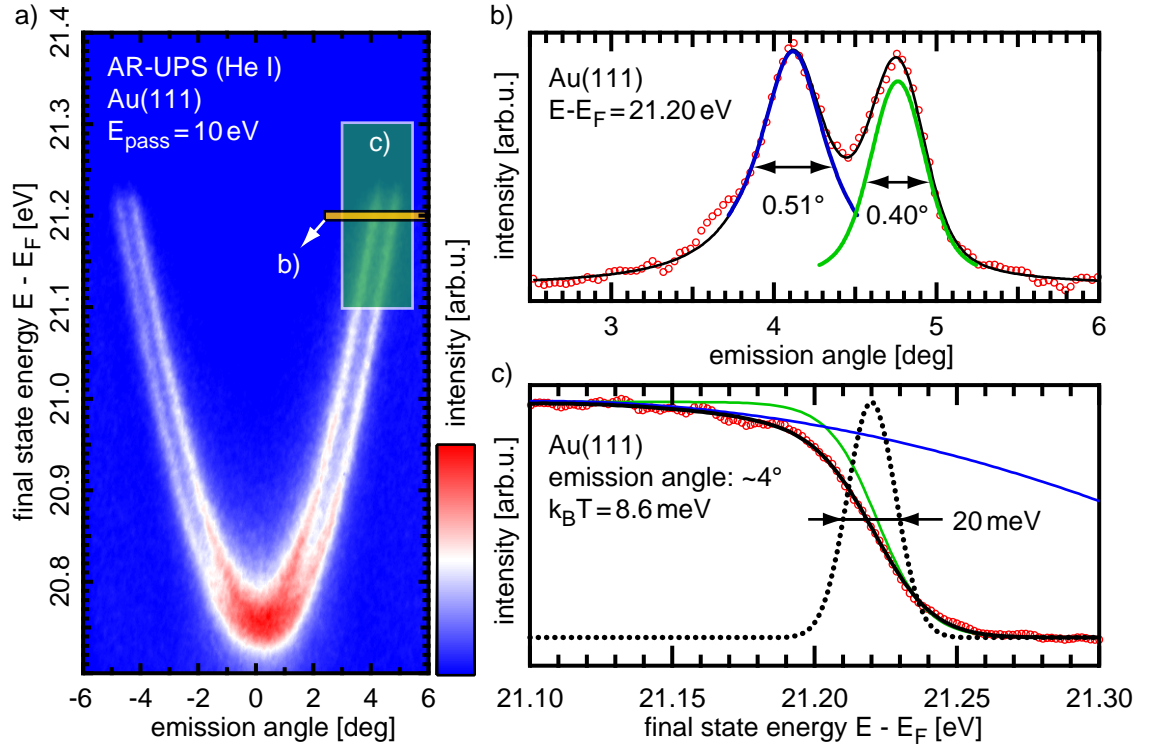


**Figure 3.3:** (a) Angle-resolved UPS spectrum of clean Au(111) at  $\sim 100$  K in the vicinity of the Fermi level. The Shockley surface state shows spin-orbit splitting (Rashba effect). (b) Background-subtracted line profile through (a) in angular direction as indicated by the orange shaded bar. The black line shows the curve fit of two Voigt profiles. The widths of the peaks are  $0.51^\circ$  and  $0.40^\circ$  (FWHM), respectively. (c) Background-subtracted line profile through (a) in energy direction as indicated by the green shaded bar. The resolution of the analyzer is determined to  $20$  meV by fitting the data by a Gaussian broadened (dotted line) product of a polynomial (blue line) and the Fermi-Dirac distribution (green line).

curve fit (solid black line) reveal a energy resolution of  $20$  meV (The black dotted line indicates the Gaussian at the Fermi level.). Referring to 2PPE measurements, the spectral width of the laser pulses limits the energy resolution to  $\sim 80$  meV<sup>4</sup>. Thus, pass energies has been chosen which allow to span the kinetic energy range of the photoelectrons on the MCP without significant energy broadening ( $E_{pass} \leq 20$  eV).

Figure 3.4(a) depicts the experimental setup of a biased sample in front of the entrance of the lens system. The green arrows indicate the electron trajectories for the case of no electric field between sample and detector. The electron trajectories between both are linear. The energy diagram of a photoelectron with a biased sample is shown in Fig. 3.4(b). The bias voltage increases the kinetic energy  $E_{kin,d}$  in the detector. This leads to a change of the trajectories as shown by the blue arrows in Fig. 3.4(a). The detection angle  $\theta_d$  is decreased. The experimental setup implies a homogeneous electric field which acts only on the movement in perpendicular

<sup>4</sup> $\Delta E \times \Delta t \geq \hbar/2 = 2.068$  eV/fs.

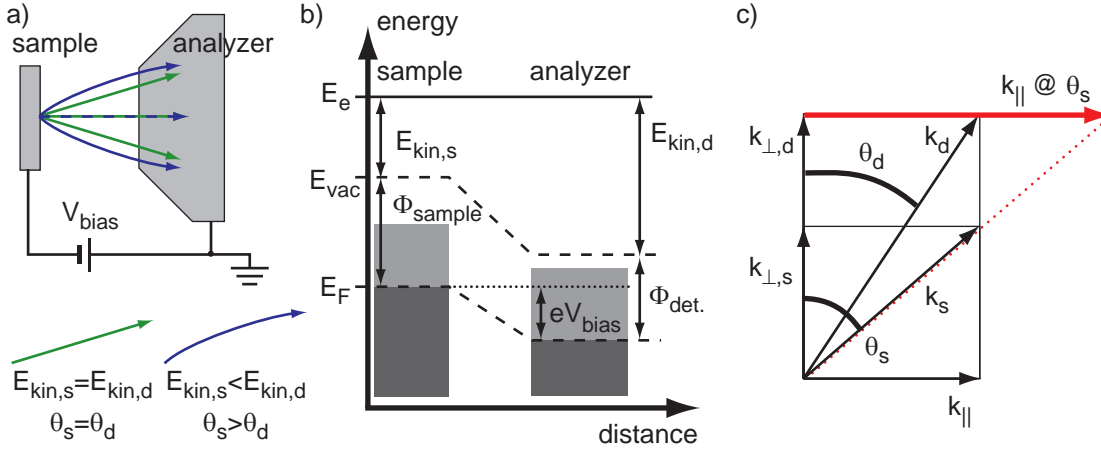


**Figure 3.4:** (a) Circuit diagram of a negatively biased sample in front of the electron analyzer. The green and blue arrows indicate electron trajectories for the non-biased and biased samples, respectively. (b) Energy diagram of a photoelectron with negative sample bias. (c) Change of the photoelectron momentum with the geometry of (a). The detected angle  $\theta_d$  is smaller than the real emission angle  $\theta_s$  at the sample surface. The red arrow indicates the increase of the observed  $k_{\parallel}$  within the given acceptance angle of the detector. Details see text.

direction, i.e., the parallel component is conserved. Figure 3.4(c) shows the wave vectors at the sample surface ( $k_s$ ) and in the detector ( $k_d$ ). This diagram leads to

$$k_{\parallel} = \sin\theta_d \sqrt{\frac{2m}{\hbar^2} E_{\text{kin},d}} \quad (3.1)$$

$$k[\text{\AA}^{-1}] = 0.5123 \sin\theta_d \sqrt{E_{\text{kin},d}[\text{eV}]} . \quad (3.2)$$

Thus, the angle-resolved detection of photoelectrons with the geometry of Fig. 3.4(a) (surface normal parallel to the detector axis) enables to determine the  $k_{\parallel}$  accurately without considerations about the influence of the electric field<sup>5</sup>. As derived from equation 3.2 a bias voltage leads to an increase of the observed  $k_{\parallel}$  in dependence of the detection angle. This is depicted in Fig 3.4(c) by the red arrow which indicates the  $k_{\parallel}$  for the biased sample at an detection angle  $\theta_s$ . The observed  $k_{\parallel}$  at this angle is increased by the factor  $\frac{\sqrt{E_k + eV_{\text{bias}}}}{\sqrt{E_k}}$ . Note that these considerations are not applicable for rotated samples where the electric field becomes inhomogeneous. For this case Hengsberger *et al.* demonstrated a correction procedure for the emission angles at even high bias voltages of up to 9 V, recently [39].

The explicit calculation of  $k_{\parallel}$  is not necessary to extract the effective electron mass  $m_{\text{eff}}m_e$  from parabolic bands in angle-resolved photoemission data. The dispersion is given by

$$E(k) = E_0 + \frac{\hbar^2}{2m_{\text{eff}}m_e} k^2 . \quad (3.3)$$

<sup>5</sup>The change of the trajectories changes the properties of the electron optics of the lens system as well. This influences the angular and energy resolution. Therefore, only adequate bias voltages  $\leq 2\text{V}$  should be applied.

The angle-dependent kinetic energy  $E_{kin,d}(\theta_d)$  and equations 3.1 and 3.3 leads to

$$E_{kin,d}(\theta_d) = \frac{E_{kin,d}(0)}{1 - \frac{1}{m_{eff}} \sin^2 \theta_d} . \quad (3.4)$$

This equation is used to determine the effective electron mass of parabolic bands from angle/resolved photoemission data.

## 3.2 The fs-laser system

The fs-laser system consists of two main parts. An all-fiber based near-IR pump laser (IMPULSE, Clark, Dexter) delivers 200 fs light pulses with pulse energies of 11  $\mu\text{J}$  at a maximum repetition rate of 2 MHz. It pumps the *i-NOPAduo* which has been developed in the group of Prof. Riedle (Munich). The detailed setup and functionality has been described elsewhere [40,41]. The key issues are: The pump laser is split into two fractions. One fraction is used to create a white-light continuum in a rotating sapphire disc. The second part is used to successively create a second- and a third-harmonic beam (SHG and THG). They are used to pump two independently tunable non-collinear parametric amplifiers (NOPAs). In the following the two different NOPA outputs will be called SHG-pumped and THG-pumped NOPA output (according to the pump light of the NOPA process). However, the key point for the experiments of the present work is the wide-range tunability of the two fs-laser pulses. Figure 3.5 summarizes the photon energies and typical pulse energies of both NOPA outputs. It is possible to span the whole energy range between 1.2 and 5.0 eV.

The detailed setup of the fs-laser system has been presented previously [31,42,43]. The laser beams are focused on the sample ( $f=500$  mm) through a fused-silica view port. The angle of incidence with respect to the axis of the analyzer is  $70^\circ$ . The influence of the polarization of the laser beams on any of the observed features has not been investigated so far. Thus, always p-polarized laser beams have been

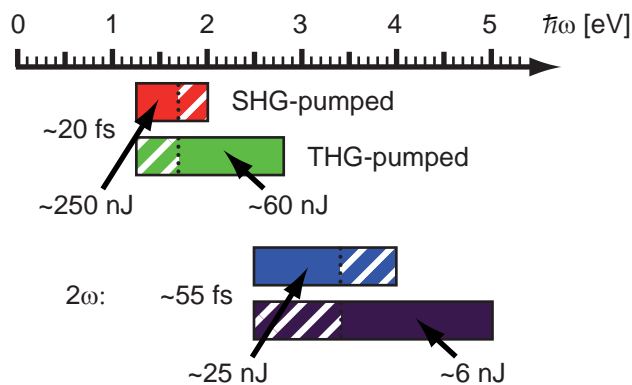


**Figure 3.5:** Photon energies of the two NOPA outputs. The solid colored areas indicate the energy ranges using a band filter (CALFLEX, splits the continuum into high and low frequency parts) for the white light separation. The striped areas indicate the theoretically possible energy ranges of the two NOPA beams using a 50:50 beam splitter instead.

used. The experimental setup has been extended by some parts. Both NOPA outputs could be additionally frequency doubled. Thus, all possible combinations of the photon energies shown in Fig. 3.5 could be realized for bichromatic-2PPE experiments. This also includes UV/UV-2PPE with two independently tunable fs-laser pulses in the UV range [43]. The optical cross-correlation of the two laser pulses could be determined *in-situ* at the laser table. This has been realized by a piezo-driven stage with a travel range of 100  $\mu\text{m}$  (P-611.Z, PI, Karlsruhe). It is mounted at the ending mirror of a prism compressor to change the delay between the two pulses periodically. Both beams are focused into a BBO crystal for difference frequency mixing. This signal is recorded by a photo diode and plotted against the time delay. The cross-correlation is determined with practical frequencies up to 1 Hz. This is used to adjust the shortest pulse length of the UV beam, which is not possible in the commercial auto-correlator (NOPA-Pal, Horiba-Jobin-Ivon). The width of the cross-correlation and the pulse length of the IR beam (determined by the auto-correlator) allow to characterize the pulse length of the UV beam.

The *i-NOPAduo* includes processes with a high non-linearity (mainly the white-light generation and the THG). Thus, small fluctuations of the pulse length, the intensity, and the exact focal point of the IMPULSE result in relatively strong fluctuations of the NOPA and the additionally frequency-doubled beams. This leads to intensity fluctuations of the 2PPE signal as well. Therefore, some data correction is necessary as described in the following section 3.3 and appendix 6.A.

### 3.3 Software development

The combination of both experimental parts, i.e., the laser system on the one side and the UHV chamber on the other side, some software development was necessary. For time-resolved 2PPE the electron analyzer acquires electron intensities at different pump-probe delays. This requires a communication between the motorized delay stage and the electron analyzer. For this purpose C-based programs has been developed<sup>6</sup>. The hard and software setup is depicted in Fig. 3.6. The *control software* adjusts the temporal delay between the laser pulses and the settings of the electron analyzer. The data of the 2D-CCD detector and the photodiodes are recorded by the *acquisition software*<sup>7</sup>. During a time-resolved 2PPE measurements or other cyclical processes, both software programs exchange data to execute the correct schedule. The software realizes a very good down-to-acquisition time ratio of typically  $\leq 2\%$ . For a detailed discussion about a typical measurement schedule see appendix 6.A.

---

<sup>6</sup>A first version was able to control the analyzer settings and the delay stage, which has been developed by S. Förster in our group.

<sup>7</sup>The main parts for the data transfer has been copied from the acquisition software of M. Huth [44].

---



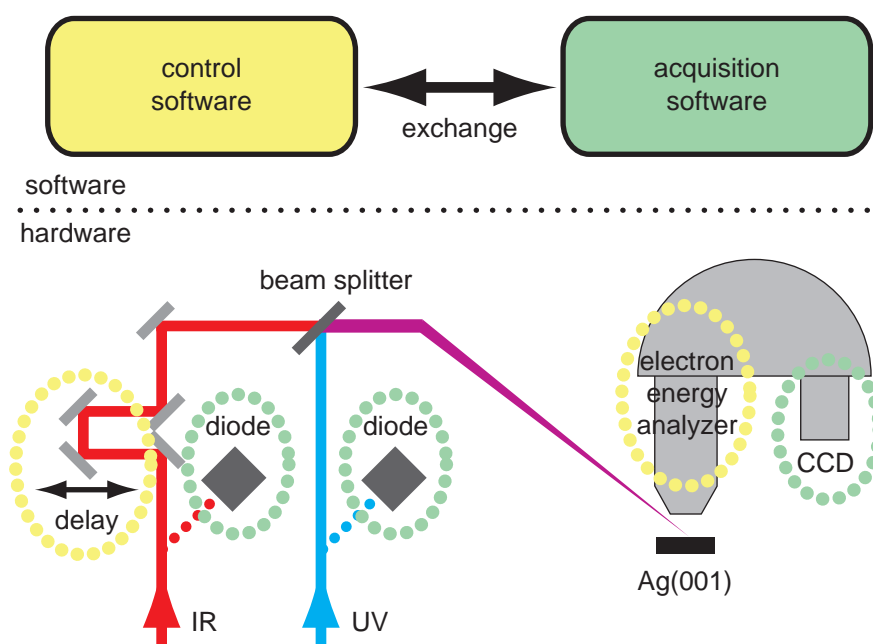


**Figure 3.6:** Functional diagram of the hard- and software setup for time-resolved two-photon photoemission. The upper part depicts the *control-* and *acquisition software*. The lower part indicates the experimental setup. The color of the dotted ovals indicate the software which controls/measures the values (details see text and appendix 6.A).



## 4 Results and discussion

In this chapter the experimental results of the investigations of electronic states of NiO/Ag(001) are presented. It is divided into four main parts. At first the growth of NiO on Ag(001) will be discussed and compared with other works. The characterization of the ultra-thin films concerning growth mode, film quality, and thickness-dependent electronic structure of occupied states will be depicted. This is essential for the interpretation of the 2PPE data presented in the following parts. The second part will deal with image-potential states at different NiO film thicknesses. In the sub-monolayer regime of the NiO film a strong influence of NiO islands on the energetics and dynamics of image states on remaining Ag regions will be demonstrated. The interplay between confinement effects of electrons above the surface (image-potential states) and electrostatic fields close to the surface will be analyzed in terms of their influence on the image potential and the *local* work function. The modification of the image-potential states compared to the bare Ag substrate will be explained by the influence of the dielectric properties of the oxide overlayer and its permittivity. Moreover, in the third part the electronic structure of Ni  $3d$  derived states will be presented. The thickness-dependent variations of these states as well as the development of a  $d_{z^2}$ -derived surface state will be analyzed. All results will be compared with scanning tunneling spectroscopy (STS) and electron energy loss spectroscopy (EELS). The differences between those methods will be discussed with respect to the inherent different electronic final states. Finally, the observation of electronic states which are neither assigned to the NiO nor observed at the bare Ag(001) surface will be discussed for the monolayer and  $\geq 4$  ML coverage. It will be shown that the structural relaxation of the NiO monolayer mediates a surface-assisted umklapp process of Ag bulk bands in the vicinity of the L point. For thicker films the antiferromagnetic ordering of NiO(001) leads to a similar reconstruction as well. This allows a very efficient umklapp process of Ag bulk states which are non-resonantly excited by three- and four-PPE processes.

### 4.1 Growth of NiO on Ag(001)

#### 4.1.1 Introduction

In the early 90's Marre and Neddermeyer [45] could show that due to the small lattice mismatch of only  $\sim 2\%$  between the NiO and the Ag a well defined ordered growth is obtained. In the following such films have been widely investigated using various experimental techniques [46–49]. A detailed analysis of the morphology and the electronic structure has been performed by Großer in our research group using scanning tunneling microscopy and spectroscopy (STM, STS) [15]. He has shown that the electronic structure of the unoccupied electronic states of the first atomic layers deviates strongly from those found for thicker films or even bulk-NiO samples [46,50–52]. However, for thicknesses larger than  $\sim 3$ –4 ML the electronic

structure of thin films becomes comparable to that found on bulk-NiO samples showing only small shifts of the energy positions of the states [52]. Using the intensity oscillations of the specular beam in low-energy electron diffraction (LEED) Wollschläger *et al.* [47] report a layer-by-layer growth up to thicknesses of 10 ML. At those coverages a mosaic structure is already observed in spot profile analysis-LEED (SPA-LEED), indicating the transition between the pseudomorphic growth of the first layers and the growth of NiO with its own lattice constant in the region of about  $\sim 5$  ML. All these aspects allow the investigation of NiO thin films using area integrating experimental methods without losing the interesting layer-resolved information. In this work time-resolved two-photon photoemission (2PPE) will be applied as a powerful tool for the investigation of the electronic structure and the dynamic of unoccupied electronic states.

So far the initial stages of the NiO growth on Ag(001) are well understood [48,50, 53,54]. The monolayer exhibits a  $(2\times 1)$  reconstruction [53,54] which is due to the formation of a hexagonal layer of stoichiometric NiO. In contrast to the NiO(111) plane where alternating  $\text{Ni}^{2+}$  and  $\text{O}^{2-}$  hexagonal layers are found the monolayer NiO on Ag(001) incorporates both ions within a single layer. Atomically-resolved STM images by Großer [15] could extend this model to an uniaxially relaxed hexagonal layer which is derived from an additional moiré pattern perpendicular to the well known  $(2\times 1)$  rows. The relaxation is in the order of 2%. The moiré pattern leads to an alternating appearance of a corrugated and a flat region. Later this nomenclature will be used to discuss the differences of the STS spectra obtained from these regions (see section 4.3.2). LEED-*IV* analysis by Caffio *et al.* [54] reveals a small vertical shift of both ions with respect to each other where the  $\text{Ni}^{2+}$  is located closer to the Ag substrate. The structure and its strong dipole moment due to the relative shift of the  $\text{Ni}^{2+}$  and  $\text{O}^{2-}$  ions is stabilized by the Ag underneath. However, this shift of the ions would lead to an increase of the work function due to the additional dipole at the surface.

### 4.1.2 Thickness-dependent electronic and morphological structure

To characterize the initial stages of the NiO growth with the available experimental techniques a wedge-shaped film profile of NiO has been prepared as described in section 3.1.2. In Fig. 4.1 (a) the work function determined from UPS data and the intensity of the half-order diffraction peak in LEED are shown in dependence of the sample position. The bare Ag(001) substrate has a work function of  $4.430\pm 0.015$  eV (see Fig. 4.2 below). Upon adsorption of NiO the work function firstly increases significantly to  $5.00\pm 0.02$  eV at the sample position of  $\sim 4.5$  mm and it decreases again to  $4.20\pm 0.02$  eV. As expected from the preparation conditions, the data point at position 0 should reflect the nearly clean Ag(001) substrate with a work function of 4.43 eV. This is not the case and a value of almost 4.6 eV is found. A possible explanation for that is a slight deviation from the ideal growth geometry as assumed in section 3.1.2 e.g., the angle calibration, the position in front of the evaporator, and the evaporation profile. For the thickness-dependent intensity of the half order diffraction peak in LEED a maximum is found at a position of  $\sim 4.5$  mm. In both independent measurements the distinct maxima coincide at the same sample position and thus at the same film thickness. Figure 4.1 (b) shows the corresponding LEED

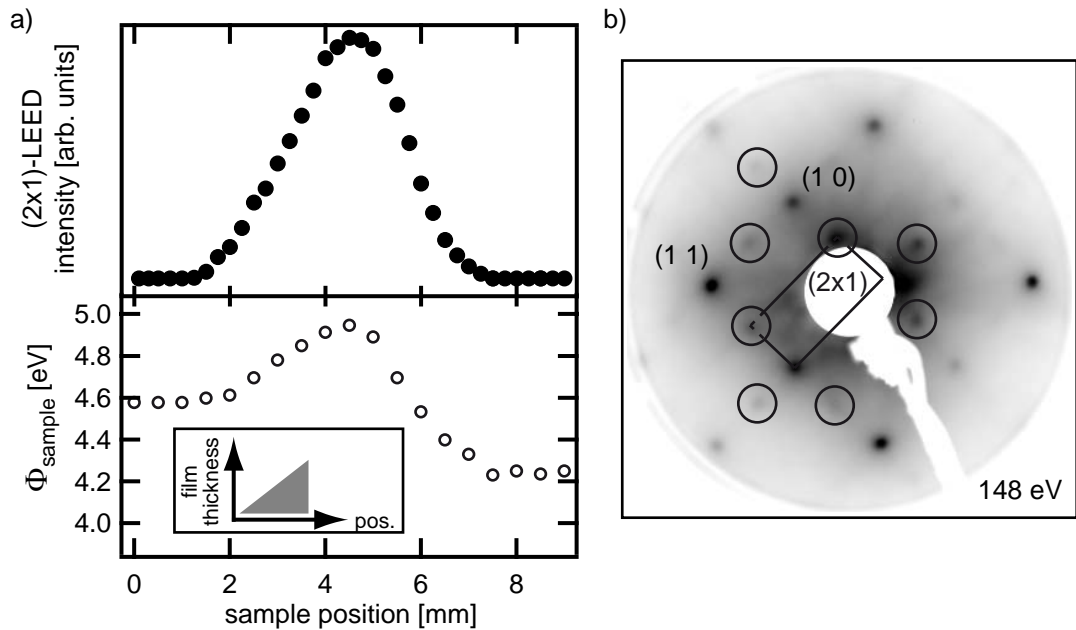


**Figure 4.1:** UPS and LEED data of a wedge-shape film profile of NiO on Ag(001) after deposition at room temperature and post annealing at 450 K. (a) The intensity of the diffraction peak of the (2x1) reconstruction (upper curve) and the work function (lower curve) in dependence of the sample position. The inset shows the theoretical film profile. (b) Corresponding LEED pattern at the maximum intensity of the (2x1) peak in (a). The circles emphasize the half-order LEED reflections.

pattern at the position of the half order diffraction peak maximum. The reciprocal unit cell of one of the two possible (2x1) domains is indicated by the rectangle. The open circles highlight the positions of the additional half-order diffraction spots.

These measurements lead to the conclusion that the preparation conditions at the sample position of  $\sim 4.5$  mm result in the monolayer coverage. On the one side the signal of the half order diffraction peaks of the (2x1) reconstruction are maximal which is attributed to the monolayer coverage. On the other side the work function shows a maximum value of 5.0 eV. The latter fact supports the results of Caffio *et al.* [54] where an increase of the work function is expected due to the structural relaxation. Figure 4.2 shows the thickness-dependent work function of the NiO. To minimize the experimental uncertainty of the wedge preparation, three single film preparations within the sub-monolayer coverage (homogeneously on the whole sample) have been prepared. The values of the work function are shown by black diamonds. A nearly linear increase of the work function in dependence of the film thickness is found. This reflects the spatial distribution of Ag(001) regions and NiO islands of monolayer thickness. Each microscopic region has its own work function and the mixture of both results in an average work function according to the surface area fractions. Later we will see that this also refines the misinterpretation of the STS spectra of the NiO monolayer by Großer [15] where an decrease of the work function was predicted (see section 4.3.2).

Based on these results, all film preparations could be converted into certain film thicknesses. Figure 4.2 shows the work function of NiO in dependence of the film

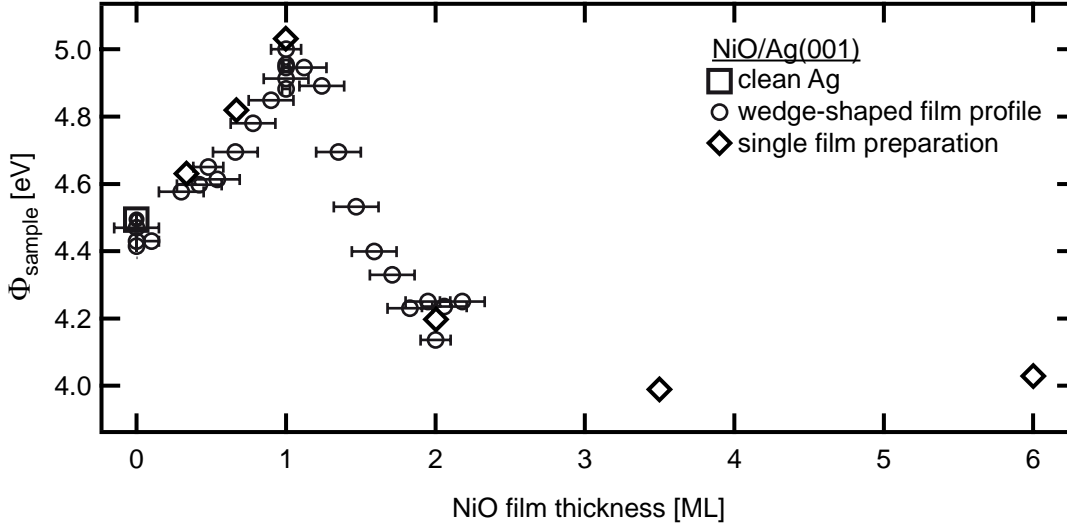


**Figure 4.2:** Thickness-dependent work function of NiO on Ag(001). The calibration of the film thickness refers to the maximum value, as expected for the NiO monolayer.

thickness of up to six monolayer. For the bilayer thickness a work function of  $4.2 \pm 0.1$  eV is observed as already discussed above. For higher film thicknesses the work function decreases and stabilizes at 4.0 eV which is slightly below 4.3–4.4 eV as reported for bulk-NiO(001) samples prepared by various methods [55–57]. This deviation observed for NiO thin films on Ag(001) might originate from growth imperfections by means of sample roughness (Smoluchowski effect) or remaining strain effects due to the pseudomorphic growth. However, at room temperature a Frank-van-der-Merve growth mode is observed. This could be verified via oscillations in the MEED pattern (medium energy electron diffraction) [58]. This result is essential for area integrative methods as 2PPE and allows layer-resolved measurements.

For the investigation of the occupied electronic structure UPS has been used. In Fig. 4.3 the valence band structure close to the Fermi level at the  $\bar{\Gamma}$  point is shown for Ag(001) and different coverages of NiO thin films. The energy scale refers to binding energy with respect to the Fermi level. The photoemission intensities for the bare Ag(001) (black curve) and the NiO monolayer (blue curve) are shown. For a better comparison, the intensity of the Ag spectrum has been reduced by a factor of 0.5. Note that this factor is only valid for the comparison of these two curves and not for higher thicknesses. Beside the decrease of the intense Ag bands at around 5 eV the spectrum of the NiO monolayer reveals three additional features at binding energies of 0.8, 3.5, and 6.2 eV, respectively. The inset of Fig. 4.3 shows an enlarged region close to the Fermi level of these two spectra. Both curves have been obtained using the same experimental conditions without any intensity normalization. Beside the feature at 0.8 eV, the absolute photoemission intensity at the Fermi level is additionally increased. This reflects the metallic character of the NiO monolayer film. The results are in good agreement with other experimental and theoretical work [59–61]. The spectrum of a bilayer thick NiO film is shown by the green curve in Fig. 4.3. The feature at 0.8 eV of the monolayer vanishes and a new relatively broad feature with low intensity occurs at  $\approx 2$  eV. The lower

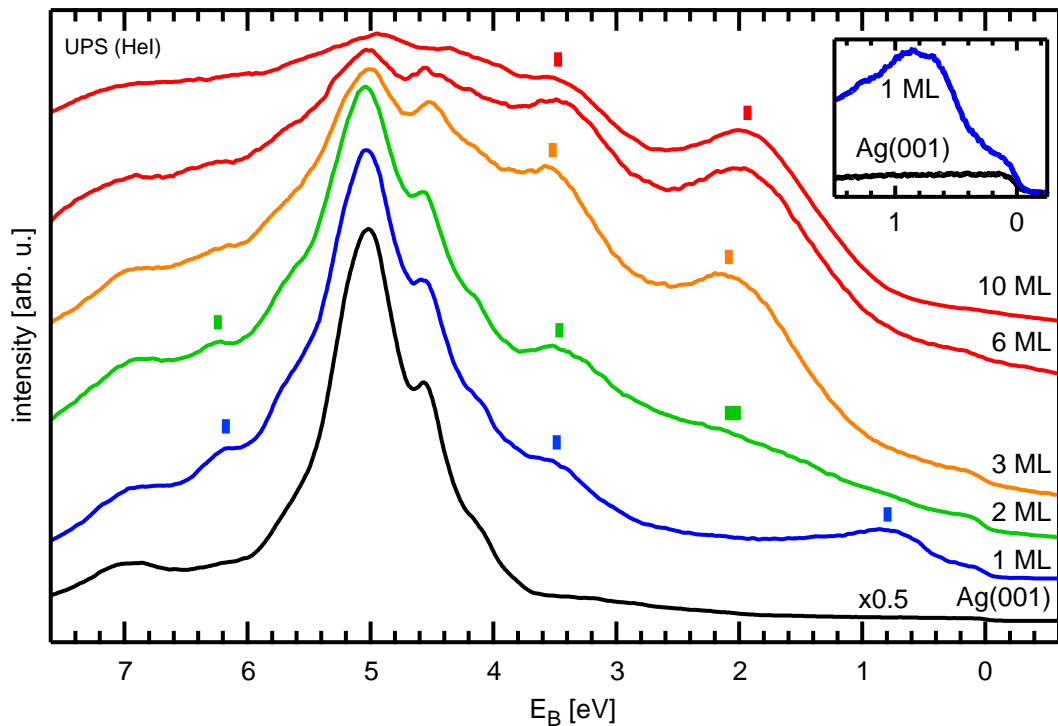


**Figure 4.3:** UPS data of the valence band of bare Ag(001) and various thicknesses of NiO thin films.

features at 3.5 and 6.2 eV persist. A dispersing state in the vicinity of the Fermi level as reported by Cheng *et al.* [62] has not been observed which might be due to the different photon energy used here. The relative intensity of the broad feature at 2 eV is smaller as reported by Cheng *et al.* and Yang *et al.* [60,62]. At higher coverages of  $\geq 3$  ML (orange and red curves), an increase of the intensity of the feature at  $\approx 2$  eV is observed. At 10 ML coverage it is found at  $1.95 \pm 0.05$  eV. This feature is assigned to the  $d^8 \rightarrow d^8 L^{-1}$  transition in the NiO which is also observed at bulk NiO samples [52,63,64]. Thus, the NiO thin films of  $\geq 3$  ML already reveal the electronic structure similar to bulk NiO(001).

## 4.2 Image-potential states of NiO/Ag(001)

In this section the investigations of image-potential states (IPS) using time-resolved 2PPE for different coverages of NiO/Ag(001) will be presented. After a brief introduction which will deal with the basics of IPS of metal substrates, some main aspects of IPS observed at different adsorbate systems and the possibility to use IPS as a sensor for local properties of the sample, namely the *local work function* will be discussed. Afterward the IPS of the Ag(001) substrate upon sub-monolayer adsorption of NiO will be presented and the influence of the adsorbate to the energetics and dynamics of image states will be analyzed in terms of local work function, confinement, and electrostatic field effects. Then the image states of the NiO bilayer on Ag(001) will be discussed and analyzed with respect to the dielectric continuum model. Furthermore, the observation of image states at higher coverages will be presented and compared with the results of the bilayer coverage.

### 4.2.1 Introduction

#### Image-potential states

Electrons in front of polarizable surfaces induce an electric field which acts as an attractive potential. In the presence of a gap of the projected band structure, bound states are formed. These unoccupied states above the Fermi level have been theoretically predicted by Echenique and Pendry in 1978 [7] and are called image-potential states (IPS). This is due to the possibility to describe the potential by the electric field between the electron and an positively charged *image charge* below the surface. Quantum mechanically the problem could be reduced to a one dimensional description, similar to the hydrogen atom with an electron in the potential

$$V(z) = E_{vac} - \frac{Ze^2}{z}, \text{ with} \quad (4.1)$$

$$Z = \frac{1}{4} \frac{\epsilon - 1}{\epsilon + 1}, \quad (4.2)$$

where  $E_{vac}$  is the vacuum level and  $Ze$  the virtual image charge ( $e$  is the elementary charge) in the distance  $z$  relative to the surface. Thus, a Rydberg series of electronic states converging to the vacuum level is found. The binding energies  $E_n$  are determined via

$$E_n = 13.6 \frac{Z^2 m_{eff}}{(n + a)^2}, \quad (4.3)$$

where  $n$  is the quantum number of the state ( $n=1,2,\dots$ ),  $m_{eff}$  the effective electron mass, and  $a$  the quantum defect. The latter describes the coupling of the wave function of the IPS in the vacuum region to the exponentially damped Bloch wave function in the bulk. The value of  $a$  depends on the position of the state within the band gap and changes between 0 (at the conduction band minimum) and 0.5 (at the valence band maximum). The difference of the wave function in the bulk determines a *s* or *p* like character. The motion of the electrons parallel to the surface is nearly free which is due to the fast response of the electrons in the solids. This means the



effective mass of the image-potential states is close to one. For metal surfaces the polarizability  $\epsilon$  approaches infinity, and thus, equation 4.3 can be written as

$$E_n = \frac{0.85}{(n+a)^2} . \quad (4.4)$$

Experimentally the IPS states have been verified by inverse photoemission [65,66] and two-photon photoemission [67]. Since then, the IPS states have been investigated on many metal surfaces [8,11,28,32,68–71] and on various adsorbate systems [12,72–78]. The dynamics of IPS, which lead to a certain time-dependent intensity in the 2PPE spectra, are theoretically well understood [79,80].

The investigation of IPS of NiO ultra-thin films with its static dielectric constant  $\epsilon$  of 12 enables to explore the region in between the highly polarizable metal substrates and the rare gas adlayers ( $\epsilon=1$ ). The change of the properties of the IPS e.g., the binding energies and dynamics, as well as the influence of the electronic structure of the oxide layer opens the door to a new playground of IPS which has not been investigated so far.

### Image-potential states and the local work function

Figure 4.4 shows a cartoon of a Ag(001) sample with a distribution of NiO islands (monolayer thickness). The coverage corresponds to 0.3 ML. A side view of (a) is shown in Fig. 4.4 (b). Electrons in the IPS are indicated above a NiO island and a Ag region, respectively. As shown in section 4.1.2 the difference between the work functions of the NiO monolayer islands and the Ag(001) regions is in the order of 0.5 eV. Since the IPS form a Rydberg-like series which converges to the vacuum level, a difference between the IPS properties, whether the electron is above a NiO island or a Ag region, is expected as well.

Fischer *et al.* investigated IPS during the growth of Ag on Pd(111) [81]. Both metals exhibit a large difference in the work function. However, during growth

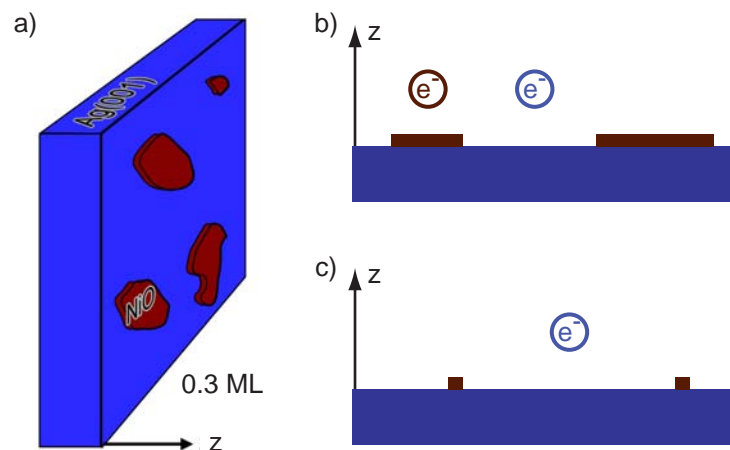


**Figure 4.4:** (a) Illustration of the morphology of 0.3 monolayer NiO (brown islands) on Ag(001) (blue substrate). (b) Side view of (a). Electrons in the image-potential state indicated as classical particles above NiO and Ag regions. (c) Same as (b) at a lower coverage.

within the sub-monolayer coverage the IPS of Pd(111) as well as 1 ML Ag islands are observed, each at fixed energy positions which are equal to ones found on the bare Pd(111) and a corresponding closed monolayer of Ag/Pd(111). This was interpreted within the concept of the local work function. That means the two IPS electrons in Fig. 4.4(b) are characterized via the local surface structure. With other words, electrons above a Ag island *feel* the local work function of Ag which determines the binding energy of the IPS. Similar results has been reported using *Photoemission of Adsorbed Xenon* (PAX) where the emission lines of physisorbed Xenon atoms are influenced by the local electric field due to the vacuum level alignment (local work function). A comparison of both methods has been given by Wandelt [82].

The concept of the local work function was supposed to be independent of the size of the atomic structures. But as reported by Fischer *et al.* [83] (again Ag/Pd(111) at low temperatures) the size of the corresponding surface regions influences the IPS as well. For the IPS of small Ag islands (diameter of 0-5 nm) an energy shift is observed. This was explained by an additional energy contribution due to 3-dimensional localization. It could be shown that a simple particle-in-a-box model is able to explain energy shifts of IPS which are laterally confined at small Ag islands. A typical length scale where confinement effects influence the IPS was given by 1–10 nm.

However, other experiments of the same group on Na/Cu(111) [84] reveal that the pure pinning of the IPS to the local vacuum level is not realized. Na adsorption causes a work function shift of  $\geq 2.5$  eV within the first 0.3 ML of Na coverage. The situation is depicted in Fig. 4.4(c) showing a much smaller amount of deposited material. The substrate region sizes are still large, far away from any confinement length scales. Especially within in the 0.02 ML Na adsorption a downshift of the IPS energy is observed. A theoretical description of that behavior has been reported by Kazansky *et al.* [85], recently. They recognized that the local work function is not a rigid potential. They calculated the influence of a distribution of single Na ions on a Cu(111) surface (an ionic character of Na on Cu(111) between 0–0.4 ML coverage is observed, details see [84] and references therein). As a result they obtained an effective potential of the IPS on Cu(111) regions which shows strong deviations to the normally assumed  $\frac{1}{z}$ -image potential, converging to the vacuum level.

In section 4.2.2 the sub-monolayer coverage of NiO/Ag(001) and the influence of NiO islands on the IPS of remaining Ag regions will be discussed. A description of the *local work function* and its *distance dependence* will be presented by means of classical electrostatic field considerations.

### 4.2.2 IPS of Sub-ML NiO coverages

In this section the IPS upon sub-monolayer (sub-ML) deposition of NiO will be discussed. The actual (sub-ML) coverage of a growing NiO film determines the size of NiO islands and remaining Ag(001) regions. With the additional work function difference between Ag and NiO islands of monolayer thickness, any of the two effects, namely confinement or surface potential effects as depicted in section 4.2.1 should influence the properties of the IPS. It will be shown that the growing NiO film influences the IPS of remaining Ag(001) regions at even low coverage. The presence of small NiO islands changes the energetic position and the dynamics of the IPS.

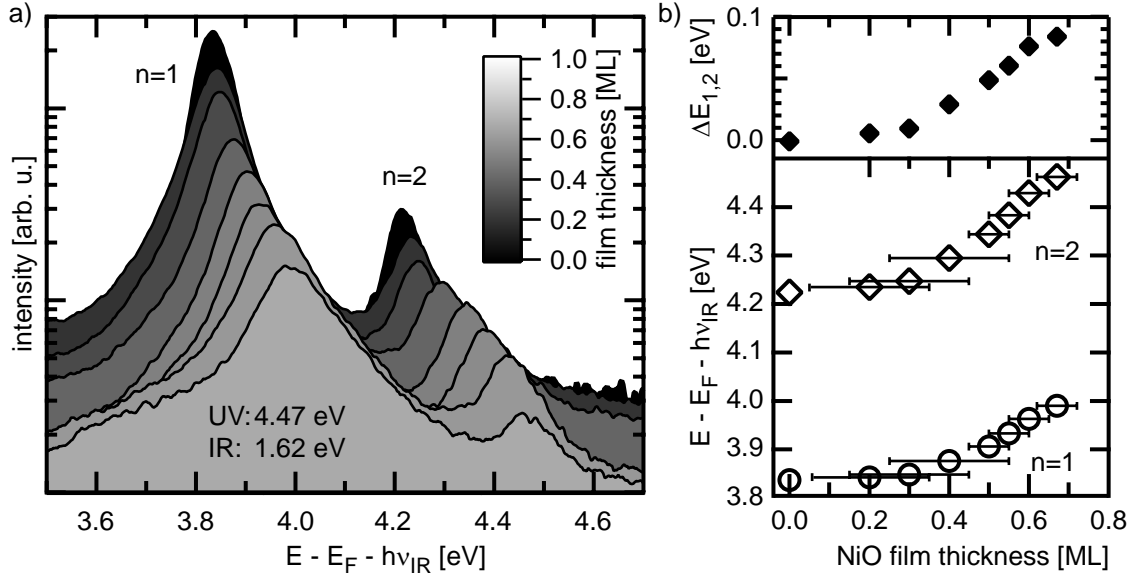


**Figure 4.5:** (a) Semilogarithmic plot of thickness-dependent 2PPE spectra of the IPS  $n=1$  and  $n=2$  of remaining Ag regions at various NiO film thicknesses between 0–0.7 ML. The upper spectrum shows the Ag(001) data. (b) The peak positions of the  $n=1$  (open circles) and  $n=2$  (open diamonds) IPS in (a) in dependence of the film thickness. The upper part shows the relative energy difference between  $n=2$  and  $n=1$  with respect to bare Ag(001) in dependence of the NiO film thickness.

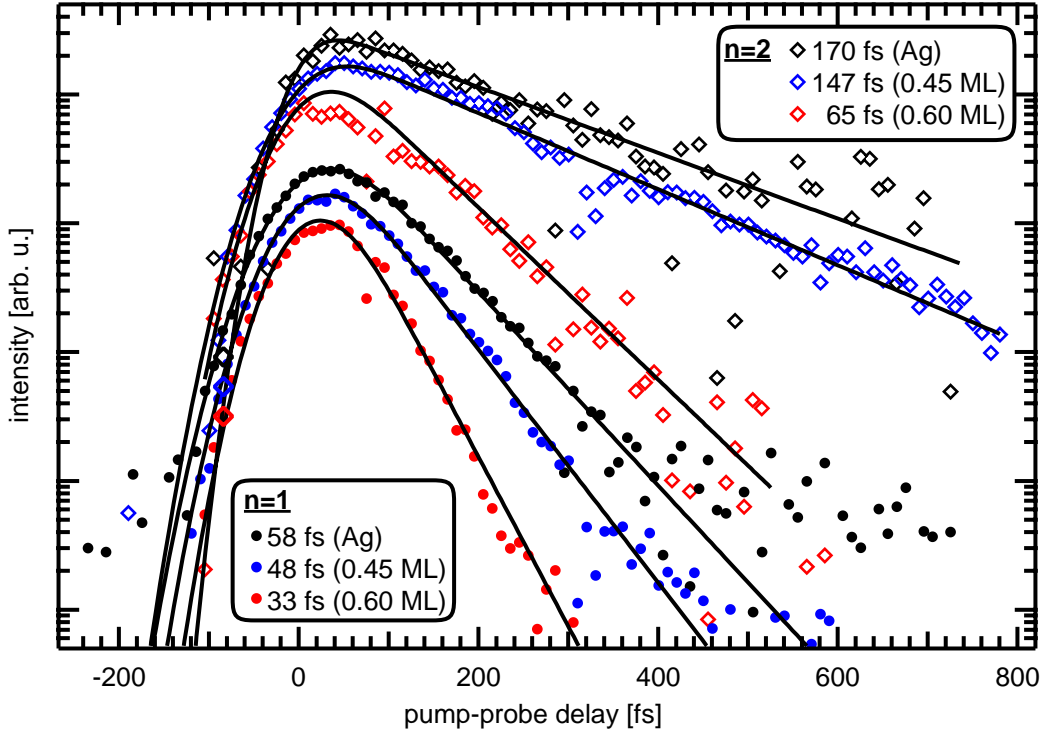
This will be interpreted as a change of the effective image potential which is modeled via classical electrostatic field considerations.

Figure 4.5 (a) shows a series of bichromatic 2PPE spectra with respect to the intermediate state energy obtained at different sub-ML NiO coverages. This energy scaling is obtained by subtracting the probe photon energy from the final state energy with respect to the Fermi level<sup>1</sup>. The gray level below the spectra indicates the nominal layer thickness between 0–1 ML as given by the color-code, where black corresponds to bare Ag(001) and white to the complete monolayer coverage. For a better reading the raw data of the spectra are shown on logarithmic scale without any normalization or vertical offset<sup>2</sup>. With increasing thickness the intensity of the 2PPE spectra decreases and an upshift of both states to higher intermediate state energies is observed. Additionally, the main feature ( $n=1$  IPS state) shows an asymmetric profile with a tail to larger energies. At a film thickness of 0.7 ML a broad feature at  $\sim 3.7$  eV becomes evident as a shoulder of the  $n=1$  IPS. This feature is assigned to an unoccupied Ni-3d state (feature A) of the NiO monolayer, which will be discussed in more detail in section 4.3.2. The lower part of Fig. 4.5 (b) shows the peak positions of both states with respect to the film thickness where the open circles represent the  $n=1$  and the open diamonds the  $n=2$  IPS. For bare Ag(001) the  $n=1$  and 2 IPS are identified at  $3.83 \pm 0.05$  and  $4.22 \pm 0.05$  eV, respectively. At

<sup>1</sup>For the determination of the intermediate state energy the pump-probe mechanism is necessary.

This can be explored by varying the photon energies of both laser beams. For the case of an established probe mechanism, this energy scale will be used in the following sections.

<sup>2</sup>Except the red spectrum of bare Ag(001) which has been taken from a different data set.



**Figure 4.6:** Semi-logarithmic plot of the normalized time-resolved intensities of the  $n=1$  and  $2$  image-potential states on Ag regions of bare Ag(001) (black), 0.45 ML (dark gray), and 0.60 ML NiO (light gray), respectively. The red and green solid lines represent the curve fittings using a cross-correlation of 85 fs to determine the lifetimes. (Note: the deviations between data points and curve fit of the  $n=2$  state at 0.6 ML thickness are due to strong laser fluctuations which are not correctable with the recorded laser intensities.)

0.8 ML coverage the states shift to higher energies of  $3.99 \pm 0.05$  and  $4.46 \pm 0.05$  eV, respectively. Note that the large error bars of the film thickness for the first three data points are due to the uncertainty of the wedge-shaped film profile preparation described in section 4.1.2. For the other data points the low-energy cutoff (average work function) in the 2PPE spectra could be used to determine the film thickness with a higher accuracy. The upper part of Fig. 4.5 (b) shows the change of the relative shift of both states with respect to the bare Ag(001) substrate. Up to 0.3 ML no significant change of the energy difference between the  $n=1$  and  $2$  state is observed ( $\Delta E_{1,2} \sim 0$  eV). But with increasing film thickness the relative distance increases as well. At the 0.8 ML coverage the energy between both states is increased by  $85 \pm 10$  meV.

In Fig. 4.6 the time-resolved intensities of the  $n=1$  and  $2$  IPS of bare Ag(001) and two different NiO thicknesses are shown on a semi-logarithmic scale. The good signal to noise ratio allows to follow the intensity of the  $n=1$  and  $2$  state over almost three orders of magnitude. For bare Ag(001) (black data points) the well known lifetimes of  $58 \pm 10$  and  $170 \pm 10$  fs have been determined [31]. With increasing film thickness a shortening of the lifetimes of both states is observed. Lifetimes of  $48 \pm 10$

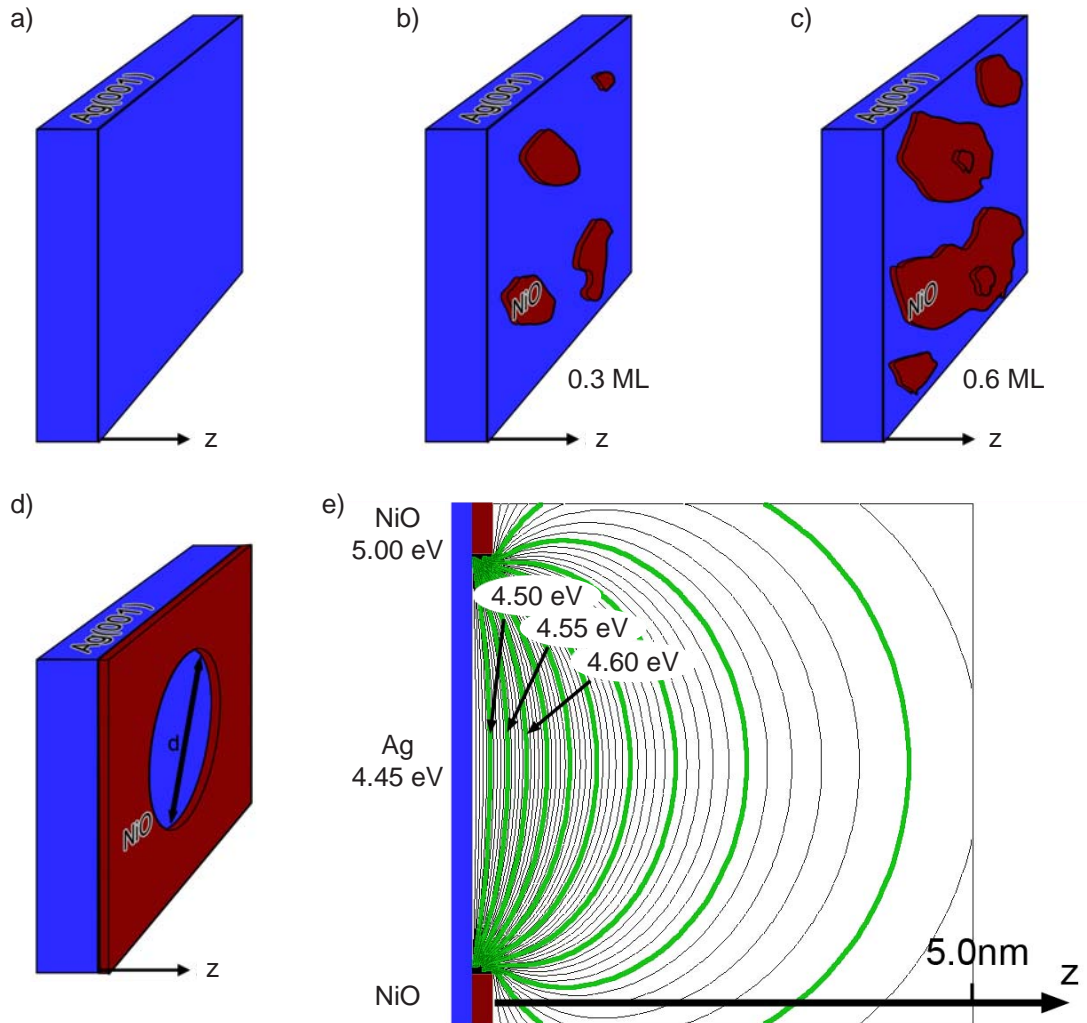


**Figure 4.7:** Model of the morphology of sub-ML NiO/Ag(001): (a) bare Ag(001), (b) and (c) 0.3 and 0.6 ML, respectively. In (c) a possible start of the bilayer growth is indicated. (d) Simplified model of (b) and (c) using a circular Ag region surrounded by NiO, where the average diameter  $d$  is determined by the NiO coverage. (e) Calculation of the electric potential in the vacuum caused by a solid structure as shown in (d) (here a side view of a cut through the center of the circular Ag region is shown), where electrostatic potentials of 4.45 and 5.00 eV for the Ag and the NiO have been assumed, respectively. The given isoelectric lines (in eV) correspond to a diameter  $d$  of 4 nm.

and  $33 \pm 10$  fs for the  $n=1$  and  $147 \pm 10$  and  $65 \pm 10$  fs<sup>3</sup> of the  $n=2$  state have been determined at coverages of 0.45 and 0.60 ML, respectively.

For the interpretation of the experimental observation and the development of a model some facts about the morphology of the NiO sub-monolayer are necessary. Figure 4.7(a) depicts the clean Ag(001) substrate whereas (b) and (c) show the 0.3 and 0.6 ML NiO coverage. The NiO on Ag(001) shows a Frank-van-der-Merwe like growth (layer-by-layer) which has been observed in STM [15,53], LEED [47],

<sup>3</sup>The large deviations of the data points with respect to the curve fit between 0–100 fs is due to laser fluctuations. The diode data do not allow for data correction which might be caused by additional spatial beam instabilities.

MEED [58], and the combination of LEED and UPS as shown in section 4.1.2. This leads to the observation of mainly monolayer thick islands within the sub-ML NiO films as indicated in Fig.4.7 (b) and (c). Only small patches of the starting bilayer growth are observed [15] as depicted in Fig.4.7 (c) as well. The size distribution of different NiO islands and accordingly the mean size of remaining Ag regions is an important issue in this context. As shown by Großer [15] the growth of 0.8 ML NiO at 380 K results in Ag regions with a typical diameter of 2.5–5 nm. The corresponding ML-thick NiO islands exhibit diameters of 7–20 nm. Assuming a constant nucleation density for island growth the typical island sizes mentioned above can be inverted comparing a 0.8 with a 0.2 ML coverage. Here diameters of 2.5–5 nm and 7–20 nm for NiO islands and Ag regions are expected, respectively. Note that these are typical length scales where Fischer *et al.* already predict the influence of confinement effects [83]. But the lateral confinement of IPS does not treat the observed relative energy shift between the  $n=1$  and 2 state as shown in Fig. 4.5 (b). The confinement should act on both electronic states similarly. For this reason a description according to an effective potential of the IPS is preferred.

The model includes the following assumptions. The IPS above a Ag regions at a certain sub-ML NiO coverage are influenced by the surrounding NiO monolayer islands. Thus, the normal image potential ( $\propto \frac{1}{z}$ ) is modified due to inhomogeneities of the electrostatic potential close to the surface (due to local work function differences). Without calculating the exact charge distribution (as reported by Kazansky *et al.* [85] for Na/Cu(111)) which indeed determines the shape of the electrostatic field at the surface a simple model is used. The electric field will be evaluated by calculating the classical electrostatic potential of the surface morphology. For each surface region, i.e., a NiO island or a Ag region, the potential at  $z=0$  has been assumed to be homogeneous. The value is given by the corresponding work function. This is doubtless true for Ag and its free-electron gas which should produce such homogeneity. In the case of NiO this is not necessarily the case, although a metallic character of the NiO monolayer is observed (see also 4.1.2 and [60,61]). However, the main contribution to the local work function of the NiO monolayer is the structural relaxation where the  $\text{Ni}^{2+}$  and  $\text{O}^{2-}$  ions have different  $z$  positions [54] and form an additional surface dipole. This formation has a certain dipole moment at each Ni-O site (forget about the quasi-hexagonal in-plane structure [15,54]). The 2D lattice of the monolayer averages over all *single* dipoles and forms a macroscopic surface dipole. This ensures a sufficiently homogeneous potential of a NiO island at  $z=0$  in this model. The values used for the calculations are 4.45 eV and 5.0 eV for Ag and NiO regions, respectively. These are equivalent to the observed work functions of the single phases which justifies their application<sup>4</sup>. To simplify the calculation the *real* surface structure as depicted in Fig. 4.7 (b) and (c) is replaced by a spherical Ag region surrounded by NiO as shown in (d). The NiO coverage determines the island size as well as the size of the remaining Ag region. Thus, the diameter  $d$  of the Ag region in this model represents the average Ag region size and correlates with the NiO coverage.

---

<sup>4</sup>From STS the local work function of the NiO monolayer can be estimated between 5.5–5.8 eV (see discussion of the IPS at the end of this section). A local electrostatic potential of  $>5.5$  eV for the NiO region would increase the effects described here but would not change the fundamental discussion.

For a Ag region with a diameter of 4 nm the isoelectric lines are shown in Fig.4.7 (e), as a side view of (d). Without going into detail, a strong increase of the electrostatic potential of 0.4 eV within a vertical distance of 5 nm is observed. The latter distance agrees well with the characteristic length scale of the main probability density of IPS [8]. For that reason the potential close to the surface should have a significant influence on the IPS. Note that this model also describes the average work function which is determined by the electrostatic potential at large distances ( $z \rightarrow \infty$ ). The effective image potential of the IPS is calculated as a sum of the normal  $\frac{1}{z}$  image potential and the inhomogeneous (and  $z$ -dependent) electrostatic potential. This is intuitively justified because the convergence of the image potential to the vacuum level has to be fulfilled for  $z \rightarrow \infty$ . This is given by the average work function.

The calculation of the electrostatic field of particular region sizes  $d$  (according the average size of a certain coverage) leads to the  $z$ -dependent electrostatic potentials as shown in Fig. 4.8 by dotted lines. Figure 4.8 (a) shows the trivial result for  $d=\infty$ , i.e., the bare Ag(001) without any change of the potential. Naturally, no change of the image potential (black solid line) is observed. The dashed lines indicate the energy positions of the  $n=1$  and 2 IPS. In Fig. 4.8 (b) the result for a 20 nm Ag region is shown. This corresponds to a coverage of roughly 0.2 ML. At a distance of 3 nm the electrostatic potential is increased by 150 meV. According to that the effective image potential is changed as shown as red solid line (sum of the  $\frac{1}{z}$  potential and the red dotted line). The expected energies of the IPS are shown by red dashed lines. They can be estimated from simple quantum mechanical considerations. They have higher energies compared to the ones of the bare Ag(001) (black dashed lines). This is due to a *smaller* effective width of the potential at small distances  $z$ . With the same arguments the results of 12 and 4 nm Ag regions (according to 0.5 and 0.8 ML coverages) are shown in Fig. 4.8 (c) and (d), respectively.

This model is able to explain the results of Fig. 4.5 (b) (page 31). At first, the relative energy shift between the  $n=1$  and 2 IPS is explained by an energy-dependent change of the *normal*  $\frac{1}{z}$  potential. The change of the *width* of the effective image potential is larger within the energy region of the  $n=2$  as compared to the  $n=1$  IPS. This leads to a larger shift of the  $n=2$  IPS. Secondly, the model explains the observed asymmetric peaks. As shown in Fig. 4.7 (e) (page 33) the electrostatic potential is not only determined by the diameter  $d$ . Additionally a lateral dependence within a single Ag region is observed as well. A larger gradient of the potential at the edges is observed. This causes an additional upshift. The sum over the whole Ag regions and additionally the sum over all possible regions sizes (distribution of the diameter  $d$ ) results in an asymmetric peak with a tail at higher energies.

The proposed model is able to explain the energy shift of the IPS of Ag at sub-ML NiO coverages. In retrospect, the model delivers comparable results as the theoretical calculation of the effective image potential by Kazansky *et al.* [85] for the description of Na/Cu(111) data [84]. Additionally, it is able to explain the data of Ag/Pd(111) [81,83] as well, without the influence of any lateral confinement of IPS. The fact that during room temperature growth of Ag islands no energy shift is observed [81] could be explained by the large diffusion length of Ag atoms. The Ag and Pd regions are sufficiently large ( $d > 30$  nm) to suppress any influence of the potential from neighboring regions. In contrast the growth at low temperatures suppresses the diffusion of the Ag atoms. Thus, only small islands are formed and a shift of the IPS energies has been observed [83]. This is explained by the influence

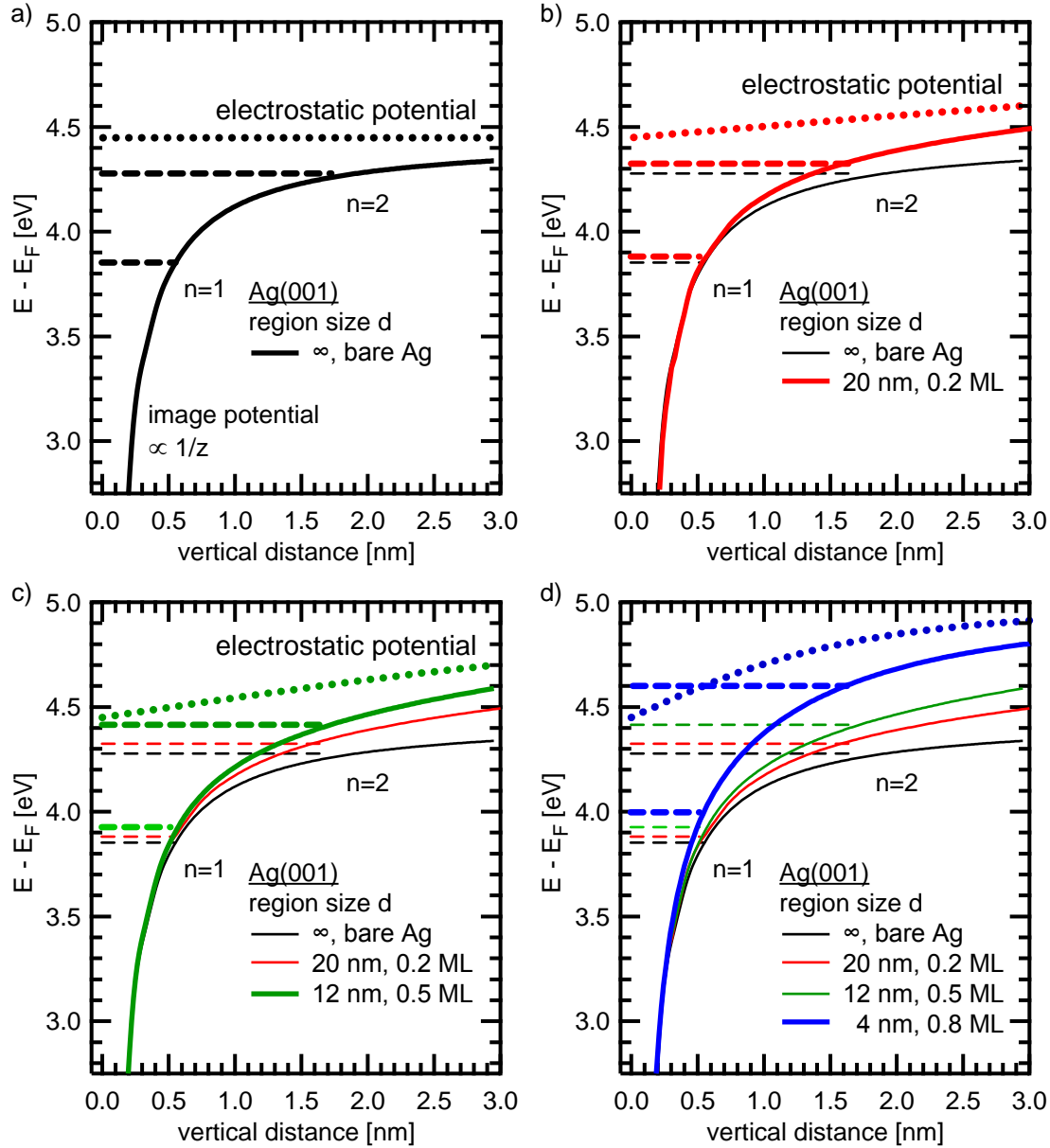


**Figure 4.8:** (a)-(d) Electrostatic potential (dotted lines) of the bare Ag substrate, 0.2, 0.5, and 0.8 ML NiO, respectively, in dependence of the vertical distance to the surface according to the model of Fig. 4.7. The solid lines represent the effective image potential as a sum of the image potential ( $\propto \frac{1}{z}$ ) and the electrostatic field. The expected energy positions of the  $n=1$  and  $2$  image-potential states are shown as horizontal dashed lines. Note the larger energy shift of the  $n=2$  state with increasing NiO coverage.

of the electrostatic potential to the formation of the effective image potential of the IPS due to the typical Ag island sizes. Upon *heating* of the cooled sample to room temperature, only IPS of the Ag monolayer are observed. This indicates that the formation of monolayer thick Ag is energetically favored compared to islands of higher thicknesses. This supports the above mentioned large Ag regions during room temperature growth and the large diffusion length as well. Note that the growth of



NiO/Ag(001) is different. The diffusion length of NiO is much smaller<sup>5</sup>. Thus, the single island structure persists during growth at room temperature. This increases the influence of the modified effective potential at lower coverages.

With a closer look to the thickness-dependent 2PPE data presented in Fig. 2 of Ref. [81] at a coverage of 0.63 ML, a *downshift* and a broadening of the n=1 IPS of the Pd(111) substrate is observed. At this coverage the Pd regions gets as small as confinement effects should be considered. However, the feature shifts to a smaller energy. This is the opposite direction as expected from confinement (confinement would shift the state upwards, anyway). The potential model described here directly predicts this observation. The effective image potential of the region with the larger local work function (namely the remaining Pd(111) regions) is decreased due to a decrease of the electrostatic potential. It would be interesting to investigate coverages between 0.63 and 1.0 ML Ag/Pd(111) to prove the model.

The second issue, namely the shortening of the lifetime with increasing NiO coverage (see Fig. 4.6 page 32), is also reasonable within the presented model. The z-dependent modification of the effective potential compared to the normal  $\frac{1}{z}$ -image potential gives rise to the following conclusion. The difference of calculated effective potential and the normal  $\frac{1}{z}$ -potential increases at larger distances. This is by definition equivalent to the difference of the z-dependent electrostatic potential and the local work function at z=0. This dependence in z causes a decrease of the probability density of the IPS with increasing distance. Therefore, an increase of the amplitude close to the surface and consequently the amount of  $\Psi^2$  in the sub-surface area (*bulk penetration*) is expected as well. To put it simply, the wave function is expected to be *pushed* closer to the surface. This leads to an increase of the overlap with bulk states and the scattering probability. The lifetime  $\tau$  of an IPS can be estimated via the bulk penetration model [70,86,87]

$$\tau^{-1} \cong p \cdot \Gamma_b \quad , \quad \text{with} \quad (4.5)$$

$$p = \int_{-\infty}^0 |\Psi^2| dz \quad , \quad (4.6)$$

where  $p$  describes the probability to find the electron below the surface and  $\frac{1}{\Gamma_b}$  the lifetime of bulk states at the energy of the IPS. According to equation 4.5 the comparison of two lifetimes  $\tau_a$  and  $\tau_b$  leads to

$$p_b = \frac{\tau_a}{\tau_b} p_a. \quad (4.7)$$

Thus, the n=1 IPS shows an increase of the bulk penetration  $p$  by a factor of 1.2 and 1.8 and the n=2 IPS by a factor of 1.2 and 2.6 for the 0.45 and 0.60 ML coverage, respectively.

Kazansky *et al.* determined the wave functions of image states of Na/Cu(111) using the calculated effective potential [85]. An increase of the  $\Psi^2$  maximum to larger distances and a decrease of the bulk penetration  $p$  has been reported. This is reasonable, because the work function decreases upon Na adsorption. This decreases the effective potential at larger distances and therefore increases the probability

---

<sup>5</sup>The smallest diffusing unit is NiO instead of a single metal atom. However, the diffusion mechanisms of the NiO on Ag is still an open issue. The effective diffusion through diffusing atoms of the substrate is favorable. This is accompanied by the embedding NiO islands [15].

density as well. This determines a larger lifetime of the IPS. However, Wang *et al.* reported a shortening of the lifetime upon Na adsorption using linewidth analysis of monochromatic 2PPE [88]. Instead of a pure lifetime decrease they attributed the observation to an adsorbate scattering induced linewidth broadening. Therefore, the predictions of Kazansky *et al.* could not be verified directly.

In summary, all facts point to a misinterpretation of the Ag/Pd(111) data in terms of confinement. Additionally, the picture of the local work function in combination with IPS is not true. The IPS are not suited as a good sensor for the local work function. The main reason is the relatively *large distance* to the surface which involves a strong influence of the surrounding areas on the effective potential of the IPS. As soon as the structures get *small enough* (depending on the work function differences or other potentials involved) the IPS electrons above a certain surface patch *feel* the surrounding surface composition very sensitively. The changes of the IPS properties have been discussed via modeling the electrostatic potential close to the surface which leads to the formation of an effective image potential which strongly differs from the normal  $\frac{1}{z}$ -image potential. Note that the potentials given in Fig. 4.8 (page 36) are due to the assumptions mentioned above and are not representative for any further calculation on this topic. Therefore, a complete description of the effective potential similar to the calculations of Kazansky *et al.* [85] is necessary. However, this is not the scope of this work.

With the growing NiO film the observation IPS of NiO islands are expected as well. The experimental data of the sub-monolayer coverage do not show any feature in the expected energy region. The large work function of the NiO monolayer films leads to large intermediate state energies of the IPS. Despite of the wide-range tuneability of the laser system, the study of that energy region ( $h\nu_{UV} \geq 4.8 \text{ eV}$ ) is still a sophisticated experimental issue. However, an indication of their existence is shown as a small side aspect of the monolayer investigations in sections 4.4.2 (Fig. 4.45 (b) on page 91).

The determination of the work function of the NiO monolayer should be reviewed here. The UPS data reveal a value of 5.0 eV. This might be influenced by film imperfections e.g., step edges. Another approach is to estimate the work function from the STS data. Therefore, the energy of the first field emission resonance can be used. Comparing the data of the bare Ag(001) substrate and its well-known work function, the work function of the NiO monolayer is estimated between 5.5–5.8 eV. This supports the above mentioned large intermediate state energy of the IPS. Thus, the IPS are not accessible at the sub-monolayer coverage due to the smaller average work function.

### 4.2.3 Image states of 2 ML NiO/Ag(001)

The atomic structure of the NiO bilayer is similar to the rock salt structure of the NiO bulk [48,50]. Thus, the formation of the bulk-like properties is expected as well, despite of any thin-film induced deviations. In this section the IPS of the NiO bilayer on Ag(001) will be presented. The data will be analyzed in terms of the dielectric properties of the NiO.

An angle-resolved 2PPE spectrum of the NiO bilayer is shown in Fig. 4.9 (a) where the color code shows the normalized intensity of the photoelectrons with respect to the final state energy and the emission angle. The intensity has been

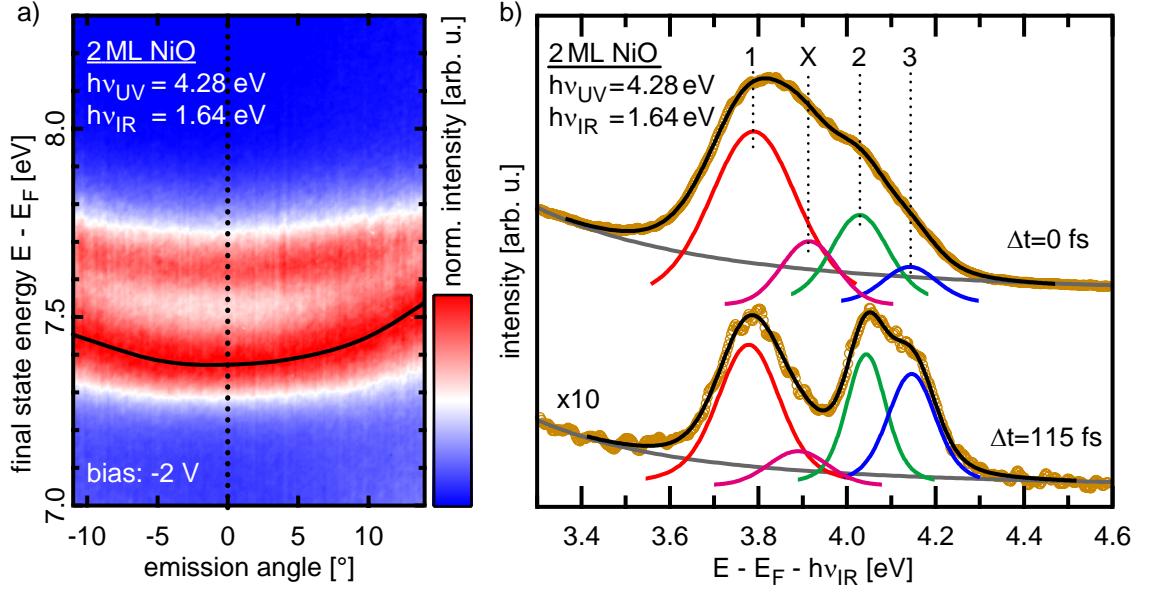


**Figure 4.9:** (a) Angle-resolved 2PPE of the NiO bilayer on Ag(001) obtained for  $h\nu_{UV}=4.27$  eV and  $h\nu_{IR}=1.68$  eV with bias voltage -2 V. The intensity of each angular line has been normalized to maximum. (b) Line profiles through (a) at  $0^\circ$  and pump-probe delays of 0 and 115 fs, respectively, with respect to the intermediate state energy. Four features are identified (blue and green curves). The applied background is shown by the gray line.

normalized for each angular direction with respect to the intensity maximum in the energy region between 7.2 and 7.8 eV. The photon energies have been adjusted to 4.27 and 1.67 eV for the UV and the IR pulse, respectively, and a bias voltage of -2 V has been applied to increase the observed  $k_{\parallel}$  range within the given detection angles. Two dispersing features at  $\sim 7.40$  and  $\sim 7.65$  eV are observed. The solid black line follows the intensity maximum of the main feature. A parabola-like shape is found (the curve does not show a parabolic fit). As it will be shown by time-resolved 2PPE below the states are UV-pumped and IR-probed. Two line profiles at normal emission for pump-probe delays of 0 and 115 fs are shown in Fig. 4.9 (b), respectively. The photoelectron intensity is plotted with respect to the intermediate state energy. The comparison of the two spectra reveals the contribution of four states to the 2PPE signal. A feature X at  $3.93 \pm 0.05$  eV and the IPS  $n=1-3$  at 3.78, 4.04, and 4.14 eV (each  $\pm 0.05$  eV) are identified, respectively. The change of the relative intensities of all states indicates different lifetimes.

The angle-resolved peak positions of the  $n=1$  IPS are shown in Fig. 4.10. The energy axis corresponds to the measured kinetic energy in the electron analyzer of the biased sample. Accordingly, the angular axis shows the detection angle on the CCD detector. An effective mass of 1.0 has been fitted to the data as shown by the solid black line. The dotted lines show the parabolic dispersion of effective masses of 0.85 and 1.3, respectively. This is used to estimate the experimental error of the effective mass which is in the order of  $\sim 0.1 m_e$ <sup>6</sup>.

<sup>6</sup>Experimental problems of the  $\mu$ -metal shielding might influence the angular information.

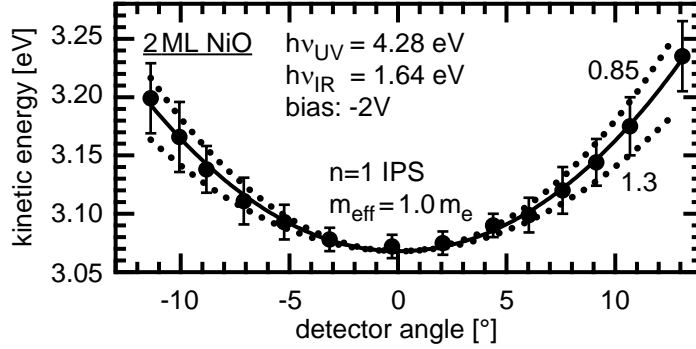


**Figure 4.10:** Angle resolved peak positions of the  $n=1$  IPS of 2 ML NiO at a pump-probe delay of 100 fs. The sample has been biased at -2 V. The solid black line shows a parabolic dispersion with  $m_{eff}=1.0 m_e$  and the dotted lines of 0.85 and 1.3, respectively.

The time-resolved intensities of the four states are shown in Fig. 4.11 on semi-logarithmic scale. The intensities have been determined by fitting the peaks at each pump-probe delay similar to Fig. 4.9 (b). For a better reading the intensities are shifted with respect to each other and background subtracted. The data points represent the intensity of all individual peaks. Due to space charge effects (energy shift and peak broadening) it has been assumed that these effect act on all features similarly. The data have been modeled as follows. At first, the background has been subtracted using the background subtraction method B (see Appendix 6.B). Secondly, the energy positions ( $E_{n,0}$ ) and widths ( $w_{n,0}$ ) of the image states have been determined at large pump-probe delays, where the influence of space charge effects is not evident. Having these parameters fixed, the peaks at small delays show an additional energy shift ( $E_n=E_{n,0}+\Delta E$ ) and a larger width ( $w_n=b \times w_{n,0}$ ) similar for all states. The existence of the feature X between the  $n=1$  and 2 state causes an energy shift of these states in different directions (electrons of feature X cause an acceleration of  $n=2$  and 3 IPS electrons and deceleration of  $n=1$  electrons). For that reason the higher IPS are not well represented at small delays and therefore not shown here. However, the signal-to-noise ratio allows to follow the 2PPE signal over more than two orders of magnitude. For all features an asymmetric intensity profile is observed. The linear slope at positive delays is due to the lifetime and reveal the pump-probe mechanism of the states (UV-pumped and IR-probed). A lifetime of  $31 \pm 5$  fs of the  $n=1$  IPS has been determined as shown by the black line. Due to the good agreement between the data points and the curve fit the location of time delay  $\Delta t=0$  and the cross-correlation of  $60 \pm 5$  fs is well defined. The latter is shown by the dashed line. Accordingly, the intensity profiles of the  $n=2$  and 3 states reveal lifetimes of  $50 \pm 5$  and  $120 \pm 15$  fs, respectively<sup>7</sup>. For the feature X a short lifetime of  $15 \pm 3$  fs is found. The lifetimes reported here are comparable to values found on the well-defined bare Ag(001) substrate. This allows to characterize the surface morphology which should be well ordered as well. Any noticeable existence of surface defects e.g., step edges and adatoms, would lead to a significant decrease of the lifetimes [10–14].

<sup>7</sup>For the curve fit the position of  $\Delta t=0$  and the cross-correlation width has been fixed.

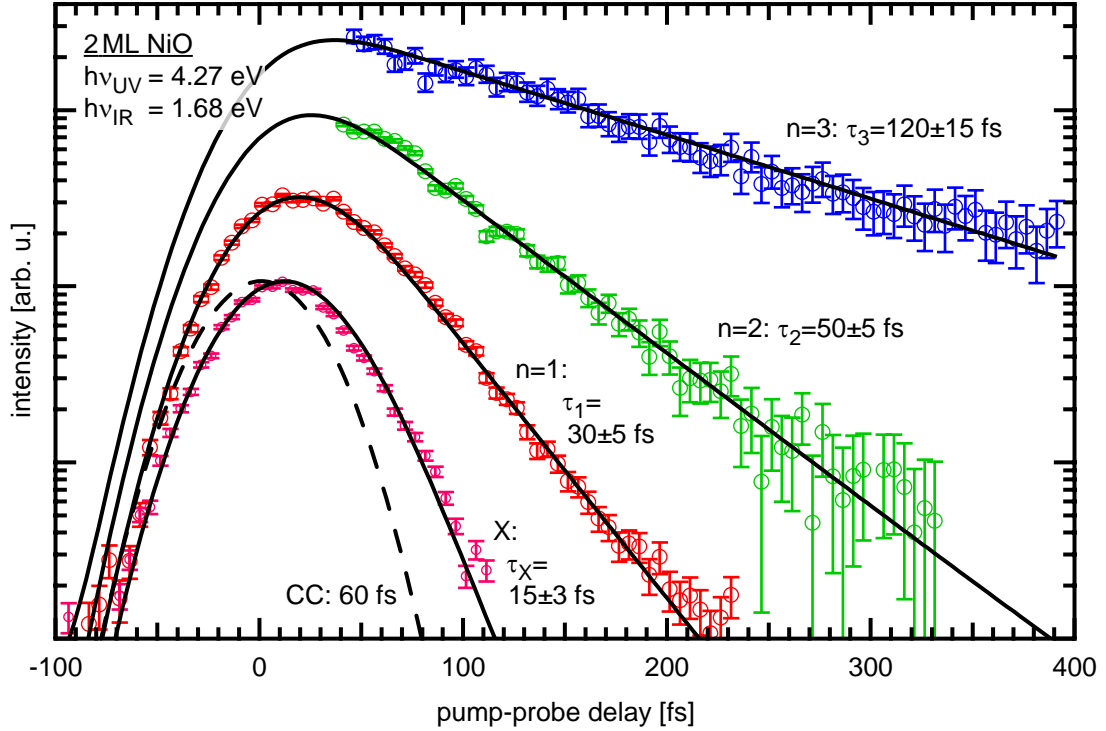


**Figure 4.11:** Semi-logarithmic plot of the time-resolved intensities of the three image states and the feature X identified in Fig. 4.9 (b). The black lines show the corresponding curve fits. The cross-correlation trace of 60 fs (FWHM) is shown as dashed line.

Note that an alternative way of data analysis is depicted in Appendix 6.C. The time-dependent intensities are estimated by integration of all electrons in a certain energy region. This should be dominated by one of the observed features. Similar values of the lifetimes have been obtained which justifies this method. In section 4.2.5 this method will be applied to the data of an 8 ML NiO film where the modeling via individual peaks fails.

The parabolic dispersions with an effective mass of  $1 \times m_e$  and the relatively large lifetimes of the features 1–3 are typical for IPS. In contrast to metal substrates, an oxide overlayer and its dielectric properties should have a strong impact to the IPS properties, with respect to their binding energies and dynamics. According to equation 4.3 the binding energies of the IPS are determined by the permittivity  $\epsilon$  and the quantum defect  $a$ . Whereas the former one describes the polarizability of the surface, the latter one is determined by the electronic structure. The permittivity of thin NiO films has not been investigated so far. The  $I$ - $V$  characteristic of 2 and 3 ML NiO films in STS indicates the onset of the insulating character [50]. Whereby, a difference between both thicknesses is still observed. This means that the NiO bilayer could still have a metallic character. This would lead to relatively large values of the permittivity (compare with metal substrates:  $\epsilon$  approaches  $\infty$ ). On the other side, thickness-dependent permittivities of other oxides have been reported [89–92]. In all references, film thicknesses up to 1000 Å (a few hundred monolayers!) show much smaller values compared to the corresponding bulk ones. This could be explained by the film morphology. The thin films exhibit an amorphous structure,

whereas crystalline phases develop at larger thicknesses<sup>8</sup>. This explains the smaller permittivities of thin films. However, the well defined growth conditions of NiO on Ag(001) lead to a perfect crystalline phase<sup>9</sup>. Thus, the thickness-dependent permittivities of these films are not comparable to the other works.

Due to the strong variation of the work function of the NiO films within the first layers, the determined value of 4.2 eV for the nominal bilayer thickness might not reflect the *real* work function of the bilayer. But this is necessary to calculate the binding energies of the IPS. Therefore, another approach will be used. The intermediate state energies of the IPS lead to the following conclusions. The n=3 state at 4.14 eV limits a possible uncertainty of the work function to definitively  $4.14 \leq \Phi \leq 4.23$  eV. The lower border is due to the fact that the state has to have a binding energy with respect to  $E_{vac}$ , whereas the upper border is due to the largest possible binding energy of 94 meV<sup>10</sup>. This limited range of the work function determines the values of the binding energies of the IPS. According to equation 4.3 the combination of the work function  $\Phi$ , the intermediate state energies  $E(n)$ , and the possible values of the quantum defect  $a$  (between 0–0.5) allow to calculate the permittivity

$$\epsilon = \frac{1 + \mathcal{S}}{1 - \mathcal{S}}, \quad (4.8)$$

$$\text{with } \mathcal{S} = 4 \sqrt{\frac{(\Phi - E(n))(n + a)^2}{13.6}}. \quad (4.9)$$

The calculated permittivity of all combinations of  $a$  and  $\Phi$  for the n=1–3 IPS are shown in Fig. 4.12 (a)–(c), respectively. The solid black lines indicate the permittivity for different values of  $a$  (0.0, 0.1, 0.2, etc.) in dependence of the assumed work function. The red, green, and blue shaded areas indicate the possible combination of all parameters. Figure 4.12 (d) shows the additive color mixing of the colored regions of (a)–(c). Thus, the white area (sum of red, green, and blue) shows the region where a single value of  $\Phi$  and  $\epsilon$  matches all three IPS. The horizontal dashed line indicates the bulk value of  $\epsilon=12$  [9]. Assuming this value and an effective mass of  $m_{eff}=1 m_e$  (see Fig. 4.10) equation 4.3 leads to

$$E_n = \frac{0.609}{(n + a)^2}. \quad (4.10)$$

The calculated work function for  $\epsilon=12$  is 4.19 eV, as indicated by ① in Fig. 4.12 (d). This value is close to the experimentally obtained value of 4.20 eV, as indicated by the vertical dashed line. This leads to binding energies of the IPS of 0.41, 0.15, and 0.05 eV, respectively. Thus, equation 4.10 can be used to determine the quantum defect  $a$ . The corresponding values are 0.22, 0.01 and 0.49, respectively. A strong variation of the quantum defect is observed. This result clearly deviates from the observation of the bare metal substrate, where the quantum defect varies only slightly within the band gap. For the NiO one has to consider that there might be

<sup>8</sup>The films have been prepared on a glass substrate with Al films as electrodes. The preparation conditions are far away from any crystalline growth.

<sup>9</sup>This is evident in the large lifetimes of the IPS as discussed above.

<sup>10</sup>Given by  $\epsilon=\infty$  and  $a=0$  according to equation 4.3.

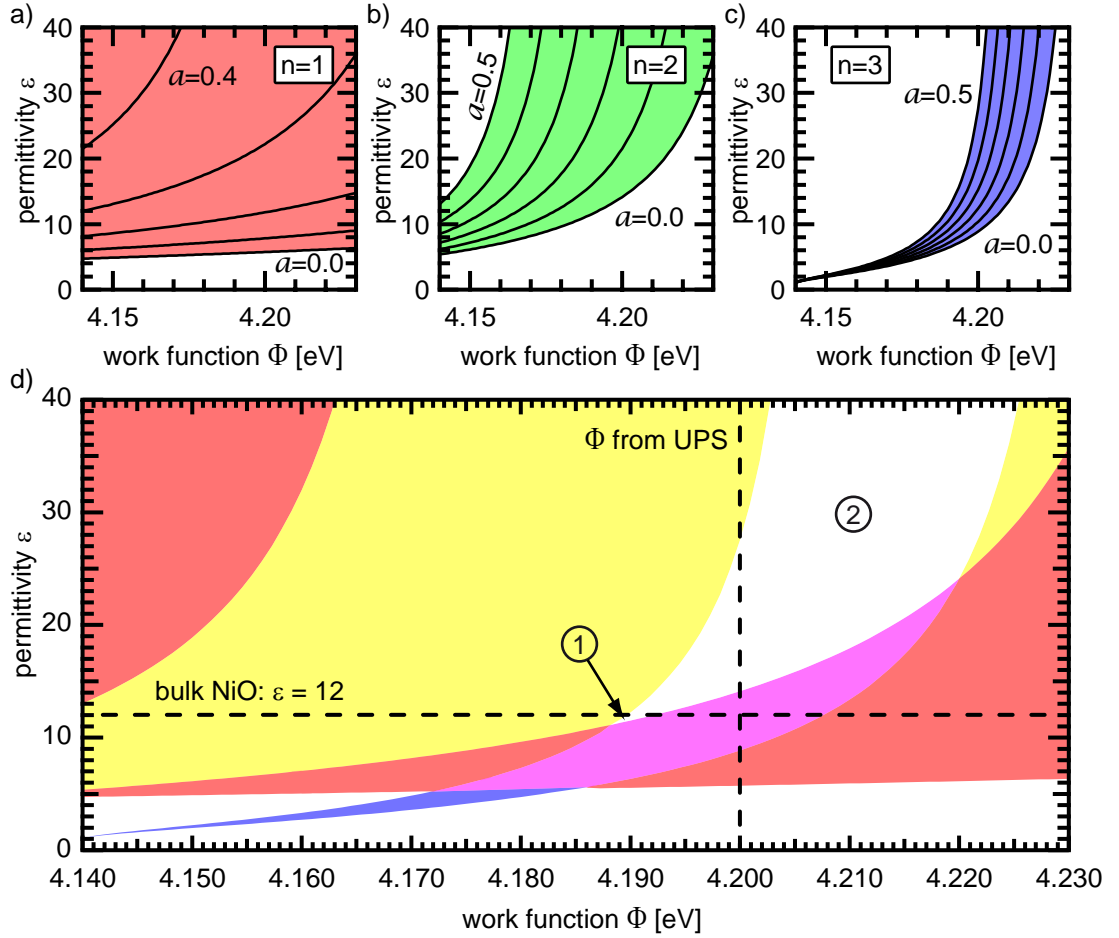


**Figure 4.12:** (a–c) Solid black lines show the calculated permittivities of the 2 ML NiO in dependence of the work function and for the given values of the quantum defect  $a$  of the  $n=1$ –3 IPS, respectively. The colored areas indicate the overall range. (d) Additive color mixing of the areas of (a)–(c). The white region illustrates the coincidence of all three regions.

no band gap anymore in this particular energy region. This determines the coupling of the IPS to the surface and influences the quantum defect.

As mentioned above, a possibly metallic behavior of the NiO bilayer has to be considered as well. This leads to a permittivity definitely larger than 12 as indicated by ② in Fig. 4.12 (d) and thus, other values of  $\Phi$  and  $\epsilon$ <sup>11</sup>. This issue needs to be further investigated in future experiments. The preparation of a well-ordered and defect-free bilayer NiO film is the crucial point and might be obtained using the preparation conditions as predicted in section 4.3.4.

The origin of feature X is not evident, yet. Its energetic position leads to two possible states. First it might originate from the  $n=1$  image state of small remaining Ag(001) patches within the NiO bilayer. But one has to consider a shift to a lower intermediate state energy compared to bare Ag(001) according to the discussion in the previous section. Secondly, the feature X might originate from the feature B of small remaining NiO monolayer patches within the nominal bilayer thickness.

<sup>11</sup>However, any combination of  $\Phi$  and  $\epsilon$  in Fig. 4.12 leads to strong variations of  $a$ .

This feature will be discussed in more detail in section 4.4.2 (resonantly excited Ag-*sp* band transition). To discriminate between IPS or Ag-*sp* band transition UV photon energy dependent spectra are necessary. The intermediate state energy of the possible IPS should be independent of the pump photon energy whereas the feature B shows an additional energy shift. One experimental problem might be the low work function of  $\sim 4.2$  eV of the bilayer film which prevents to adjust the pump pulse much above 4.2 eV. This is necessary to examine the possible Ag-*sp* band transition in more detail (details see analysis of feature B in section 4.3.2 and 4.4.2).

#### 4.2.4 Image states of lacerated NiO films – Heating the monolayer and bilayer

For a NiO ultra-thin films it is expected that the films lacerate after reaching a critical temperature [15,53]. During laceration of a closed NiO film regions of uncovered Ag are formed at the sample surface. This leads to the occurrence of IPS of the Ag regions which are typically observable by bichromatic 2PPE. In Fig. 4.13 (a) an angle-resolved 2PPE spectrum of a monolayer NiO film upon annealing at  $\sim 600$  K is shown at a pump-probe delay of 200 fs. The intensity has been normalized with respect to the  $n=1$  IPS state. All features reveal an obvious parabolic dispersion. Line profiles at an emission angle of  $0^\circ$  are shown in Fig. 4.13 (b) where the UV and IR photon energies have been modified. The data are shown with respect to the intermediate energy of the IR probed states. All observed features coincide at the same energy position. Note that the upper curve shows a deviation for energies above 4.3 eV compared to the other spectra which is due to the excitation limit of the

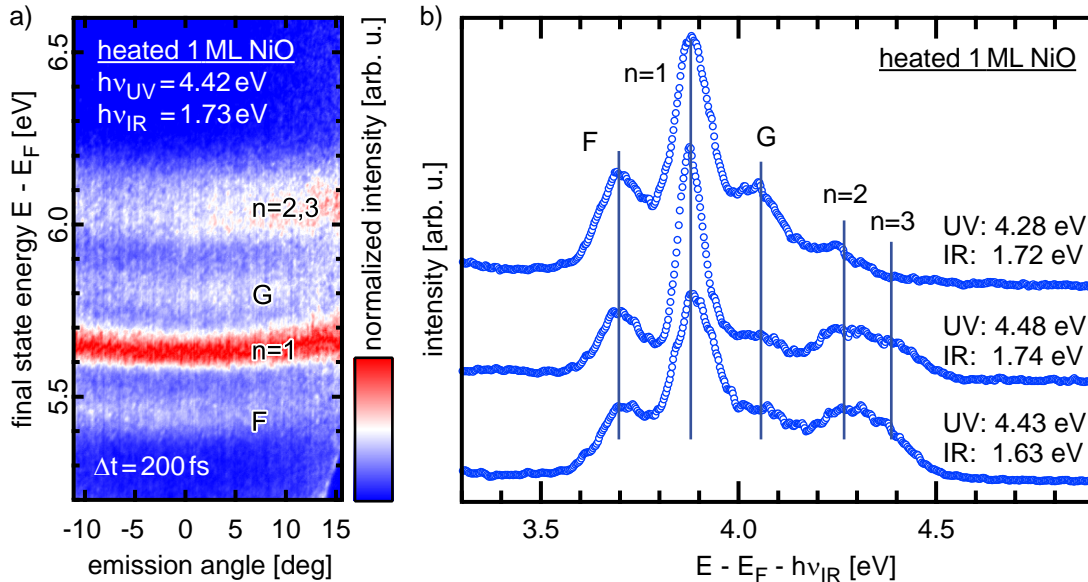


**Figure 4.13:** (a) Angle-resolved 2PPE of a monolayer NiO after annealing at  $\sim 600$  K at a pump-probe delay of 200 fs. The intensity of each angular direction has been normalized with respect to the  $n=1$  feature. (b) Line profiles through AR-2PPE similar to (a) at  $0^\circ$  for different UV and IR photon energies. The IR photon energy has been subtracted from the energy scaling of (a).



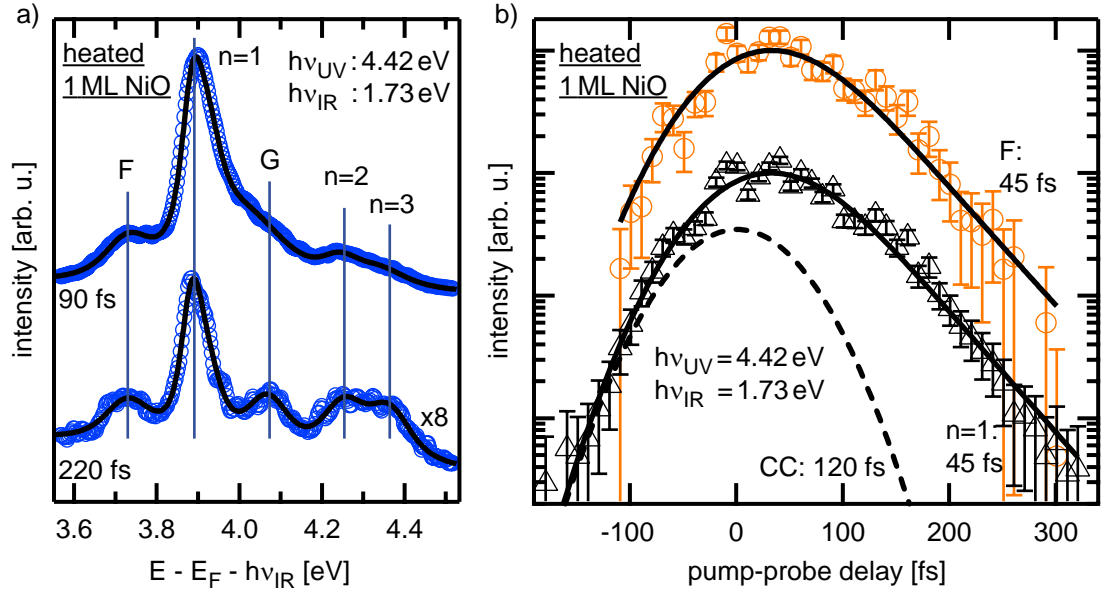


**Figure 4.14:** (a) 2PPE spectra at different pump-probe delays of a monolayer NiO upon annealing at  $\sim 600$  K. (b) Semi-logarithmic plot of the time-resolved intensities of the feature F at 3.73 eV (blue circles) and the  $n=1$  IPS of Ag regions (black triangles). The solid lines indicate a curve fit where for both states a lifetime of 45 fs is determined. The dashed line represents the cross-correlation (CC) of both laser pulses of 120 fs (FWHM).

UV photon of 4.28 eV. Similar to Fig. 4.13 (b) spectra at different pump-probe delays are shown in Fig. 4.14 (a). Five features are identified. According to the following discussion a series of image-potential states ( $n=1-3$ ) is identified. They are found at 3.89 ( $n=1$ ), 4.24 ( $n=2$ ), and 4.34 eV ( $n=3$ ) (each  $\pm 0.05$  eV), respectively. These values are in perfect agreement with the IPS of the bare Ag(001) substrate [31]. Two additional features F and G are observed at 3.73 and 4.01 eV, respectively. These states originate from the NiO island of the lacerated film because they are absent on the clean Ag substrate. The features F and G are assigned to the first and second IPS of NiO islands with higher thicknesses. To avoid confusions in the following discussion, the IPS of the Ag regions will be called  $n=1-3$  IPS whereas the IPS of the NiO regions will be called states F and G. The energies of F and G are slightly below the values found for the IPS of the bilayer film. This could have two reasons. At first, the energy shifts due to space charge effects ( $\leq 50$  meV). Or secondly, the lower local work function of NiO  $> 2$  ML (see section 4.1.2) leads to a lower intermediate state energy despite of similar binding energies of the IPS.

The time-resolved intensities of the state F and the  $n=1$  IPS are shown in Fig. 4.14 (b) with respect to the pump-probe delay. A lifetime of  $45 \pm 10$  fs of both states is observed. The cross-correlation between the laser pulses is 120 fs as shown by the dashed line. For the  $n=2$  and  $n=3$  IPS the statistics of the measurements are not sufficient to extract a lifetime with a significant accuracy.

Similarly, the NiO bilayer film has been heated above  $\sim 700$  K. The 2PPE spectrum is shown in Fig. 4.15 (a) using photon energies of 4.27 and 1.68 eV. Two features F at 3.69 eV and the  $n=1$  IPS of the Ag(001) at 3.94 eV are observed. The energies agree well with the states of the lacerated monolayer film within an accuracy of

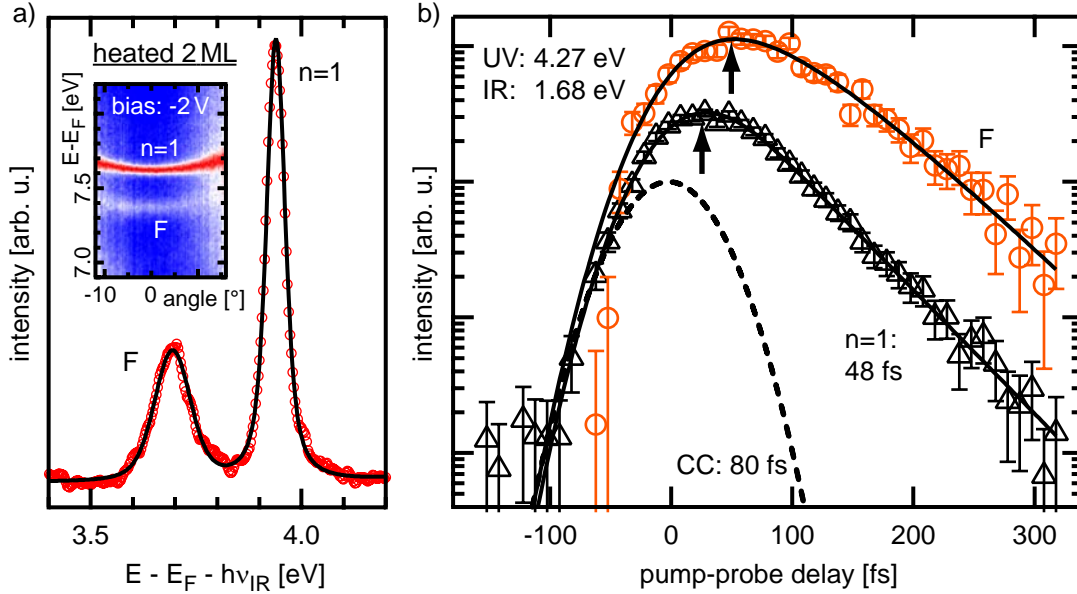


**Figure 4.15:** (a) 2PPE spectrum of NiO bilayer after annealing at  $\sim 700$  K at a pump-probe delay of 100 fs. The inset shows the angle-resolved data at a bias of -2 V (color-code: same as in Fig. 4.13 (a)). (b) Semi-logarithmic plot of the time-resolved intensities of the feature F (orange circles) and the n=1 IPS (black triangles). Note the shifted intensity maximum of feature F despite of a similar linear slope of both curves at large delays.

50 meV. The inset shows the normalized angle-resolved data. A parabolic dispersion of both states is observed as well. The time-resolved intensities of the two states are shown in Fig. 4.15 (b) on semi-logarithmic scale. Both curves show an asymmetric intensity with respect to  $\Delta t=0$ . The linear slopes at large delays ( $\geq 100$  fs) are identical indicating a lifetime of  $\sim 48$  fs. However, the intensity maximum of state F is shifted to larger delays in comparison to the n=1 IPS as shown by the black arrows. Assuming two states with similar lifetimes, the time-dependent intensity profiles should have an identical shape as well. Thus, the shift of the intensity maximum of state F has to originate from a different excitation or relaxation process. This will be analyzed as follows.

Figure 4.16 (a) shows a side view of a lacerated NiO film. The IPS electrons are indicated as classical particles above the Ag and NiO regions. At first the IPS of the Ag region will be considered. The excitation ① describes the pump mechanism. This is expected to be unchanged in comparison to the clean Ag(001) substrate. Thus, this state is used to characterize the experimental setup by means of the the cross-correlation and the temporal overlap of the pump and probe pulse ( $t=0$ ). A lifetime of  $48 \pm 5$  fs has been determined as shown by the black line in Fig. 4.15 (b). This corresponds to a shortening of 9 fs with respect to the clean Ag. The parameters of  $t=0$  and the cross-correlation of 80 fs are well defined. Two different excitation processes could be considered for the excitation of state state F. The excitation ② and ③ describe the transition of an electron from occupied Ag and NiO states, respectively. The contribution of the Ag substrate depends on the transmittance of the electrons through the oxide film whereas the available density of states of the NiO determines the contribution of the oxide. However,

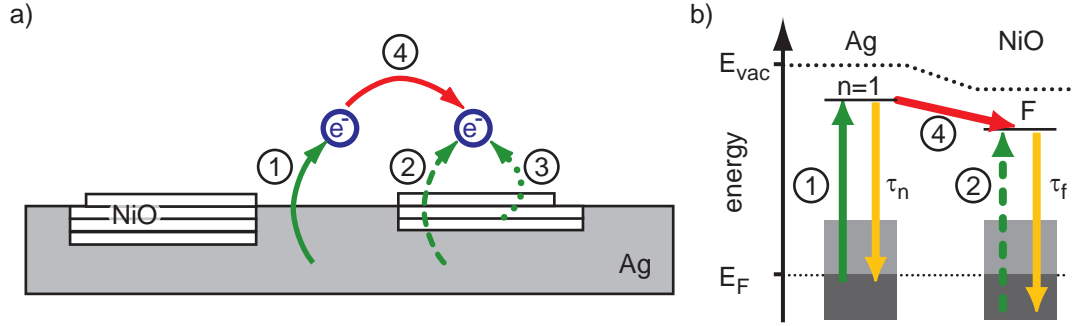


**Figure 4.16:** (a) Classical description of the population and relaxation of IPS of Ag and NiO regions of lacerated NiO thin films (details see text). (b) The corresponding energy diagram for the decay of  $n=1$  IPS electrons of Ag and the IPS of NiO (state F). The lifetimes are  $\tau_n$  and  $\tau_f$ . The  $n=1$  state additionally decays via the state F. Note the energies are not to scale.

in both excitation processes the pump-probe scheme is similar to the one of the  $n=1$  IPS. In the case of a similar lifetime, this should lead to an identical time-dependent intensity (without shift of the intensity maximum). Since a theoretically similar lifetime is observed accompanied with a shift of the intensity maximum the population of the state F deviates from a simple pump-probe mechanism.

As shown by the transition ④ in Fig. 4.16 (a) a relaxation of the IPS of the Ag into the state F is assumed. This should obviously change the time-dependent population of the state F. Additionally to the *normal* excitation ② and the decay with the lifetime  $\tau_f$ , the population is determined by the relaxation ④. A corresponding energy diagram of the excitation and relaxation mechanisms is depicted in Fig. 4.16 (b). Energetically, the transition ④ is basically allowed due to the energy gain. The IPS is populated at  $t=0$  and the population decays exponentially in time with a lifetime of  $\tau_n$ . Assuming an excitation of the state F exclusively via the decaying IPS electrons, the population of the state F can be described by the following differential equation

$$\dot{F}(t) = -\frac{1}{\tau_f}F(t) + N_0 e^{-\frac{t}{\tau_n}}, \quad \text{with } F(t=0) = 0 \quad (4.11)$$

where  $F(t)$  is the time-dependent population of state F,  $\tau_f$  the corresponding lifetime,  $\tau_n$  the effective lifetime of the image state, and  $N_0$  a numerical coefficient to describe the amount of relaxing electrons. Whereas the first term describes the decay of the population of state F the second term describes its effective time-dependent excitation from the IPS. The analytical solution of equation 4.11 is

$$F(t) = N_0 \frac{\tau_n \tau_f}{\tau_n - \tau_f} \left( e^{-\frac{t}{\tau_n}} - e^{-\frac{t}{\tau_f}} \right), \quad t \geq 0 \quad (4.12)$$

The sum of two exponential decays in the last part also includes two reasonable special cases. At first, the case  $\tau_f \approx 0$  which leads to  $F(t) \propto e^{-\frac{t}{\tau_n}}$ , i.e., the population of state F directly reflects the population of the IPS. And second, the case  $\tau_n \approx 0$

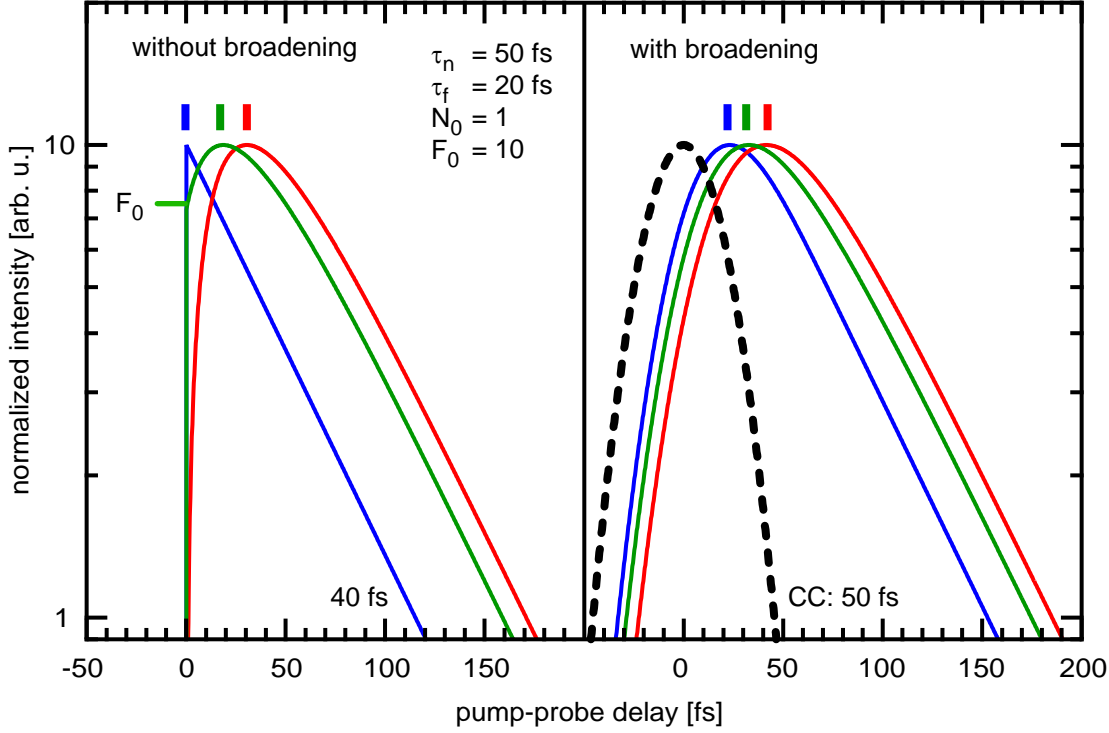


**Figure 4.17:** Semi-logarithmic plot of the calculated population curves for an unoccupied state which is populated via different excitation processes. Left without and right with temporal broadening (FWHM 50 fs) due to the cross-correlation (CC) of the laser pulses. Blue curve: simple exponential decay with a lifetime  $\tau=40$  fs. Red curve: population of a state with  $\tau_f=20$  fs via another exponentially decaying state with  $\tau_n=50$  fs. Green curve: same as red with additional direct excitation via the pump laser pulse (equivalent to 80% relaxation, 20% direct excitation). The vertical lines indicate the position of the particular intensity maximum. Note the identical linear slopes at large delays for all curves.

leads to  $F(t) \propto e^{-\frac{t}{\tau_f}}$ , i.e., the population of state F is created at  $t=0$  and a simple exponential decay is observed<sup>12</sup>.

Considering the direct excitation of state F via the pump laser pulse at  $t=0$  (transition ② and ③ in Fig. 4.16), the boundary condition of equation 4.11 is modified to  $F(0) = F_0$ . This leads to

$$F(t) = F_0 e^{-\frac{t}{\tau_f}} + N_0 \frac{\tau_n \tau_f}{\tau_n - \tau_f} \left( e^{-\frac{t}{\tau_n}} - e^{-\frac{t}{\tau_f}} \right), \quad t \geq 0 \quad (4.13)$$

where the second term is identical to equation 4.12 and the first term reflects the simple exponential decay of the starting population at  $t=0$ .

Exemplary, Fig. 4.17 shows the time-dependent population  $F$  (lifetime  $\tau_f$ ) with different excitation schemes on semi-logarithmic scale. On the left side the curves show the result without temporal broadening. The solid blue curve represents a simple exponential decay with a lifetime of 40 fs. This is identical to the expected

<sup>12</sup>Note that for these considerations the fraction in the first part of equation 4.12 is neglected which would typically be 0 due to the product  $\tau_n \tau_f$  in the denominator.

population of the  $n=1$  IPS of the Ag region. The solid red curve indicates the relaxation of the IPS with a lifetime  $\tau_n=50$  fs via the state F with a lifetime  $\tau_f=20$  fs which is described by equation 4.12. The coefficients  $N_0=1$  and  $F_0=10$  has been used. Comparing these two curves, a shift of the intensity maximum to a larger delay time of 28 fs is observed. The result with an additional population  $F_0$  at  $t=0$  is shown by the green solid line. This causes an additional shift of the intensity maximum to smaller delay times of 16 fs. Independent of the pump-probe mechanism the slopes of the different curves (blue, red, and green) at large delay times are nearly identical. For the sake of completeness the temporal broadened curves are shown on the right hand side where a cross-correlation of 50 fs (FWHM) has been applied as shown by the black dashed line. The similar linear slopes remain upon temporal broadening.

The described relaxation mechanism of electrons out of the image-potential state into the state F is able to explain the experimental observation of the relative shift of the position of the intensity maximum. The curve fit of the time-resolved intensity of state F in Fig. 4.15 (b) (page 46) reveals lifetimes  $\tau_f=41$  fs and  $\tau_n=48$  fs with a ratio of 80% relaxation (according to parameter  $N_0$ ) and 20% direct excitation (according to parameter  $F_0$ ) as shown by the black line. The percentage values reflect a contribution of both mechanisms to the integral time-dependent 2PPE signal. Note that this model also explains the shortening of the lifetime of the  $n=1$  IPS with respect to the clean Ag(001) substrate. As expected, the occurrence of an additional decay channel decreases the lifetime.

## 4.2.5 Image states of higher NiO coverages

### Image-potential states of 4 ML NiO

Figure 4.18 shows mono- as well as bichromatic 2PPE spectra of 4 ML NiO/Ag(001) with respect to the intermediate state energy (photon energies as indicated). The lower spectrum (bichromatic 2PPE) reveals two IR probed features K and F at  $3.50\pm 0.05$  eV and  $3.74\pm 0.05$  eV, respectively. A similar spectrum is achieved using monochromatic 2PPE (upper solid line). The spectrum is shifted by 140 meV to higher energies. This is explained by a space charge induced energy shift<sup>13</sup>. As indicated by the blue dashed line, both features F (F') and K (K') coincide upon a shift of the spectrum by -140 meV.

Angle-resolved data using monochromatic 2PPE with a photon energy of 4.02 eV are shown in Fig. 4.19 (a). The color-coded electron intensity is shown with respect to the final state energy above  $E_F$  and the detected angle. For the features F and K a parabolic dispersion is observed. Analyzing the angle-dependent peak position as shown in Fig. 4.19 (b) an effective mass of  $(0.98\pm 0.15) m_e$  has been determined. The large error bars account for the experimental conditions of space charge effects and problems of the  $\mu$ -metal shielding (see section 3.1.3). The dispersion of the feature F becomes evident due to the vanishing electron intensity at emission angles  $\geq 5^\circ$ . The energy and the dispersion agrees well with the observations of the state F at the lacerated NiO monolayer and bilayer films which have been discussed in section 4.2.4.

<sup>13</sup>A much higher pulse energy has been applied for the monochromatic 2PPE. The electrons at lower energies (secondaries and features H and J, see section 4.3.5) contribute to >95% of the total amount of electrons and cause the energy shift of electrons at higher kinetic energies.

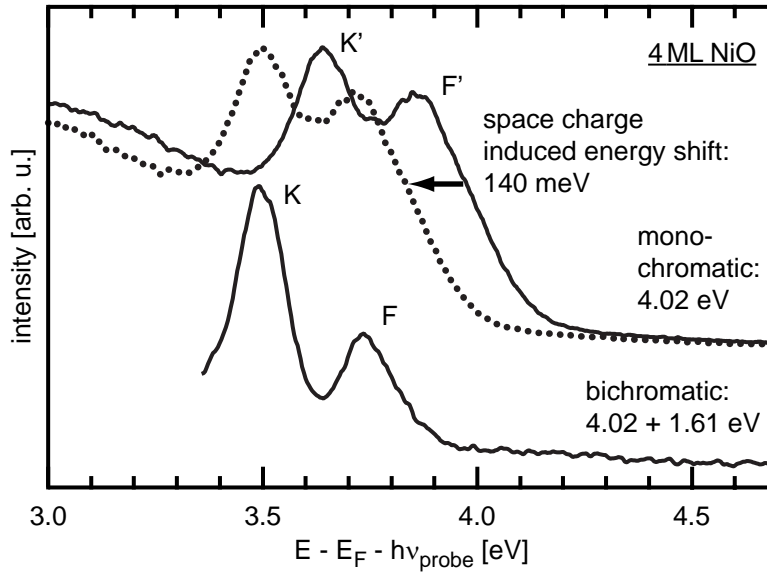


**Figure 4.18:** Monochromatic 2PPE (upper solid curve) in comparison with bichromatic 2PPE (lower line) of 4 ML NiO/Ag(001) (post-annealed at  $\sim 500$  K). The features of both spectra coincide upon a shift of  $-140$  meV (dotted line) which is explained by space charge effects.

Bichromatic 2PPE has been used to study the electron dynamics of the features K and F. In Fig. 4.20 (a) 2PPE spectra at different pump-probe delays are shown. For a better reading all spectra are color shaded. The respective color will be used as label for the following description. The lower gray curve shows the raw data at a delay  $t=0$ . The blue and magenta spectra correspond to the monochromatic

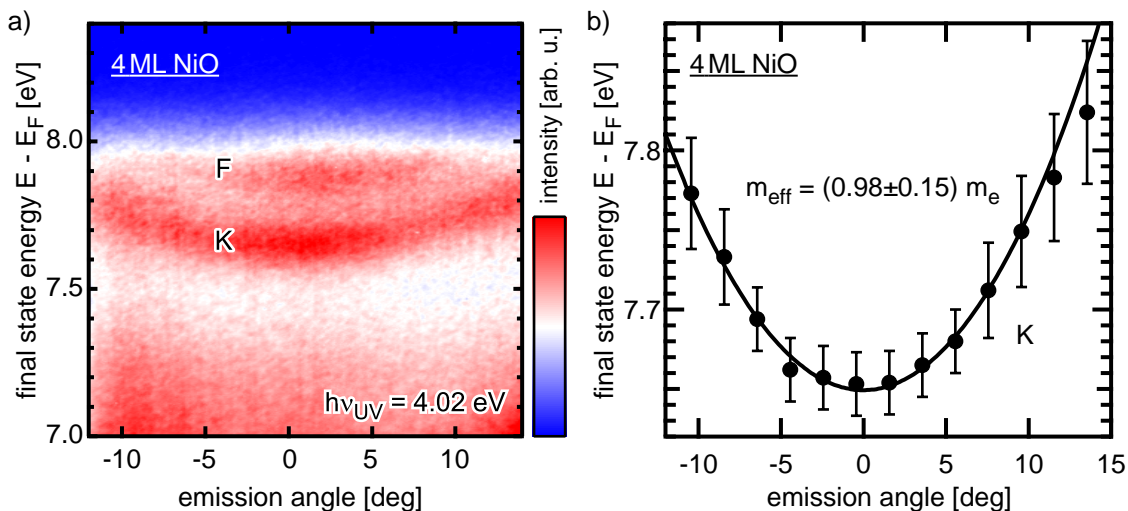


**Figure 4.19:** (a) Angle-resolved data of monochromatic 2PPE of 4 ML NiO (see Fig. 4.18) in the energy region of state F and K. (b) Angle-dependent peak position of state K revealing an effective mass of  $0.98 m_e$ . Note that the space charge effected energy shift has not been subtracted here but is implemented in the curve fit.

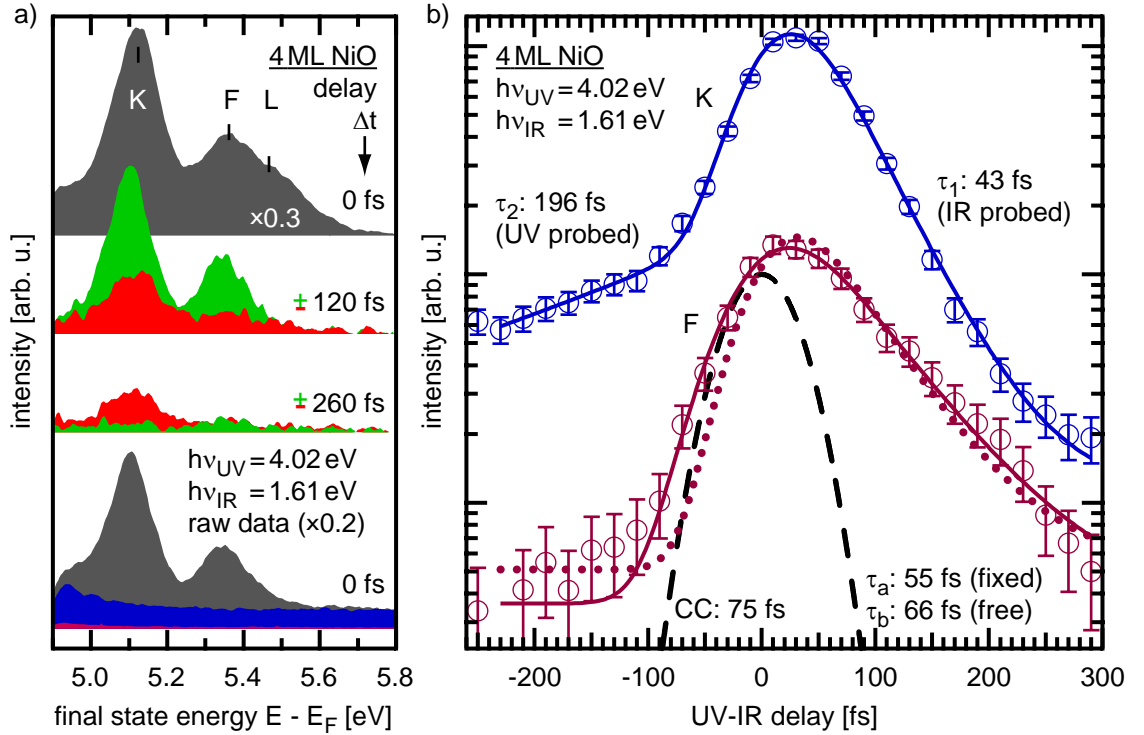


**Figure 4.20:** (a) 2PPE spectra of 4 ML NiO at different pump-probe delays. Lower gray curve: raw data at  $\Delta t=0$ . Blue and magenta curves: monochromatic UV and IR, respectively. Upper curves: background subtracted spectra where the green and red color indicate positive and negative delays, respectively (details see text). (b) Time-resolved intensities of feature K (blue) and F (magenta). The magenta solid and dashed lines are fits for state F using different fit parameters (see text). For state K an IR as well as UV probed contribution is found. The black dashed line represents the cross-correlation of 75 fs (FWHM).

spectra using the single UV or the IR beam, respectively. The pulse energies are similar as used for the time-resolved 2PPE. The blue, i.e., the non-resonant UV excited electrons contribute mainly to the background of the gray spectrum. It has been used to subtract the background of all spectra at different time-delays<sup>14</sup>. The results for time delays 0,  $\pm 120$ , and  $\pm 260$  fs are shown in the upper spectra where red indicates negative (IR pulse first) and green positive delays (UV pulse first). At  $t=0$  a small shoulder of state F at higher energies is observed which is assigned to an additional short-lived feature L which will not be further discussed here (see the retrospect of the data in section 4.4.3). The time-dependent intensities of the features F and K are shown in Fig. 4.20 (b). The intensity of the feature F is asymmetric with respect to  $t=0$ . The dotted line shows the curve fit of a temporal broadened exponential decay. The cross-correlation and the position of  $t=0$  has been extracted from the measurement of state K (see below). A lifetime of  $\tau_a=55$  fs is determined. The experimental data are not well described via this fit. To check the influence of the laser-dependent parameters (CC and  $t=0$ ), the solid line shows

<sup>14</sup>see appendix 6.B, background subtraction method A.

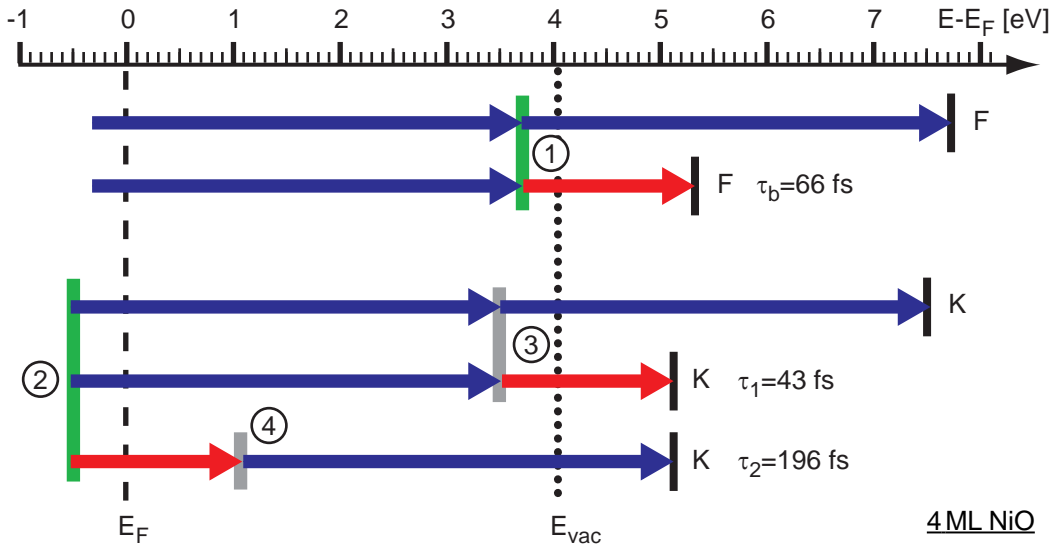


**Figure 4.21:** Energy diagram of mono- and bichromatic 2PPE of the states F and K of 4 ML NiO. Feature F is assigned to the  $n=1$  IPS at 3.74 eV. Due to its photon energy and pump-probe delay dependence the feature K is attributed to a hot-electron excitation from an occupied initial state at -0.52 eV (details see text). Lifetimes  $\tau_{1,2}$  from Fig. 4.20

the fit with a slightly larger cross-correlation and a lifetime  $\tau_b=66\pm 5$  fs. A better agreement with the experiment is obtained. However, both fitting procedures allow to restrict the lifetime of the feature F to  $60\pm 10$  fs. This is in good agreement to the state F of the lacerated NiO monolayer as shown in section 4.2.4.

The time-dependent intensity of feature K seems to be more complicated. The intensity maximum is shifted to positive delays as well. But referring to the maximum the intensity drop at positive delays is much stronger as at negative delays. This issue is already evident in the single spectra of Fig. 4.20 (a) where the feature F is well defined at -260 fs but not observed at +260 fs. Without any considerations of the electronic states involved in the 2PPE process the time-dependent intensity has been modeled using two different pump-probe mechanisms. To describe the shift of the intensity maximum to positive delays (UV first) an IR probed contribution is assumed. Furthermore an UV probed contribution is supposed to describe the persistent 2PPE intensity at negative delays (IR first). The result is shown by the blue solid line. Lifetimes of  $43\pm 10$  fs for the IR probed and  $196\pm 15$  fs for the UV probed contributions have been determined, respectively. The cross-correlation of 75 fs is shown as a black dashed line. A perfect agreement with the measurement is achieved.

To get a better overview of the results, the pump-probe schemes of the features F and K for mono- and bichromatic 2PPE are shown in Fig. 4.21, respectively. The feature F is assigned to an unoccupied state ① at  $3.74\pm 0.05$  eV. This is manifested by the equivalent intermediate state energy for different probe energies and the IR-probed character in the time-resolved 2PPE. This state is assigned to the first IPS of the 4 ML NiO film. The upper two schemes for feature K using UV and IR probe photons predict an unoccupied intermediate state ③ at  $3.50\pm 0.05$  eV with a lifetime of  $43\pm 10$  fs. Additionally an unoccupied intermediate state ④ at  $1.09\pm 0.05$  eV with



a lifetime of  $196 \pm 15$  fs is identified via the UV-probed contribution. The dispersion with an effective mass of  $(0.98 \pm 0.15) m_e$  is observed for the IR as well as the UV probed contribution. This would mean two states ③ and ④ have to exhibit the same dispersion in  $k_{\parallel}$  direction. However, the physical origin of both possible states ③ and ④ is not clarified yet. An unoccupied interface state between the Ag substrate and the NiO film could be considered. Another possibility would be the observation of an initial state ② at  $0.52 \pm 0.05$  eV below  $E_F$ . The observed lifetimes of the corresponding *virtual states* ③ and ④ might be explained by the generation of hot electrons, however, the observed lifetimes are larger than typically expected.

Since the substrate is Ag(001) the results will be compared with results of other noble metals. Shumay *et al.* [32] reported time-resolved 2PPE of IPS of Ag(001) and Cu(001). In the time-dependent intensities of the UV-pumped and IR-probed IPS they found contributions from electrons with an opposite pump-probe scheme as well. Apparently, they determined the intensities of the states by simply integrating over all electrons in the corresponding energy range which is possible due to the good separation of all states to each other. In dependence of the energy position of the intermediate state (IR-pumped) relative to  $E_F$  lifetimes of 190 and 145 fs are evident at 0.90 and 1.27 eV, respectively. These values agree well with the observations of feature K. A closer analysis of hot-electron excitations have been reported by Petek and coworkers [93,94] for low-indexed Cu surfaces. Typical lifetimes are 5–65 fs for intermediate energies of 3.2 and 1.3 eV, respectively. A deviation from the  $(E - E_F)^{-2}$  dependence predicted by Fermi-liquid theory was found. They modeled the decay of hot electrons in the framework of Fermi-liquid theory and added electron–electron scattering with bulk electrons. A qualitative agreement with the experiment was found. The theoretical decay rates are by one order of magnitude higher which was assigned to several assumptions in the calculation. However, the experimental lifetimes are of the same order of magnitude as observed for NiO/Ag(001) presented here.

The main difference between the feature K and the hot-electron excitations is that the feature K appears as an separate and well defined peak in the spectrum. To clarify this issue in more detail additional measurements are recommended. To mention only two:

- Bichromatic 2PPE with large pump energy variation
  - to check whether feature K originates from the occupied state ②
  - a possible resonance of the transition from state ② to ①
- Bichromatic time-resolved 2PPE using different pump and probe energies
  - UV and IR energy-dependent positions of ③ and ④
  - energy-dependent hot-electron relaxation times of ③ and ④

Although no final conclusions are possible an additional important remark is necessary. The parabolic dispersion of feature K with  $m_{eff} = 0.98 m_e$  and the position of the occupied initial state at 0.52 eV can not be simply explained by band structure calculations of the Ag substrate or the NiO film. At first, the highest occupied bands of NiO are attributed to *d*-bands and are located  $< 2$  eV below  $E_F$ . Moreover *d*-bands are highly localized which results in a low dispersion. The observation of an interface state between the Ag substrate and the NiO film would be reasonable as well.

### Image-potential states of 8 ML NiO

Thin films of up to 10 ML are still influenced by the substrate where small deviations from the bulk properties are present. Although NiO is an insulator, thin films still exhibit a sufficient conductivity for most experimental techniques, like STS and 2PPE. The investigation of image-potential states of thicker NiO films is of great interest. It will help to analyze the decoupling of the states from the influence of the metal substrate. An eight monolayers NiO film has been prepared to explore this interesting layer thickness.

An angle-resolved bichromatic 2PPE spectrum is shown in Fig. 4.22 (a) with respect to the final state energy referenced to  $E_F$  using 4.17 and 1.78 eV photon energies, respectively. An energetically broad feature at 5.65 eV is evident with a small angular-dependent deviation of the energy position as shown by the dotted line<sup>15</sup>. The angle-dependent energy shift between emission angle  $0^\circ$  and  $10^\circ$  is about 50 meV. This shift is similar to the data obtained for IPS of Ag(001) [31]. Thus, the effective mass of the involved unoccupied electronic state is in the order of  $\sim 1 m_e$ . In Fig. 4.22 (b) line profiles through (a) at  $0^\circ$  are shown. For comparison the lower dotted spectra correspond to the data of the NiO bilayer (see Fig. 4.9 (b) on page 39). The UV and IR photon energies have been modified as indicated. The energy scale refers to the intermediate state energy assuming an IR probe photon. This assumption is proved by the red, magenta, and green curves, where the IR energy has been modified by almost 0.2 eV from 1.61 to 1.78 eV, respectively, with a constant UV energy of 4.17 eV. The main feature at 3.9 eV coincides in all three spectra. In

<sup>15</sup>Note that the angle-dependent electron intensity is not symmetric around  $0^\circ$  which is due to experimental problems during this specific measurement period.

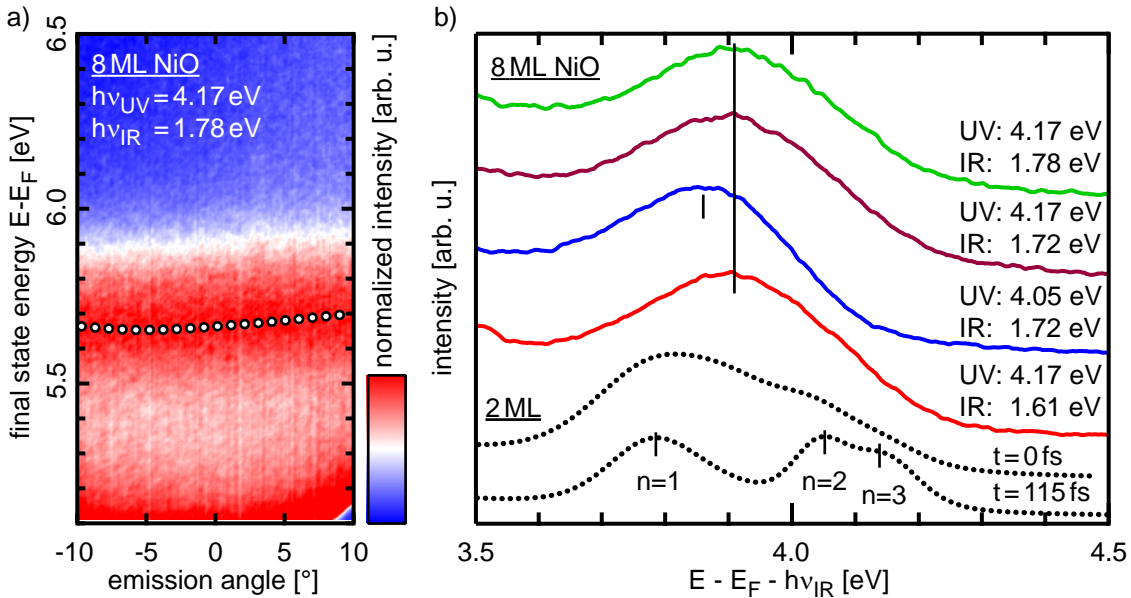


**Figure 4.22:** (a) Angle-resolved 2PPE of 8 ML NiO with respect to the final state energy referenced to the Fermi level. (b) Line profiles through (a) at  $0^\circ$  with different pump and probe energies. The energy scale shows the intermediate state energy. The black dotted lines show the data of the bilayer coverage of NiO.

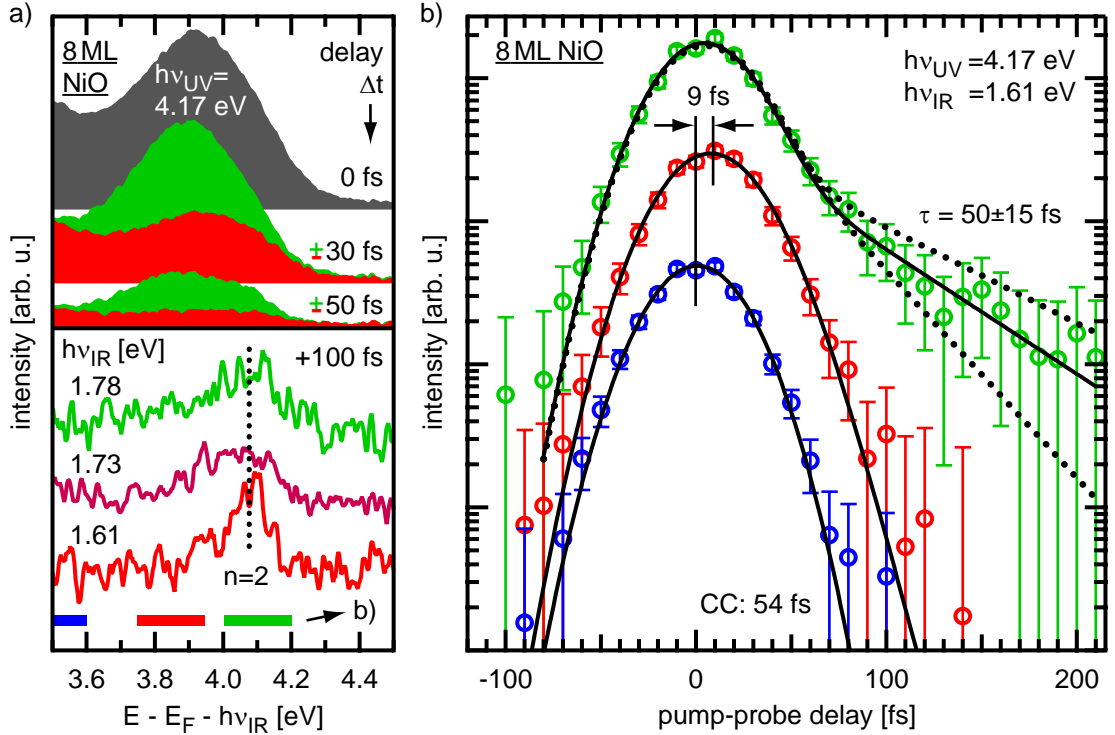


**Figure 4.23:** (a) Upper part (filled curves): 2PPE spectra obtained for  $h\nu_{UV}=4.17$  eV and  $h\nu_{IR}=1.78$  eV at pump-probe delays of 0,  $\pm 30$ , and  $\pm 50$  fs, respectively, where green indicates a positive delay (IR after UV) and red vice versa. Lower part (solid lines): Spectra taken at +100 fs delay using different IR photon energies (color of the spectra similar to Fig. 4.22 (b)). The observed feature at  $\sim 4.1$  eV coincides in all spectra. Note that in all spectra the background has been subtracted. (b) Time-resolved intensities integrated over the energy regions as indicated in (a) by the blue, red, and green bars, respectively. CC indicates the cross-correlation of 54 fs. For a better reading the curves are vertically shifted with respect to each other.

the case of an UV energy of 4.05 eV the main feature shifts to 3.85 eV (blue spectrum). This means that the energy position of the main feature depends not only on the IR (one IR probe photon) but also on the UV energy. Note that the observed shift of 0.05 eV is smaller than the UV energy difference of 0.12 eV.

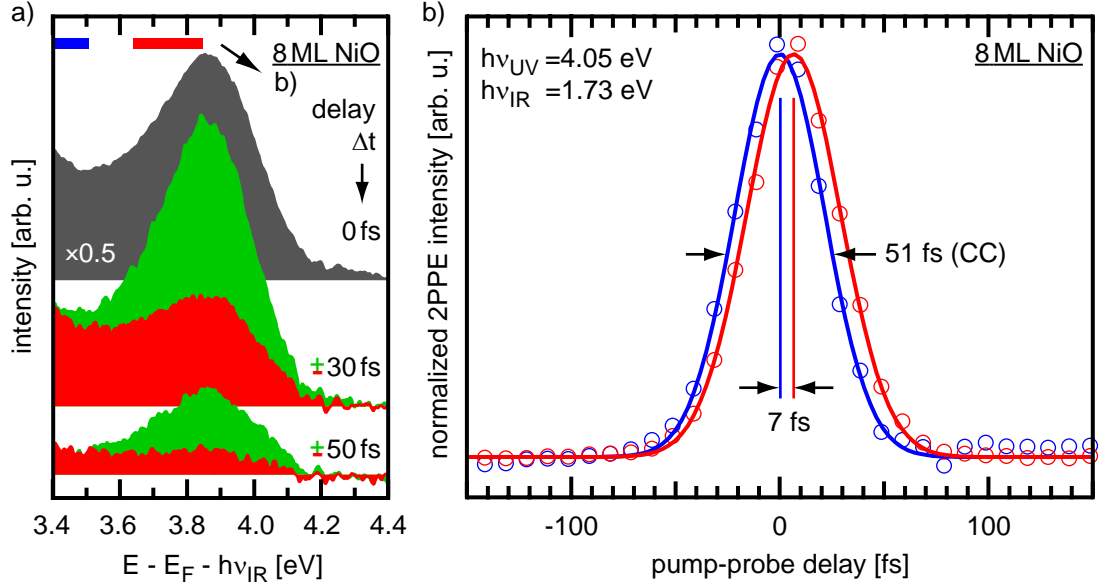
Spectra at different pump-probe delays using a pump photon energy  $h\nu_{UV}$  of 4.17 eV are shown in Fig. 4.23 (a). The upper part shows spectra probed with  $h\nu_{IR}=1.78$  eV. The filled gray spectrum refers to  $\Delta t=0$ . The filled red and green spectra correspond to  $\pm 30$  and  $\pm 50$  fs delay, where green indicates the positive delay (IR after UV). The electron intensity at low energies around 3.5 eV is similar in the red and the green spectra, whereas the main features around 3.9 eV shows a larger intensity at positive delays. The lower part of Fig. 4.23 (a) shows spectra at a delay of +100 fs. The colors of the spectra indicate different photon energies similar to Fig. 4.22 (b). A feature at  $4.08 \pm 0.05$  eV is observed. Comparing this state with the  $n=2$  IPS of the NiO bilayer (see Fig. 4.22 (b)) a perfect agreement is found. Therefore, the state at 4.08 eV is assigned to the  $n=2$  IPS of the 8 ML NiO film as well. Thus, it is assumed that the intensity at 3.5–4.0 eV originates mainly from the  $n=1$

image state. To determine the lifetime of the IPS, the time-resolved intensities are shown in Fig. 4.23 (b) on semi-logarithmic scale. Here the electron intensity from each spectrum at a given delay has been integrated over the regions as indicated by the blue, red, and green bars in Fig. 4.23 (a), respectively<sup>16</sup>. For the low energy part at 3.5 eV (blue circles) a symmetric intensity with respect to  $t=0$  is observed. A Gaussian fit (blue solid line) reveals a width of 54 fs (FWHM). The electrons in this energy region are assigned to non-resonant 2PPE electron excitations from occupied bands leading to a featureless but time-dependent background in the spectrum. Thus, the time-resolved intensity reflects the cross-correlation of the two laser pulses of  $54 \pm 5$  fs. For the energy region around 3.8 eV where the  $n=1$  IPS is expected (red circles) the intensity profile is symmetric as well. The Gaussian fit (red solid line) reveals a shift of the intensity maximum to  $9 \pm 3$  fs and a slightly increased width compared to the red curve. In case of a small lifetime-to-cross-correlation ratio the lifetime can be estimated from the shift of the intensity maximum [28]. The fact that the integrated electron intensity includes both, the intensity of the  $n=1$  image state and the time-dependent background, the tr-intensity at around 0 fs is overestimated and does not reflect the pure  $n=1$  population trace. The given value of 9 fs is therefore the definitely *lowest* boundary for the lifetime of the  $n=1$  state ( $\tau_1 \geq 9 \pm 3$  fs). The energy region at 4.1 eV of the  $n=2$  image state (green circle) reveals an intensity profile with a symmetric part between  $\pm 50$  fs and a linear contribution (on log. scale) above 70 fs. The symmetric part can be explained with the same arguments as for the  $n=1$  image state. The non-resonant electron contribution of the background is reflected in an overestimation of the  $n=2$  intensity. However, this intensity decays faster due to its very short lifetime of  $\sim 0$  fs. This means, at large delays  $\geq 70$  fs mainly the  $n=2$  IPS intensity contributes to the signal. The good signal-to-noise ratio still allows to follow the 2PPE signal over one order of magnitude. To model this profile a two component fit has been applied and is shown by green solid line. The sum of two temporal-broadened single exponential decays reveals time constants of  $\leq 1$  fs and 50 fs for the short and long-lived component, respectively. To estimate the experimental error of the latter one the fits using 35 and 65 fs are shown as dotted lines, respectively. This leads to a lifetime  $\tau_2$  of the  $n=2$  image state observed here of  $50 \pm 15$  fs. This agrees well with the value found for the  $n=2$  IPS of the NiO bilayer.

Referring to the lower UV energy of 4.05 eV the delay-dependent 2PPE spectra are shown in Fig. 4.24 (a) in the same manner as already described for Fig. 4.23 (a). Due to the lower pump photon energy the  $n=2$  state is only partially excited which results in less intensity at +50 fs delay. The time-resolved intensities integrated over the energy regions as indicated by the blue and red bars, respectively, are shown in Fig. 4.24 (b). In contrast to the intensity profiles in Fig. 4.23 (b) a linear scale has been chosen. For a better comparison the intensities have been additionally normalized with respect to the intensity maximum of the Gaussian fit. For the lower energy region a cross-correlation of  $51 \pm 5$  fs is determined. The red data points obtained at higher intermediate state energies are shifted to positive delays by  $7 \pm 3$  fs with respect to the blue curve. The Gaussian fit reveals a shift of  $7 \pm 3$  fs which borders

---

<sup>16</sup>Similar data analysis has been shown in section 4.2.3 and appendix 6.C for the IPS of the NiO bilayer.



**Figure 4.24:** Same as Fig. 4.23 with photon energies of 4.05 and 1.73 eV, respectively. Here tr-intensities in (b) on linear scale and normalized to the maximum intensity. CC is the cross-correlation of 51 fs (FWHM). The horizontal shift of 7 fs between blue and red is evident in all data points.

the lifetime of the  $n=1$  IPS to definitely  $\geq 7$  fs. This is in good agreement to the observation using the different pump photon energy above.

One important remark concerning the spectra at pump-probe delay of 0 fs is necessary. As already described in Fig. 4.22 (b) the intensity maximum is observed at an intermediate state energy of 3.90 and 3.85 eV for pump energies of 4.17 and 4.05 eV, respectively. The electron intensities have been assigned to the  $n=1$  and 2 image states. For the  $n=2$  state at 4.08 eV a good agreement of the energy position and lifetime in comparison with  $n=2$  IPS of the NiO bilayer was found<sup>17</sup>. Thus, it is expected that the energy of the  $n=1$  IPS agrees as well. Therefore, the intensity maximum of the spectra shown here are expected at  $\sim 3.8$  eV independently of the pump photon energy. From that one can conclude that the observed intensity maximum at 3.9 eV at delay 0 does not only originate from a mixture of the two IPS. Note that the  $n=1$  IPS at the bilayer coverage has been determined to 30 fs which deviates significantly from the lifetime observed here. Possibly another state in this energy region with a shorter lifetime is involved as well. This might explain the apparent short lifetime of the  $n=1$  of  $\geq 9$  fs only which is misinterpreted due to an artificially increased maximum of the tr-intensity profile at a delay of 0 fs (see appendix 6.C). The discussion of the additional state will be readopted in the observation of Ag bulk bands via the surface reconstruction of the antiferromagnetically ordered NiO film in section 4.4.3.

<sup>17</sup>At the NiO bilayer the  $n=1$  and 2 IPS were found at 3.78 and 4.04 eV with lifetimes of 30 and 50 fs, respectively (see section 4.2.3).

## 4.3 Unoccupied Ni-3*d* states of NiO films

In this section the 2PPE results of NiO ultra-thin films, which are ascribed to electronic states of the oxide will be analyzed. After a brief introduction the results of the oxide monolayer will be discussed in the first part. Two unoccupied Ni-3*d* states have been observed which are in good agreement with the observations in STS. The second part will deal with 2 and 3 ML film thickness. The observed energy differences between the states of different film thicknesses allow the characterization of the behavior of mono- and bilayer NiO films upon heating at elevated temperatures, as presented in the third part of this section. The role of the NiO bilayer during film growth will be highlighted. Afterward, the results of  $\geq 4$  ML concerning the observation of the Ni-3*d*<sub>z<sup>2</sup></sub> derived surface state will be presented. Although a good agreement between 2PPE and STS is found for most of the unoccupied electronic states, the observed deviations between both methods will be discussed in the last part of this section. The effect of different electronic final states for different experimental techniques as well as the influence of the Ag substrate will be depicted.

### 4.3.1 Introduction

The electronic structure of transition metal oxides has been intensively investigated since the last decades. The single-particle band-structure calculations as local-density approximation (LDA) predict small band gaps. In contrast to that, relatively large values of the band band gap are found in experimental investigations. This apparent contradiction drove many investigations in that field. The main reason of the insulating gap is the strong Coulomb correlation between the *d* electrons. They are localized at the metal ion and prevent the formation of electron bands of freely movable electrons. This leads to the concepts of Mott-Hubbard and charge-transfer insulators to understand the occurring effects in the electronic structure and the band gap. Due to the absence of band-like states, electron excitations are realized between two individual metal ions. The energy final state of this electron transition determines the band gap. For a Mott-Hubbard transition the Coulomb correlation energy *U* is required to transfer the electron from one to another metal ion. The final state is characterized by a hole at one and an additional electron at the other ion and the electron configuration can be written as

$$3d^n + 3d^n + U \rightarrow 3d^{n-1} + 3d^{n+1} , \quad (4.14)$$

where *n* is the number of electrons per metal ion in the unperturbed system. For the case of a charge-transfer insulator the creation of the hole at the metal ion is accompanied by a direct electron transfer from the ligand (L) to the metal ion. This screening gains energy and leads to the charge-transfer energy  $\Delta$  required for the transition. The final state is characterized by a hole at the ligand ion and an additional electron at another metal ion as

$$3d^n L + 3d^n L + \Delta \rightarrow 3d^n L^{-1} + 3d^{n+1} L . \quad (4.15)$$

The size of *U* and  $\Delta$  relative to each other determines the type of the gap and the insulator. A Mott-Hubbard insulator shows  $U < \Delta$  whereas  $\Delta < U$  characterizes the charge-transfer insulator. The NiO is a prototype of a charge-transfer insulator and

has been intensively investigated [52,63,95–99]. The picture of the physical processes during electron excitation and the origin of the optical band gap has been reviewed by Hüfner [64].

Any spectroscopy of electron transitions in the NiO is influenced by correlation effects. This causes energy shifts which depend on the electronic final state. Depending on the experimental method, as photoemission for the spectroscopy of occupied states or inverse photoemission (IPE), electron energy loss spectroscopy (EELS), and two-photon photoemission (2PPE) for the spectroscopy of unoccupied states, the involved states are *different*. The PES does not reveal an obvious occupied state at a fixed energy. The remaining hole determines the energy of the emitted photoelectron. On the other side the IPE does not reveal an obvious unoccupied state. The additional excess electron causes correlation effects as well which determine the observed energy for the transition. For EELS and 2PPE the situation is totally different. Here a transition between occupied and unoccupied states is observed which is neither comparable with PES nor with IPS. However, the investigation of a strongly correlated electron system with a large variety of experimental methods, including their fundamental differences, are necessary to understand the detailed physical processes.

Despite of the extensive investigations of the bulk NiO, much less is known about the electronic properties of ultra-thin films. The study of these systems enables to apply more experimental and theoretical methods and promises a deeper understanding of the electronic structure of strongly correlated electron systems. In the first stage of thin-film growth, it is obvious that the electronic structure differs to that found for bulk NiO samples. This is due to the influence of the neighboring substrate and the structural relaxations. However, after reaching a certain thickness, the electronic states should approach the ones found for bulk samples. Thus, the results of thicker films with quasi-bulk properties could be compared with other experimental methods on bulk samples. This helps to analyze and interpret the data obtained for ultra-thin films.

Scanning tunneling spectroscopy data in dependence of the NiO film thickness between 1–8 ML are shown in Fig. 4.25 (data taken from a previous work of Großer [15]). The NiO monolayer shows two different spectra, green and black, depending on the particular region within the (2×1) reconstructed layer (labeled corrugated and flat). The uniaxial reconstruction of the monolayer film leads to a moiré pattern of apparent flat and corrugated regions (for details see Ref. [15]). The dotted vertical line indicates the value of the work function  $\Phi_{ML}$  based on the photoemission onset measured here (see section 4.1.2). The features at energies above  $\Phi_{ML}$  originate from field emission resonances (FER), i.e., tunneling into the unoccupied Stark-shifted IPS in front of the sample [15]. The features at energies below  $\Phi_{ML}$  are assigned to unoccupied Ni-3d states of the NiO film. Note that the bare Ag(001) substrate does not show any pronounced features in this energy range, except of the relatively flat unoccupied *sp*-band up to 2 eV (not shown here, see [15]). The energy difference of the monolayer feature at  $\sim 3.8$  eV, observed in both spectra and the occurrence of an additional feature at 4.4 eV in the flat monolayer region (black spectrum) has not been clarified, yet. Accordingly, the STS spectra of  $\geq 2$  ML could be interpreted. At energies above  $\Phi$  the spectra are dominated by FER, whereas the features below  $\Phi$  are assigned to unoccupied Ni-3d states as well. At a film thickness of 3 ML a feature occurs at 1.6 eV. This feature shifts to the higher energies of 2 eV with increasing

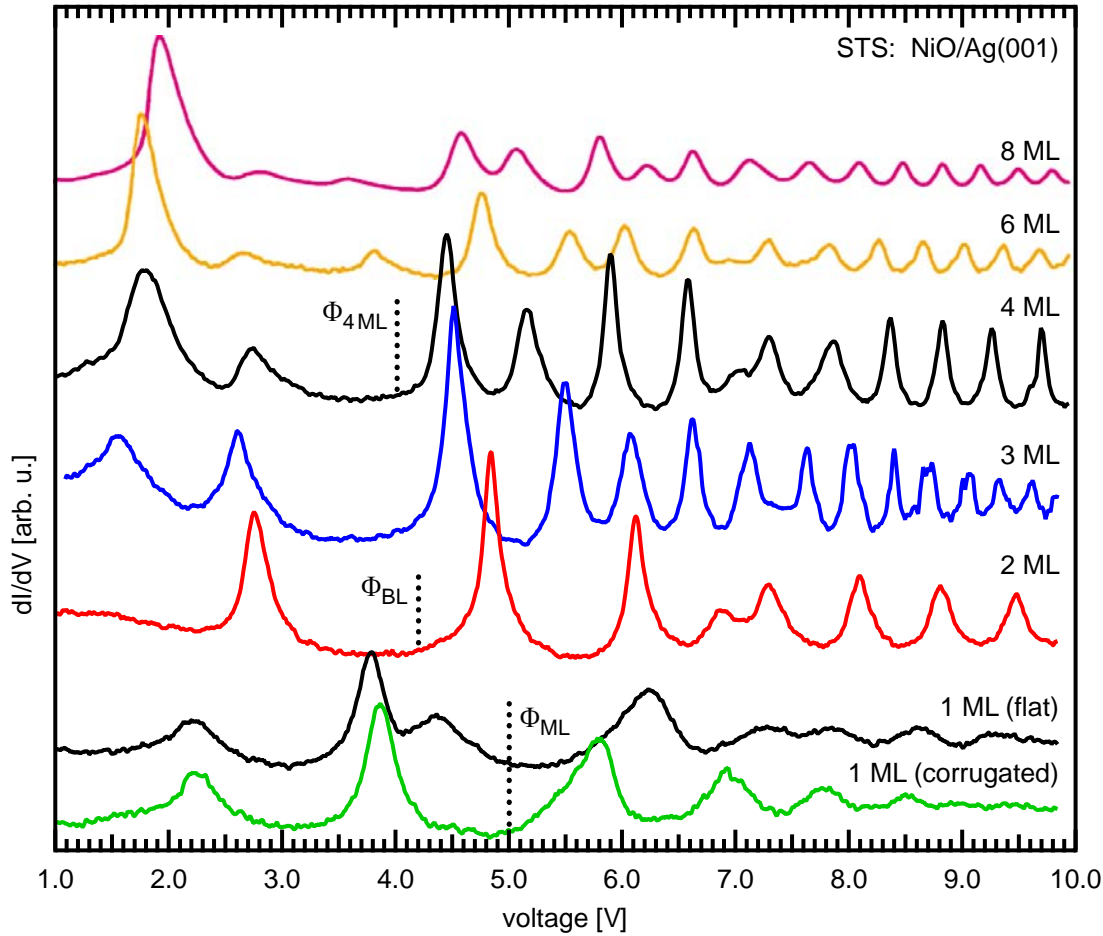


**Figure 4.25:** Scanning tunneling spectroscopy of 1–8 ML NiO/Ag(001) (data taken from [15]). The dashed lines indicate the position of the vacuum level as determined by UPS. The states above  $\Phi$  are field emission resonances and correspond to tunneling into Stark-shifted image potential states. Below  $\Phi$  the spectrum is dominated by unoccupied Ni  $3d$  states. For the monolayer two different spectra are observed depending of the position with respect to uniaxial reconstructed surface. For thicknesses  $\geq 3$  ML the  $d_{z^2}$ -derived surface state of NiO(001) is observed which is located at 1.6 eV for 3 ML and shifts to higher energy of  $\sim 2.0$  eV for 8 ML.

film thickness. Additionally a strong increase in the differential conductance, i.e., an increase in the density of states is observed [15]. The feature is assigned to an unoccupied Ni- $3d_{z^2}$  derived surface state.

### 4.3.2 The first monolayer NiO/Ag(001)

For the growth of NiO ultra-thin films on Ag(001) the monolayer plays a unique role because it shows neither the bulk atomic structure of NiO due to its two-dimensionality and relaxation nor the bulk electronic structure due to the absence of the 3D lattice and the vicinity of the Ag substrate. In this section the electronic structure of unoccupied states of the NiO monolayer and their dynamics will be discussed.



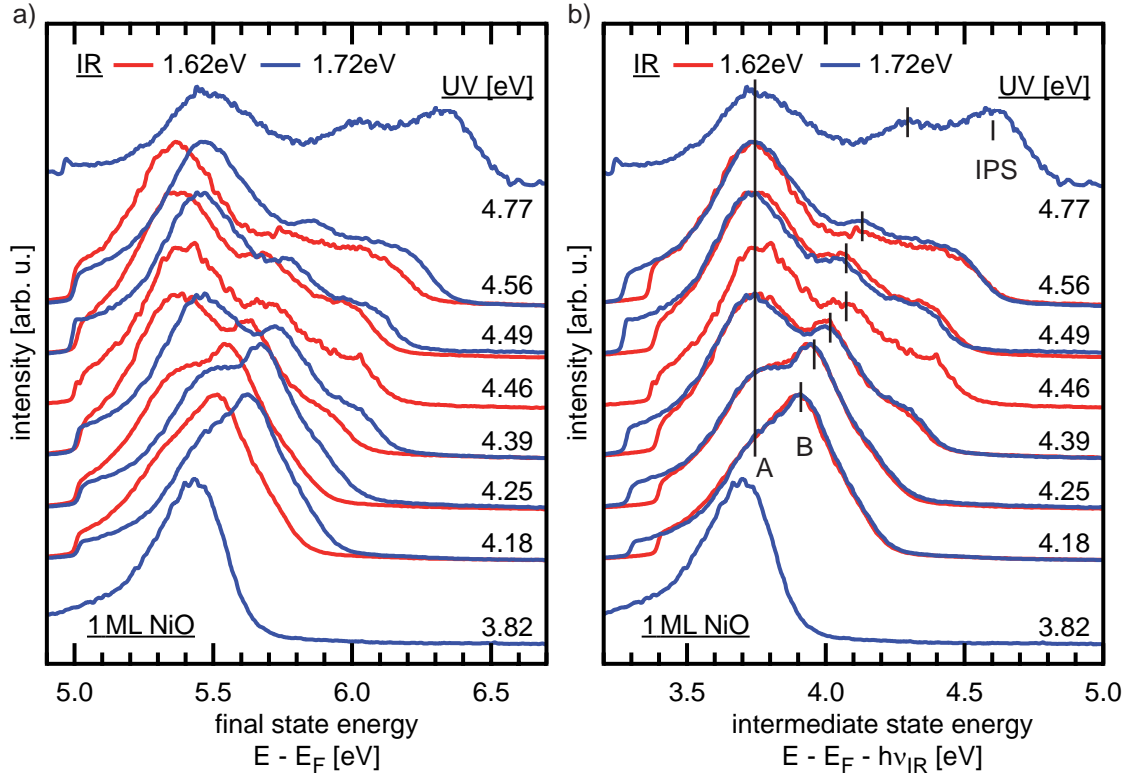


**Figure 4.26:** (a) 2PPE spectra of the NiO monolayer on Ag(001) using different UV and IR photon energies as indicated. The energy scale is the final state energy with respect to the Fermi level. (b) Same data as in (a) with respect to the intermediate state energy by subtracting the IR photon energy.

Bichromatic two-photon photoemission has been used to analyze the electronic structure of unoccupied states. In Fig. 4.26 (a) 2PPE spectra for different UV and IR photon energies are shown as a function of the final state energy. The red and blue spectra correspond to IR energies of  $\sim 1.6$  and  $\sim 1.7$  eV, respectively. In Fig. 4.26 (b) the IR photon energy has been additionally subtracted from the energy scale. On this energy scale both spectra with different IR photon energies (red and blue spectra) coincide for each UV photon energy. This means that the observed states are IR-probed (see section 2.2). This energy scaling ( $E - E_F - h\nu_{probe}$ , where  $h\nu_{probe}$  corresponds to  $h\nu_{IR}$  in Fig. 4.26 (b)) directly reveals the energy position of the intermediate state with respect to the Fermi level. The UV energy has been modified over a wide range between 3.8 and 4.8 eV. For an UV energy of 3.8 eV a broad asymmetric feature at  $\sim 3.7$  eV is observed. In all other spectra with larger UV energies two obvious features A and B are evident. For an UV energy of 4.18 eV the separation is small. Thus, at a lower energy feature A appears as a shoulder of feature B. With increasing UV energies the separation gets larger. For an UV energy of 4.77 eV a third feature IPS is observed at 4.6 eV. The peak positions of the features A and B in dependence on the UV energy are shown in Fig. 4.27. The position of feature A at  $3.73 \pm 0.05$  eV is independent of the UV photon energy and exhibits a relatively large width of 300 meV. This explains the asymmetric feature observed at 3.8 eV UV energy because the intermediate state is only partially excited. In

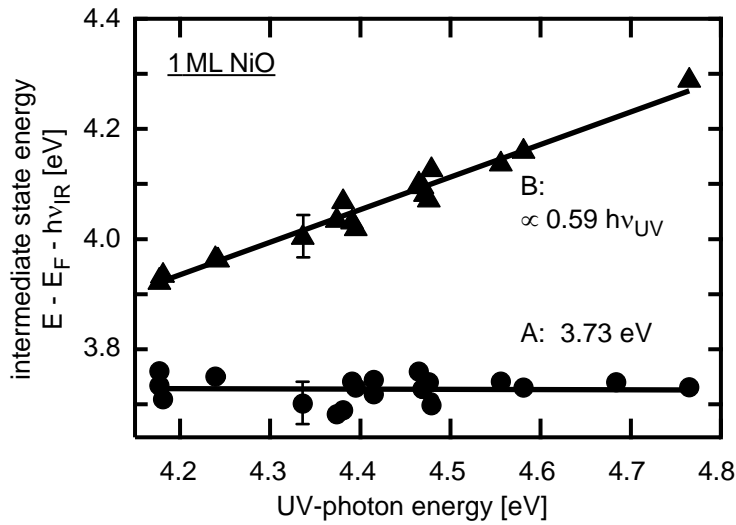


**Figure 4.27:** UV photon energy dependence of the features A and B found in bichromatic 2PPE spectra of Fig. 4.26 (error bars as indicated at two of the data points). Feature A is independent of the UV photon energy and feature B shows a linear dependence with a non-integer slope of 0.59.

contrast to that the feature B shows a linear dependence of the intermediate state energy. It shifts by  $0.59 \pm 0.05$  times the UV energy.

The bichromatic 2PPE spectra using UV and IR photons do not show features, originating from IR pumped and UV probed states, i.e., unoccupied states in the vicinity of the Fermi level. To explore the energy region between 1.5 and 4.5 eV in more detail monochromatic 2PPE using one single UV laser pulse has been performed. To extend the possible UV photon energy range both NOPA outputs have been frequency doubled (see section 3.2). The corresponding 2PPE spectra are shown in Fig. 4.28 with respect to the intermediate state energy (assuming one UV probe photon). The photon energy has been modified over a wide range of 0.9 eV. The upper spectrum, taken at a photon energy of 4.42 eV reveals again the features A and B at 3.73 eV and 4.05 eV, respectively<sup>18</sup>, as has been seen already in bichromatic 2PPE. Thus, independent of the probe photon energies of 1.6 and 4.4 eV an equivalent intermediate state energies of A and B is observed. This means the feature is dominated by the density of intermediate states and is not influenced by the transition into the final state.

At smaller intermediate state energies an additional weak feature C at  $\sim 2.3$  eV is observed. For a photon energy of 3.28 eV from the SHG-pumped NOPA output (lower curve) the obvious feature C at  $2.40 \pm 0.05$  eV is evident. It shifts to 2.32 and  $2.30 \pm 0.05$  eV for photon energies of 3.41 and 3.53 eV, respectively. For the latter photon energy a second feature at  $\sim 3.5$  eV appears. This peak originates from the feature A at 3.73 eV which is partially excited due to its relatively large width of 300 meV. Although it is only partially excited, the intensity is larger compared to feature C. This is explained by a much higher transition probability of the feature A.

To compare the results of 2PPE and STS, spectra of both methods are shown on the same energy scale in Fig. 4.29 (b) for bichromatic 2PPE. The feature A at 3.75 eV

<sup>18</sup>The position of feature B in monochromatic 2PPE depends on the chosen photon energy as well.

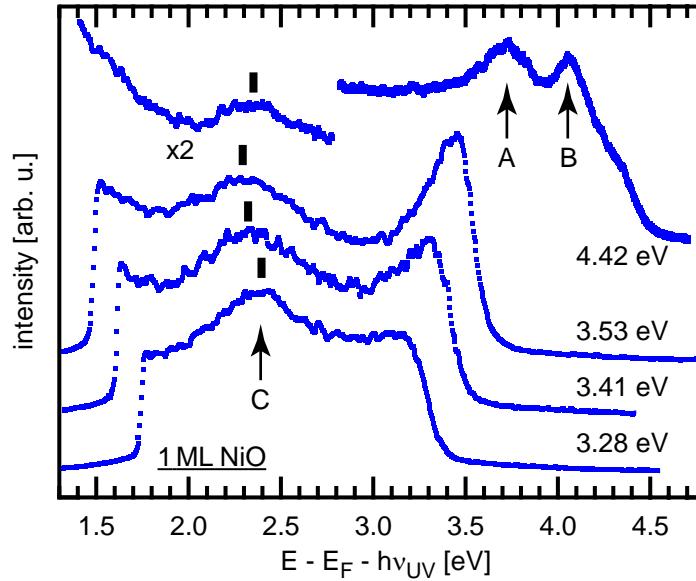


**Figure 4.28:** Monochromatic 2PPE spectra of the NiO monolayer on Ag(001) using different photon energies between 3.28 and 4.42 eV. The features A and B refer to the features observed in bichromatic 2PPE as well. The feature C shows a small shift upon photon energy variation.

in 2PPE agrees well with a feature found in the STS data. The comparison of both methods shows energy differences of +40 meV and +110 meV for the flat (black) and corrugated (green) region, respectively. The observed energy shift of feature A in STS (black and green curve) is not resolved in the less spatially resolved method 2PPE but might cause the large width of this feature in the 2PPE spectrum. The energy difference between STS and 2PPE might be understood in terms of the different electronic final states of both experimental methods. The photoemission final state is characterized by a hole (screened or not) in the sample (N-1 final state)

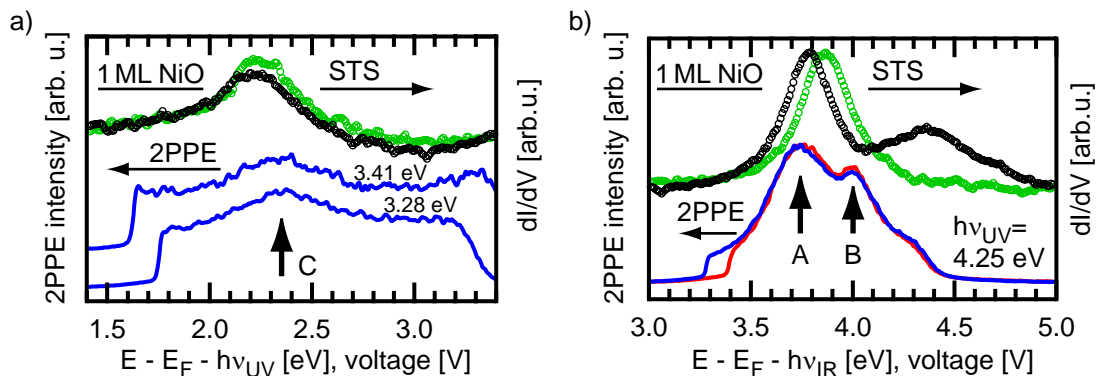


**Figure 4.29:** STS data in comparison with (a) monochromatic- (data from Fig. 4.28) and (b) bichromatic 2PPE (data from Fig. 4.26). The arrows indicate the corresponding feature in 2PPE data which are assigned to the states observed with STS.

whereas in STS an additional electron is put in the electronic system ( $N+1$  final state) which will be discussed in more detail in section 4.3.6.

Figure 4.29 (a) shows the comparison of STS and monochromatic-2PPE at lower intermediate state energies. A good agreement between both methods is found as well. The feature C at 2.35 eV shows an energy difference of -100 meV compared to the corresponding feature in STS. Surprisingly the energy difference is in the opposite direction as observed for the feature A. For both states, A and C, the final states are equivalent within each experimental method. Thus, an energy difference between 2PPE and STS based on the different final states should have the same direction for both transitions. That issue will be discussed in section 4.3.6 as well, where a possible explanation is given by the constant-current mode of the STS measurements.

As discussed for feature A in Fig. 4.27, no significant shift of the intermediate state energy is observed over a wide range of the pump photon energy. This can be explained in terms of a simple intermediate state pump-probe mechanism. The intermediate state energy is independent of the pump energy, i.e., the feature is independent of the initial state energy as well. In contrast to that the feature C shows an additional energy shift in monochromatic 2PPE spectra in the order of 100 meV. This means the initial or the final state effects influence the apparent intermediate state energy. The origin of the energy shift cannot be resolved with the monochromatic 2PPE data presented here. To investigate the influence of initial, intermediate, and final states a more detailed study of this issue is necessary. Using bichromatic 2PPE, with two independently tunable photon energies in the UV range, would enable additional measurements modes e.g., the constant-initial and the constant-final state mode. The laser system used here delivers enough pulse energies to frequency double both and to perform bichromatic 2PPE with two independently tunable laser pulses in the UV range. This setup has been tested by Blättermann [43], recently, where the investigation of IPS of Ag(001) using bichromatic 2PPE ( $UV_1+UV_2$ ) has been reported.

The features A and C are assigned to unoccupied Ni-3*d* states. Note that during the work of Großer [15] the measurement of the work function was not available and thus the feature at  $\sim 3.8$  eV has been misinterpreted as the first field emission resonance whereas the feature at 2.2 eV was assigned to an unoccupied Ni-3*d* state. The combination of UPS, 2PPE, and STS clarifies the obvious assignment of the spectral features.

To investigate the dynamics of the unoccupied states time-resolved 2PPE data of the features A and B are shown in Fig. 4.30. In (a) the color-coded intensity of the 2PPE spectra are shown with respect to the pump-probe delay. The integrated 2PPE intensities over the energy regions of the Ni-3*d* state, feature B, and the electrons close to the low energy cutoff (BG - for background) are shown in Fig. 4.30 (b) on semi-logarithmic scale. The intensity profiles have been background subtracted according to the intensity at large delays and additionally normalized to the intensity maximum. For a better reading the three curves are shifted in vertical direction relative to each other<sup>19</sup>. The data of the Ni-3*d* state (features A) have been fitted with a single temporal broadened exponential decay as shown by the solid black line. A good agreement between experimental data and fit is achieved. A lifetime

<sup>19</sup>Note that the results of the Ag-*sp* resonance (feature B) will be discussed in section 4.4.2.

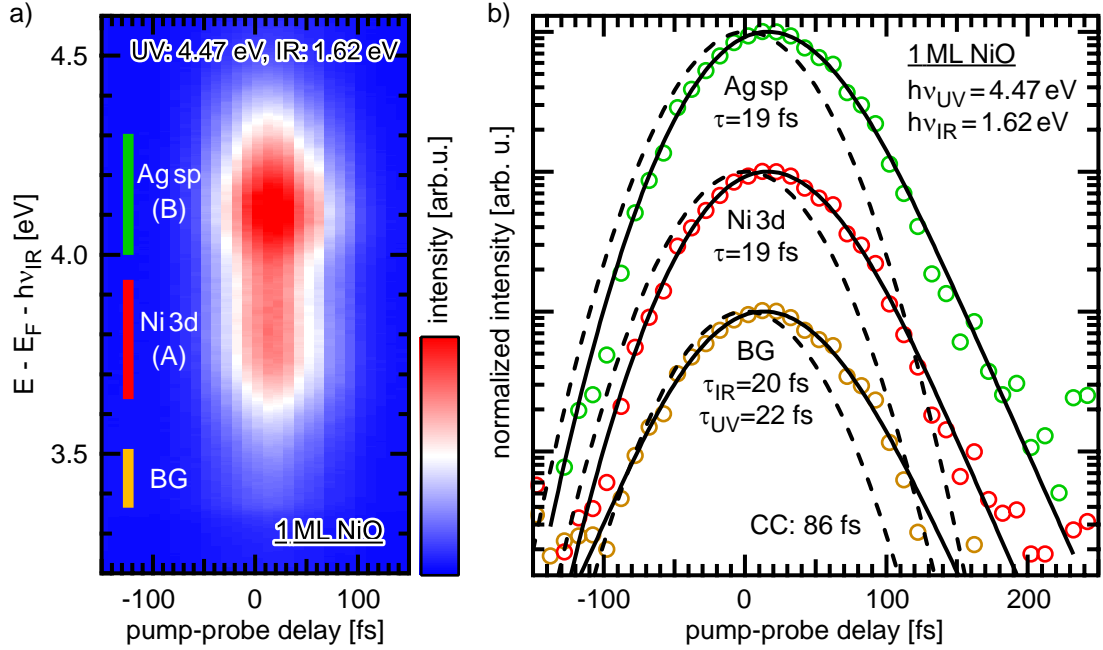


**Figure 4.30:** (a) Color-coded 2PPE spectra of the NiO monolayer in dependence of the pump-probe delay ( $h\nu_{UV}=4.47$  eV and  $h\nu_{IR}=1.62$  eV, photodiode corrected data). (b) Line profiles through (a) at energy positions of the time-dependent background (BG), the feature A (Ni 3d), and the feature B (Ag sp) as indicated by the vertical bars in (a). The black solid lines represent curve fits. For features A and B a temporal broadened exponential decay and for the BG region a mixture of UV and IR probed contributions have been applied. The dashed lines show the cross-correlation (CC) traces of 86 fs (FWHM).

of  $19 \pm 10$  fs and a cross-correlation (CC) of  $86 \pm 10$  fs (FWHM) have been extracted. The latter one is shown by the dashed black line. The large value of the cross-correlation determines the relatively large error<sup>20</sup>. Comparing the cross-correlation curve with the data points at negative delays a difference between the Ni-3d state and the BG region becomes evident. The data points of the latter one coincide with the dashed line. This is explained by an additional UV-probed contribution to the electron intensity. The solid black line shows the curve fit with weighted IR and UV-probed contributions. A perfect agreement with experimental data is achieved. The lifetimes are 20 and 22 fs for the IR and UV probed contribution, respectively. As already discussed in section 4.2.5 (IPS of 4 ML NiO), the UV contribution originates most likely from hot-electron excitations. But the lifetime of 22 fs is about 10 times smaller than observed in section 4.2.5 or on Ag [32] and Cu [94] surfaces. The apparent lifetime of the BG region at positive delays (IR probed) with the absence of a certain feature in the spectrum is explained by contributions of the energetically broad Ni-3d state in this energy region.

The feature IPS at relatively high intermediate state energies of  $4.60 \pm 0.05$  eV (see Fig. 4.26 (b) on page 61 and Fig. 4.45 (b) on page 91) is assigned to the image-

<sup>20</sup>As shown in section 4.2, it is possible to achieve cross-correlations of about 50 fs (FWHM) which would help to investigate the short-lived states of the NiO monolayer with a higher accuracy.

potential state on the NiO monolayer. This is assured by the observed dispersive behavior of this feature, as it will be shown in section 4.4.2 below<sup>21</sup>. As shown in section 4.1.2 the NiO monolayer has an average work function of 5.0 eV which leads to an IPS binding energy of 400 meV. This is smaller compared to the binding energy of the  $n=1$  image state on Ag(001) of 561 meV [10,31]. But it agrees well with the binding energy of the  $n=1$  image state of the NiO bilayer (see section 4.2.3). However, some more considerations about the value of the IPS binding energy have to be mentioned. Deduced from the metallic character of the NiO monolayer (see section 4.1.2), the approach of the permittivity to infinity is expected. This leads to equation 4.4 (page 29) for the calculation of the IPS binding energies. Note the difference of the nominator of 0.85 compared 0.609, derived for the NiO bilayer with a permittivity of 12 (compare equation 4.10 on page 42). Thus, larger values of the IPS binding energies might be possible. The quantum defect  $a$  in the denominator of equation 4.4 acts in the opposite direction. This is determined by the electronic structure, which is different for Ag(001), the NiO monolayer, and the bilayer. The monolayer feature A at 3.73 eV should lead to an increase of  $a$  compared to the Ag(001) substrate due to the absence of electronic states in this energy region at Ag(001). This should lead to a binding energy of the  $n=1$  IPS of the NiO monolayer of  $<561$  meV. The last issue is the work function of the NiO monolayer, which is necessary to determine the binding energy from the intermediate state energy. The average value of 5.0 eV based on UPS might be influenced by film imperfections (small remaining Ag regions, small islands of the starting bilayer, and the Smoluchowski effect). Thus, a larger value of the monolayer work function is not precluded. This assumption is supported by STS spectra as shown in Fig. 4.25. The first field emission resonance of the NiO monolayer occurs between 5.8 and 6.2 eV. Comparing these values with the one found for bare Ag(001) ( $\sim 4.7$  eV [15]), the local work function of a defect-free NiO monolayer can be estimated to  $\sim 5.5$  eV. This increases the value of the IPS binding energies derived from the 2PPE spectra<sup>22</sup>. In conclusion of these considerations, the binding energy of the  $n=1$  IPS of the NiO monolayer is not fixed, yet, but most likely larger than the above mentioned value of 400 meV.

### 4.3.3 The bi- and trilayer of NiO/Ag(001)

With the bilayer the formation of a quasi-rock salt structure becomes possible and is indeed observed by LEED and STM [48,50]. Thus, a change of the electronic structure in comparison to the strongly substrate influenced monolayer is expected. The results of 2PPE of unoccupied Ni-3d states of the NiO bi- and trilayer will be presented in this section.

Monochromatic 2PPE spectra of the NiO bilayer are shown in Fig. 4.31 by solid green lines. The photon energy has been varied between 3.28 and 4.18 eV. The energy scale refers to the intermediate state energy. A feature D is evident in all spectra and is observed at a constant intermediate state energy of 2.6 eV. The corresponding STS

<sup>21</sup>See angle-resolved 2PPE data in Fig. 4.45 (b) on page 91. The presentation of the data here would go beyond the scope of the discussion.

<sup>22</sup>The estimation of  $\Phi_{ML} \sim 5.5$  eV leads to a binding of 0.9 eV of the  $n=1$  IPS of the NiO monolayer. This value is surely too large but it demonstrates the upper limit of the work function estimation from field emission resonances.

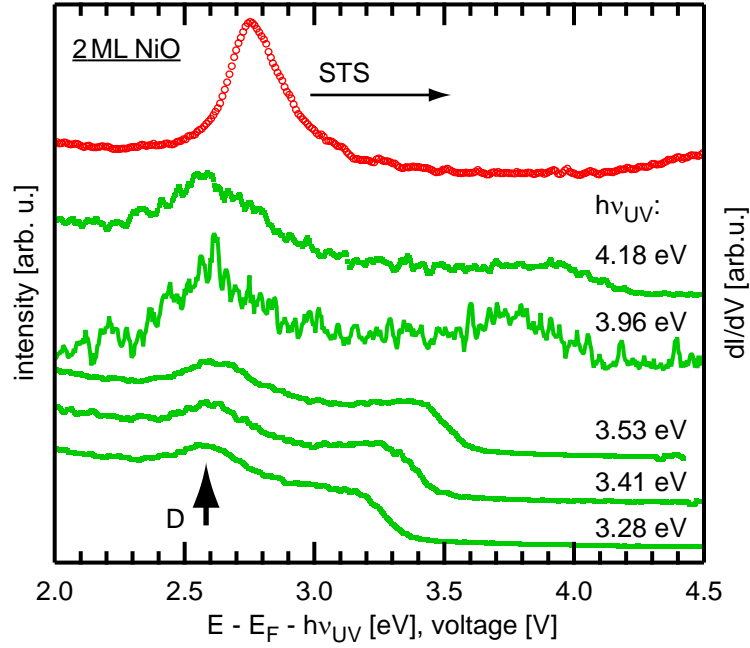


**Figure 4.31:** Comparison of monochromatic 2PPE and STS [15] for the bilayer NiO.

spectrum of a defect-free bilayer island is shown in red above. As already observed for the unoccupied states of the NiO monolayer, a good agreement between both methods is found. The feature in STS observed at 2.75 eV shows a deviation of +150 meV compared to 2PPE.

To investigate the trilayer of NiO, the mono- and bilayer films have been heated at elevated temperatures. As already seen in section 4.2.4 the films start to lacerate and the formation of individual islands of larger thickness is observed. Figure 4.32 (a) shows monochromatic 2PPE spectra of the heated monolayer (solid lines) and the heated bilayer film (dashed lines). Note that a closer analysis of the heated films will be given in the following section 4.3.4 below. Therefore only the main aspects will be mentioned here. The blue curve represents the 2PPE spectrum of the monolayer as discussed in the previous section and shows the feature C at 2.3 eV. The dashed green curve corresponds to the bilayer as shown above with the feature D at 2.6 eV. Heating the two different film thicknesses at specific temperatures (see section 4.3.4) the orange spectra have been obtained, where the solid curve corresponds to the heated monolayer. A pronounced feature E at 2.3–2.4 eV is found. The layer-resolved STS data in the equivalent energy range are shown in Fig. 4.32 (b). The corresponding unoccupied Ni-3d states, namely the features C, D, and E are found at 2.23, 2.74, and 2.62 eV, respectively. Comparing these energy positions with the 2PPE data a good agreement between both methods is observed with deviations of up to 200 meV. However, the energy shifts between the states of different thicknesses, i.e., the energy shifts from C to D and from D to E, have the same directions in both methods as indicated by the arrows.

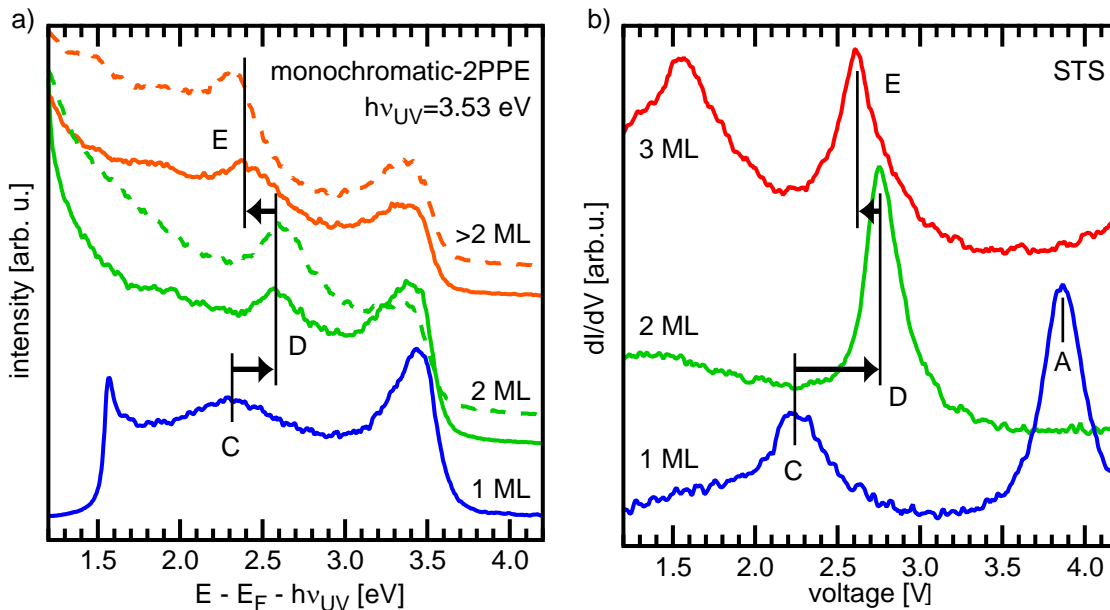


**Figure 4.32:** (a) Monochromatic-2PPE spectra of an annealed NiO monolayer (solid) and bilayer (dashed line) from Fig. 4.33. The spectra are dominated by features C, D, and E according to the indicated film thicknesses. (b) Layer resolved  $dI/dV$  spectra of the mono-, bi-, and trilayer NiO showing the feature C, D, and E, respectively. The arrows indicate the relative energy shifts between different thicknesses which have the same directions in both methods.

#### 4.3.4 Heating the monolayer and bilayer of NiO

In the previous two sections the electronic structure of unoccupied states of the mono-, bi-, and trilayer of NiO has been discussed. It has been found that the layer-resolved electronic structure observed by 2PPE allows to discriminate between different layer thicknesses. This is used to investigate the temperature stability of mono- and bilayer films upon heating at elevated temperatures. It will be shown that 2PPE is able to probe the transition of a closed NiO thin film to a mixture of thicker NiO islands surrounded by the Ag substrate. Thereby, 2PPE is very sensitive to the actual NiO island thickness. The role of the NiO bilayer for the ongoing growth will be depicted.

As already seen in section 4.2.4 a NiO thin film lacerates upon heating. This restructuring is accompanied by the formation of NiO islands with higher thicknesses (higher with respect to the starting thickness before lacerating) and Ag regions in between. In a first step the formation of bilayer regions is favored [53]. For the bilayer a lacerating of the film is expected as well, but the temperature might differ from the value of the monolayer due to a different atomic configuration of the starting rock salt structure.

In Fig. 4.33(a) monochromatic 2PPE spectra of a series of several heating steps up to 700 K for a NiO monolayer on Ag(001) are shown. The energy axis corresponds to the intermediate state energy. At 450 K two features at 2.30 eV (C) and 3.4 eV are observed as already discussed in section 4.3.2. Up to temperatures of 500 K no change of the spectrum is evident. At a temperature of 550 K an upshift of the main



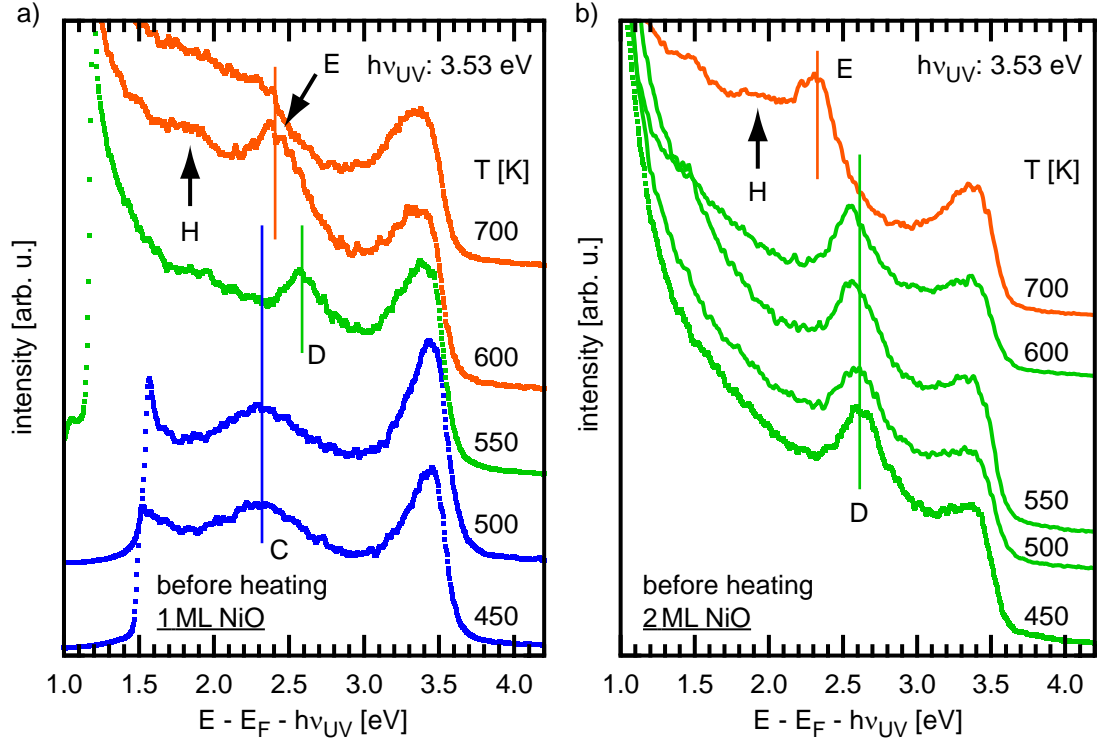


**Figure 4.33:** Monochromatic 2PPE spectra with a photon energy of 3.53 eV of (a) the monolayer and (b) the bilayer of NiO on Ag(001) upon annealing to the indicated temperatures. The vertical lines illustrate the corresponding position of the features C, D, E, and H of its first occurrence.

peak to 2.60 eV (D) and a broad feature at  $\sim 2.0$  eV is observed. Upon heating to 600 K, the main feature shows an additional downshift to 2.4 eV (E) accompanied by the formation of a feature at 1.9 eV (H). After heating to 700 K a notable decrease of the intensity of the main feature at  $\sim 2.3$  eV is observed. Note that in all spectra a feature at 3.4 eV is evident. A similar series has been recorded for a NiO bilayer as shown in Fig. 4.33 (b). The main feature C is evident at 2.60 eV. After annealing at temperatures of up to 500 K no changes in the spectra are observed. Between 550 and 600 K a downshift to 2.55 eV is observed, where a small shoulder at 2.60 eV remains, leading to an asymmetric peak. After further heating to 700 K two features at 2.35 (C) and 3.4 eV are evident.

Summarizing the observations from Fig. 4.33 (a) and (b) the following conclusions can be made. The monolayer is stable upon annealing up to 500 K as visible in the blue spectra with the pronounced monolayer feature C. The occurrence of the feature D at 550 K indicates the restructuring to NiO islands of bilayer thickness (compare Fig. 4.33 (b)). The temperature of 550 K is comparable to the observations of Bertrams and Neddermeyer who reported a temperature of 470 K for the lacerating of the monolayer film [53]. This discrepancy might be due to difficulties of the exact temperature measurement. The data presented here allow for a very accurate determination of the temperature because the thermocouple was directly fixed at the Ag(001) crystal. Further annealing to 600 K and above leads to an ongoing restructuring of the oxide film accompanied by the formation of island with effectively higher film thicknesses, i.e., three or more monolayers. The pronounced

feature E in the orange spectra observed at 2.4 eV is attributed to the NiO trilayer, as already discussed in the previous section. This restructuring of thin films to islands of larger thicknesses has been investigated by Großer using STM [15] as well as by Polzin using high-resolution EELS<sup>23</sup> [58]. Both methods reveal that the average thickness of the NiO islands increases with increasing annealing temperature. Note that the small feature H at lower energies is not well defined in the data shown here. It might originate from two different states. At first the unoccupied Ag-*sp* band which is observed up to 1.9 eV (compare Fig. 4.41 on page 85) might lead to an increased intensity in this energy region. The contribution from the Ag-*sp* band of the substrate is in principle possible due to the formation of large Ag surface regions. The second possibility is the observation of the feature H (as it is already indicated by the label H). This feature is attributed to the unoccupied  $d_{z^2}$ -derived surface state of NiO(001) observed at 4 ML NiO and will be discussed in the following section. The lacerating of a closed bilayer film occurs at 650 K<sup>24</sup>, i.e., at  $\sim 100$  K higher temperature as observed for the monolayer film and supports the expectation of a higher stability of the bilayer. The feature at 3.4 eV which is observed for all heating temperatures of the monolayer but also for the bilayer at higher temperatures can be understood by the presence of very small monolayer regions and originates from the partially excited Ni-3*d* state at 3.73 eV. This interpretation is reasonable for the annealed monolayer at 550 K because the low-energy cutoff observed at  $\approx 1.1$  eV leads to a work function of  $\approx 4.6$  eV ( $\Phi = 1.1 \text{ eV} + h\nu_{UV} = 4.6 \text{ eV}$ ). This value indicates that the surface consists not only of Ag and NiO bilayer regions because a mixture of  $\Phi_{Ag} = 4.5 \text{ eV}$  and  $\Phi_{NiO, bilayer} = 4.2 \text{ eV}$  would result in a total work function less than 4.5 eV. This means although the 2PPE spectrum is dominated by the bilayer feature D small monolayer regions have to persist.

The observed transformations of the surface morphology in dependence of the heating temperature is depicted in Fig. 4.34 (a). The upper row shows the transformation of the NiO monolayer and the lower row the transformation of the bilayer. From STM it is known that the NiO islands of lacerated films are embedded into the Ag substrate [15] as indicated in Fig. 4.34 (a)<sup>25</sup>. Several heating steps will be analyzed in terms of energy considerations as shown in Fig. 4.34 (b) and (c). During growth of the monolayer (①) the film reconstructs in an energetically favorable state ② as shown in Fig. 4.34 (b). The monolayer is observed up to temperatures of 500 K. The absence of any bilayer islands (state ④) is explained by an energy barrier in between. The barrier limits the diffusion of the adsorbed material. At a temperature of 550 K (Fig. 4.34 (c)) the barrier ③ can be passed and the diffusion increases. Thus, the formation of bilayer islands (state ④) becomes possible. This particular temperature is interesting because no trilayer feature is observed in 2PPE. This can be understood by an additional barrier ⑤ which prevents the formation of trilayer islands. Note that the formation of trilayer out of bilayer islands is observed at 600 K (upper row). In contrast to that the transition temperature is around 700 K for the formation out of a closed bilayer (lower row). This means that the *closed* bilayer exhibit a larger stability against the formation of trilayer islands

<sup>23</sup>The energy loss of the Fuchs-Kliwer phonon of NiO is sensitive to layer/island thickness as well.

<sup>24</sup>Based on the results here a similar study has been performed by Polzin using HREELS. The lacerating of the bilayer is observed at 650 K [58].

<sup>25</sup>These structural details do not influence the 2PPE spectra. The effective island thickness should determine the features in 2PPE and not the periphery (interface to vacuum or Ag).

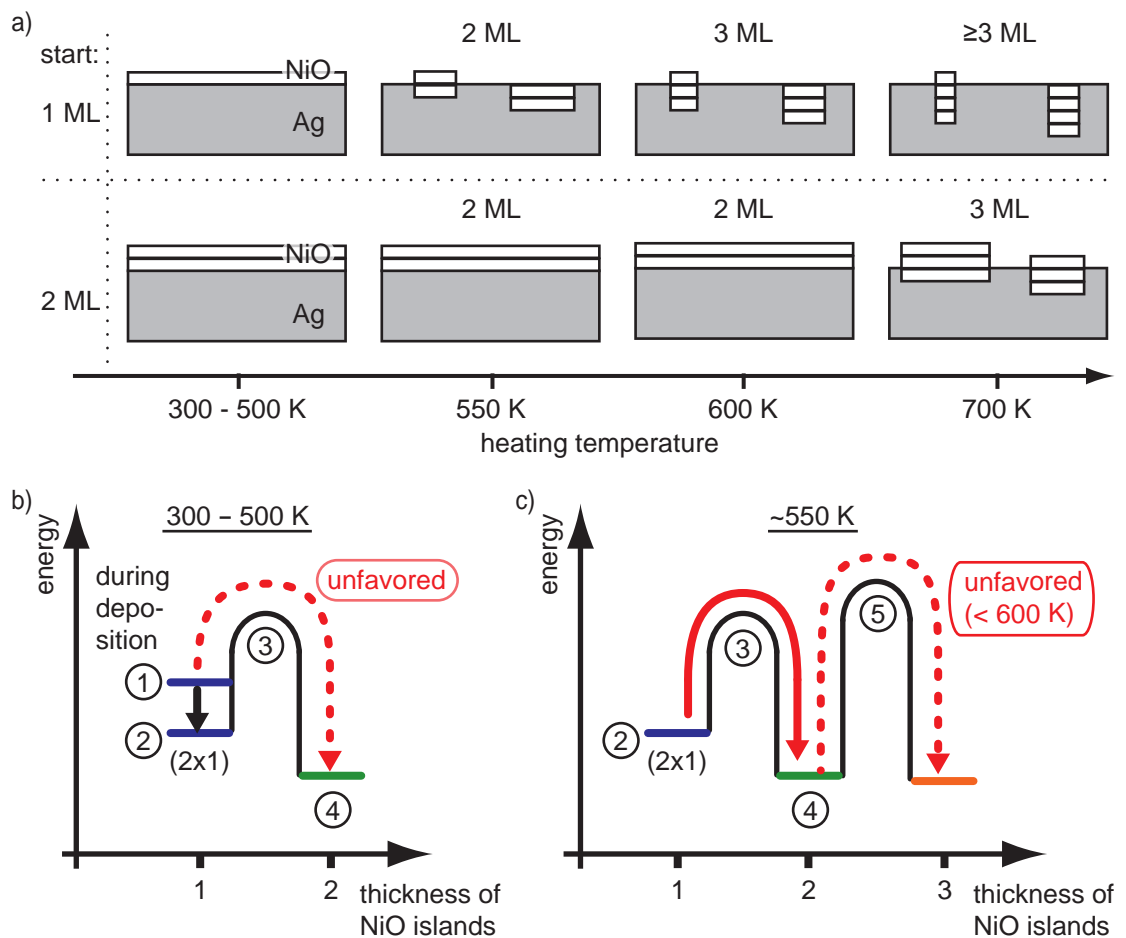


**Figure 4.34:** (a) Model of the morphology of a monolayer and bilayer NiO film upon heating derived from 2PPE data. (b) and (c) show energy considerations for the heating of a NiO monolayer at different temperatures. The limited diffusion leads to energy barriers ③ and ⑤ which determine the temperature for the formation of islands with higher thicknesses.

compared to an *individual* bilayer island. Instead of a pure higher stability, the transformation of the closed bilayer might be kinetically hindered due to absence of free Ag regions<sup>26</sup>.

Note that all observations reported here clearly show the existence of the closed NiO monolayer film. Wollschläger *et al.* reported the formation of bilayer islands during room temperature growth investigated by the intensity oscillations of the specular LEED beam [47]. The oscillations start at 2 ML thickness with an ongoing period of 1 ML. The intensity drops completely in the 0–2 ML region. This has been misinterpreted by the formation of the bilayer islands until the film is closed accompanied with a layer-by-layer growth above 2 ML. However, MEED investigations by Polzin also show an intensity drop in this thickness region, although a closed monolayer could be prepared as well [58]. Thus, the absence of the *peak* at the monolayer coverage might have other reasons in terms of the amplitude of the scattering probability of the NiO monolayer film.

<sup>26</sup>The material transport is mainly driven by the mobility of the Ag substrate [15].

For the preparation of closed thicker NiO films the post-ordering of an as-grown film at room temperature is always difficult due to the limited diffusion on the one side and the lacerating of the film on the other side. The observations of the temperature stability discussed above lead to the following recipe for the preparation of well-ordered NiO films of  $\geq 2$  monolayers thickness. As a first step, the growth should be realized at a temperature of 550 K. All adsorbed NiO material directly forms islands of bilayer thickness until a closed bilayer is reached. This film should exhibit a better ordering compared to the growth at room temperature. This is due to the direct pseudomorphic growth instead of the required reordering of the hexagonally reconstructed monolayer to the pseudomorphic bilayer. A well-ordered bilayer supports the ongoing growth of NiO films of higher thicknesses.

### 4.3.5 Four and eight monolayers NiO/Ag(001)

#### Four monolayers NiO/Ag(001)

For thicker NiO films it is expected that the atomic and electronic structure adapts to that found at bulk NiO samples. To investigate this transition between substrate-influenced NiO ultra-thin films and bulk-like NiO a closed four monolayers NiO film has been prepared. In LEED and STM a pseudomorphic growth is still observed, i.e., the NiO film exhibits the lattice constant of Ag. However, the electronic properties approach the NiO bulk as already seen in UPS (see section 4.1.2). Figure 4.35 (a) shows normal-emission monochromatic 2PPE data with respect to the intermediate state energy using photon energies between 3.8 and 4.1 eV. For comparison the lower black curve refers to data of the bare Ag(001). The upper dashed spectra have been obtained at the as-grown NiO film whereas the lower solid spectra correspond to a

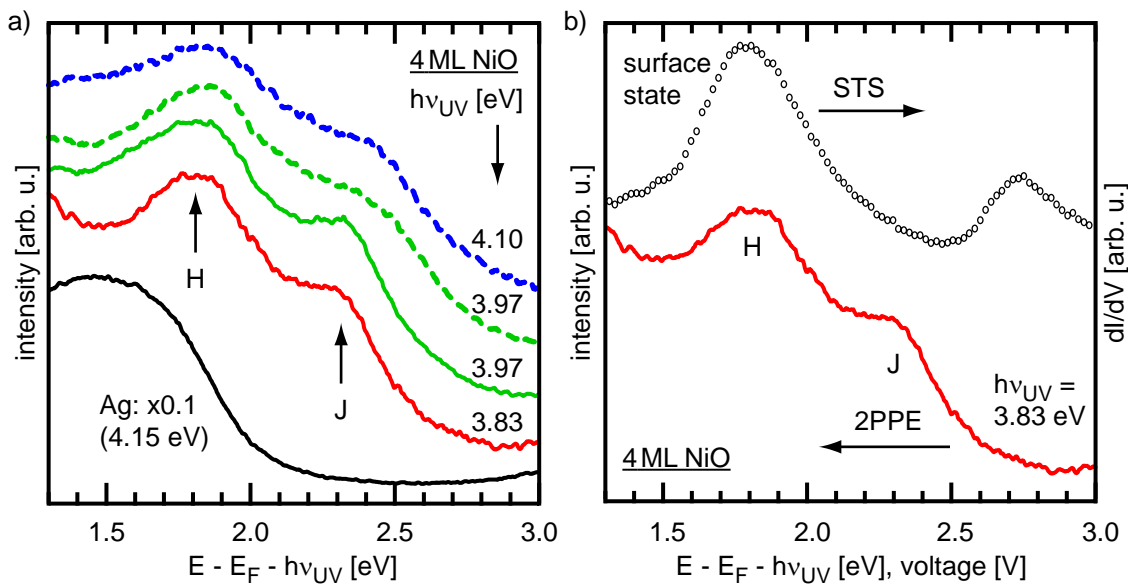


**Figure 4.35:** (a) Monochromatic 2PPE of 4 ML NiO as prepared (dashed lines) and annealed at  $\sim 500$  K (solid lines). The lower black curve shows a spectrum of Ag in this energy region. (b) Comparison of 2PPE and STS in the vicinity of the  $d_{z^2}$ -derived surface state of NiO(001).

post-annealed film at  $\sim 500$  K. Two features H and J are evident at 1.8 eV and 2.3 eV, respectively. Feature J gets more pronounced at the annealed films and shifts to lower energies.

In Fig. 4.35 (b) the spectra of STS and 2PPE are shown on the same energy scale. In STS two Ni-3d derived states are observed at 1.80 and 2.75 eV, respectively. The first one is interpreted as the  $d_{z^2}$ -derived surface state of NiO(001) which develops at film thicknesses  $\geq 3$  ML [15]. For the feature H in 2PPE a good agreement between both methods is observed. This result is similar to the observations of the states found at the monolayer and bilayer coverages.

In the vicinity of feature J no corresponding state in STS is evident. The energy difference to the second feature in STS at 2.75 eV is  $\sim 450$  meV. This difference between both methods is larger, compared to the energy differences found for the other features in the sections 4.3.2 and 4.3.3. The energy of the feature J is similar to the one found for feature E of the lacerated monolayer and bilayer films, which has been assigned to the trilayer thickness. This means either the feature J is equivalent to feature E<sup>27</sup> and is observed at trilayer islands of the nominal 4 ML film or vice versa the feature E does not originate from the trilayer film<sup>28</sup>.

### **Eight monolayers NiO/Ag(001)**

The LEED pattern of the 8 ML film reveals additional satellite spots in the vicinity of the specular and first order diffraction spots (not shown here). The satellites are oriented along the direction of the (1 1) spot as reported by Wollschläger *et al.* [47]. This is assigned to the formation of a mosaic structure of the NiO with (110) glide planes. This indicates the transition of the NiO lattice constant to the expected bulk value. Thus, an approach to the real bulk electronic structure without the influence of the Ag substrate should be observed as well. Figure 4.36 (a) shows normal-emission monochromatic 2PPE spectra for 8 ML NiO with respect to the final state energy using photon energies between 3.45 and 4.17 eV. For photon energies between 3.88 and 4.17 eV two features P and Q are evident. The former one vanishes (or possibly coincides with Q) at photon energy of 3.64 eV. The spectrum below, obtained with an UV energy of 3.45 eV, does not show any feature with a comparable width of the feature P and Q. Note that the absolute intensities of the observed features are quite low. Thus, the laser power has been increased to reach reasonable acquisition times and signal-to-noise ratios. Under these conditions the spectra show energy shifts due to space charge effects<sup>29</sup>. This shift has been determined from spectra obtained with much lower laser power and applied to the data of Fig. 4.36. To analyze the pump-probe mechanism, the photon-energy dependent peak positions are shown in Fig. 4.36 (b). The final state energy of both features depends linearly on the photon energy. A linear fit reveals a slope of  $2.04 \pm 0.20$  for the feature Q as shown by the black line. This indicates that this feature in the 2PPE spectrum originates from an occupied state (see section 2.2). The 2PPE excitation is realized via the absorption of two photons without a long-lived intermediate state. In contrast a slope of  $1.33 \pm 0.20$  is found for the feature P. To estimate the significance

<sup>27</sup>This makes the new label J redundant.

<sup>28</sup>This makes the label E redundant as introduced in section 4.3.3.

<sup>29</sup>The energy broadening due to space charge effects has been incorporated in the experimental error of the peak positions.

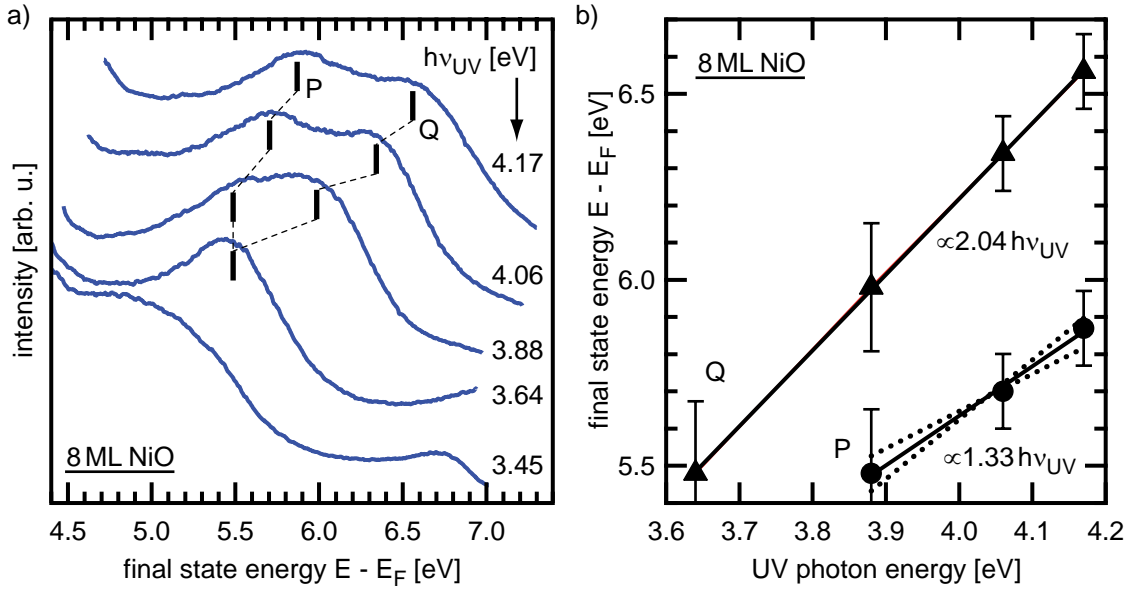


**Figure 4.36:** (a) Monochromatic 2PPE spectra of 8 ML NiO/Ag(001) in dependence of the UV photon energy. (b) Peak positions of the features P (circles) and Q (triangles) with respect to the photon energy. A linear dependence of both features is observed with slopes of 1.3 and 2.0, respectively. For comparison the dotted lines indicate linear slopes of 1.0 and 1.6.

of this value, the dotted lines indicate linear dependencies with slopes of 1.0 and 1.6, respectively. Thus, a slope of 1.0 is possible within the error bars. This indicates an unoccupied electronic state. An additionally involved occupied state with a slightly different dispersion would also explain the observed non-integer slope, as already observed for the feature B in section 4.3.2<sup>30</sup>.

In Fig. 4.37 (a) the 2PPE spectra are shown with respect to the initial state energy referred to  $E_F$ . As expected from the photon energy dependence in Fig. 4.36 (b) the feature Q is found at a constant energy of  $-1.78 \pm 0.10$  eV. To compare the data with photoelectron spectroscopy (PES), the UPS spectrum for a 10 ML film is shown by the red line. The feature at -1.9 eV is assigned to the excitation of a Ni-3d electron with an additional electron transfer from the ligand to the metal ion in the NiO ( $d^8 \rightarrow d^8 L^{-1}$  transition). An energy difference of 120 meV to the 2PPE feature is observed. To compare the results with bulk NiO(001) by Shen *et al.* [52] the PES data obtained with different photon energies are shown by green lines. A feature at -1.6 eV is evident. A good agreement within 300 meV between 2PPE and PES is found. Thus, the feature Q originates from the  $d^8 \rightarrow d^8 L^{-1}$  transition as well, which is excited via 2PPE.

Figure 4.37 (b) shows the 2PPE data with respect to the intermediate state energy to analyze the unoccupied state of the feature P. For photon energies of 3.88 and 4.06 eV the feature P is found at  $\sim 1.6$  eV and shifts to 1.70 eV for 4.17 eV photon energy as shown by the solid black line. The dotted black line indicates a possible coincidence with the feature Q for a photon energy of 3.64 eV. The magenta line in Fig. 4.37 (b) shows STS data of 8 ML NiO on the same energy scale [15]. The

<sup>30</sup>See also the detailed discussion of the monolayer feature B in section 4.4.2.

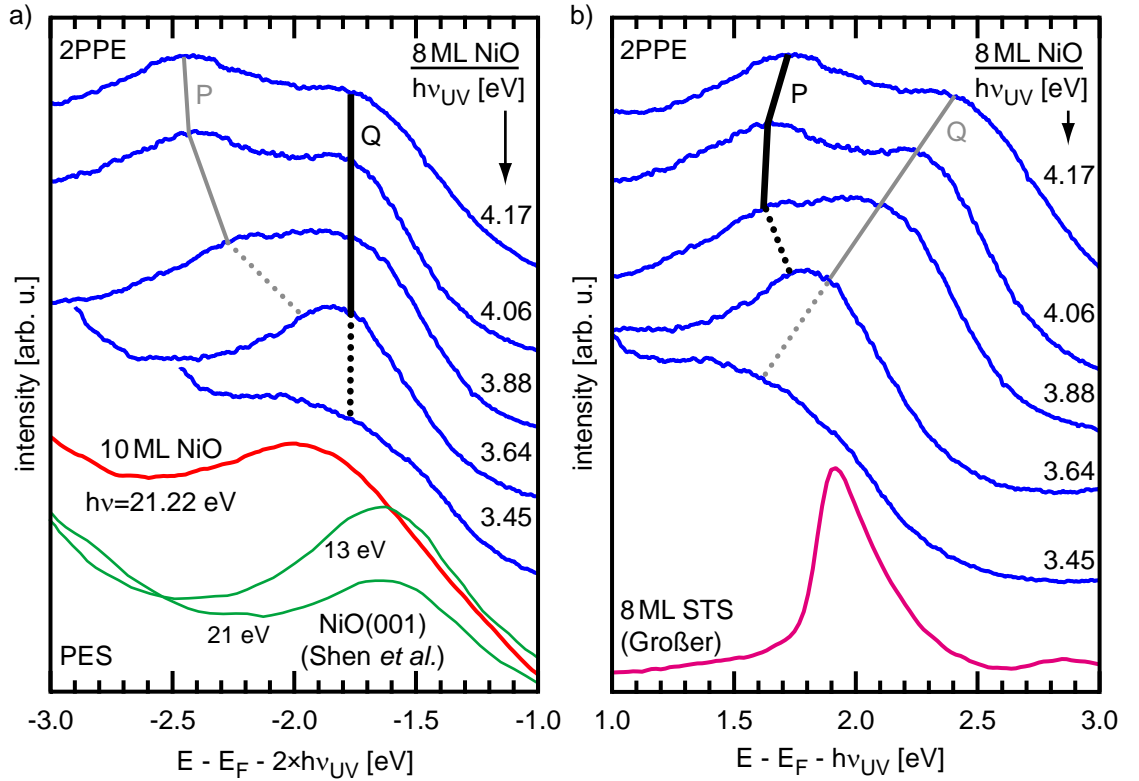


**Figure 4.37:** Monochromatic 2PPE from Fig. 4.36 with respect to (a) the initial state and (b) the intermediate state energy. The green spectrum in (a) corresponds to the UPS data for a 10 ML NiO film. The red spectra show data from bulk NiO(001) with different photon energies (adopted from [52]). In (b) the corresponding STS spectrum is shown by the green line (adopted from [15]).

asymmetric peak at 1.9 eV is assigned to the Ni-3d<sub>z<sup>2</sup></sub> derived surface state as already observed for 4 ML NiO. For the case that feature P originates from the NiO surface state a difference of 0.3 eV between both methods is observed. This deviation can be explained in terms of final state effects or method intrinsic energy shifts in STS. The latter issue will be further discussed in the following section 4.3.6 and appendix 6.D. According to the discussion there, the voltage drop of the applied bias in STS within the dielectric NiO film causes an artificial upshift of electronic states in the order of >100 meV.

The photon-energy dependence of the feature P could not be clarified at this stage of investigation. Further measurements using bichromatic 2PPE with both photon energies in the UV range are necessary. The constant-intermediate and constant-final state mode could distinguish between the influence of the involved initial, intermediate, and final states. As an outlook, a possibly resonant transition between initial and intermediate bands has to be mentioned to explain the photon-energy dependence of the feature P. Although the data have been obtained at normal emission, the dispersion of the involved bands in  $k_{\perp}$  direction could lead to a photon-energy dependent position of the intermediate state (see a similar discussion for the Ag-*sp* resonance of the monolayer feature B in section 4.4.2). As already found above, the intermediate state is assigned to a Ni-3d<sub>z<sup>2</sup></sub> derived surface state of NiO(001). An unoccupied state in this energy region has been observed

by Dudarev *et al.* in layer-resolved local spin density approximation calculations (LSDA+U). This state is localized at the topmost NiO layer (surface state) [100]. Similar results of the existence of a Ni-3*d* surface state have been reported by Köderitzsch *et al.* [101] and Däne *et al.* [102]. The band structure has been calculated using the self-interaction corrected (SIC)-LSDA method with implemented multiple scattering theory within the Korringa-Kohn-Rostoker algorithm (KKR). However, a surface state does not show any dispersion in  $k_{\perp}$  direction which would help to understand the photon-energy dependence of the feature P. In addition to the surface states, the calculations reveal *d* bands of NiO at  $\sim 0.7$  eV higher energies. These bands should in principle show dispersion in  $k_{\perp}$  direction<sup>31</sup>. The energy difference to the experimental data might originate from the excited final state in photoemission, where correlation effects might modify the electronic structure. Kunes *et al.* reported the  $k$ -resolved band structure of NiO using the *ab initio* band structure method and the dynamical mean-field theory with a quantum Monte-Carlo impurity solver [103], recently. An *excellent agreement* with PES data of Shen *et al.* [52] has been achieved for the occupied electronic band structure. Orbitally decomposed spectral functions show an unoccupied Ni-*d* band with  $e_g$  symmetry, which disperses from 1.3 to 1.7 eV along the  $\Gamma X$  direction, i.e., the corresponding  $k_{\perp}$  direction of the NiO(001) surface. Thus, the calculations reveal a dispersing unoccupied *d* band of bulk NiO which might explain the experimental observation of the present 2PPE results. Note that the energy increases along  $\Gamma X$ , i.e., the dispersion points upwards. To understand the peak position of feature P with a non-integer dependence on the photon energy, the band of the initial state requires a dispersion in  $k_{\perp}$  direction as well. According to the discussion of the monolayer feature B in section 4.4.2 the dispersion of the involved bands should have the opposite curvatures, to realize the non-integer dependence on the photon energy. The only possible initial states for the transition into the unoccupied Ni-3*d* band are the occupied O-2*p* or Ag-*sp* bands<sup>32</sup>. The former one corresponds to a charge transfer from the oxygen to the Ni<sup>2+</sup> ion. The calculation of Kunes *et al.* reveals O-2*p* bands which show dispersive behavior (up- and downward directed dispersion is observed) and might explain the experimental observation. However, a transition from the O-2*p* bands into the Ni-3*d* bands is most unlikely, because the O-2*p* bands have energies of  $>4$  eV below  $E_F$ . Thus, transitions of that type would require a two-photon excitation into the unoccupied intermediate state, i.e., a 3PPE process in total. This is not observed in the laser-power dependent spectra (not shown here), where a feature of a 3PPE process would vanish very rapidly in comparison to the 2PPE process of the  $d^8 \rightarrow d^8 L^{-1}$  transition (feature Q). A transition from Ag-*sp* bands has to be considered as well. But the Ag-*sp* band exhibits an upward dispersion along the  $\Gamma X$  direction (compare Fig. 4.40 on page 83 below). This is in contradiction to the expected involved occupied band with an opposite curvature of the corresponding Ni-3*d* band of the intermediate state. As mentioned above, further experiments on this topic will clarify the influence of the involved bands on the 2PPE of feature P.

<sup>31</sup>Of course the dispersion of a *d*-band is expected to be small due to its localized character.

<sup>32</sup>... due to the parity selection rule which prohibits *d-d* transitions



### 4.3.6 Unoccupied states – comparison of experimental methods

The previous sections about the spectroscopy of unoccupied states in 2PPE and the comparison with STS reveal similar results with respect to the energy position. In this section the excitation processes of 2PPE, electron energy loss spectroscopy (EELS), inverse photoemission (IPE), and STS will be analyzed regarding their similarities and differences. The consequences of the electronic final states and the role of the Ag substrate will be discussed.

Whereas theory as e.g., LSDA calculates the ground state of the electronic system, an excited state is intrinsically observed in experimental methods due to the perturbation with photons or electrons and the existence of holes or excess electrons. This leads to energy shifts between the experimentally observed states and the theoretically calculated ones. In the case of negligible electron-electron ( $e-e$ ) and electron-hole ( $e-h$ ) interaction, as observed for most metal samples, the energy difference between the ground state and the excited state is very small. Simply speaking, an electron does not feel any difference between the ground and the excited state due to the *missing* interaction (free-electron approximation). For the case of NiO, this situation changes drastically. The significant electron-electron interaction in the strongly correlated electron system has to be taken into account, i.e., the free-electron approximation is not applicable. This causes energy shifts between the excited and ground state. For NiO contributions of charge transfer effects are expected as well. Thus, the existence of holes and excess electrons leads to different types of excited final states which additionally change the experimentally determined energy of the electronic states.

Before the fundamental differences between the experimental methods will be discussed, some results of the spectroscopy of unoccupied states of NiO are summarized in Fig. 4.38. The rows (a) and (b) represent the 2PPE and STS results of 4 and 8 ML NiO. Note that the occupied state at 1.4 eV below  $E_F$  in STS in row (b) has been determined at the 6 ML NiO coverage [15]. In row (c) an unoccupied feature at 1.5 eV is evident as observed by 2PPE on NiO/Ni(001) [104]. This feature shifts to 1.9 eV upon adsorption of nitrogen monoxide which indicates a surface state character. A combined PES and IPE study by Portalupi *et al.* reveals a  $d^9$  and a  $4s$  transition at 3.1 and 5.8 eV above  $E_F$ , respectively. The  $d^8 \rightarrow d^8L^{-1}$  transition has been observed at -2.6 eV [46]. The rows (e) to (g) show results of EELS data by Müller *et al.* [51], Freitag *et al.* [105], and Fromme *et al.* [106]. The EELS determines the energy difference (energy loss) needed for the transition between the involved occupied and unoccupied electronic states. Thus, this method does not reveal the energy positions of the unoccupied states<sup>33</sup>. The vertical bars show the value of the energy loss with respect to  $E_F$ . The energy losses are sorted according to the involved surface or bulk states, respectively. Comparing the energies of the observed unoccupied states above the Fermi level, strong variations between the different experimental methods, as 2PPE, STS, and IPE<sup>34</sup> are evident. These differences should mainly originate from the different electronic final states.

<sup>33</sup>Since the transition between occupied and unoccupied states is observed, the energy loss determines the *maximum* energy of an unoccupied state. Due to the band gap around  $E_F$  the energy of the unoccupied state is normally smaller than the value of the observed energy loss.

<sup>34</sup>EELS does not reveal the energy of the unoccupied state.

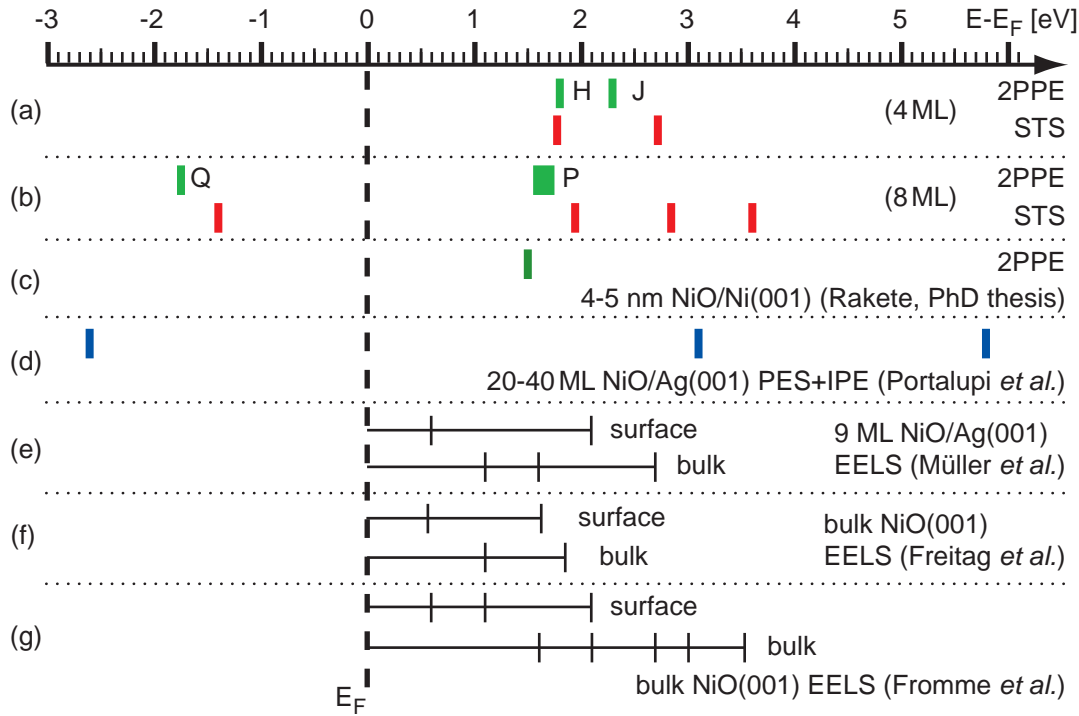


**Figure 4.38:** Energy diagram of various experimental methods. Rows (a) and (b) show the results of 2PPE (this work) and STS [15] of 4 and 8 ML NiO/Ag(001). In row(c) additional 2PPE data of NiO/Ni(001) [104] are shown. The PES and IPE results of NiO/Ag(001) [46] are indicated in row (d), whereas the rows (e) to (g) show EELS results of NiO/Ag(001) [51] and bulk NiO [105,106]. The energy losses determined from EELS spectra are plotted with respect to  $E_F$ .

The fundamental electron excitations of the different experimental techniques are shown in Fig. 4.39 in terms of energy diagrams. The horizontal axis denotes the distance  $z$  along the surface normal. The projected band structure of the Ag(001) substrate is indicated as gray-shaded areas whereas the two horizontal gray lines indicate two bands of the oxide film. The dark and light gray mark the occupied and unoccupied states, respectively. Note that the energy is not to scale. In Fig. 4.39 the monochromatic 2PPE excitation process between occupied and unoccupied states in the oxide film is shown. The length of the arrows indicates the photon energy  $h\nu_{UV}$ . The resulting final state of that transition is characterized by a residual hole in the oxide film ( $N-1$ ), where  $N$  stands for the number of electrons in the unperturbed system. In the case of ultra-thin NiO films, the first step, i.e., the transition from occupied NiO states might be replaced by a transition from occupied Ag states as depicted in Fig. 4.39 (b). The remaining hole in the Ag substrate is immediately screened by the free-electron gas. Thus, the final state after the 2PPE process is characterized by a neutral electron configuration of the NiO film (*pseudo N*). This scenario enables to observe the ground state of the electronic system. EELS delivers information about unoccupied electronic states as well. In Fig. 4.39 (c) a typical excitation process is shown. The incoming electron causes the transition from an occupied state into an unoccupied state. The energy, needed for the transition, is measured as an energy loss of the scattered electron. This kind of transition underlies

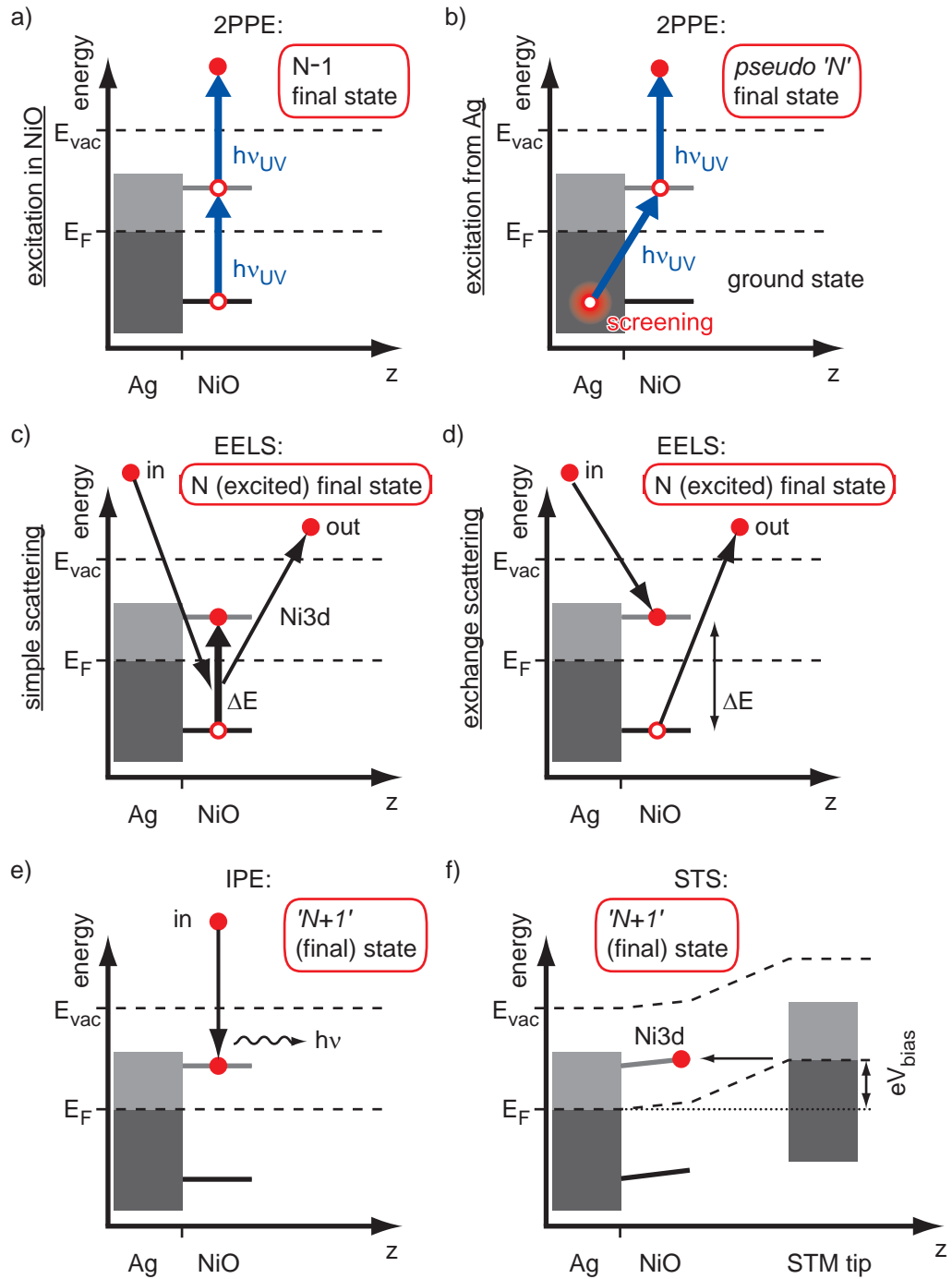


**Figure 4.39:** Energy diagrams of electron excitations for different experimental methods for NiO ultra-thin films on a Ag substrate. (a) 2PPE process with an electron transition from occupied into unoccupied NiO states. (b) Same as (a) but the excitation is realized via electrons from occupied Ag states. (c)+(d) Electron transitions between NiO states in EELS with simple scattering and exchange scattering, respectively. The latter one enables the optically forbidden (parity selection rule)  $d-d$  transitions. (e) and (f) shows the transitions in IPS and STS, respectively, which result in the same electronic final state.

the same selection rules as mentioned above. In contrast to that the exchange scattering enables to measure transitions which are normally forbidden via the dipole selection rules. The mechanism is depicted in Fig. 4.39 (d) where the incoming electron occupies the normally unoccupied state and an afore occupied electron is released with a lower energy according to the energy difference between both levels (compare Auger process). Similar to that, the spin-flip exchange scattering in EELS as investigated the first time by Fromme *et al.* [107] using complete spin-polarized EELS<sup>35</sup>, enables also the observation of transitions which are normally forbidden via the spin selection rule. However, both EELS processes are characterized by a neutral but excited final state (N) with one electron and one hole (eh). The IPE process is depicted in Fig. 4.39 (e). The incident electron occupies an electronic state above  $E_F$  and emits a photon with the corresponding energy difference. The final state has an additional electron in the system (N+1). The identical final state is found in STS as well, as shown in Fig. 4.39 (f). The Fermi level of the tip is shifted by  $eV_{bias}$  until the electron can tunnel into the unoccupied state of the oxide film (see also appendix 6.D).

Since all processes (except (b)) describe an excited final state, correlation effects of the electronic system of NiO are expected. This leads to energy shifts which are determined by the relaxation mechanisms. The PES of occupied states already reveals the influence of correlation effects, namely the charge transfer effects. The excitation of a Ni-3d electron leads to two different final states. The  $d^8 \rightarrow d^7$  with a missing electron at the metal ion and the  $d^8 \rightarrow d^8 L^{-1}$  transition [52,63]. The latter one corresponds to an excitation of a d electron accompanied with a charge transfer from the ligand ion to the metal ion (screening). Both final states have the (N-1) character but the position of the remaining hole determines the energy of the final state. The energy difference is in the order of 5 eV [63,96]. The 2PPE excitation described in Fig. 4.39 (a) describes the similar process also with a N-1 final state. This explains the good agreement of the feature Q observed at the 8 ML coverage and the  $d^8 \rightarrow d^8 L^{-1}$  transition in PES (see Fig. 4.37 (a)). Note that the  $d^8 \rightarrow d^8 L^{-1}$  transition in 2PPE involves a virtual intermediate state in contrast to the excitation scheme of Fig. 4.39 (a). The identical final state of IPE and STS leads to the observation of a moderate agreement of the unoccupied states as shown in Fig. 4.38 rows (b) and (d). The energy difference between both methods is about 300 meV.

The comparison of 2PPE (N-1 or N final state) and STS (N+1 final state) should lead to energy differences of  $>1$  eV due to the expected correlation effects of the electron system. However, energy shifts of  $\leq 300$  meV have been observed for 4 and 8 ML coverage. This apparent contradiction might be rejected as follows. At first the 2PPE process is realized by the pump-probe scheme as shown in Fig. 4.39 (b), i.e., the initial state electron comes from the Ag substrate. This is justified via the observation of these states with photon energies below the band gap of 4.2 eV. The projected band structure of Ag delivers occupied electronic states up to the Fermi level. Additionally, the parity selection rule for the excitation process is fulfilled. Thus, the feature in the 2PPE spectrum is characterized by the ground state of the electronic system (due to the N final state). The good agreement with the feature found in STS implies a small contribution of correlation effects of the

---

<sup>35</sup>This method refers to a spin-polarized incident beam as well as a spin-polarized detection of the scattered electrons.

electron system in the presence of an excess electron. These considerations explain the good agreement between 2PPE and STS.

It remains to analyze the observed (although) small energy difference between STS and 2PPE of the  $d_{z^2}$ -derived surface state. At 4 ML coverage a perfect agreement between both methods is found at 1.8 eV (see feature H in Fig. 4.35 (b)). At 8 ML coverage the 2PPE feature shifts to  $\sim 1.6$  eV (see feature P in Fig. 4.37 (b)), whereas in STS an upshift to 1.9 eV is observed. According to theoretical calculations a lowering of the surface state energy with increasing film thickness is expected [108]. This agrees well with the observations in 2PPE of this work and with the unoccupied state at 1.5 eV observed at  $\sim 20$  ML NiO/Ni(001) [104]. The upshift of the state in STS can be explained by the internal voltage drop of the applied bias voltage within the oxide film. An estimation of typical values is depicted in more detail in appendix 6.D. However, this results in a method-intrinsic shift of the *measured* energy of a given state in STS in comparison to its *real* energy. This effect is as already indicated in Fig. 4.39 (f), where the energy position of the NiO states depends on the distance  $z$ . Depending on the tunneling conditions (the density of states, the tunneling current which determines the tip-sample distance, etc.) the voltage drop can exceed 200 meV easily. Thus, the shift of the feature in STS is an artifact of the experimental method itself rather than an effect of the thickness-dependent electronic structure of the oxide film. In summary, this consideration leads again to a perfect agreement between STS and 2PPE.

Finally the electron transitions observed in EELS have to be related to the 2PPE data. A comparison between both methods in this sense is difficult due to the different excitation selection rules. 2PPE underlies the dipole selection rules which prohibits e.g.,  $d-d$  transitions. As depicted in Fig. 4.39 (d), EELS is not limited to this selection and is able to observe  $d-d$  transitions via the exchange scattering. The energy losses summarized in Fig. 4.38 are assigned to those  $d-d$  transitions. Note that the energy losses are smaller than the value of the optical band gap. The excitation energies derived from EELS enable to estimate the energies of the involved unoccupied states. Since the measured energy loss corresponds to the energy difference between the occupied and unoccupied state, the value determines the maximum energy of the unoccupied state. For the energy losses assigned to surface and bulk states, minimum values of  $\sim 0.6$  and  $\sim 1.0$  eV have been found, respectively. These values are far off the energies of the unoccupied states derived from 2PPE. This might be explained by the totally different electron transitions, realized in 2PPE and EELS, in combination with the expected correlation effects of the electron system. Thus, the correlation effects involved during the electron transitions in EELS and 2PPE are different and lead to different apparent energies of the unoccupied states.

In summary the electron excitations of 2PPE, STS, IPE, and EELS have been discussed. The good agreement between 2PPE and STS spectra is explained by two mechanisms. At first the occupied initial state in 2PPE is most likely a band of the Ag substrate which leads to the observation of the electronic ground state. And secondly, no or only small correlation effects are expected in STS in the presence of the excess electron. The energy shift of the  $d_{z^2}$ -derived surface state in dependence of the film thickness in STS is explained by a method-intrinsic energy shift due to the voltage drop of the applied bias voltage within the oxide film. The comparison of EELS and 2PPE leads to the conclusion, that the type of transition ( $d-d$  transition

in EELS and dipole-allowed transition in 2PPE) determines different correlation effects. This leads to different apparent energies of the involved unoccupied states.

---

## 4.4 NiO assisted observation of Ag bulk bands

Laser-excited photoemission data of NiO/Ag(001) show features which can neither be assigned to IPS nor to electronic states of the NiO overlayer. A feature at the monolayer coverage will be discussed in sections 4.4.2 and analyzed in terms of Ag bulk transitions. Similar to that the data of thicker NiO films will be reviewed in section 4.4.3. It will be shown that the reconstruction of NiO on Ag(001) enables the spectroscopy of Ag bulk bands along wave vectors  $k$  which are normally not accessible at the Ag(001) surface.

### 4.4.1 Introduction

The calculation of the band structure of a solid is an essential tool for the understanding of the electronic properties. The comparison with experimental results enables to interpret the data on the one side but it helps to develop and improve new theoretical methods on the other side as well. The band structure of Ag is shown in Fig. 4.40 (a) along high symmetry directions (from [109]). The occupied bands are located below the Fermi level ( $E-E_F=0$ ). The dispersing bands, which cross the Fermi level are assigned to the Ag- $sp$  bands, whereas the  $d$  bands around 5 eV exhibit much less dispersion. The vacuum level of the Ag(001) surface is indicated by the dotted line. Photoemission enables to investigate the electronic structure by ana-

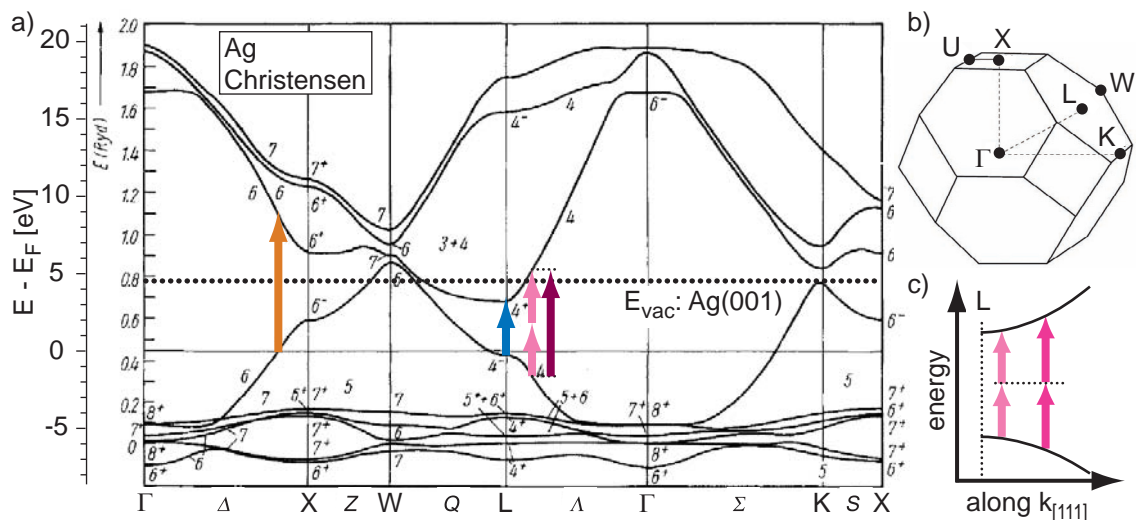


**Figure 4.40:** (a) Relativistic band structure calculation of Ag along high symmetry directions [109]. The left axis represents the energy in eV with respect to the Fermi level (1 Ryd=13.606 eV). The arrows indicate optical band-to-band transitions between occupied and unoccupied Ag- $sp$  bands. (b) 3D representation of the Brillouin zone with the corresponding high-symmetry points (adopted from [110]). (c) Cartoon of the band structure in the vicinity of the L point in  $\Gamma$ L direction (this direction corresponds to  $k_{\perp}$  for photoemission on Ag(111)). The arrows indicate 2PPE transitions between both  $sp$  bands via a virtual intermediate state (dotted line). The photon energy dependence pretends a real intermediate state at the position of the virtual one.

lyzing the angular and energy distribution of the emitted photoelectrons. Electrons with kinetic energies around 50 eV show a minimum of the mean free path in the solid. Thus, the observation of photoelectrons in this energy range is very surface sensitive because the electrons originate from the topmost layers of the investigated sample. By exciting an electron from an occupied state above the vacuum level, the photoemission signal is not only determined by the corresponding occupied state and its density of states. As indicated by the orange, blue, and dark magenta arrows, the possibility of a transition between occupied and unoccupied bands above  $E_F$  influences the signal in photoemission as well. Thus, a resonant excitation of an electron between bulk bands leads to a higher signal in the photoemission spectrum. The variation of *all* experimental parameters e.g., the photon energy, the angle of the incident light, the surface orientation, and the emission angle enables to determine the involved occupied as well as unoccupied bands. The surface orientation for example defines the direction of the observed wave vector  $k_{\perp}$  in normal emission e.g., the  $\Gamma L$  direction for the (111) and the  $\Gamma X$  direction for the (001) surface orientation, respectively. Exemplary, some experimental investigations of photoemission from bulk Ag are presented in [111–116] and corresponding theoretical calculations in [109,117–120]. With decreasing photon energies the number of possible transitions decreases as well, up to the point that only one single transition between the highest occupied band and the lowest unoccupied band determines the feature in the spectrum. This has been shown in the same group by Miller *et al.* [121,122] and Hansen *et al.* [123], where direct transitions between Ag-*sp* bands for Ag(111) and Ag(001) have been investigated, respectively, using photon energies between 6 and 19 eV.

A 2PPE investigation of the Ag(111) surface has been reported by Giesen *et al.* [67]. They showed the first successful observation of IPS with 2PPE. Besides the IPS an additional feature has been found in the 2PPE spectra. The photon energy dependence reveals a shift of the peak with a  $1 \times \Delta h\nu$  dependence. Thus, the feature has been assigned to an unoccupied state at 2.6 eV above  $E_F$ . About ten years later Pawlik *et al.* [23] investigated the Ag(111) surface by two- as well as one-photon photoemission. The frequency doubled beam has been used to obtain 1PPE. The feature, reported by Giesen *et al.*, has been observed in these 2PPE experiments as well. But in 1PPE a feature at the same final state energy occurred as well. Thus, the feature in 2PPE does not originate from an unoccupied state. Pawlik *et al.* assigned the feature to a resonant transition between occupied and unoccupied Ag-*sp* bands in the vicinity of the L point as indicated by light and dark magenta arrows in Fig. 4.40 (a). The corresponding pump-probe mechanism in 2PPE for different photon energies is depicted in Fig. 4.40 (c). This reflects the experiments of Giesen *et al.*. The dispersion of both bands with an opposite curvature causes an energy shift of the final state similar to the photon energy difference. With increasing photon energy the final state energy shifts to higher values accompanied with a downshift of the initial state energy. The virtual intermediate state pretends an unoccupied state as indicated by the dotted line. Thus, the band structure in  $k_{\perp}$  direction has to be considered in 2PPE experiments as well. The influence of the concrete experimental conditions on the *sp*-band transitions on Ag(111) has been reported by Winkelmann *et al.* [24], recently.

With decreasing photon energies the wave vector of the *sp*-band transition approaches the L point as indicated by the blue arrow in Fig. 4.40,(a). Here the



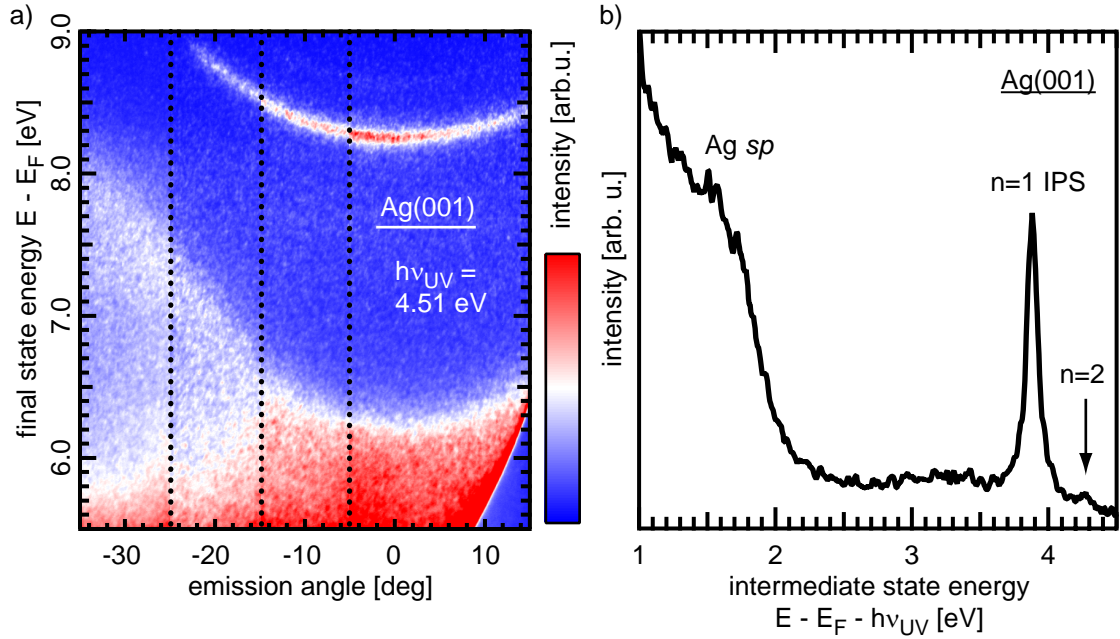


**Figure 4.41:** (a) Angle-resolve monochromatic-2PPE spectra of Ag(001) with respect to the final state energy. In angular direction four different measurements have been assembled as indicated by the dotted lines. The dispersing feature at 8.3 eV (at  $0^\circ$ ) originates from the  $n=1$  IPS. The increased intensity up to 6.3 eV (at  $0^\circ$ ) corresponds to the lower Ag- $sp$  band above  $E_F$ . (b) 2PPE spectrum at an emission angle of  $0^\circ$  with respect to the intermediate state energy. The  $sp$  band spans up to 2 eV.

energy of the unoccupied  $sp$  is below the vacuum level. Thus, a 2PPE experiment with such photon energies addresses the unoccupied  $sp$  band as an intermediate state. This has been reported by Hao *et al.* [25] for the Cu(111) surface, recently.

The Ag(001) surface orientation investigated here determines the  $\Gamma X$  direction as the corresponding  $k_\perp$  direction in photoemission. The occupied  $sp$  band crosses the Fermi level as can be seen in Fig. 4.40 (a). The orange arrow indicates an optical transition between the  $sp$  bands. The energy of this transition is larger than 8 eV (experimentally  $\sim 10$  eV has been determined [123]). Thus, resonant transitions between these bands are not expected at the Ag(001) surface with the laser setup used here ( $h\nu \leq 5$  eV). However, the spectroscopy of the unoccupied fraction of the lower  $sp$  band above  $E_F$  is accessible in 2PPE. Figure 4.41 (a) shows angle-resolved 2PPE data of bare Ag(001) with respect to the final state energy. The well-known IPS is found as a dispersing feature at an energies of 8.3 eV. The non-resonantly excited lower  $sp$  band leads to a higher 2PPE intensity up to 6.3 eV. This energy position determines the lower edge of the band gap of the projected band structure of Ag(001) at the  $\bar{\Gamma}$  point. The angle-resolved image reveals the theoretically expected dispersion of this edge in  $k_\parallel$  direction [109]. Figure 4.41 (b) shows a normal emission 2PPE spectrum with respect to the intermediate state energy. The  $sp$  band edge is found at 2.0 eV. This is in good agreement with the theoretical prediction (energy of the lower  $sp$  band at X point in Fig. 4.40 (a)) and IPE data of Giesen *et al.* [68].

In the following sections the observation of features which originate from electron transitions in the band structure of the Ag substrate will be discussed. The

NiO overlayer influences the accessible wave vectors perpendicular to the surface ( $k_{\perp}$ ) which changes the effective projected band structure for photoemission from Ag(001).

#### 4.4.2 Ag-*sp* band resonance – surface-assisted umklapp process at the NiO monolayer

In the following feature B in the 2PPE spectra of the NiO monolayer (see Fig. 4.26 on page 61) will be discussed and it will be shown that it originates from a resonant transition between occupied and unoccupied Ag-*sp* bands. The results will be compared with other experimental and theoretical work.

The intermediate state energy of the feature B is independent of the probe photon energy ( $h\nu_{IR}$ ). Thus, the observed feature originates from an unoccupied electronic state above the Fermi level. In contrast, the intermediate state energy depends linearly on the pump photon energy. The energy shift correlates with  $\sim 0.6$  times the change of the photon energy. This leads to a non-integer slope of 0.59 of the pump photon energy dependent peak position of the feature B (see Fig. 4.27 on page 62). This implies that the peak position is influenced by the dispersion of the initial as well as the intermediate state. As shown in section 4.4.1 a resonant excitation between two dispersing bands influences the photon energy dependent peak position in the 2PPE spectrum. The exact dependency is related to the relative dispersion of both bands. Note that a dispersion in  $k_{\perp}$  direction is necessary to explain the experimental observation. Therefore, the electronic states of the NiO monolayer are not responsible for the feature B because of its two-dimensionality<sup>36</sup>. As shown in the previous section the projected band structure of Ag(001) at the  $\bar{\Gamma}$  point does not exhibit bands where resonant transitions in the given energy range are possible. It will be shown that the 2PPE feature originates from a resonant transition between Ag-*sp* bands in the vicinity of the L point.

The  $(2\times 1)$  reconstruction of the NiO monolayer changes the surface Brillouin zone (SBZ) as depicted in Fig. 4.42 (a) where a top-view of the bulk Brillouin zone (BZ) of the fcc lattice is shown (compare with the 3D illustration of Fig. 4.43 (a)). The projected  $(1\times 1)$  SBZ of the Ag substrate is shown by the black dashed square. The  $(2\times 1)$  reconstruction leads to a smaller SBZ as indicated by the green solid rectangle. The green dotted rectangle represents the  $(2\times 1)$  SBZ which is shifted by a reciprocal lattice vector  $G_{(2\times 1)}$ . The center coincides with the  $\bar{X}$  point, which again coincides with the L point of the bulk BZ. Thus, the surface reconstruction of the NiO monolayer leads to a back folding of the  $\bar{X}$  to the  $\bar{\Gamma}$  point (umklapp process). Thus, transitions with projected wave vectors at  $\bar{X}$  contribute to the signal in normal photoemission after the umklapp to  $\bar{\Gamma}$ . All possible wave vectors of this projection coincide with the red line in the bulk BZ of the fcc lattice shown in Fig. 4.43 (a) ( $[001]$  projection through  $\bar{X}$ ). In the following this projection will be called " $[001]_{\bar{X}}$  projection". The gray shaded area highlights the common plane of the reciprocal high symmetry directions  $\Gamma X$ ,  $\Gamma K$ , and  $\Gamma L$ . To illustrate the consequences of the surface assisted umklapp process the Ag band structure (from [109]) is shown in Fig. 4.43 (b) in a three-dimensional plot. Two dimensions represent the common plane of  $\Gamma X$ ,  $\Gamma K$ , and  $\Gamma L$  (the gray shaded area corresponds to the one of (a)). The third

<sup>36</sup>In a 2D system no dispersion in the remaining third dimension is possible.

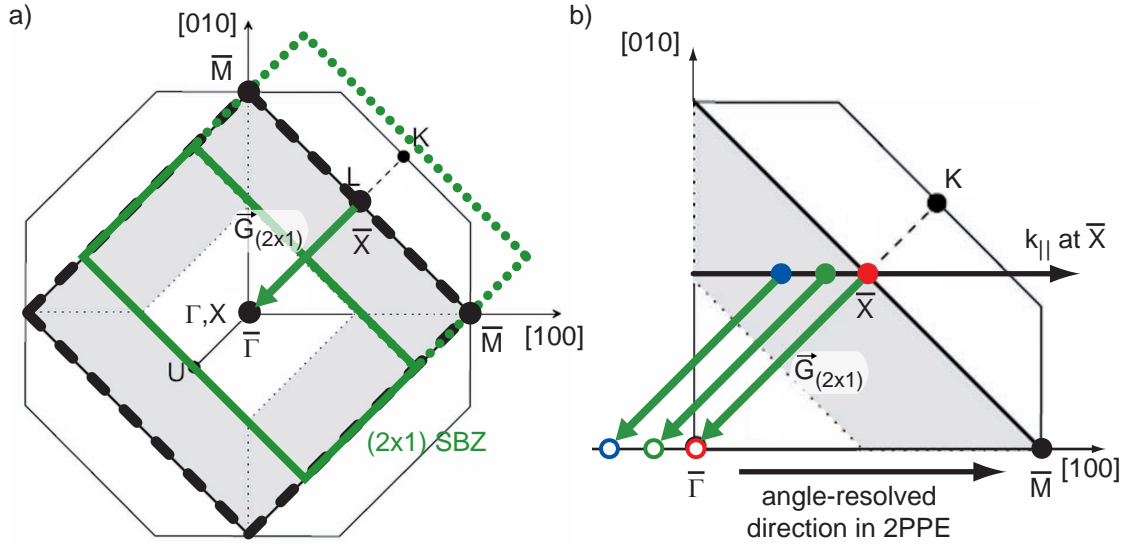


**Figure 4.42:** (a) Projected surface-Brillouin zone (SBZ) of the (001) surface orientation of the fcc lattice (adopted from [110], 3D Brillouin zone see Fig. 4.43 (a)). The (1x1) Ag SBZ is shown as black dashed line. The (2x1) reconstruction of the NiO monolayer leads to a (2x1) SBZ as indicated by the green solid line. The center of the first extended (2x1) SBZ (green dotted line) coincides with the  $\bar{X}$  point. Upon photoemission the reciprocal lattice vector  $\vec{G}_{2\times 1}$  allows for a back folding of the  $\bar{X}$  to the  $\bar{\Gamma}$  point. (b) Enlarged region of (a) where the red, green, and blue dots indicate projections of the Brillouin zone which are, after back folding, observable in  $k_{||}$  along the  $\bar{\Gamma}\bar{M}$  direction.

dimension represents the energy. The occupied  $d$ -bands below  $E_F$  are depicted as thin lines whereas the occupied and unoccupied  $sp$ -bands are emphasized as thicker lines. The different colors correspond to the different high symmetry directions. The red arrow indicates again the  $[001]_{\bar{X}}$  projection similar to (a).

Christensen calculated in addition to the band structure of the high symmetry directions the band structure of single points within the Brillouin zone to achieve a 3D data set [109]. This is used to estimate the band structure of the  $[001]_{\bar{X}}$  projection, i.e., the band structure in the yellow shaded area of the 3D illustration in Fig. 4.43 (b). The red dots in Fig. 4.43 (c) show the calculated points of Christensen along the  $[001]_{\bar{X}}$  projection. The black lines indicate the parabolic approximations of both bands according to

$$E[\text{eV}] = E_0[\text{eV}] + \frac{3.810}{m_{eff}[m_e]} k^2[\text{\AA}^{-2}] \quad (4.16)$$

where  $E_0$  is the energy at the band minimum/maximum,  $k$  the wave vector, and  $m_{eff}$  the effective electron mass in units of the free electron mass  $m_e$ . Values of  $m_{eff,occ} = -1.32$  and  $m_{eff,unocc} = 0.29$  for the occupied and unoccupied band have been determined, respectively. The different signs account for the opposite curvatures. This is similar to the properties of the bands in  $\Gamma L$  direction as described in section 4.4.1 at the Ag(111) and Cu(111) surfaces. The arrows indicate optical transitions between both bands with the given photon energies. This is used to de-

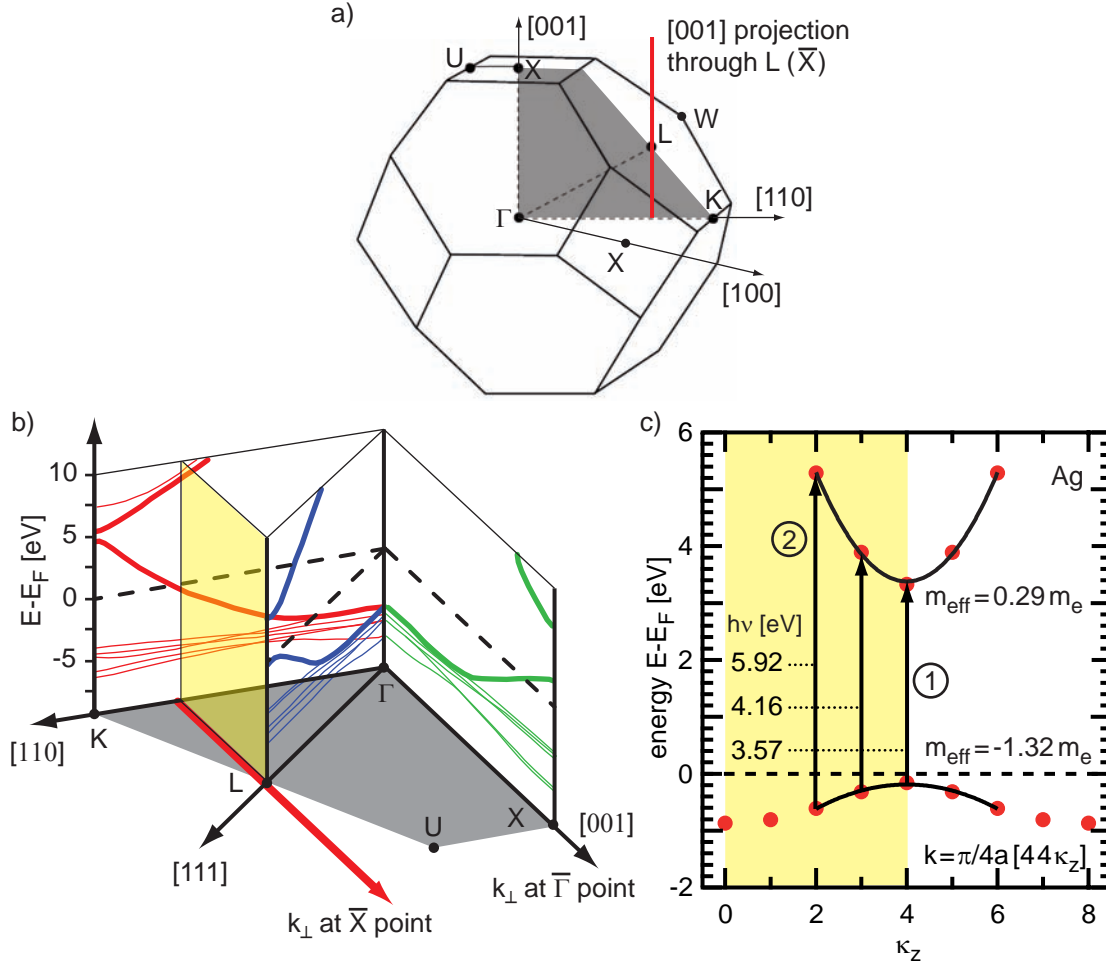


**Figure 4.43:** (a) Brillouin zone of the fcc lattice and the corresponding high-symmetry points (adopted from [110]). The red line indicates the projection through the L point with respect to the (001) surface (called  $[001]_{\bar{X}}$  projection). The gray shaded area marks the common plane of the  $\Gamma X$ ,  $\Gamma K$ , and  $\Gamma L$  directions. (b) Three dimensional illustration of the band structure of Ag along symmetry lines of the gray shaded area of (a). The yellow shaded area indicates the region (E vs. k) which corresponds to the projection through L ( $\bar{X}$ ). Transitions at these wave vectors will be observed at the  $\bar{\Gamma}$  point due to the surface assisted umklapp process. (c) Band structure of Ag along the projection through the L point [109] (wave vectors with  $\kappa_z > 4$  are beyond the Brillouin zone).

termine the photon energy dependent energy of the intermediate state upon optical transitions. The transition ① in Fig. 4.43 (c) leads to

$$h\nu_1 = E_g \quad (4.17)$$

with the energy gap  $E_g$  at the L point. With the parabolic approximation of equation 4.16 the transition ② defines

$$h\nu_2 = E_g + \frac{3.81}{m_{eff,unocc.}} k^2 - \frac{3.81}{m_{eff,occ.}} k^2 . \quad (4.18)$$

Rearranging the difference between both equations leads to

$$s = \frac{\Delta E_{intermediate}}{\Delta h\nu} = \frac{m_{eff,occ.}}{m_{eff,occ.} - m_{eff,unocc.}} \quad (4.19)$$

where  $s$  describes the linear slope of the intermediate state energy in dependence of the photon energy. Thus, the calculations of Christensen predict a photon energy dependent transition into the unoccupied  $sp$  band with a linear slope of 0.81. From the 2PPE data as shown in section 4.3.2 (Fig. 4.27 on page 62) a slope of 0.59 for the photon energy dependent position of the unoccupied  $sp$ -band is observed.

To rate this discrepancy Fig. 4.44 summarizes theoretical as well as experimental results of the Ag- $sp$  bands at the L point in a similar plot as Fig. 4.43 (c)<sup>37</sup>. The calculation of Christensen and the parabolic approximation is shown by black symbols/lines. The open blue squares show the theoretical results of Eckhardt *et al.* [118]. The position of the band bottom of the unoccupied band agrees well in both calculations. The experimental results are shown by solid symbols, respectively. Note that at the data points c and f different methods lead to same energy of the bands. However, theory underestimates the energy of the unoccupied  $sp$  band. This is a hint to an insufficient accuracy of the theoretical description. Beyond the L point the dispersion of the band is given by the effective masses and the energy at the band bottom. Since the  $[001]_{\bar{x}}$  projection in 2PPE does not enable to determine the  $k_{\perp}$  of the initial and intermediate state, the exact dispersion can not be extracted. However, the band gap of Ag at the L point can be determined to  $4.18 \pm 0.05$  eV. This value is given by the UV photon energy of the 2PPE spectrum where the minimum intermediate state energy of the Ag- $sp$  resonance is observed. This assumption is reasonable because the band gap of the occupied and unoccupied Ag- $sp$  bands has its minimum at the L point [109]. This leads to energies of the occupied and unoccupied states at the L point of  $-0.26 \pm 0.05$  eV and  $3.92 \pm 0.05$  eV, respectively. These values are given by the calculated intermediate state energy for the transition at the L point. They are in good agreement with other experimental work obtained at the Ag(111) surface as summarized in Fig. 4.44. Here it should be noted that all experimental methods, including PES [112,124,125], IPE [126], reflection/transmission spectroscopy [127,128], and 2PPE agree within  $\pm 100$  meV. According to the discussion of section 4.3.6 the different electronic final states of the metallic substrate states lead to similar energies due to the small  $e-e$  and  $e-h$  interaction.

In addition to the characterization of the L gap, the photon-energy dependence of the feature B reveals the relative effective masses of both bands along the  $[001]_{\bar{x}}$  projection. According to equation 4.19 the relation of the two masses of both bands is determined by the linear slope of the photon energy dependent peak position of 0.59 and leads to  $m_{eff,occ.} = \frac{s}{s-1} m_{eff,unocc.} = 1.44 m_{eff,unocc.}$ . Assuming the occupied  $sp$  band with masses between  $-0.7$  and  $-1.3 m_e$  the corresponding dispersion of the unoccupied  $sp$  band is fully characterized. The corresponding bands along the  $[001]_{\bar{x}}$  projection are shown in Fig. 4.44 by magenta lines. The calculation of Christensen reveals a three-times larger relation between the masses of the two bands ( $m_{eff,occ.} = 3 m_{eff,unocc.}$ ). Thus, the theoretical description demands a renormalization of the band structure. Despite of these findings the similar electronic structure

<sup>37</sup>The L point is found at  $\kappa_z = 4$ .

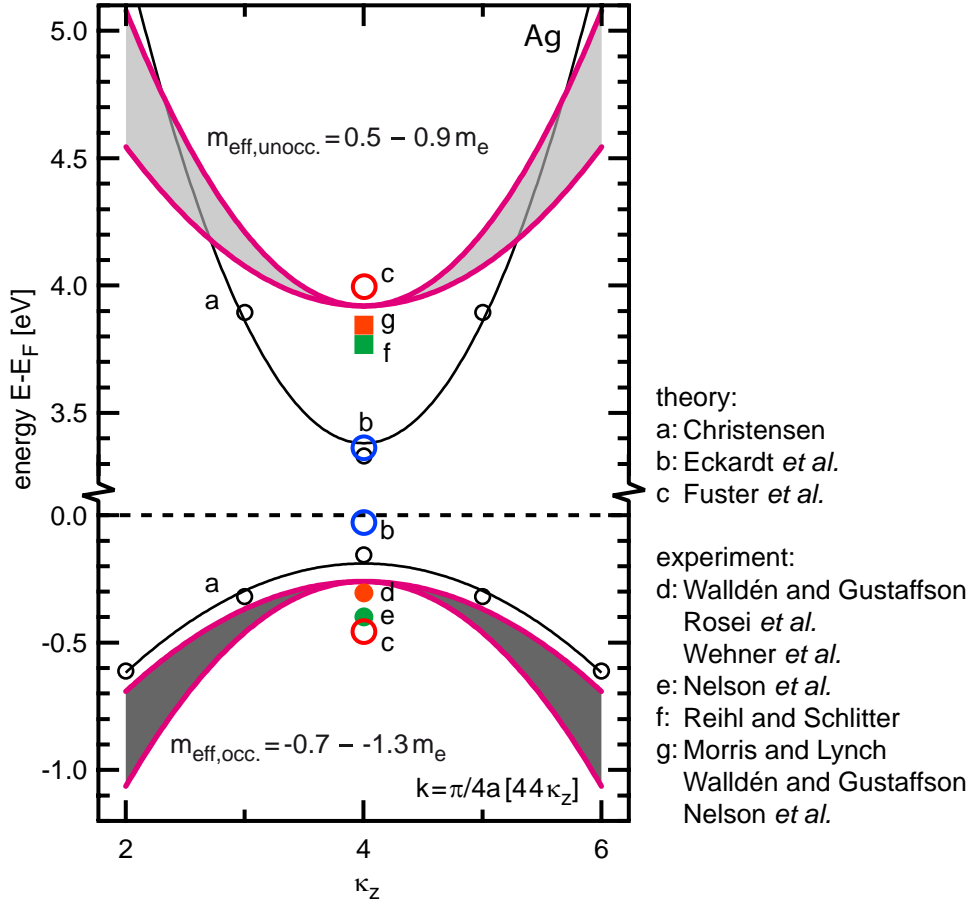


**Figure 4.44:** Band structure of Ag along the  $[001]_{\bar{x}}$  projection. The gray-shaded areas illustrate possible regions of the  $sp$  bands. Exemplary, the magenta lines indicate parabolic dispersions with effective masses of  $-0.7$  and  $-1.3$  for the occupied and  $0.5$  and  $0.9$  for the unoccupied band, respectively. These bands fulfill  $m_{eff,occ.} = 1.44 m_{eff,unocc.}$  (details see text). The magenta lines correspond to effective masses of  $0.7$  and  $1.3 m_e$  of the occupied  $sp$  band. For comparison, theoretical values of the band structure at the L point are shown: open black circles [109] (black lines show a parabolic approximation), open blue squares [118] and open red circles [119]. Experimental data of the occupied  $sp$  band [112,124,125,128] (solid circles) and the unoccupied band [124–127] (solid squares) at the L point are shown as well.

of Cu leads to similar results as observed here. The  $sp$  resonance at the L point of Cu(111) investigated with 2PPE has been reported by Hao *et al.* [25], recently. The intermediate state energy, i.e., the unoccupied Cu- $sp$  band disperses with a linear slope of 0.64 in dependence of the pump photon energy<sup>38</sup>. This value agrees well with the slope of 0.59 observed here<sup>39</sup>.

As already analyzed in section 4.3.2 the lifetime of the feature B has been determined in time-resolved 2PPE. A short lifetime of  $19 \pm 10$  fs has been observed. This means the 2PPE data reveal the lifetime of an electron in the transiently occupied

<sup>38</sup>A slope of 1.64 of the *final state* has been observed in monochromatic 2PPE [25].

<sup>39</sup>Note that the Cu(111) surface determines for the GL direction in  $k_{\perp}$ .

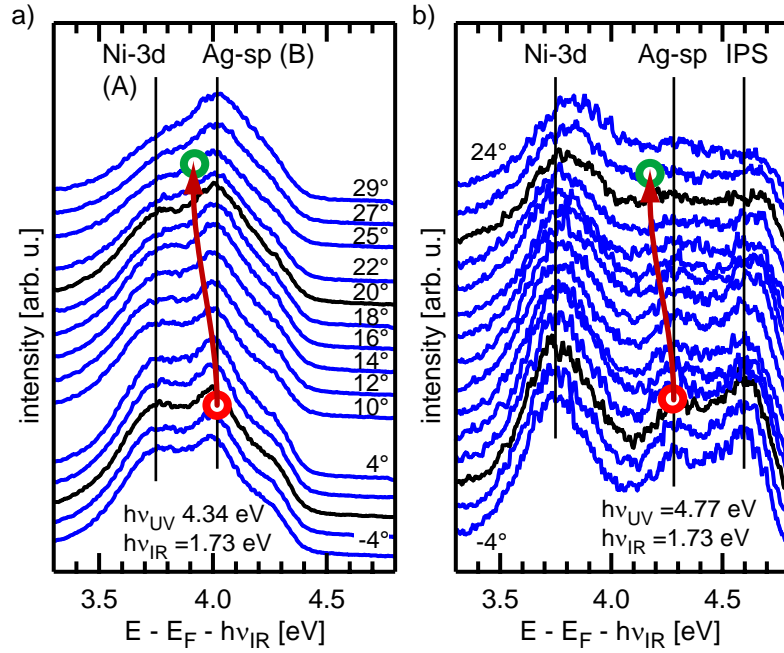


**Figure 4.45:** (a) Angle-resolved 2PPE of the NiO monolayer for  $h\nu_{UV}=4.34$  eV (pump) and  $h\nu_{IR}=1.72$  eV (probe) between  $-4^\circ$  and  $29^\circ$  and (b) for  $h\nu_{UV}=4.77$  eV (pump) and  $h\nu_{IR}=1.72$  eV (probe) between  $-4^\circ$  and  $24^\circ$  ( $+2^\circ$  between each). The black curves in both diagrams correspond to  $0^\circ$  and  $20^\circ$ , respectively. The vertical lines indicate the peak positions at  $0^\circ$ . The red and green circles indicate the expected dispersion at  $k_\perp=0$  and  $k_\perp=0.19\text{\AA}^{-1}$  from theoretical calculations [109] (compare inset of Fig. 4.46 (b)).

Ag-*sp* band at 4.15 eV in the vicinity of the L point<sup>40</sup>. As shown in Fig. 4.30 (b) this value is similar to the lifetime of the Ni-3*d* state at 3.7 eV which might influence the time-dependent intensity in this analysis due to its large energetic width. But due to the higher intensity of the Ag-*sp* resonance the determined lifetime of 19 fs is significant enough to exclude any artifact of the data analysis<sup>41</sup>.

To analyze the dispersion, angle-resolved 2PPE spectra at different emission angles are shown in Fig. 4.45 (a) and (b) with respect to the intermediate state energy (photon energies as indicated). The black spectra in both images correspond to emission angles of  $0^\circ$  and  $20^\circ$ , respectively. The vertical lines indicate the peak positions of the Ni-3*d* state, the IPS, and the Ag-*sp* resonance at an emission angle of  $0^\circ$ . The spectra reveal an angle-dependent energy position of the Ni-3*d* state and the IPS. The energy shift of the IPS is not well resolved due to the excitation limit of the UV photon energy. But the intensity decreases drastically with increasing emission angle which is interpreted by the dispersion of this state. The position of the Ag-*sp* resonance is independent of the emission angle and thus no dispersion is observed. Note that at an emission angle of  $30^\circ$ , the *sp* resonance is observed up to a  $k_\parallel$  of  $0.3\text{\AA}^{-1}$ . To compare this result with theory the band structure along the corresponding directions in the BZ is necessary. The surface-assisted umklapp

<sup>40</sup>This band has the commonly used symmetry label  $L_6^+$

<sup>41</sup>Compare with the discussion in section 4.3.2 where the time-dependent intensity of the featureless background is dominated by the Ni-3*d* state due to its large energetic width.

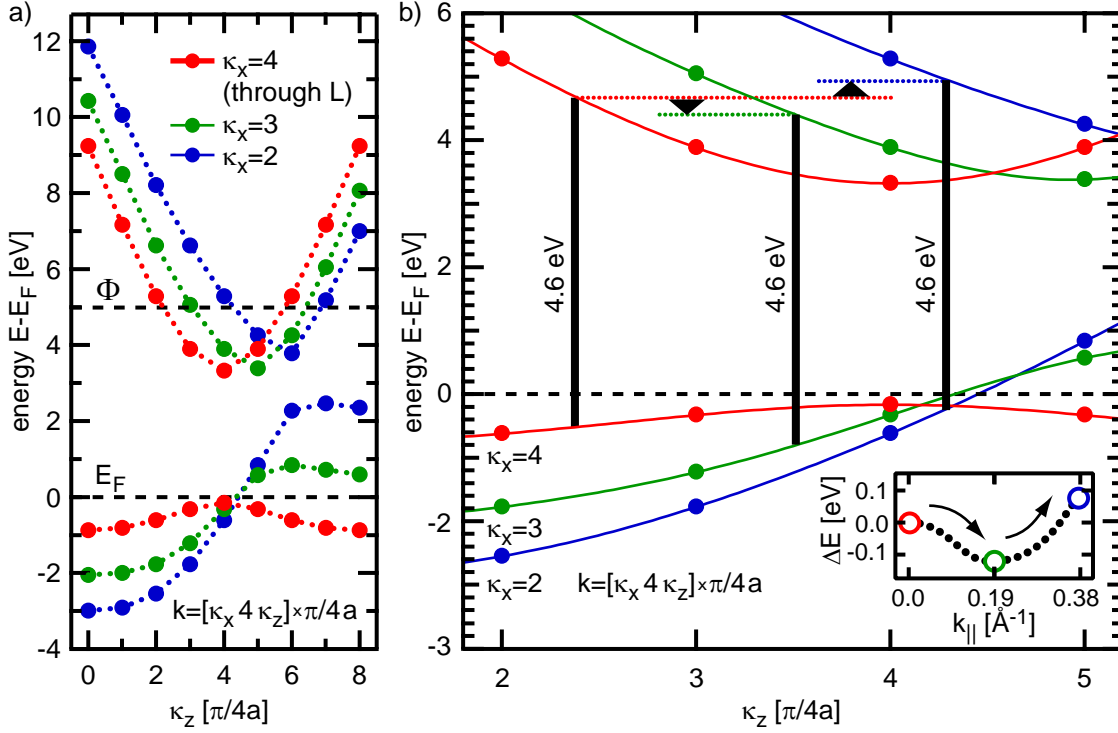


**Figure 4.46:** (a) Band structure of Ag at selected reciprocal lattice points  $\frac{\pi}{4a} (k_x, 4, k_z)$ . The red, green, and blue curves correspond to different  $k_{\perp}$  directions of the (001) surface as indicated in Fig. 4.42 (b), which are back folded to the  $\bar{\Gamma}$  point due to surface reconstruction. (b) shows an enlarged region of (a). For the interpolation between the discrete data points, a 8<sup>th</sup> order polynomial fit has been applied as shown by the red, green, and blue lines, respectively. The black vertical lines indicate optical transitions between occupied and unoccupied bands with the same photon energy. The energy differences between the populated intermediate bands are indicated by arrows which would lead to a dispersion of the state in AR-2PPE as depicted in the inset.

process described above is realized for all transitions within the BZ, where the experimental setup selects certain projections. Figure 4.42 (b) (on page 87) shows an enlarged region of the projected SBZ shown in (a). The angle-resolved direction in the experiment coincides with the  $\bar{\Gamma}\bar{M}$  direction. This geometry determines the wave vectors of the *sp*-band transitions as shown by green and blue filled circles, which are relevant for the interpretation of angle-resolved 2PPE data. After the umklapp process the transitions at these wave vectors are observed in the vicinity of the  $\bar{\Gamma}$  point as indicated by green and blue open circles, respectively.

The theoretical calculations of the band structure in  $k_{\perp}$  direction for the fixed  $k_{\parallel}$  values marked in Fig. 4.42 (b) (page 87, red, green, and blue points close to  $\bar{X}$ ) are shown in Fig. 4.46 (from [109]). The red, green, and blue bands correspond to the  $k_{\parallel}$  values within the SBZ. To get information about the predicted dispersion of the bands an enlarged region of (a) is shown in Fig. 4.46 (b). For the interpolation between the discrete points a polynomial fit (up to  $\kappa^8$ ) has been applied as shown by the solid lines. For a given pump photon energy the transition between the occupied and the unoccupied band is possible, where the energy difference be-



tween both bands matches the photon energy. This is depicted exemplary for 4.6 eV (vertical black bars). For each pair of bands (red, green, and blue) the transition is realized at different values of  $\kappa_z$ . Starting from the transition between the red bands (back folded to  $\bar{\Gamma}$ ) the energy position of the intermediate state shifts, at first, to lower values for the green and than to a higher values for the blue bands, respectively, as indicated by the horizontal dotted lines and the arrows in between. According to this, an energy shift of  $\geq 100$  meV within  $k_{\parallel}$  of  $0.2 \text{ \AA}^{-1}$  should be observed in an angle-resolved measurement as depicted in the inset of Fig. 4.46 (b). This theoretically expected relative energy shift in dependence of  $k_{\parallel}$  is indicated in the angle-resolved data of Fig. 4.45 (a) and (b) as red green circles, respectively (the circles do not indicate the theoretical energy positions!)<sup>42</sup>. This leads again to a disagreement between theory and experiment, where no dispersion is observed in Fig. 4.45 within the corresponding  $k_{\parallel}$  region. Note that the considerations about the expected dispersion from the theoretical calculations do not include the density of states (DOS) and the transition matrix elements. The highest DOS is expected for the red bands. Thus, these transitions should dominate the photoemission spectrum. However, this dominance refers only to the observed photoelectron intensity. The contributions from the green and blue bands at  $k_{\parallel} \neq 0$  might be smaller, but, nonetheless the energy shift should be present. The DOS determines only the observability of that shift. Even if the DOS of the green and blue occupied bands is negligibly small with respect to the red band, the transition between the latter one should not dominate the electron intensity at larger  $k_{\parallel}$  values. Therefore, it is most likely that the corresponding band structure in the observed  $k$  region does not match the theoretical prediction.

To clarify the deviations between theoretical predictions and the experimental observations presented here, more investigations concerning that issue are necessary. At first, a new set of theoretical calculations which is able to describe the L gap more precisely is highly demanded for a better comparison with the experimental data. A new approach would change the data along the  $[001]_{\bar{x}}$  projection as well. Secondly, the 2PPE measurements should be extended to probe-photon energies in the UV range to span a larger  $k_{\parallel}$  region. This would help to distinguish between the influence of the density of states and the pure band dispersion.

### 4.4.3 Umklapp process mediated by antiferromagnetic NiO(001)

In this section features in multi-photon photoemission spectra of 4 and 8 ML NiO films are analyzed in terms of spectroscopy of Ag bulk bands via the NiO overlayer. In the first part monochromatic multi-photon photoemission processes (multi-PPE) with photon energies in the IR range will be discussed. The possibly involved states, namely the IPS and Ag-*sp* bands will be discussed. According to the findings in the previous section, the possibility of a surface-assisted umklapp process of Ag-*sp* bands will be depicted. This interpretation will be used in the second part of this section, to review the bichromatic 2PPE data of 4 and 8 ML NiO films of section 4.2.5. An Ag-*sp* resonance, can explain an otherwise not assigned photoemission feature as well.

<sup>42</sup>The corresponding  $k_{\parallel}$  value of  $0.19 \text{ \AA}^{-1}$  in the given energy range is given at  $25^\circ$  in Fig. 4.45 (a) and at  $22^\circ$  in (b).

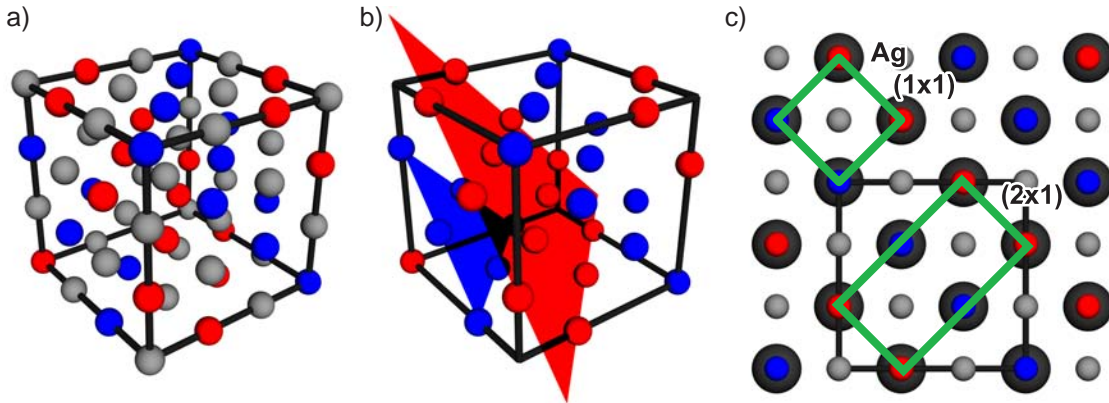


**Figure 4.47:** Sphere model of 4ML of NiO with its antiferromagnetic ordering (AF2 type). (a) A  $(4 \times 4 \times 4)$  ML<sup>3</sup> cell of NiO where the gray spheres indicate the O<sup>2-</sup> ions and the red and blue spheres the Ni<sup>2+</sup> ions with opposite magnetic moment, respectively. The spins are oriented within the (111) plane and antiparallel oriented with respect to the neighboring (111) plane [129]. (b) Only Ni<sup>2+</sup> ions of (a) with two (111)-oriented lattice planes of alternating magnetic moments. (c) Topview of 4ML NiO on the topmost Ag layer (black spheres). The black lines indicate the cell of (a). Due to the magnetic ordering a  $(2 \times 1)$  reconstruction with respect to the Ag substrate is formed. Note the Ni<sup>2+</sup> ions of the first layer are on Ag-fcc sites which are not visible due to the O<sup>2-</sup> ions above.

With increasing film thickness of NiO the atomic structure approaches the bulk structure. Thus, the well-known antiferromagnetic ordering of NiO is favored [129]. Alteri *et al.* reported a Néel temperature of 390 K for a 3 ML NiO film on Ag(001) by analyzing temperature-dependent X-ray absorption spectroscopy (XAS) [130]. This value is below the Néel temperature of 525 K for bulk NiO [131]. However, it shows that the 3 ML NiO film exhibits the antiferromagnetic ordering at a temperature sufficiently above room temperature. Figure 4.47 (a) shows a model of NiO (thickness of 4 ML) with an antiferromagnetic order of type AF2. The red and blue spheres indicate the Ni<sup>2+</sup> ions with opposite magnetic moment. The spins are oriented within the (111) plane and are antiparallel aligned with respect to the adjacent (111) plane [129]. The gray spheres indicate the O<sup>2-</sup> ions. To highlight the antiferromagnetic ordering the same structure is shown in Fig. 4.47 (b) where the oxygen ions have been omitted. The planes of Ni<sup>2+</sup> ions with equivalent magnetic moment are indicated by red and blue triangles, respectively. In Fig. 4.47 (c) a top-view of 4 ML NiO on Ag(001) is depicted, where the Ag atoms are indicated by the larger black spheres. The corresponding  $(1 \times 1)$  unit cell of the Ag substrate is shown by the green square. In the lower part the boundary of the cell from (a) is shown by the black square. Each Ni<sup>2+</sup> ion of the top-most layer coincides with one Ag atom<sup>43</sup>, as expected for pseudomorphic growth [47,53,132]. The antiferromagnetic ordering implies a  $(2 \times 1)$  magnetic unit cell due to the existence of two inequivalent Ni<sup>2+</sup> ions of opposite magnetic moments as shown by the green rectangle. The  $(2 \times 1)$  superstructure leads to the observation of half-order spots in LEED as reported for bulk

<sup>43</sup>Note that Ni<sup>2+</sup> ions of the first layer are in the corresponding fcc sites of the Ag(001) substrate, i.e., below the oxygen ions of the 4<sup>th</sup> layer.

NiO(001) in the literature e.g., by Palmberg *et al.* [133] and Hayakawa *et al.* [134], which can be explained by exchange reflexion. The observation of half-order spots in the LEED pattern could not be verified in the present study<sup>44</sup>. The absence of the half order LEED spots could be explained by the low signal to background ratio. Palmberg reported for bulk NiO an intensity ratio of only 2-6% compared to the intensity of the main LEED reflections [133]. This suppresses the observation of these low intensity spots at the grown NiO film. On the other side the typical electron energies for the LEED investigations here were  $>60$  eV. This is in contrast to the typically used  $\sim 30$  eV reported in the literature. An energy dependent cross section is expected, anyway<sup>45</sup>, and might explain the missing reflections here. Comparable to the discussion in the previous section, the antiferromagnetically induced ( $2\times 1$ ) unit cell of the NiO overlayer might mediate a surface-assisted umklapp process as well.

### Multi-photon photoemission of NiO films on Ag(001)

Using photon energies in the IR range and sufficiently high pulse energies, it is possible to observe features which originates from 3PPE as well as 4PPE processes. In Fig. 4.48 (a) multi-PPE spectra of 4 ML NiO, taken at normal emission are shown

<sup>44</sup>Note in addendum after submission: The half order LEED reflections could be verified for a 150 ML NiO film using electron energies of 30 eV.

<sup>45</sup>The LEED-IV characteristic is not only determined by the interference of the diffracted electron waves. The cross section of the diffraction depends on the electron energy as well.

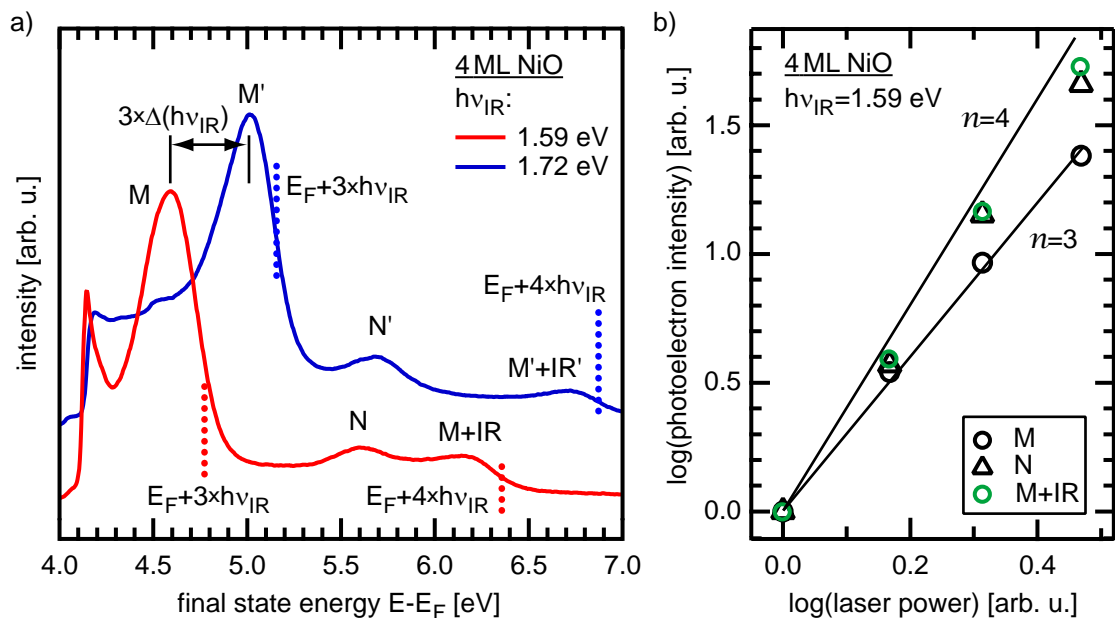


**Figure 4.48:** (a) Monochromatic 2PPE spectra of 4 ML NiO/Ag(001) using different IR photon energies. Three features M, N, and M+IR are observed where M+IR is the corresponding feature of M with an additional absorbed photon. The dotted lines indicate the 3PPE and 4PPE excitation limit from  $E_F$ . (b) Bilogarithmic plot of the photoelectron intensity with respect to the laser power of features M, N, and M+IR. The black lines indicate a linear slope of  $n=3$  and  $4$ , respectively.

with respect to the final state energy ( $E-E_F$ ). The IR photon energies has been adjusted to 1.59 (red spectrum) and 1.72 eV (blue spectrum), respectively. In the red spectrum three features M, N, and M+IR are evident at 4.60, 5.60, and 6.17 eV, respectively. The energy difference between M and M+IR is 1.57 eV, similar to the photon energy determined with the optical spectrometer. Thus, the electrons observed at M+IR originates most likely from the same state which leads to feature M, excited with one additional absorbed IR photon. This means that the M+IR feature corresponds to an above-threshold photoemission (see discussion below). The blue spectrum also shows three features namely M', N', and M'+IR'. They are located at 5.00, 5.70, and 6.73 eV, respectively. An energy difference of 1.73 eV between feature M' and M'+IR' is observed, which corresponds to the applied photon energy as well. Regardless of any intermediate states, the final state energy of all observed features requires at least a three- or four-photon absorption to excite electrons from occupied states. The three and four photon excitation limits are indicated by the dotted red and blue lines, respectively. To investigate the number photons involved in the multi-PPE process, laser power dependent spectra has been recorded with pulse energies between 45 and 130 nJ (25–30 fs). The intensities of all features in dependence of the laser power are shown in Fig. 4.48 (b) on a double-logarithmic plot. To discriminate between the three or four photon photoelectron emission the well-known relationship is used

$$I = A \times P^n \implies \log(I) = n \times \log(P) + \log(A) \quad (4.20)$$

where  $I$  is the photoelectron intensity,  $A$  the proportionality factor, and  $P$  the applied laser power. The integer number  $n$  determines the slope of the intensity curve in this plot and reveals the number of photons involved in the photoemission

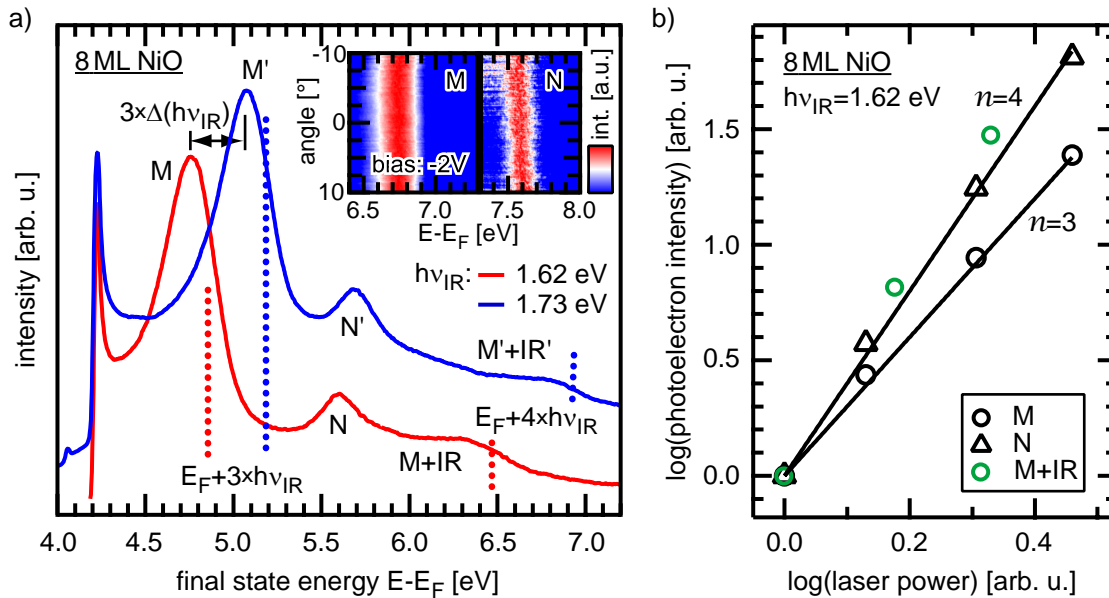


**Figure 4.49:** Same as Fig. 4.48 for 8 ML NiO/Ag(001) (photon energies as indicated). The inset of (a) shows the angle-resolved data for  $h\nu_{IR}=1.62$  eV at a bias voltage of -2 V. The intensity has been normalized for each angular profile within the energy range for feature M (left) and feature N (right).

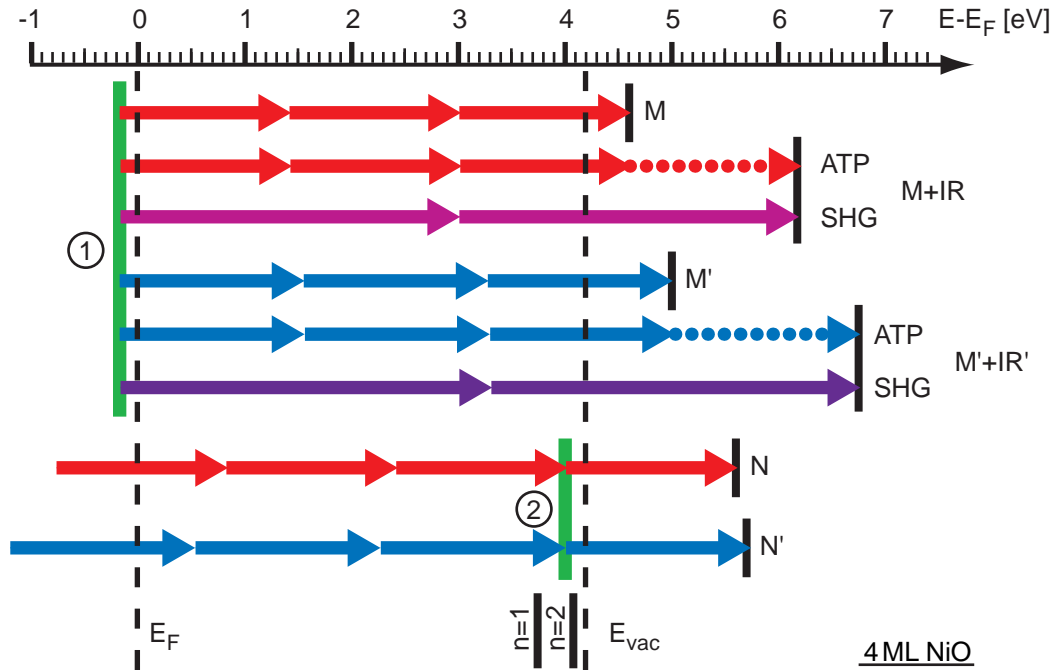


**Figure 4.50:** Energy diagram for 3PPE and 4PPE at 4ML NiO. The red and blue arrows indicate the photon energy of 1.59 and 1.72 eV, respectively. An occupied state ① at -0.17 eV and an unoccupied state ② at 3.98 eV, as shown by green lines, lead to the features M, N, and M+IR in multi-PPE spectra of Fig 4.48 (a). The M+IR feature correspond to an above-threshold photoemission (ATP). The expected positions of the IPS  $n=1$  and  $n=2$  are indicated by black lines (see section 4.2.5).

process. The solid black lines indicate a linear dependence with a slope of  $n=3$  and  $n=4$ , respectively, according to a three- or four-photon photoemission process (3PPE and 4PPE). For the feature M a perfect agreement with a slope of  $n=3$  is observed. This means that the feature M originates from a 3PPE process. For the other states N and M+IR a slope of  $\sim 3.7$  is observed. These features are interpreted as 4PPE processes. The deviation of the slope to the expected value of  $n=4$  is explained by experimental error since the laser fluctuations (intensity as well as pulse length) have a stronger influence to the 4PPE process as compared to the 3PPE one.

Analogical measurements have been recorded for a 8 ML film as shown in Fig. 4.49 (a). The red and blue curves show the multi-PPE spectra for 1.62 and 1.73 eV, respectively. The shape of the spectra is comparable to the ones obtained at the 4 ML NiO film showing all three features M, N, and M+IR. Similar to the 4 ML film the photon energy dependence of the feature M shows a shift of  $3 \times \Delta(h\nu_{IR})$ , whereas the feature N shifts with  $1 \times \Delta(h\nu_{IR})$ . The laser power dependent intensities of all features are shown in Fig. 4.49 (b) using pulse energies between 90 and 250 nJ (25–30 fs). A good agreement with expected 3PPE and 4PPE dependencies is observed as indicated by the solid black lines.

Figure 4.50 shows the energy diagram for the electron transitions of the 4 ML film discussed above. The final state energies of the features M (M'), N (N'), and M+IR (M'+IR') are indicated by black lines. For each feature the number of involved photons and the photon energy dependent shift is known. This leads to the pump

probe mechanisms according to the two different photon energies as shown by the red and blue arrows, respectively. The scheme for the feature M reveals an occupied state ① at  $-0.17 \pm 0.02$  and  $-0.16 \pm 0.02$  eV for the feature M and M', respectively. According to this the feature M+IR originates from that initial state as well, but an additional photon is involved in the photoemission process. Note that the feature M+IR can be used to determine the *exact* photon energy with a higher accuracy. This decreases the experimental error in comparison to the values of the optical spectrometer. The approaching bulk-like properties of the NiO film  $\geq 4$  ML reveal the expected electronic structure. The highest occupied states originating from the  $d^8 \rightarrow d^8 L^{-1}$  transition have been determined at  $\sim 2$  eV below  $E_F$  in UPS (see Fig. 4.3 on page 27) and at 1.8 eV below  $E_F$  in 2PPE (see feature Q in Fig. 4.37 on page 75). Thus, the observed feature close to the Fermi level in multi-PPE spectra has to originate from the Ag(001) substrate.

The feature M has two reasonable origins. At first a possible interface state between the Ag(001) substrate and the NiO film develops. This would be surprising, because the existence of an interface state in this energy region has been neither reported in the literature nor observed with UPS or STS. However, experiments with similar excitation energies (multi-PPE with IR photon energies) and energies of the excited photoelectrons ( $\sim 1$  eV) have never been investigated so far. On the one side, the cross section of photons in this energy might be increased in comparison to typically used energies for UPS. This would lead to a higher photoemission signal. On the other side a change of the mean free path of the excited electrons is expected. Offi *et al.* reported the photon energy dependent attenuation length of low-energy electrons for the case of CoO/Ag(001) [135], recently. Values of  $>15$  ML for 5 eV electrons which tends to increase with decreasing electron energy have been reported. Similar values are expected for NiO/Ag(001) as well, due the similarities of both systems. Thus, the possible existence of an electronic state located at the interface of the Ag(001) and the NiO might be exclusively observable with multi-PPE due to the low energy of the excited photoelectrons. The second possibility of the origin of feature M is the observation of the Ag-*sp* band. With the same arguments as in section 4.4.2, the projected band structure of Ag(001) ( $\Gamma X$  direction) does not deliver such a sharp feature.

It remains to consider an umklapp process of the  $[001]_{\bar{X}}$  projection to the  $\bar{\Gamma}$  point. This is reasonable because the antiferromagnetic ordering of the NiO film enables the back folding due to its  $(2 \times 1)$  structure with respect to the Ag(001) substrate, as shown in the beginning of this section. Comparing the observed energies of the occupied state in multi-PPE with the energy of the occupied *sp* band at the L point<sup>46</sup> a good agreement within 100 meV is observed. This deviation is explained by space charge effects which shift the final state electrons to higher kinetic energies and therefore the calculated intermediate/initial state energies as well.

The multi-PPE spectra show besides the pronounced 3PPE feature, originating from an occupied state below  $E_F$ , the corresponding above-threshold photoemission (ATP) feature of the same state. This is indicated by the dotted arrows in the multi-PPE schemes of Fig. 4.50. The observation of ATP from metal surfaces has been observed at various metal surfaces e.g., polycrystalline Cu [137] and Au [138],

---

<sup>46</sup>The occupied and unoccupied *sp* band at the L point has been characterized at  $-0.26 \pm 0.05$  and  $3.92 \pm 0.05$  eV, respectively.

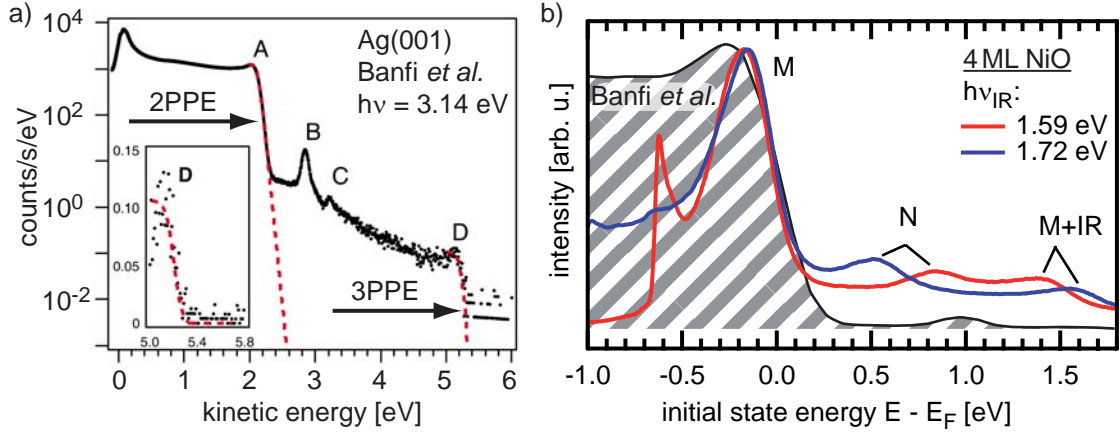


**Figure 4.51:** (a) Semilogarithmic plot of multi-PPE of Ag(001) adopted from Banfi *et al.* [136]. The label A and D indicates the 2 and 3PPE of electrons from the Fermi edge. The latter one corresponds to a ATP with  $\sim 10^{-4}$  less intensity than A. The 3PPE features B and C are assigned to IPS. (b) Comparison of multi-PPE of 4 ML NiO as shown in Fig. 4.48 (a) with the data of Banfi *et al.* on linear scale with respect to the initial state energy.

Pt(111) [139], and the (001) and (011) surfaces of Cu [140]. It has been found that the photoemission from the surface enhances the ATP process by more than four orders of magnitude compared to similar experiments in the gas phase. The ATP from Ag(001) has been reported by Banfi *et al.*, recently, as shown in Fig. 4.51 (a) [136]. Using a photon energy of  $\sim 3.1$  eV, 2PPE as well as 3PPE processes from the Fermi edge have been observed (labels A and D), where the latter one corresponds to the ATP because the 2PPE process enables to excite the electron above the vacuum level. Figure 4.51 (b) shows the multi-PPE spectra of 4 ML (red and blue spectra) together with the data of Banfi *et al.* (gray-striped spectrum) with respect to the initial state energy. Large differences between both measurements are evident. The gray-striped spectrum exhibits a homogeneous, almost constant intensity below the Fermi level with a small *feature* at  $-250$  meV. The spectrum agrees well with the the UPS data shown in Fig. 4.3 (page 27). In contrast to that a well defined feature *below*  $E_F$  is evident at the NiO data with a strong decrease of the intensity at lower energies. This difference reveal that the origin of the feature M is not due to the projected band structure of Ag(001) ( $\Gamma X$  direction in Fig. 4.40 on page 83).

Banfi *et al.* reported an intensity ratio of  $\sim 10^{-4}$  between the 2PPE and 3PPE (ATP) Fermi edge intensity [136]. This is far off from the value obtained here, where a ratio of 0.1 between 3PPE and 4PPE is observed. Note that the spectra in Figs. 4.48 (a) and 4.49 (a) are shown on linear scale, in contrast to Fig. 4.51 (a) (log scale). The origin of this discrepancy is not clarified yet. Of cause the photon energy here is by a factor of two smaller and has to be considered in the estimation of transition matrix elements. Additionally, the presence of the NiO film influences the photoemission process as well. However, Fann *et al.* reported ATP processes from the Pt(111) surface [139]. Using a photon energy of 1.84 eV, a feature originating from 4PPE as well as 5PPE (ATP) process from occupied states via the  $n=1$  IPS has been found. The intensity ratio between both is in the order of 3%. This agrees

well with the ratio between 4PPE and 3PPE observed here. Thus, the intensity ratio between the 4PPE (ATP) and 3PPE feature might be influenced by the electronic structure of the NiO film. Although no intermediate state is obviously involved<sup>47</sup>, the NiO film influences the photoemission. This determines the transitions between electronic states and the transmission process, and therefore the intensity of excited photoelectrons.

For completeness another process has to be mentioned. The antiferromagnetic NiO (centrosymmetric order) allows for second harmonic generation (SHG) [141–143]. The photon energies are similar to the ones, used for the multi-PPE experiments here. Assuming the SHG of the incident IR light, the SHG photons could excite electrons as indicated by the violet arrows in Fig. 4.50. Whether the ATP process (with 4PPE) or the SHG process (with 2PPE) causes the feature M+IR depends on the transition rates. As mentioned above, the probability of a 4PPE process is expected to be quite small. However, the SHG probability is small as well. But the probability of the subsequent 2PPE process<sup>48</sup> is by orders of magnitude higher compared to the 4PPE process. These two different rates (decrease of available photons and increase of the electron transition probability) might cancel out and lead to a significant contribution in the photoemission spectrum.

The inset of Fig. 4.49 (a) (page 96) shows the angle-resolve multi-PPE spectra of 8 ML NiO. The sample has been biased at -2 V to increase the  $k_{\parallel}$  region. The intensity of each angular spectrum has been normalized to the intensity maximum within the region of the feature M (left side) and the feature N (right side). Both features show no dispersion<sup>49</sup>. The negligible dispersion of the feature M, i.e., the possibly occupied Ag-*sp* band at the  $[001]_{\bar{X}}$  projection, agrees well with the predicted dispersion from angle-resolved 2PPE of the feature B at the NiO monolayer coverage (see Fig. 4.45 and discussion in section 4.4.2).

According to the energy diagram in Fig. 4.50, the feature N originates from an intermediate state ② at  $3.98 \pm 0.02$  eV. The expected positions of the IPS of the 8 ML film are indicated in the lower part. Considering a possible energy shift due to space charge effects, the state ② might coincide with the  $n=1$  IPS. This is in contradiction to the negligible dispersion observed by angle-resolved data, as shown in the inset Fig. 4.49 (a)<sup>50</sup>. Thus, the state ② originates most likely from another transition. As already discussed in section 4.4.2 the projected band structure of Ag(001) does not show possible states in the given energy region which could explain this feature. The unoccupied *sp* band is energetically too high ( $\sim 8$  eV above  $E_F$  [109, 118]) to contribute as an intermediate state. Assuming a direct transition between the occupied and unoccupied *sp* bands the energy needed is far off the observed 3PPE and 4PPE energies (band-to-band transition  $\sim 10$  eV [123]). However, the unoccupied *sp* band of the  $[001]_{\bar{X}}$  projection agrees well with the state ② (note the influence of space charge effects). Thus, the umklapp process might explain the occurrence of feature N. Thereby, the non-resonantly excited intermediate state ②

<sup>47</sup>An intermediate state would influence the photon-energy dependent peak position.

<sup>48</sup>Note that the 2PPE process with SHG photons is not an ATP process.

<sup>49</sup>A small energy shift (asymmetric with respect to  $0^\circ$ ) is observed due to a badly shielded electromagnetic field in the vacuum chamber.

<sup>50</sup>Compare the dispersion of the IPS of the 2 ML coverage in Fig. 4.9 (a) on page 39, using similar experimental conditions. The energy shift due to the dispersion is  $\sim 100$  meV within an emission angle of  $10^\circ$ .



is dominated by the highest density of available unoccupied states, which is indeed found at the L point.

Both features M and N (feature M more definitely than feature N, however) can be assigned to Ag-*sp* band transitions which becomes visible in the normal emission multi-PPE spectra due the back folding of the  $\bar{X}$  to the  $\bar{\Gamma}$  point. Whereas the structural relaxation of the NiO monolayer leads to the  $(2\times 1)$  reconstruction, it is the antiferromagnetic ordering of thicker NiO films which determines the  $(2\times 1)$  unit cell. Note that for both features discussed here the occupied and unoccupied Ag-*sp* bands are *not resonantly excited*. Both bands lead to a feature in the spectrum *separately*.

Since the surface-assisted umklapp process is mediated by the antiferromagnetic ordering of the NiO film the following experiments are highly recommended. The antiferromagnetic ordering is characterized by the Néel temperature. It would be interesting to investigate the multi-PPE spectra in dependence of the sample temperature. At temperatures above the Néel temperature the features should vanish because of the absence of the  $(2\times 1)$  unit cell. This would allow to measure the thickness-dependent Néel temperatures of ultra-thin NiO films on Ag(001). The fact that the feature M, i.e., the multi-PPE of an electron from the occupied Ag-*sp* band is still observed at a film thickness of 8 ML, lead to the conclusion that the oxide exhibit a high transmittance of electrons in this energy region. This is similar to the investigation of the attenuation length of CoO/Ag(001) by Offi *et al.* [135]. For 5 eV electron the attenuation length is  $>15$  ML, sufficient for the films observed here. Thus, the long mean free path should remain at film thicknesses of  $>8$  ML. This would enable to investigate the antiferromagnetic properties of the substrate-influenced ultra-thin films ( $\theta_N=390$  K of 3 ML NiO/Ag(001) [130]) right up to the transition to bulk-like properties of thick NiO films. At high coverages the (possibly observable) Néel temperature should approach the bulk value ( $\theta_N=535$  K of 30 ML NiO/Ag(001) [130] and  $\theta_{N,\text{bulk NiO}}=525$  K [131]).

### Retrospect of bichromatic 2PPE of NiO film on Ag(001)

According to the observation of the surface-assisted umklapp process of the  $\bar{X}$  to the  $\bar{\Gamma}$  point in multi-PPE, the features observed in bichromatic 2PPE spectra will be reviewed. Bichromatic 2PPE data of 4 ML NiO as shown in Fig. 4.20 (page 51). In the upper gray shaded spectrum at a delay of 0 fs, three features K, F, and L are evident. The latter one appears as a significant shoulder of feature F at  $\sim 5.5$  eV ( $\rightarrow 3.9$  eV intermediate state energy). At a delay of +120 fs this feature vanishes completely as seen in the green spectrum below, i.e., the lifetime of the feature L is smaller than the lifetime of the feature F. For the feature F a lifetime of  $\sim 60$  fs is observed (see Fig. 4.20 (b) and detailed discussion in section 4.2.5). Thus, the lifetime of the feature L is much smaller and in the order of  $<30$  fs. The energy position and the short lifetime is similar to the Ag-*sp* resonance at the NiO monolayer coverage, which has been discussed in section 4.4.2. This implies that the feature L originates from the Ag-*sp* resonance as well.

The influence of of the feature L becomes more evident at bichromatic 2PPE of 8 ML NiO as shown in Fig. 4.22 (page 54). The intensity contribution from the IPS is smaller which increases the dominance of the Ag-*sp* resonance in the spectra. The intensity maximum at 3.9 eV for a UV energy of 4.17 eV (pump) is independent of

the IR energy (probe) as indicated by the vertical black line. The blue spectrum correspond to a UV energy of 4.05 eV, i.e., 120 meV below the former ones. But the intensity maximum shifts only by  $\sim 50$  meV as indicated by the vertical black lines. This means the intensity maximum shows an energy shift which is smaller than the change of the pump-photon energy. This is a similar behavior as observed for the feature B of the NiO monolayer discussed in section 4.4.2.

In conclusion the antiferromagnetic properties of the NiO overlayer leads to the observation of Ag-*sp* bands at the L point. The  $(2\times 1)$  magnetic unit cell mediates the umklapp process of the  $\bar{X}$  (L point) to the  $\bar{\Gamma}$  point. This explains the occurrence of otherwise not assigned photoemission features in the multi-PPE spectra.

## 5 Summary

In the present work the electronic structure of unoccupied states of ultra-thin NiO films on Ag(001) has been investigated using time-resolved two-photon photoemission. The direct comparison with scanning tunneling spectroscopy data [15] demonstrates for the first time the advantage of the application of two complementary experimental techniques for the investigation of strongly correlated electron systems.

In the sub-monolayer coverage of NiO, image-potential states (IPS) of the remaining Ag(001) substrate are identified. They shift to higher intermediate state energies with increasing coverage, i.e., with decreasing Ag region size. The energy shift is already observed at relatively small coverages, where still large Ag regions exist. Additionally, the shift of the  $n=2$  state is larger compared to the  $n=1$  state. This is explained by the microscopic change of the image potential above a Ag region surrounded by NiO monolayer islands. The difference of the work function between Ag(001) and the NiO monolayer is  $\sim 0.5$  eV. This affects a change of the electrostatic potential close to the sample surface. Electrostatic field considerations show that the lateral distribution of NiO within the sub-monolayer coverage changes the explicit shape of the image potential of an electron above a NiO-surrounded Ag region. This model enables to estimate the energy shifts of the IPS in dependence of the Ag region size, which scales with the nominal sub-monolayer coverage. For the NiO bilayer a series of IPS has been identified with lifetimes of 30, 50, and 120 fs of the  $n=1-3$  IPS, respectively. The binding energies reveal that the NiO bilayer is fully characterized by a permittivity close to the bulk value. This manifests the detailed investigation of IPS of an oxide system for the first time. Upon heating the film lacerates and the IPS of the Ag substrate evolve. The time-resolved intensities of both IPS species reveal a relaxation of IPS electrons from Ag to NiO islands. The observed time-dependent population could be modeled by simple rate equations. At NiO films of larger thicknesses, the IPS are not as obvious as compared to the bilayer coverage. This indicates a much smaller cross-section of the excitation processes. However, the long-lived contribution of the 2PPE intensity agrees well with the  $n=2$  IPS of the bilayer and manifests the existence of the IPS of thicker NiO films as well.

The spectroscopy of unoccupied Ni-3*d* states reveals strong variations of the electronic structure within the first few monolayers. The results are compared with layer-resolved scanning tunneling spectroscopy data [15]. For each film thickness a good agreement between both methods is observed. The energy difference of the spectral features are in the order of a few 100 meV. Due to the strongly correlated electron system of NiO the different electronic final states of both methods should lead to much larger difference. This apparent discrepancy is explained by the excitation process in 2PPE. The excitation from an initial state within the Ag substrate does not create a hole within the oxide film and prevents the influence of correlation effects.

The explicit assignment of spectral features to distinct island thicknesses enables to investigate the temperature stability of the thin films and reveals information about transformation kinetics. The NiO monolayer is stable up to 500 K and starts to lacerate at 550 K. The first transformation step is characterized by the formation of islands with mainly bilayer thickness. The absence of any trilayer contribution in the 2PPE spectra highlights the special role of the bilayer for NiO growth on Ag(001). Above 600 K islands with effective thicknesses of  $\geq 3$  ML are formed as well. In contrast to the monolayer the closed NiO bilayer lacerates at 650 K. This means the transition between bilayer to trilayer islands depends on the film properties, where a closed film has a higher stability compared to a single bilayer island of the lacerated monolayer film. This is explained by the influence of the Ag substrate to the transformation processes which is kinetically hindered at closed films. An unoccupied state at 1.6 eV above the Fermi level is assigned to a  $d_{z^2}$ -derived surface state of NiO(001). In contrast to STS measurements, the energy of this state is almost independent of the film thickness. This discrepancy is explained by a method-intrinsic energy shift in STS due to the voltage drop within the dielectric oxide film.

Spectral features in the 2PPE data which are neither IPS nor states of the NiO film are assigned to resonant electron transitions between occupied and unoccupied Ag-*sp* bands. This transition is located in the vicinity of the L point within the three-dimensional fcc Brillouin zone of the Ag substrate. The observation of this transition at the Ag(001) surface is realized via a surface-assisted umklapp process. At the NiO monolayer the umklapp is mediated by the structural relaxation accompanied with the formation of a  $(2 \times 1)$  reconstruction. This leads to a back-folding of the projected L point to the  $\bar{\Gamma}$  point. In contrast to the structural relaxation, the umklapp at larger film thicknesses is mediated by the antiferromagnetic ordering of NiO. The magnetic structure leads to a  $(2 \times 1)$  unit cell of the NiO(001) as well. The absence of the corresponding diffraction peaks of the  $(2 \times 1)$  reconstruction in LEED demonstrates the sensitivity of this umklapp process for this particular transition in photoemission.

Beside the results obtained so far, many new interesting questions arose. At first it has to be noted that the presented results seem to give only a small insight into the fascinating physical properties of unoccupied electronic states of the transition metal oxide NiO. The investigation of resonant transitions between occupied and unoccupied states for detailed band mapping will be one of the main issues in future projects. However, the data demonstrate the first successful application of the new experimental setup with a fully tunable femtosecond laser system to a strongly correlated electron system. Secondly, the results also demonstrate the advantages of the experimental setup. It will be possible to investigate the electronic structure of unoccupied states and their dynamics with less limits of the tunability of the excitation source.

## 6 Appendix

### 6.A Intensity correction of 2PPE data due to laser fluctuations

The fluctuations of the laser system influence the 2PPE data significantly. Thus, the measurement and control software has been extended to a simultaneous recording of the laser intensities during 2PPE measurements. This enables the data correction. For this purpose the following aspects have to be fulfilled:

1. The measurement of the laser intensities has to be integrative to avoid runaway values.
2. The time period of one measurement has to be smaller than the typical fluctuation period.
3. The correlated assignment of the electron and laser intensities has to be very accurate.

The first item is apparent for fluctuating signals. A single measurement normally does not reflect the actual averaged value. The integration serves the averaging in the given period. The second item is apparent as well. The averaging should not destroy the information about the fluctuation. Typical fluctuation periods are in the order of seconds. Thus, a measurement period of 100 ms is sufficient to recognize the fluctuations. The third item is as simple as important. The exact time of each measurement is necessary to ensure the correct correlation of the two data sets.

Experimentally the laser intensities are recorded by photo diodes. Parasitic reflections at the interface of optical components are used as shown in Fig. 6.1. Figure

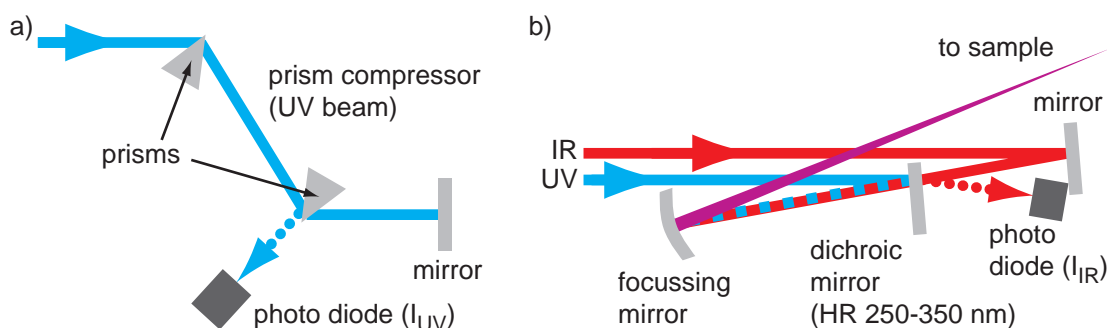


**Figure 6.1:** Schematic view of the photo diode positions. (a) Path of the UV beam through the prism compressor. The intensity is detected by the reflexion at one of the prisms. (b) Path of the UV and IR beam close to the vacuum chamber. Both beams are combined via a wide-range dichroic mirror. The intensity of the IR beam is detected by the reflexion at the dichroic mirror.

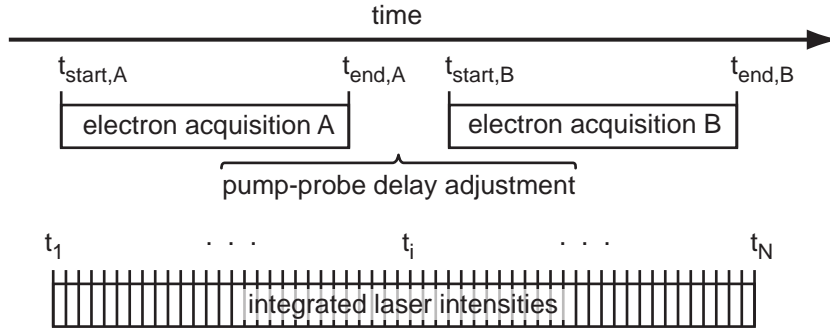


**Figure 6.2:** Time schedule of a time-resolve 2PPE measurement. The horizontal boxes in the upper part indicate the acquisition time of the electron intensity at the electron analyzer of two images A and B. The simultaneous recording of the laser beam intensities is depicted in the lower part. The difference of the counter value between  $t_i$  and  $t_{i+1}$  reveal the averaged laser intensity in this period.

(a) shows the beam path of the UV beam through the prism compressor. The reflection at one of the prisms is used to measure the intensity of the UV beam. Figure 6.1 (b) depicts the collinear combination of the UV and IR beam. The UV beam is reflected at a wide-range dichroic mirror (HR 250–350 nm, HT > 450 nm, Layertec, Melingen) whereas the IR beam is transmitted. The IR beam intensity is obtained by the back reflection at the dichroic mirror for the combination of both beams. The UV sensitive photo diodes<sup>1</sup> (active area  $6 \times 6 \text{ mm}^2$ , Hamamatsu, Herrsching am Ammersee) are mounted on a current-to-frequency amplifier/converter (Digiboard, Scitec) which converts the photo current to a TTL signal. The frequency is proportional to the photo current. The TTL signal is detected with counter units of a PCI card (PCI2511, Measurement Computing Corp. via Plug-In Electronic, Eichenau). The counter realizes the integration intrinsically.

A typical time schedule of a time-resolved 2PPE measurement using the improved software is shown in Fig. 6.2. Depicted is the case of a measurement of two 2PPE spectra A and B at different pump-probe time delays. The acquisition of the electron intensity is shown in the upper part. The times  $t_{start}$  and  $t_{end}$  indicate the starting and finishing of the acquisition. The time measurement is realized via the *RDTSC* function of the C environment. It returns a 64 bit integer number which is equivalent to the value of time step counter (TSC) register of the CPU. This time measurement is accurate within a few microseconds<sup>2</sup>. However, in the software schedule the time  $t_{start}$  is taken before the command for the image acquisition is executed. It takes  $\sim 150 \text{ ms}$  before the real measurement at the Sencam camera starts. The time between  $t_{end,A}$  and  $t_{start,B}$  is caused by the adjustment of the pump-probe delay. The laser intensities are recorded simultaneously. The period is adjusted to  $\sim 100 \text{ ms}$ <sup>3</sup> as depicted in the lower part of Fig. 6.2. The averaged laser intensity of one period is

<sup>1</sup>The sensitivity range is 190–1100 nm. The label *UV sensitive* is used to enhance the extended sensitivity range in the UV.

<sup>2</sup>The modern >GHz CPUs lead to a theoretical time resolution of nanoseconds. Practically the resolution is in the order of microseconds because the operating system determines the exact execution of the command which itself takes many CPU ticks.

<sup>3</sup>The exact time is again measured by the CPU counter.

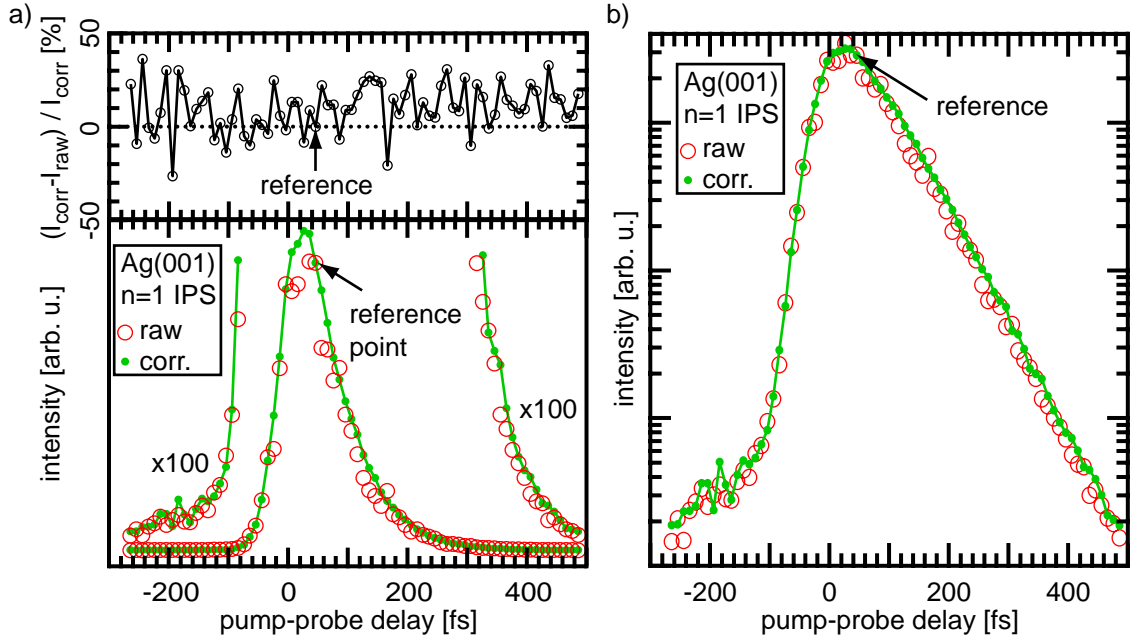


**Figure 6.3:** (a) Time-resolved intensity of the  $n=1$  image-potential state (IPS) on linear scale (open red circles: raw data, green points: corrected data). The upper part shows the normalized intensity difference between corrected and raw data. (b) Same as (a) on logarithmic scale.

determined by the difference of the counter values between  $t_i$  and  $t_{i+1}$ . All obtained time values are used to correlate the electron spectroscopy data with laser intensity data.

The data correction uses the relation between the electron intensity  $N_e$  and the laser intensities  $I_{IR}$  and  $I_{UV}$  of the two laser pulses. For the case of a UV pumped and IR probed electronic state the relation is given by

$$N_e \propto I_{UV} \times I_{IR} . \quad (6.1)$$

For each electron spectrum the integrated product  $I_L$  of the laser intensities is calculated by

$$I_L = \sum_{t_i=t_{start}}^{t_i=t_{end}} I_{UV,i} \times I_{IR,i} \quad (6.2)$$

For the example shown in Fig. 6.2 the electron intensities of each spectrum is corrected with respect to the reference spectrum (A or B in the given example) via

$$N_{corr,X} = \frac{I_{L,X}}{I_{L,ref}} \times N_{e,X} \quad (6.3)$$

where X denotes spectrum A or B.

An example for the successful data correction is shown in Fig. 6.3. The intensity of the  $n=1$  image-potential state (IPS) is shown with respect to the pump-probe delay. The lower part of Fig. 6.3 (a) shows the data on linear scale, where the open red circles indicate the raw data and the green points the corrected one. The upper panel shows the relative intensity difference between corrected and raw data. This is

equivalent to  $(1 - \frac{I_{L,X}}{I_{L,ref}})$  according to equation 6.3 and is a measure for the influence of the laser fluctuations to the 2PPE signal. Values of up to 40% are found. The effect of the data correction becomes more evident on logarithmic scale as shown in Fig. 6.3 (b). Note that a logarithmic scale normally suppresses the impression of fluctuations. However, the curve of the corrected data is much smoother as compared to the raw data.

## 6.B Methods for background subtraction

The background of 2PPE data of *simple* systems, as for example the image-potential states of Ag(001) [31], can often be described by an simple offset or an slightly slope due to the missing of electronic states in between. For the NiO data presented here the situation is more complicated. First the quality of the sample is not as well defined as pure metal substrates due to limitations of the preparation conditions. Despite of a layer-by-layer growth, the sample might consist of a distribution of regions of Ag substrate and NiO islands of different thicknesses. These inhomogeneities lead to additional features in the spectrum. This might lead to mixture of 2PPE spectra, where electronic states of different film thicknesses are close each other or a small, almost featureless background is formed. To describe the significant features of the nominal film thickness with a sufficiently high accuracy a good description of the background is necessary. This becomes important for the analysis of time-resolved 2PPE at all pump-probe time delays (which correspond to a dataset of up 200 individual spectra). In this section two different methods for the background subtraction will be depicted.

### Background subtraction method A time-delay independent background

Depending on the actual sample, the experimental setup sometimes demands high photon fluxes of the pump or probe beam to reach reasonable electron counting rates<sup>4</sup>. Thus, an increase of the (*featureless*) background intensity in the 2PPE spectrum is observed, which is dominated by monochromatic 2PPE processes of the pump and the probe beam. This leads to difficulties of the data analysis. For the case that the background is independent of the pump-probe time delay the following method could be applied to subtract the background easily. Figure 6.4 (a) shows the raw data of time-resolved 2PPE spectra of 8 ML NiO as analyzed in section 4.2.5. The red and green color indicate negative and positive delays, respectively. The black curve shows the spectrum at a delay=0. The intensity differences at energies above 4.7 eV are due to laser fluctuations. To eliminate the background, the spectrum at large time delays (-200 fs) is taken as reference as shown by the violet curve (fittingly at delays where the probe pulse comes first to avoid the influence of long-lived contributions). A region of interest (ROI) is defined where no time-

<sup>4</sup>This could be due to low cross-sections of the investigated electron transitions or simply insufficient laser power of one of the two laser beams. However, the NiO shows a relatively high monochromatic 2PPE background, in contrast to the bare metal substrate.



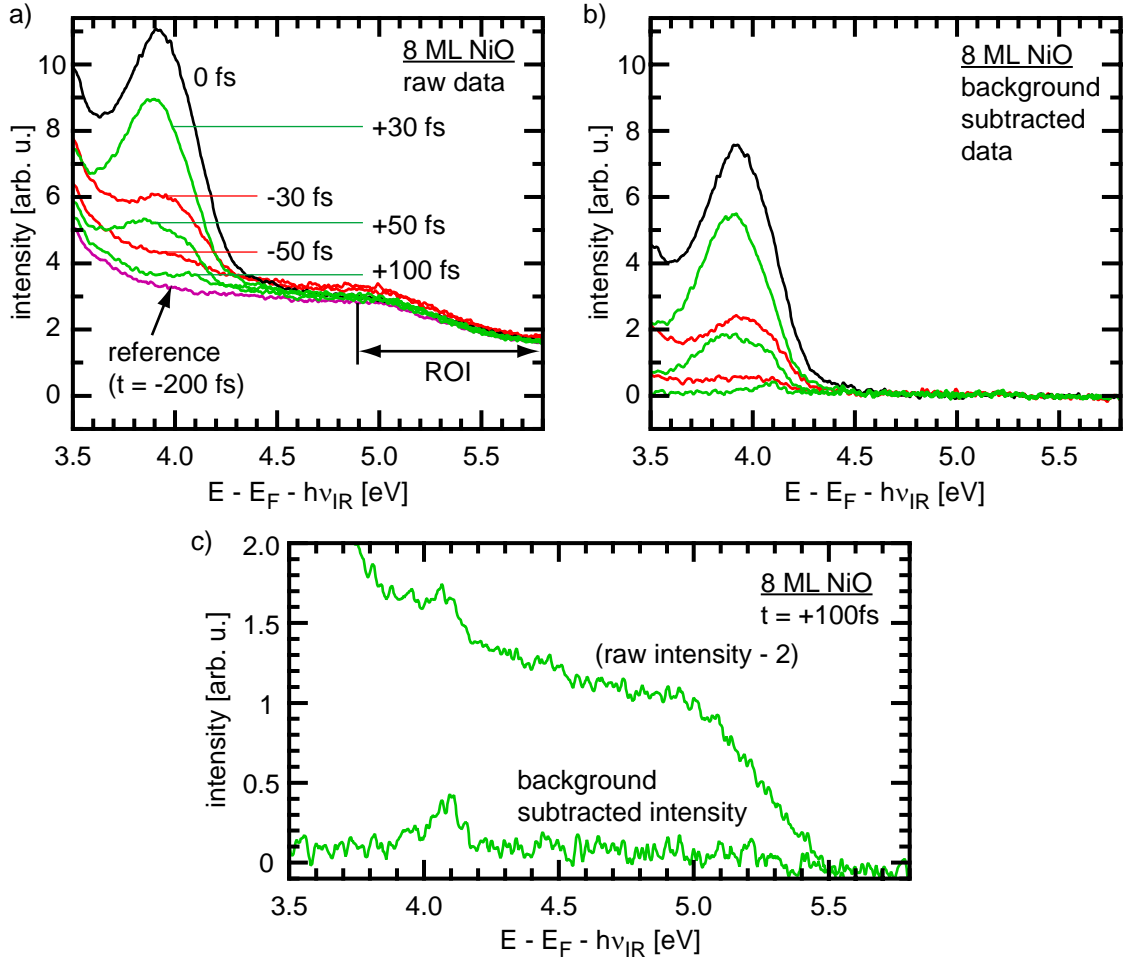


**Figure 6.4:** Time-resolve 2PPE spectra of 8 ML NiO (see Fig. 4.23). (a) Raw data at different time delays. The violet curve correspond to a delay of -200 fs which is used as the reference spectrum for the background subtraction. (b) Background subtracted data according to equation 6.4. (c) Comparison of raw and subtracted data at a time delay of 100 fs. For a better reading, the raw data intensity has been shifted by -2.

dependent features are found. The ratio of the integral over the ROI is used to subtract the background according to

$$I_{noBG}(\Delta t) = I_{raw}(\Delta t) - p \times I_{raw}(\Delta t_{ref.}) , \quad (6.4)$$

$$\text{with } p = \frac{\int_{ROI} I_{raw}(\Delta t)}{\int_{ROI} I_{raw}(\Delta t_{ref.})} \quad (6.5)$$

Figure 6.4 shows the result of the background subtracted data. Only the time-dependent features remain in all spectra. For a better comparison, the spectra at 100 fs time delay are shown in Fig. 6.4(c). The raw data has been shifted to lower intensities. The integrated signal to background ratio of the feature at 4.1 eV is less than 10%. The fluctuations of laser system would dominate the integrated electron intensity in the vicinity of this feature. This suppresses any determination of the

lifetime. This method has been applied for the analysis of the IPS of thicker NiO films in section 4.2.5.

## Background subtraction method B time-delay dependent background

In addition to the monochromatic 2PPE background, as discussed in the previous section, a time-delay dependent background might occur. This originates in most cases from non-resonant 2PPE from occupied states. The time-dependent intensity can be used to determine the exact position of  $t=0$  (both pulses at the same time) and the cross-correlation between both laser pulses. However, in some cases it is fortunate to eliminate this background as well, to enable a better description of the *real* data. Similar to the method A a ROI is defined, where none of the targeted features occur. The data within the ROI are fitted by an arbitrarily shaped curve e.g., a polynomial. The fit result is subtracted from the data in the whole energy range. This method has been applied for the analysis of the IPS of the 2 ML NiO film in section 4.2.3.

## 6.C Lifetime analysis using integrated intensities

In this section an alternative analysis of the time-resolved 2PPE data is depicted. The best way to determine the intensity of 2PPE features in dependence of the pump-probe time delay is to fit the peaks of the spectrum. However, in some cases the shape of the spectra does not allow to identify individual peaks or it consists of a mixture of different peaks close to each other. To approximate the lifetimes of the observed unoccupied states the intensity is integrated over a certain energy range. For the case of significant differences of the lifetimes of the different states the integrated 2PPE intensities at large delays should reflect the largest lifetime of one of the involved states. As an example for the validity of this method is shown in Fig. 6.5. Figure (a) shows the color-coded 2PPE spectra in dependence of the pump-probe delay of the IPS of the 2 ML NiO film (similar data as in section 4.2.3). The orange (background), red ( $n=1$ ), green ( $n=2$ ), and blue ( $n=3$  IPS) bars indicate the energy regions of different features in the spectrum. The integrated intensities of these regions in dependence of the pump-probe delay are shown in Fig. 6.5 (b) on a semi-logarithmic plot. Due to the asymmetry of all curves with respect to  $\text{delay}=0$ , all detected electrons are supposed to be UV-pumped and IR-probed<sup>5</sup>. For the image potential states a linear decrease at delays  $\geq 150$  fs is observed. The fit of the data reveal lifetimes of 32, 63, and 120 fs of a corresponding single-exponential decay, respectively. This is in good agreement with the data obtained in section 4.2.3 and verifies the applicability of this method. The value of the cross-correlation is estimated to 70 fs as shown by the dashed line. The Gaussian has been fitted to the background intensity (orange data points) at negative delays. This reveal a time-constant of 23 fs of IR-probed contributions. The disagreement between the intensities of the IPS and a single exponential decay around  $\text{delay}=0$  is due to contributions of the feature X which not clearly evident in the data. This artificially

<sup>5</sup>Of course UV-probed contributions might be considered as well, but this depends on the significance of the distinct data.

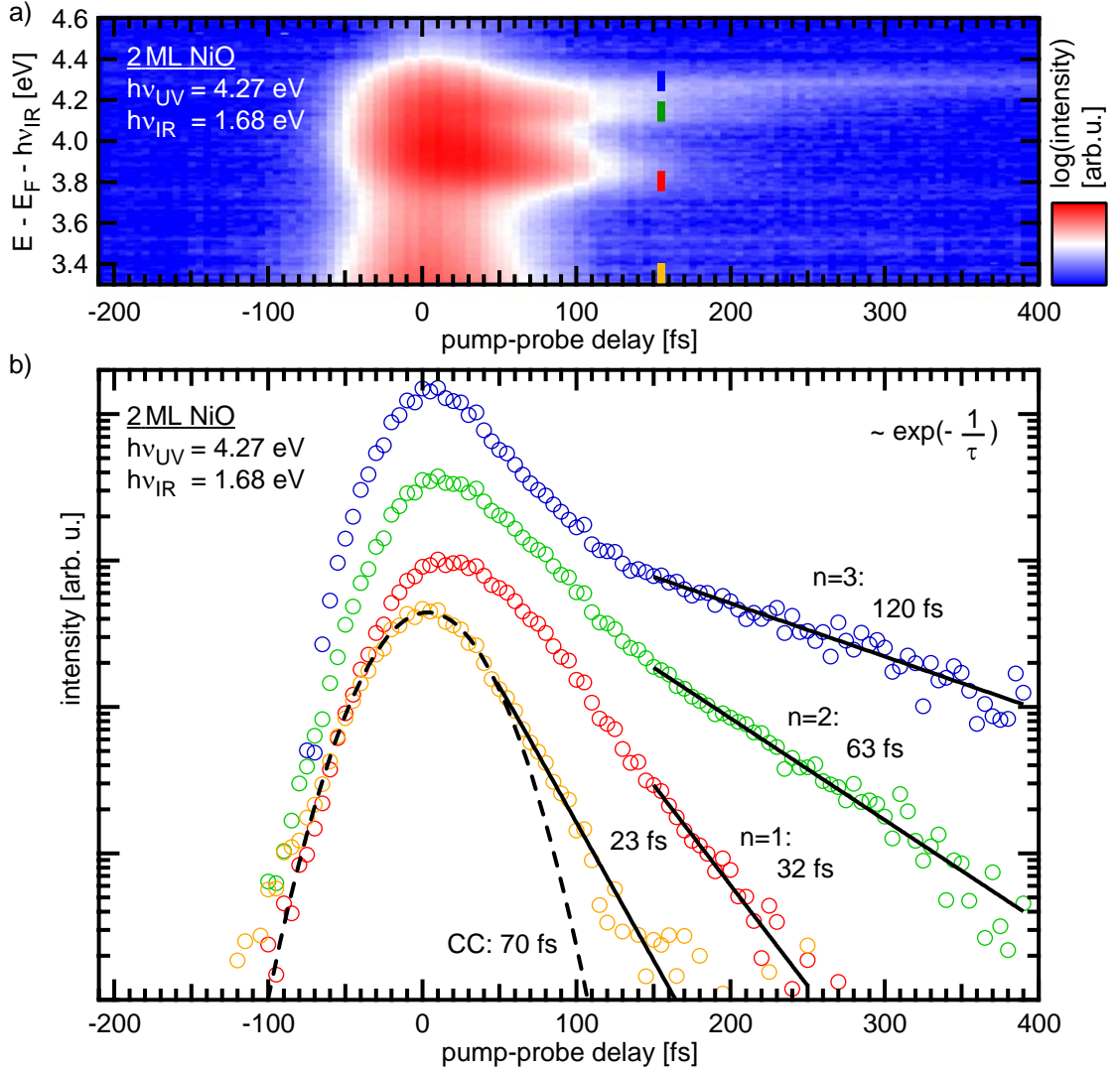


**Figure 6.5:** (a) 2D-plot of the time-resolved 2PPE intensities of the IPS of bilayer NiO (see section 4.2.3) on logarithmic scale. The data has been background subtracted using background subtraction method A (see section 6.B above). (b) Line profiles through (a) averaged over 0.1 eV as indicated by the vertical bars. An exponential fit at large delays reveal lifetimes of 32, 63, and 120 fs for the  $n=1-3$  IPS, respectively.

increase the intensity of all states at small delays. Note that the amount of the artificial increase of the intensity (ratio between intensity of the targeted state and the artificial contribution from another state) depends on the relative lifetimes of the involved states. For the case of the small lifetimes or bad intensity ratios this method does not reveal the real lifetimes. However, an estimation of the lowest border is accessible<sup>6</sup>.

<sup>6</sup>As shown in section 4.2.5 for the 8 ML NiO.

## 6.D Method-intrinsic energy shift in STS

In this section the influence of a dielectric material on the STS measurements will be discussed. In the case of the dielectric NiO, with a static dielectric constant  $\epsilon_r=12$  [9], the voltage drop within the NiO film has to be considered. The tunneling junction is depicted in Fig. 6.6 (a). The gray-shaded areas indicate the projected band structure of occupied and unoccupied states of the metal substrate and the STM tip. The highest occupied and lowest unoccupied states of the NiO are indicated as well. They are considered to span the whole thickness  $d$  of the oxide film. STS investigates the differential conductance of the sample in dependence of the applied bias voltage. As soon as the Fermi level of the tip is energetically at the same position of an unoccupied state, the  $dI/dV$  signal increases. The internal voltage drop within the oxide film causes a small slope of the energy of the electronic state in dependence of the distance, i.e., the energy increases at larger distances with respect to  $E_F$  of the substrate. The slope determines the exact energy of the state at the surface. The highest  $dI/dV$  signal in STS is expected when the Fermi level of the tip matches the energy of the state at the surface. This means the voltage drop increases artificially the determined energy position of the unoccupied state. Thus, the energy equivalent of the voltage drop in the oxide ( $eV_{ox}$ ) has to be subtracted from the corresponding bias value ( $eV_{bias}$ ) to get the energy of the unoccupied state with respect to the Fermi level.

To determine the voltage drop within the oxide film an equivalent circuit is depicted in Fig. 6.6 (b) using simple capacitors for the representation of the tunneling junction. The lower capacitor shows the *real* situation of a capacitor, where the

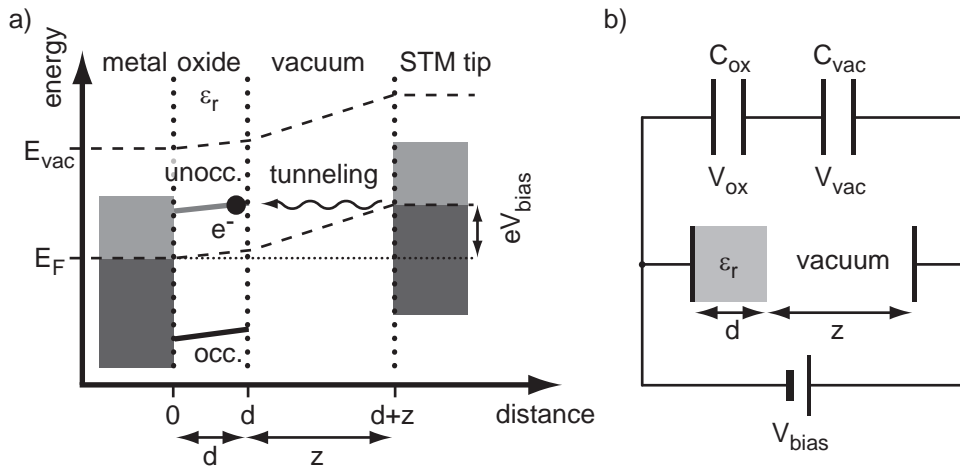


**Figure 6.6:** (a) Model of a one-dimensional tunneling junction of a metal sample covered with an oxide ultra-thin film. The bias voltage  $V_{bias}$  shifts the Fermi level of the tip by  $eV_{bias}$  [eV]. The dielectric properties of the oxide ( $\epsilon_r$ ) causes a voltage drop ( $V_{ox}$ ) within the oxide. (b) Shows the equivalent circuit of (a) using a simple capacitor representation. The lower capacitor depicts the volume fractions of a capacitor which is partially filled with dielectric material ( $\epsilon_r$ ) and vacuum. The upper part shows the equivalent representation of two capacitors with different capacitances.

plates represent the metal substrate and the metal tip, respectively<sup>7</sup>. The tunneling barrier consists of the NiO film (thickness  $d$ ) on the one side and the vacuum (thickness  $z$ ) on the other side. This representation could be further simplified by splitting the partially filled capacitor into two single capacitors, represented by their capacitances  $C_{vac}$  and  $C_{ox}$ , respectively. These are determined via

$$C_{vac} = \frac{\epsilon_0 A}{z} \quad \text{and} \quad C_{ox} = \frac{\epsilon_0 \epsilon_r A}{d} \quad (6.6)$$

where  $A$  represents the area of the capacitor. In this series circuit it is well known that each capacitor carries the same amount of charges  $Q$ . The voltages within the circuit are given by

$$V_{bias} = V_{vac} + V_{ox} = \frac{Q}{C_{vac}} + \frac{Q}{C_{ox}} = \frac{Q}{\epsilon_0 A} \left( z + \frac{d}{\epsilon_r} \right). \quad (6.7)$$

This leads to

$$V_{ox} = \frac{1}{1 + \epsilon_r \frac{z}{d}} V_{bias} \quad (6.8)$$

which represents the value of the voltage drop in the oxide film in dependence of the three variable parameters  $d$ ,  $z$ , and  $V_{bias}$ . As an example, typical tunneling parameters are assumed. For a 4 ML NiO film ( $d=0.836$  nm), a bias voltage of 2 V, and a vacuum gap  $z$  of 0.3 nm, equation 6.8 leads to a voltage drop of 377 meV. This value leads to a significant shift of features in the STS spectra and has to be considered for the determination of the energies of unoccupied states.

Although equation 6.8 in principal delivers an approximate value of the energy shift of electronic states in STS, the main problem is that the exact value of the vacuum gap  $z$  is still unknown. This depends on many parameters (the tunneling current, the tunneling matrix elements, the density of states, etc.). However, with increasing film thickness a larger increase of  $d$  with respect to the value of  $z$  is expected<sup>8</sup>. As an additional example, the voltage drop within in a 8 ML NiO film at a bias voltage of 2 V and a similar value of  $z$  of 0.3 nm is given by 634 V. This is 258 meV larger than the voltage drop within the 4 ML film at the same bias voltage. With other words, a feature in STS could show an upshift of the energy with increasing film thickness due to the increase of the voltage drop instead of a thickness-dependent energy position. Note that the energy of the electronic state could decrease as well. Therefore, the ratio between *real* energy shift of the state and the value of the voltage drop determines an up- or downshift in the thickness-dependent STS spectra. This clearly demonstrates the significance of the internal voltage drop within the oxide film for the interpretation of STS spectra.

<sup>7</sup>In this model the tip is represented by a planar plate although a certain radius of the tip apex in addition to the imaging nano-tip of a few atoms size is expected. The electric field at the nano-tip is not as homogeneous as shown in Fig. 6.6. However, this does not influence the *basic* results depicted here.

<sup>8</sup>The vacuum gap  $z$  is expected to be always in the order of an atom diameters, whereas the film thickness  $d$  exceeds a few nanometer easily.



## 7 Bibliography

- [1] O. Svelto. *Principles of lasers*. Plenum Press, New York, 3 (reprint) edition, 1993.
- [2] E. Hanamura, Y. Kawabe, and A. Yamanaka. *Quantum nonlinear optics*. Springer, Berlin, 2007.
- [3] G. Ertl. Surface science and catalysis - Studies on the mechanism of ammonia-synthesis: The P.H. Emmett award address. *Catalysis Reviews-science and Engineering*, 21(2):201–223, 1980.
- [4] G. Ertl. Primary steps in catalytic synthesis of ammonia. *Journal of Vacuum Science & Technology A-vacuum Surfaces and Films*, 1(2):1247–1253, 1983.
- [5] K. Nakamoto, Y. Kawato, Y. Suzuki, Y. Hamakawa, T. Kawabe, K. Fujimoto, M. Fuyama, and Y. Sugita. Design and read performance of GMR heads with NiO. *Ieee Transactions On Magnetism*, 32(5):3374–3379, September 1996.
- [6] J. Zaanen, G. A. Sawatzky, and J. W. Allen. Band-gaps and electronic-structure of transition-metal compounds. *Physical Review Letters*, 55(4):418–421, 1985.
- [7] P. M. Echenique and J. B. Pendry. Existence and detection of Rydberg states at surfaces. *Journal of Physics C-solid State Physics*, 11(10):2065–2075, 1978.
- [8] U. Höfer, I. L. Shumay, C. Reuß, U. Thomann, W. Wallauer, and T. Fauster. Time-resolved coherent photoelectron spectroscopy of quantized electronic states on metal surfaces. *Science*, 277(5331):1480–1482, September 1997.
- [9] R. Newman and R. M. Chrenko. Optical properties of nickel oxide. *Physical Review*, 114(6):1507–1513, 1959.
- [10] S. Schuppler, N. Fischer, T. Fauster, and W. Steinmann. Bichromatic 2-photon photoemission spectroscopy of image potential states on Ag(100). *Applied Physics A-materials Science & Processing*, 51(4):322–326, October 1990.
- [11] M. Weinelt, C. Reuß, M. Kutschera, U. Thomann, I. L. Shumay, T. Fauster, U. Höfer, F. Theilmann, and A. Goldmann. Decay and dephasing of image-potential states due to surface defects and disorder. *Applied Physics B-lasers and Optics*, 68(3):377–381, March 1999.
- [12] C. Reuß, I. L. Shumay, U. Thomann, M. Kutschera, M. Weinelt, T. Fauster, and U. Hofer. Control of the dephasing of image-potential states by CO adsorption on Cu(100). *Physical Review Letters*, 82(1):153–156, January 1999.

- 
- [13] M. Roth, M. T. Pickel, J. X. Wang, M. Weinelt, and T. Fauster. Electron scattering at steps: Image-potential states on Cu(119). *Physical Review Letters*, 88(9):096802, March 2002.
- [14] T. Fauster, M. Weinelt, and U. Höfer. Quasi-elastic scattering of electrons in image-potential states. *Progress In Surface Science*, 82(4-6):224–243, 2007.
- [15] S. Großer. *Wachstum und lokale elektronische Struktur von ultra-dünnen NiO- und CoO-Schichten auf einer Silberoberfläche*. PhD thesis, Martin-Luther-Universität Halle-Wittenberg, 2008.
- [16] H. Hertz. Über einen Einfluss des ultravioletten Lichtes auf die elektrische Entladung. *Ann. Phys.*, 267(8):983–1000, 1887.
- [17] Wilhelm Hallwachs. Über den Einfluss des Lichtes auf electrostatisch geladene Körper. *Ann. Phys.*, 269(2):301–312, 1888.
- [18] A. Einstein. Über einen die Erzeugung und Verwandlung des Lichtes betreffenden heuristischen Gesichtspunkt. *Ann. Phys.*, 322(6):132–148, 1905.
- [19] W. Eberhardt and F. J. Himpsel. Dipole selection-rules for optical-transitions in the fcc and bcc lattices. *Physical Review B*, 21(12):5572–5576, 1980.
- [20] B. Feuerbacher and R. F. Willis. Photoemission and electron states at clean surfaces. *Journal of Physics C-solid State Physics*, 9(2):169–216, 1976.
- [21] F. Reinert and S. Hüfner. Photoemission spectroscopy - from early days to recent applications. *New Journal of Physics*, 7:97, April 2005.
- [22] W. Wallauer and T. Fauster. Two-photon excitation processes and linewidths of surface and image states on Cu(111). *Surface Science*, 374(1-3):44–50, March 1997.
- [23] S. Pawlik, R. Burgermeister, M. Bauer, and M. Aeschlimann. Direct transition in the system Ag(111) studied by one- and two-photon photoemission. *Surface Science*, 402-404:556 – 560, 1998.
- [24] A. Winkelmann, V. Sametoglu, J. Zhao, A. Kubo, and H. Petek. Angle-dependent study of a direct optical transition in the *sp* bands of Ag(111) by one- and two-photon photoemission. *Phys. Rev. B*, 76(19):195428, Nov 2007.
- [25] Z. F. Hao, J. I. Dadap, K. R. Knox, M. B. Yilmaz, N. Zaki, P. D. Johnson, and R. M. Osgood. Nonequilibrium band mapping of unoccupied bulk states below the vacuum level by two-photon photoemission. *Physical Review Letters*, 105(1):017602, July 2010.
- [26] R. Loudon. *The quantum theory of light*. Oxford University Press, 3, reprint edition, 2004.
- [27] J.C. Diels and W. Rudolph. *Ultrashort laser pulse phenomena: fundamentals, techniques, and applications on a femtosecond time scale*. Academic Press, San Diego, 1997.
-



- 
- [28] T. Hertel, E. Knoesel, M. Wolf, and G. Ertl. Ultrafast electron dynamics at Cu(111): Response of an electron gas to optical excitation. *Physical Review Letters*, 76(3):535–538, January 1996.
- [29] M. Wolf, A. Hotzel, E. Knoesel, and D. Velic. Direct and indirect excitation mechanisms in two-photon photoemission spectroscopy of Cu(111) and CO/Cu(111). *Physical Review B*, 59(8):5926–5935, February 1999.
- [30] M. Weinelt. Time-resolved two-photon photoemission from metal surfaces. *Journal of Physics-condensed Matter*, 14(43):R1099–R1141, November 2002.
- [31] K. Duncker, M. Kiel, and W. Widdra. Momentum-resolved lifetimes of image-potential states on Ag(001). In preparation.
- [32] I. L. Shumay, U. Höfer, U. Thomann, W. Wallauer, and T. Fauster. Lifetimes of image-potential states on Cu(100) and Ag(100) measured by femtosecond time-resolved two-photon photoemission. *Physical Review B*, 58(20):13974–13981, November 1998.
- [33] EV Chulkov, VM Silkin, and PM Echenique. Image potential states on lithium, copper and silver surfaces. *Surface Science*, 391(1-3):L1217–L1223, Nov 26 1997.
- [34] Anke Höfer. Wachstum von  $\alpha$ -Sexithiophen auf Au(001). Diploma thesis, Martin-Luther-Universität Halle-Wittenberg, 2007.
- [35] Specs. *Phoibos 150 user manual*. Specs, Berlin.
- [36] S. LaShell, B. A. McDougall, and E. Jensen. Spin splitting of an Au(111) surface state band observed with angle resolved photoelectron spectroscopy. *Physical Review Letters*, 77(16):3419–3422, October 1996.
- [37] F. Reinert, G. Nicolay, S. Schmidt, D. Ehm, and S. Hüfner. Direct measurements of the L-gap surface states on the (111) face of noble metals by photoelectron spectroscopy. *Phys. Rev. B*, 63(11):115415, March 2001.
- [38] G. Nicolay, F. Reinert, S. Hüfner, and P. Blaha. Spin-orbit splitting of the L-gap surface state on Au(111) and Ag(111). *Physical Review B*, 65(3):033407, January 2002.
- [39] M. Hengsberger, F. Baumberger, H. J. Neff, T. Greber, and J. Osterwalder. Photoemission momentum mapping and wave function analysis of surface and bulk states on flat Cu(111) and stepped Cu(443) surfaces: A two-photon photoemission study. *Physical Review B*, 77(8):085425, February 2008.
- [40] C. Homann, C. Schrieffer, P. Baum, and E. Riedle. Octave wide tunable UV-pumped NOPA: pulses down to 20 fs at 0.5 MHz repetition rate. *Optics Express*, 16(8):5746–5756, April 2008.
- [41] K. Duncker, M. Kiel, A. Höfer, and W. Widdra. Commensurate surface structures and concerted cis-trans-isomerization within ordered monolayers of  $\alpha$ -sexithiophene on Ag(001). *Physical Review B*, 77(15):155423, April 2008.
-

- 
- [42] K. Duncker. *Homo- und heterochirale kommensurate Molekülstrukturen in der Sexithiophen-Monolage auf einer Ag(001)-Oberfläche*. PhD thesis, Martin-Luther-Universität Halle-Wittenberg, 2008.
- [43] A. Blättermann. Femtosekunden Elektronendynamik unbesetzter Zustände von Sexithiophen auf einer Ag(001) Oberfläche. Bachelor thesis, Martin-Luther-Universität Halle-Wittenberg, 2010.
- [44] M. Huth. *Untersuchungen zur atomaren Struktur ultradünner Schichten von Mn-Oxiden auf Ag(001) und BaTiO<sub>3</sub> auf Pt(001)*. PhD thesis, Martin-Luther-Universität Halle-Wittenberg, 2010.
- [45] K. Marre and H. Neddermeyer. Growth of ordered thin-films of NiO on Ag(100) and Au(111). *Surface Science*, 287:995–999, May 1993.
- [46] M. Portalupi, L. Duo, G. Isella, R. Bertacco, M. Marcon, and F. Ciccacci. Electronic structure of epitaxial thin NiO(100) films grown on Ag(100): Towards a firm experimental basis. *Physical Review B*, 64(16):165402, October 2001.
- [47] J. Wollschläger, D. Erdös, H. Goldbach, R. Höpken, and K. M. Schröder. Growth of NiO and MgO films on Ag(100). *Thin Solid Films*, 400(1-2):1–8, December 2001.
- [48] M. Caffio, B. Cortigiani, G. Rovida, A. Atrei, C. Giovanardi, A. di Bona, and S. Valeri. Ultrathin nickel oxide films grown on Ag(001): a study by XPS, LEIS and LEED intensity analysis. *Surface Science*, 531(3):368–374, June 2003.
- [49] C. Lamberti, E. Groppo, C. Prestipino, S. Casassa, A. M. Ferrari, C. Pisani, C. Giovanardi, P. Luches, S. Valeri, and F. Boscherini. Oxide/metal interface distance and epitaxial strain in the NiO/Ag(001) system. *Physical Review Letters*, 91(4):046101, July 2003.
- [50] S. Großer, C. Hagendorf, H. Neddermeyer, and W. Widdra. The growth of thin NiO films on Ag(001) studied by scanning tunneling microscopy and spectroscopy. *Surface and Interface Analysis*, 40(13):1741–1746, December 2008.
- [51] F. Müller, R. de Masi, P. Steiner, D. Reinicke, M. Stadtfeld, and S. Hüfner. EELS investigation of thin epitaxial NiO/Ag(001) films: surface states in the multilayer, monolayer and submonolayer range. *Surface Science*, 459(1-2):161–172, July 2000.
- [52] Z. X. Shen, R. S. List, D. S. Dessau, B. O. Wells, O. Jepsen, A. J. Arko, R. Bartlett, C. K. Shih, F. Parmigiani, J. C. Huang, and P. A. P. Lindberg. Electronic-structure of NiO - Correlation and band effects. *Physical Review B*, 44(8):3604–3626, August 1991.
- [53] T. Bertrams and H. Neddermeyer. Growth of NiO(100) layers on Ag(100): Characterization by scanning tunneling microscopy. *Journal of Vacuum Science & Technology B*, 14(2):1141–1144, March 1996.
-

- 
- [54] M. Caffio, B. Cortigiani, G. Rovida, A. Atrei, and C. Giovanardi. Early stages of NiO growth on Ag(001): A study by LEIS, XPS, and LEED. *The Journal of Physical Chemistry B*, 108(28):9919–9926, 2004.
- [55] J. Szuber. Electronic-properties of the NiO(100) surface after thermal cleaning in ultrahigh-vacuum. *Journal of Electron Spectroscopy and Related Phenomena*, 34(4):337–341, 1984.
- [56] J. M. McKay and V. E. Henrich. Surface electronic-structure of NiO - Defect states, O<sub>2</sub> and H<sub>2</sub>O interactions. *Physical Review B*, 32(10):6764–6772, 1985.
- [57] H. Kuhlenbeck, G. Odörfer, R. Jaeger, G. Illing, M. Menges, T. Mull, H. J. Freund, M. Pöhlchen, V. Staemmler, S. Witzel, C. Scharfschwerdt, K. Wennenmann, T. Liedtke, and M. Neumann. Molecular adsorption on oxide surfaces - Electronic-structure and orientation of NO on NiO(100)/Ni(100) and on NiO(100) as determined from electron spectroscopies and abinitio cluster calculations. *Physical Review B*, 43(3):1969–1989, January 1991.
- [58] S. Polzin. PhD thesis (in preparation), Martin-Luther-Universität Halle-Wittenberg.
- [59] C. M. Cheng, C. C. Wang, J. Y. Yuh, D. J. Huang, and K. D. Tsuei. The electronic structure of ultrathin NiO films on Ag(100) surfaces studied by high resolution angle-resolved photoemission spectroscopy. *Journal of Magnetism and Magnetic Materials*, 310(2):E764–E766, March 2007.
- [60] S. Yang, S. Seong, and J. S. Kim. Electronic structure of ultrathin NiO films on Ag(001). *Journal of the Korean Physical Society*, 57(5):1312–1316, November 2010.
- [61] F. Cinquini, L. Giordano, G. Pacchioni, A. M. Ferrari, C. Pisani, and C. Roetti. Electronic structure of NiO/Ag(100) thin films from DFT+U and hybrid functional DFT approaches. *Physical Review B*, 74(16):165403, October 2006.
- [62] C. M. Cheng, C. C. Wang, H. T. Jeng, C. S. Hsue, B. Y. Hsu, D. J. Huang, and K. D. Tsuei. The angle-resolved photoemission study for ultrathin NiO and CoO thin films on Ag(100) surfaces. *Physica B-condensed Matter*, 403(5-9):1539–1541, April 2008.
- [63] G. A. Sawatzky and J. W. Allen. Magnitude and origin of the band-gap in NiO. *Physical Review Letters*, 53(24):2339–2342, 1984.
- [64] S. Hüfner. Electronic-structure of NiO and related 3d-transition-metal compounds. *Advances In Physics*, 43(2):183–356, March 1994.
- [65] V. Dose, W. Altmann, A. Goldmann, U. Kolac, and J. Rogozik. Image-potential states observed by inverse photoemission. *Physical Review Letters*, 52(21):1919–1921, 1984.
- [66] D. Straub and F. J. Himpsel. Identification of image-potential surface-states on metals. *Physical Review Letters*, 52(21):1922–1924, 1984.
-

- 
- [67] K. Giesen, F. Hage, F. J. Himpsel, H. J. Riess, and W. Steinmann. Two-photon photoemission via image-potential states. *Phys. Rev. Lett.*, 55(3):300–303, Jul 1985.
- [68] K. Giesen, F. Hage, F. J. Himpsel, H. J. Riess, and W. Steinmann. Binding-energy of image-potential states - Dependence on crystal-structure and material. *Physical Review B*, 35(3):971–975, January 1987.
- [69] T. Fauster. Two-photon photoemission. *Progress In Surface Science*, 46(2-3):177–186, June 1994.
- [70] T. Fauster and W. Steinmann. *Two-photon photoemission of image states*. In *Electromagnetic Waves: Recent developments in research*. Elsevier, Amsterdam, 1995.
- [71] A. Schäfer, I. L. Shumay, M. Wiets, M. Weinelt, T. Fauster, E. V. Chulkov, V. M. Silkin, and P. M. Echenique. Lifetimes of unoccupied surface states on Pd(111). *Physical Review B*, 61(19):13159–13163, May 2000.
- [72] W. Wallauer, R. Fischer, and T. Fauster. Influence of adsorbates on the image states of Pd(111). *Surface Science*, 364(3):297–302, September 1996.
- [73] J. D. McNeil, R. L. Lingle, R. E. Jordan, D. F. Padowitz, and C. B. Harris. Interfacial quantum well states of Xe and Kr adsorbed on Ag(111). *Journal of Chemical Physics*, 105(9):3883–3891, September 1996.
- [74] T. Hertel, E. Knoesel, A. Hotzel, M. Wolf, and G. Ertl. Femtosecond time-resolved photoemission of electron dynamics in surface Rydberg states. *Journal of Vacuum Science & Technology A-vacuum Surfaces and Films*, 15(3):1503–1509, May 1997.
- [75] A. Hotzel, G. Moos, K. Ishioka, M. Wolf, and G. Ertl. Femtosecond electron dynamics at adsorbate-metal interfaces and the dielectric continuum model. *Applied Physics B-lasers and Optics*, 68(3):615–622, March 1999.
- [76] K. J. Gaffney, C. M. Wong, S. H. Liu, A. D. Miller, J. D. McNeill, and C. B. Harris. Femtosecond electron dynamics at the benzene/Ag(111) interface. *Chemical Physics*, 251(1-3):99–110, January 2000.
- [77] W. Berthold, U. Höfer, P. Feulner, and D. Menzel. Influence of Xe adlayer morphology and electronic structure on image-potential state lifetimes of Ru(0001). *Chemical Physics*, 251(1-3):123–132, January 2000.
- [78] M. Rohleder, W. Berthold, J. Gudde, and U. Hofer. Photoelectron spectroscopy of Ar/Cu(100) interface states. *Applied Physics A-materials Science & Processing*, 88(3):527–534, August 2007.
- [79] P. M. Echenique, J. M. Pitarke, E. V. Chulkov, and A. Rubio. Theory of inelastic lifetimes of low-energy electrons in metals. *Chemical Physics*, 251(1-3):1–35, January 2000.
-

- 
- [80] P. M. Echenique, R. Berndt, E. V. Chulkov, T. Fauster, A. Goldmann, and U. Höfer. Decay of electronic excitations at metal surfaces. *Surface Science Reports*, 52(7-8):219–317, 2004.
- [81] R. Fischer, S. Schuppler, N. Fischer, T. Fauster, and W. Steinmann. Image states and local work function for Ag/Pd(111). *Physical Review Letters*, 70(5):654–657, February 1993.
- [82] K. Wandelt. The local work function: Concept and implications. *Applied Surface Science*, 111:1–10, February 1997.
- [83] R. Fischer, T. Fauster, and W. Steinmann. 3-dimensional localization of electrons on Ag islands. *Physical Review B*, 48(20):15496–15499, November 1993.
- [84] N. Fischer, S. Schuppler, T. Fauster, and W. Steinmann. Coverage-dependent electronic-structure of Na on Cu(111). *Surface Science*, 314(1):89–96, July 1994.
- [85] A. K. Kazansky, A. G. Borisov, and J. P. Gauyacq. Image and adsorbate state dependence on the adsorbate coverage in the Na/Cu(111) system. *Surface Science*, 544(2-3):309–319, October 2003.
- [86] P. de Andrés, P. M. Echenique, and F. Flores. Lifetime in a two-dimensional image-potential-induced electron band. *Physical Review B*, 35(9):4529–4532, March 1987.
- [87] P. de Andrés, P. M. Echenique, and F. Flores. Calculation of the lifetimes for intermediate Rydberg states. *Physical Review B*, 39(14):10356–10358, May 1989.
- [88] X. Y. Wang, R. Paiella, and R. M. Osgood. Two-dimensional electron-scattering processes on Na-dosed Cu(111) - A two-photon photoemission-study. *Physical Review B*, 51(23):17035–17039, June 1995.
- [89] A. Goswami and A. P. Goswami. Dielectric and optical properties of ZnS films. *Thin Solid Films*, 16(2):175–185, 1973.
- [90] A. Goswami and A. P. Goswami. AC behavior of vacuum-deposited praseodymium oxide-films. *Thin Solid Films*, 20(1):S3–S6, 1974.
- [91] U. Saxena and O. N. Srivastava. Unusual thickness dependence of dielectric-constant of erbium oxide-films. *Thin Solid Films*, 33(2):185–192, 1976.
- [92] S. M. Patel and V. George. Dielectric properties of  $\text{Sb}_2\text{S}_3$  Films. *Indian Journal of Physics and Proceedings of the Indian Association For the Cultivation of Science-part A*, 52(1):77–84, 1978.
- [93] H. Petek and S. Ogawa. Femtosecond time-resolved two-photon photoemission studies of electron dynamics in metals. *Progress In Surface Science*, 56(4):239–310, December 1997.
-

- 
- [94] S. Ogawa, H. Nagano, and H. Petek. Hot-electron dynamics at Cu(100), Cu(110), and Cu(111) surfaces: Comparison of experiment with Fermi-liquid theory. *Physical Review B*, 55(16):10869–10877, April 1997.
- [95] S. Hüfner, F. Hulliger, J. Osterwalder, and T. Riesterer. On the interpretation of valence band photoemission spectra of NiO. *Solid State Communications*, 50(1):83–86, 1984.
- [96] S. Hüfner, J. Osterwalder, T. Riesterer, and F. Hulliger. Photoemission and inverse photoemission spectroscopy of NiO. *Solid State Communications*, 52(9):793–796, 1984.
- [97] Z. X. Shen, C. K. Shih, O. Jepsen, W. E. Spicer, I. Lindau, and J. W. Allen. Aspects of the correlation-effects, antiferromagnetic order, and translational symmetry of the electronic-structure of NiO and CoO. *Physical Review Letters*, 64(20):2442–2445, May 1990.
- [98] S. Hüfner, P. Steiner, I. Sander, M. Neumann, and S. Witzel. Photoemission on NiO. *Zeitschrift Für Physik B - condensed Matter*, 83(2):185–192, 1991.
- [99] S. Hüfner, P. Steiner, I. Sander, F. Reinert, and H. Schmitt. The optical gap of NiO. *Zeitschrift für Physik B-condensed Matter*, 86(2):207–215, February 1992.
- [100] S. L. Dudarev, A. I. Liechtenstein, M. R. Castell, G. A. D. Briggs, and A. P. Sutton. Surface states on NiO (100) and the origin of the contrast reversal in atomically resolved scanning tunneling microscope images. *Physical Review B*, 56(8):4900–4908, August 1997.
- [101] D. Ködderitzsch, W. Hergert, Z. Szotek, and W.M. Temmerman. Ab initio study of the electronic and magnetic structure of NiO(001). *Journal of Magnetism and Magnetic Materials*, 240(1-3):439–441, February 2002.
- [102] M. Dane, M. Luders, A. Ernst, D. Ködderitzsch, W. M. Temmerman, Z. Szotek, and W. Hergert. Self-interaction correction in multiple scattering theory: application to transition metal oxides. *Journal of Physics-condensed Matter*, 21(4):045604, January 2009.
- [103] J. Kunes, V. I. Anisimov, S. L. Skornyakov, A. V. Lukoyanov, and D. Vollhardt. NiO: Correlated band structure of a charge-transfer insulator. *Physical Review Letters*, 99(15):156404, October 2007.
- [104] C. Rakete. *Photoemission und Photodesorption von NO auf NiO und Silberclustern mit Femtosekunden-Laserpulsen*. PhD thesis, Freie Universität Berlin, 2004.
- [105] A. Freitag, V. Staemmler, D. Cappus, C. A. Ventrice, K. A. Shamery, H. Kühlenbeck, and H. J. Freund. Electronic surface-states of NiO(100). *Chemical Physics Letters*, 210(1-3):10–14, July 1993.
- [106] B. Fromme, M. Möller, T. Anschütz, C. Bethke, and E. Kisker. Electron-exchange processes in the excitations of NiO(100) surface *d* states. *Physical Review Letters*, 77(8):1548–1551, August 1996.
-

- 
- [107] B. Fromme, M. Schmitt, E. Kisker, A. Gorschlüter, and H. Merz. Spin-flip low-energy electron-exchange scattering in NiO(100). *Physical Review B*, 50(3):1874–1878, July 1994.
- [108] W. Hergert and A. Ernst. Private communication.
- [109] N. E. Christensen. Band-structure of silver and optical interband transitions. *Physica Status Solidi B-basic Research*, 54(2):551–563, 1972.
- [110] F. Bechstedt. *Principles of Surface Physics*. Springer, 2003.
- [111] H. F. Roloff and H. Neddermeyer. High-resolution photoemission from Ag(100), Ag(110), and Ag(111). *Solid State Communications*, 21(6):561–564, 1977.
- [112] P. S. Wehner, R. S. Williams, S. D. Kevan, D. Denley, and D. A. Shirley. Valence-band structure of silver along  $\Lambda$  from angle-resolved photoemission. *Physical Review B*, 19(12):6164–6171, 1979.
- [113] H. Neddermeyer. Photoemission-study of the surface electronic-structure of Ag(100). *Journal of Physics F-metal Physics*, 12(11):L241–L244, 1982.
- [114] A. Goldmann and E. Bartels. High-resolution study of the  $\bar{M}$  surface-state on Ag(100). *Surface Science*, 122(2):L629–L634, 1982.
- [115] R. Courths, H. Wern, U. Hau, B. Cord, V. Bachelier, and S. Hüfner. Band-structure of Cu, Ag and Au - Location of direct transitions on the  $\Lambda$ -line using angle-resolved photoelectron-spectroscopy (ARUPS). *Journal of Physics F-metal Physics*, 14(6):1559–1572, 1984.
- [116] H. Wern, R. Courths, G. Leschik, and S. Hüfner. On the band-structure of silver and platinum from angle-resolved photoelectron-spectroscopy (ARUPS) measurements. *Zeitschrift Fur Physik B-condensed Matter*, 60(2-4):293–310, 1985.
- [117] J. R. Smith, F. J. Arlinghaus, and J. G. Gay. Electronic-structure of silver(100). *Physical Review B*, 22(10):4757–4763, 1980.
- [118] H. Eckardt, L. Fritsche, and J. Noffke. Self-consistent relativistic band-structure of the noble-metals. *Journal of Physics F-metal Physics*, 14(1):97–112, 1984.
- [119] G. Fuster, J. M. Tyler, N. E. Brener, J. Callaway, and D. Bagayoko. Electronic-structure and related properties of silver. *Physical Review B*, 42(12):7322–7329, October 1990.
- [120] H. Erschbaumer, A. J. Freeman, C. L. Fu, and R. Podloucky. Surface-states, electronic-structure and surface-energy of the Ag(001) surface. *Surface Science*, 243(1-3):317–322, February 1991.
- [121] T. Miller, W. E. McMahon, and T. C. Chiang. Interference between bulk and surface photoemission transitions in Ag(111). *Physical Review Letters*, 77(6):1167–1170, August 1996.
-

- 
- [122] T. Miller, E. D. Hansen, W. E. McMahon, and T. C. Chiang. Direct transitions, indirect transitions, and surface photoemission in the prototypical system Ag(111). *Surface Science*, 376(1-3):32–42, April 1997.
- [123] E. D. Hansen, T. Miller, and T. C. Chiang. Surface photoemission in Ag(100). *Physical Review B*, 55(3):1871–1875, January 1997.
- [124] L. Walldén and T. Gustafsson. Photoemission from Ag. *Physica Scripta*, 6(1):73, 1972.
- [125] J. G. Nelson, S. Kim, W. J. Gignac, R. S. Williams, J. G. Tobin, S. W. Robey, and D. A. Shirley. High-resolution angle-resolved photoemission-study of the Ag band-structure along  $\Lambda$ . *Physical Review B*, 32(6):3465–3471, 1985.
- [126] B. Reil and R. R. Schlittler. Empty electronic states of silver as measured by inverse photoemission. *Physical Review B*, 29(4):2267–2269, 1984.
- [127] C. E. Morris and D. W. Lynch. Piezoreflectance of dilute  $\alpha$ -phase Ag-In alloys. *Physical Review*, 182(3):719, 1969.
- [128] R. Rosei, C. H. Culp, and J. H. Weaver. Temperature modulation of optical-transitions involving Fermi-surface in Ag - Experimental. *Physical Review B*, 10(2):484–489, 1974.
- [129] W. L. Roth. Neutron and optical studies of domains in NiO. *Journal of Applied Physics*, 31(11):2000–2011, 1960.
- [130] S. Altieri, M. Finazzi, H. H. Hsieh, M. W. Haverkort, H. J. Lin, C. T. Chen, S. Frabboni, G. C. Gazzadi, A. Rota, S. Valeri, and L. H. Tjeng. Image charge screening: A new approach to enhance magnetic ordering temperatures in ultrathin correlated oxide films. *Physical Review B*, 79(17):174431, May 2009.
- [131] C. Kittel. *Einführung in die Festkörperphysik*. R. Oldenburg, 1999.
- [132] K. Marre, H. Neddermeyer, A. Chassé, and P. Rennert. Auger electron diffraction from NiO(100) layers on Ag(100). *Surface Science*, 357(1-3):233–237, June 1996.
- [133] P. W. Palmberg, R. E. Dewames, L. A. Vredevoe, and T. Wolfram. Coherent exchange scattering of low-energy electrons by antiferromagnetic crystals. *Journal of Applied Physics*, 40(3):1158, 1969.
- [134] K. Hayakawa, K. Namikawa, and S. Miyake. Exchange reflexions in low energy electron diffraction from antiferromagnetic nickel oxide crystal. *Journal of the Physical Society of Japan*, 31(5):1408, 1971.
- [135] F. Offi, S. Iacobucci, P. Vilmercati, A. Rizzo, A. Goldoni, M. Sacchi, and G. Panaccione. Attenuation lengths of low-energy electrons in solids: The case of CoO. *Physical Review B*, 77(20):201101, May 2008.
- [136] F. Banfi, C. Giannetti, G. Ferrini, G. Galimberti, S. Pagliara, D. Fausti, and F. Parmigiani. Experimental evidence of above-threshold photoemission in solids. *Phys. Rev. Lett.*, 94(3):037601, January 2005.
-



- 
- [137] S. Luan, R. Hippler, H. Schwier, and H. O. Lutz. Electron-emission from polycrystalline copper surfaces by multi-photon absorption. *Europhysics Letters*, 9(5):489–494, July 1989.
- [138] G. Farkas, C. Tóth, and A. Kőházi Kis. Above-threshold multiphoton photoelectric effect of a gold surface. *Optical Engineering*, 32(10):2476–2480, October 1993.
- [139] W. S. Fann, R. Storz, and J. Bokor. Observation of above-threshold multiphoton photoelectric emission from image-potential surface states. *Phys. Rev. B*, 44(19):10980, November 1991.
- [140] M. Aeschlimann, C. A. Schmuttenmaer, H. E. Elsayed-Ali, R. J. D. Miller, J. Cao, Y. Gao, and D. A. Mantell. Observation of surface-enhanced multiphoton photoemission from metal-surfaces in the short-pulse limit. *Journal of Chemical Physics*, 102(21):8606–8613, June 1995.
- [141] M. Fiebig, D. Frohlich, T. Lottermoser, V. V. Pavlov, R. V. Pisarev, and H. J. Weber. Second harmonic generation in the centrosymmetric antiferromagnet NiO. *Physical Review Letters*, 87(13):137202, September 2001.
- [142] I. Sanger, V. V. Pavlov, M. Bayer, and M. Fiebig. Distribution of antiferromagnetic spin and twin domains in NiO. *Physical Review B*, 74(14):144401, October 2006.
- [143] M. Nyvlt, F. Bisio, and J. Kirschner. Second harmonic generation study of the antiferromagnetic NiO(001) surface. *Physical Review B*, 77(1):014435, January 2008.
-



# Erklärung

Hiermit erkläre ich, dass ich gemäß dem §5, Absatz 2b der Promotionsordnung der Mathematisch-Naturwissenschaftlich-Technischen-Fakultät der Martin-Luther-Universität Halle-Wittenberg vom 9.11.2004, die vorliegende Arbeit selbstständig und ohne fremde Hilfe verfasst, andere als die von mir angegebenen Quellen und Hilfsmittel nicht benutzt und die den benutzten Werken wörtlich oder inhaltlich entnommenen Stellen als solche kenntlich gemacht habe.

Halle (Saale), 01.12.2011

Mario Kiel



# Lebenslauf

## Persönliche Daten

Name: Mario Kiel  
 Geburtsdatum: 05.08.1980  
 Geburtsort: Halle (Saale)  
 Familienstand: ledig, 2 Kinder

## Bildungsweg

Seit 04/2006	Promotion an der Martin-Luther-Universität Halle-Wittenberg Institut für Physik Fachgruppe Oberflächenphysik (Prof. Dr. W. Widdra)
03/2006	Abschluss des Studiums als Diplomphysiker
2000 - 2006	Studium der Physik (Diplom) Martin-Luther-Universität Halle-Wittenberg Schwerpunkt Oberflächenphysik, Anfertigung der Diplomarbeit zum Thema „Wachstum von $\alpha$ -Sexithiophen auf Au(111) und BaTiO <sub>3</sub> (111)“
1999 - 2000	Grundwehrdienst, Sachsen-Anhalt-Kaserne, Weißenfels
07/1999	Abitur am Südstadt-Gymnasium, Halle
1993 - 1999	Südstadt-Gymnasium, Halle
1991 - 1993	Sekundarschule Heinrich Heine, Halle
1987 - 1991	Grundschule Hans-Beimler, Halle

Halle (Saale), 01.12.2012



## Publikationsliste

1. M. KIEL, K. DUNCKER, C. HAGENDORF UND W. WIDDRA:  
*Molecular structure and chiral separation in  $\alpha$ -sexithiophene ultrathin films on Au(111): Low-energy electron diffraction and scanning tunneling microscopy*  
Physical Review B, 75(19):195439, 2007.
2. K. DUNCKER, M. KIEL, A. HÖFER UND W. WIDDRA:  
*Commensurate surface structures and concerted cis-trans-isomerization within ordered monolayers of  $\alpha$ -sexithiophene on Ag(001)*  
Physical Review B, 77(15):155423, 2008.
3. A. HÖFER, K. DUNCKER, M. KIEL, S. WEDEKIND UND W. WIDDRA:  
*Adsorption of  $\alpha$ -sexithiophene on Au(001): Molecule-induced partial lifting of the substrate reconstruction*  
Physical Review B, 83(7):075414, 2011.
4. K. DUNCKER, M. KIEL UND W. WIDDRA:  
*Momentum-resolved lifetimes of image-potential states on Ag(001)*  
in Vorbereitung.





# Danksagung

An dieser Stelle möchte ich bei denen bedanken, die am Erfolg der vorliegenden Arbeit beteiligt waren. Zunächst möchte ich mich bei Prof. Dr. Wolf Widdra bedanken, dass er mir die Möglichkeit gegeben hat an dem Aufbau und der stetigen Weiterentwicklung des neuen Experiments maßgeblich Teil zu haben. Für die scheinbar endlose Freiheit eigene Ideen zu erproben und diese auch erfolgreich umzusetzen, gepaart mit dem kritischen Hinterfragen über Aufwand und Nutzen sind sicher nur einige, wenn auch essentielle Aspekte die sowohl die Ergebnisse der vorliegenden Arbeit als auch das experimentelle Setup im Ganzen wesentlich geprägt haben.

Im direkten Zusammenhang mit letzterem sei auch Dr. Klaus Duncker genannt, der es geschafft hat mich für den optischen Teil des Experiments zu begeistern und an dessen Planung und Aufbau er wesentlich beteiligt war.

Da der Laser natürlich nicht mir allein gehörte, möchte ich mich auch bei Anke Höfer dafür bedanken, dass sie mir *einige Male* ihre Anteile unserer minutiös aufgeteilten Strahlzeit überlassen hat, um das ein oder (*alle*) *andere(n)* Experiment(e) in Ruhe beenden zu können.

Für eine sehr gelungene Kurzeinführung in die effiziente Programmierung in C möchte ich bei Dr. Michael Huth bedanken. Ohne seine Erfahrung und daraus resultierenden Ideen wären die entscheidenden Stellen der Software-Programmierung nicht so erfolgreich, wie sie es heute sind.

Für die gute Zusammenarbeit mit der feinmechanischen und elektronischen Werkstatt möchte ich mich stellvertretend für alle bei den Herren Benkwitz, Büttner, Schmetzdorf und Müller bedanken. Die scheinbar unendliche Anzahl von Aufträgen und die damit verbundenen Gespräche über deren Umsetzung waren stets eine schöne und lehrreiche Abwechslung zum sonstigen Laboralltag.

An dieser Stelle sei natürlich auch unserem Forschungsingenieur Ralf Kulla gedankt, der die meist unmöglichen Ideen eines Physikers in die reale Welt der Umsetzbarkeit zurückholte und mir behilflich war sie in seine Sprache zu übersetzen.

Für die Durchsicht des Manuskripts und der konstruktiven Kritik möchte ich mich bei Anke Höfer, Dr. Klaus Meinel und Dr. Cheng-Tien Chiang bedanken.

Ohne alle namentlich zu nennen, möchte ich mich natürlich rechtherzlich bei der gesamten Arbeitsgruppe Oberflächen- und Grenzflächenphysik bedanken. Das sehr

angenehme Arbeitsklima und die stetige Diskussionsbereitschaft aller werde ich ganz besonders in Erinnerung behalten.

Spezieller Dank gilt auch meinen Eltern, die mir zum einen mit ihrer Unterstützung das Studium der Physik ermöglicht haben und zum anderen stets gute Ratgeber für einige Aspekte des Lebens außerhalb der Laborarbeit waren.

Ganz besonderen Dank möchte ich meiner Lebensgefährtin Mandy Wendland und unseren Kindern Isabell und Cedric aussprechen, die mich des öfteren nach so manchem langen Arbeitstag gekonnt in das wahre Leben zurückholen konnten. Die aufgebrachte Geduld dafür, wenn sich das sprichwörtliche akademische Viertel wieder zu mehreren Stunden verlängert hat, werde ich euch nie vergessen. Ich liebe euch.

---